

INVESTIGATIONS ON MM-WAVE IMAGING RADAR FOR SHAPE AND FAULT DETECTION OF TARGETS

Ph.D. THESIS

by

SMRITI AGARWAL



**CENTER OF NANOTECHNOLOGY
INDIAN INSTITUTE OF TECHNOLOGY ROORKEE
ROORKEE-247667 (INDIA)
JUNE, 2015**

INVESTIGATIONS ON MM-WAVE IMAGING RADAR FOR SHAPE AND FAULT DETECTION OF TARGETS

A THESIS

*Submitted in partial fulfillment of the
requirements for the award of the degree
of*

DOCTOR OF PHILOSOPHY
in
NANOTECHNOLOGY

by

SMRITI AGARWAL



**CENTER OF NANOTECHNOLOGY
INDIAN INSTITUTE OF TECHNOLOGY ROORKEE
ROORKEE-247667 (INDIA)
JUNE, 2015**

**©INDIAN INSTITUTE OF TECHNOLOGY ROORKEE, ROORKEE-2015
ALL RIGHTS RESERVED**



INDIAN INSTITUTE OF TECHNOLOGY ROORKEE ROORKEE

CANDIDATE'S DECLARATION

I hereby certify that the work which is being presented in the thesis entitled **“INVESTIGATIONS ON MM-WAVE IMAGING RADAR FOR SHAPE AND FAULT DETECTION OF TARGETS”** in partial fulfillment of the requirements for the award of the Degree of Doctor of Philosophy and submitted in the **Center of Nanotechnology of the Indian Institute of Technology Roorkee** is an authentic record of my own work carried out during a period from July, 2010 to June, 2015 under the supervision of Prof. Dharmendra Singh, Professor, Department of Electronics and Communication Engineering, Indian Institute of Technology Roorkee.

The matter presented in the thesis has not been submitted by me for the award of any other degree of this or any other Institute.

(SMRITI AGARWAL)

This is to certify that the above statement made by the candidate is correct to the best of my knowledge.

Dated:

(DHARMENDRA SINGH)

Supervisor

The Ph. D. Viva-Voce Examination of **Mrs. Smriti Agarwal**, Research Scholar, has been held on

Chairman, SRC

Signature of External Examiner

This is to certify that the student has made all the corrections in the thesis.

Signature of Supervisor

Head of the Department

To the blessed memory of my father

Abstract

In recent years, millimeter wave (MMW) frequency (30GHz-300GHz) has received tremendous interest among researchers pertaining to its unique favorable features in contrast to the over flooded microwave frequency band, such as, finer resolution, higher data rate and size reduction. This makes it an ideal spectrum for applications, like, personal screening, medical imaging, quality monitoring, wireless communication etc. [183]. MMW frequency offers interesting applications in stand-off imaging because of its non-ionizing radiation in contrast to ionizing X-rays; its ability to penetrate through packaged materials in contrast to visible and IR systems; its higher resolution capability in contrast to microwave imaging. Thereby, MMW imaging has emerged as a preferable modality for finding fine details of the targets which may be useful to identify different target's characteristics, like, crack, void, delamination, corrosion, moisture content & porosity etc. For all these reasons, MMW technique is becoming increasingly important in different industrial, scientific and military applications.

Antenna is an indispensable component of any RF based system. At MMW frequency, design of a simple, compact and cost effective antenna is quite challenging because of metallic losses, dielectric losses, higher order/ surface wave modes loss, resonances as well as radiations in transmission line structures. Planar antenna technologies are worthwhile owing to its low profile, light weight, low cost, conformable and rigid characteristics [86]. Recently, the increasing demand of miniaturized and multi-tasking systems has excel the need for dual resonant MMW antennas that provide concurrency as well as redundancy [18]. However, dual band antenna at MMW frequency is still the least explored with few reported works using split ring resonator (SRR) [128], flip-chip assembly [285] and movable plate [184] techniques etc. Most of these reported antennas require sophisticated and high precision fabrication techniques, which make them complex and cost inefficient. Hence, major effort is needed to be paid in this direction for a simple, compact and cost-effective MMW dual band antenna design.

MMW imaging is one of the fascinating and rapidly expanding area for object's identification for security applications and for quality monitoring for industrial applications. Henceforth, critical investigation of digital image processing techniques in context to MMW imaging is currently becoming a new focused area of research. Various research works are carried out and going on for stand-off target's detection and its shape identification using different imaging techniques [52, 337, 352]. However, more focus is still required in this direction to develop an efficient MMW imaging methodology for accurate, non-invasive target's detection, shape identification and material classification.

In addition, target's recognition process can be made more robust by employing size and rotation invariant capability for correct target's shape identification in a real scenario. To enable reliable recognition of target's shape, the essential information in the form of unique, invariant features is extracted, like, scale invariant feature transform (SIFT), wavelet transforms, Harris corner detector, discrete Fourier descriptors etc. [215]. However, these algorithms are not fully adaptive and still significant research is required to develop a robust methodology which can be applied successfully to reconstruct target's images towards varying orientation, scale and translation errors due to non-uniform illumination and target's deformations.

Non-invasive inspection of different goods towards fatigue, wear and tear without hampering its utility and efficacy is also constantly desired. Since, MMW has the capability to penetrate through opaque material and can extract target's characteristic information, it provides a good solution towards non-invasive, easy and accurate quality inspection [144]. Quality monitoring of packaged goods (packaged ceramic tiles) for industrial applications is one of the fascinating domain, which needs special attention for a competent and cost efficient manufacturing. Thereby, a critical investigation of different image post-processing techniques towards their accurate crack detection capability requires special emphasis. In addition, a robust methodology is needed to be developed for an automatic, adaptive quality monitoring (*i.e.*, fault detection) of packaged goods for industrial applications.

As per aforementioned research gaps, following tasks have been carried out in this thesis work: (i) Design of a simple, cost-effective and compact MMW dual frequency planar antenna, (ii) Stand-off target's shape identification and its material classification using MMW imaging system, (iii) Development of size and rotation invariant target's shape identification algorithm for MMW imaging system, (iv) Development of an adaptive quality monitoring algorithm to detect fault (crack) in packaged ceramic tiles for industrial applications with MMW imaging

system. This thesis consists of seven chapters. *Chapter 1* presents the introduction which consists of motivation, scope and objectives of the thesis. *Chapter 2* provides a brief literature review for the considered objective(s), their limitations and research gaps.

Chapter 3 explores the design for MMW concurrent dual frequency planar antenna. Designing of an antenna at MMW is a quite challenging task because of several limitations, which are needed to be undertaken, for an optimal antenna performance, like, *choice of suitable substrate*: since at MMW frequency, surface waves are more likely to be excited which reduces antenna radiation efficiency; *fabrication constraint*: commonly used techniques at lower microwave frequencies, viz., slot, notch, spur, multiple stacked patches, metamaterials etc. needs stringent fabrication and alignment accuracies (due to correspondingly low wavelength $\lambda/2 \approx 1.5$ mm to 2.5 mm), so a relatively simpler technique is needed to be used without complicating the fabrication procedure or raising the cost. Therefore, in this chapter, a single layer, simple, compact and conformable antenna structure has been proposed operating concurrently at the two MMW frequencies 60 GHz and 85 GHz, which are having future commercial, strategic and industrial applications. The technique investigated for concurrent MMW antenna operation is *stub loaded rectangular patch* because of its simple and feasible fabrication. The proposed MMW antenna design was firstly simulated and analyzed using 3D full wave EM solver HFSS on Rogers RT5880 substrate ($\epsilon_r = 2.2$, $h = 5$ mil (0.127 mm), $\tan\delta = 0.002$). Further, fabrication and measurement of MMW antenna prototype was performed and measured results were found in close approximation with that of simulated ones, giving fractional bandwidth 1% /6.4 % and measured gain 8.95 dBi/5.37 dBi, at 60/85 GHz, respectively. At MMW, in order to maintain measurement compatibility with GSG probe, a 50Ω coplanar waveguide (CPW) feedline and a wideband CPW to microstrip transition structure were separately designed and later on integrated into the antenna structure in order to couple maximum power from CPW feed to the radiating patch. The designed antenna structure is simple, cost-effective and compact having 3.7 mm^2 cross-sectional area.

Chapter 4 explores the capability of MMW frequency towards standoff target's shape identification and its material classification. For this, a stepped frequency continuous wave (SFCW) active imaging radar system was ingeniously designed at our MISTA lab, IIT Roorkee, India using vector network analyzer (VNA) operating in V band (60 GHz) [6]. For complete target's data acquisition, C-scan (horizontal and vertical scanning) methodology was used, which gives us target's information in terms of length and width. The data acquired undergoes several

signal pre-processing steps, *such as*, frequency to time domain (IFFT) conversion, time to spatial domain conversion, relative calibration and windowing for generating C-scan images. This C-scan image is known as raw C-scan image. The main aim of this chapter is to identify the shape and classify the material of the targets. So, raw C-scan image undergoes several post-processing steps, *viz*, clutter removal, thresholding, edge detection and classification. One of the major problem for this type of radar images is the clutter. To remove clutter, we have applied singular value decomposition (SVD) technique, which has the advantage of improved image quality, compressibility and is better in preserving edge details as compared to other techniques, like, Principle Component Analysis (PCA), Factor analysis (FA) and Independent Component Analysis (ICA) [46]. After removing the clutter, thresholding based image segmentation was carried out because of its simplicity of implementation. The image statistics based mean and standard deviation global thresholding has been used. Edges are useful features for segmentation and object identification in images, which characterize object boundaries. Criterion relevant to edge detector's optimum performance is good detection, good localization and single response. The common edge detection algorithms were critically analyzed and it was found that canny based edge detector is better than the other techniques, like, sobel, prewitt, roberts, laplace [210]. Therefore, canny based edge detector has been used after thresholding to identify the shape of the respective targets, *i.e.*, triangle, square, circle, rectangle. Various models, like, estimation of dielectric is one of the way to identify and classify the target's material. But in this work an image analysis based technique, *i.e.*, probability density function (*pdf*) based approach has been proposed to classify the target's materials (we have considered wood and metal only). It has been observed that this pdf based approach has a good potential to classify the target's materials.

Chapter 5, proposes a novel artificial neural network (ANN) based scale and rotation invariant image reconstruction model. Neural network has been used as an effective signal processing technique for classification/recognition of targets for various applications, like, speech recognition, character recognition, pattern recognition etc. Correct shape identification is one of the challenging problems because it suffers from orientation and size deformations in any practical environment. In chapter 4, while target's shape identification; we have not considered orientation and size effect. Whereas, in this chapter we have proposed a pattern recognition based neural network algorithm to identify target's shape, which has the capability to minimize any orientation and size variations. For algorithm development, we have used four different regular target's shapes (*i.e.*, rectangle, square, triangle, and circle). A single shape has been considered

in different sizes and is put into different orientation angles (randomly ranging from 0° to 90°), thereby, experimental data set of total 33 samples of C-scan data is captured using the MMW imaging system having varying combinations of orientations and sizes of different considered regular shaped targets. As we want to recognize shape, the output training data was generated in accordance to the input target's size and was in binary (0, 1) matrix form. For image recognition problem formulation, a multilayer feed-forward neural network has been used. Any independent target's data when fed as the input to the ANN model, the output generated will be the correct target's shape and size irrespective of its orientation. The proposed methodology, thus, has the capability to identify the target's shape by minimizing size and orientation error.

Chapter 6 deals in non-invasive undercover fault detection methodology for industrial quality control applications using the ingeniously designed MMW radar system. Accurate monitoring and classification of packaged ceramic tiles (cracked/non-cracked) is quite important, which could otherwise result in financial/ reputational loss to the company, besides it is particularly challenging because of non-uniform illumination, alignment errors and insufficient contrast in practical industrial scenario. Our main purpose is the fault detection, and here, we have considered crack as a fault. Therefore, large number of packaged ceramic tile targets with different crack and non-crack configurations were used for algorithm development and its validation. For this purpose, two approaches have been proposed. First: feature extraction based classification approach. Second: Spatial statistical based approach. In the first approach, critical investigation of different commonly used feature extraction techniques has been done for accurate model development with minimum false alarm. For this, an automatic feature based neural network classifier model has been proposed by investigating five different commonly used feature extraction techniques, *i.e.*, discrete fourier transform (DFT), Daubechies wavelet transform (WT), texture features, principal component analysis (PCA) features and histogram of oriented gradient (HOG) based features. Out of these, the optimal classification accuracy has been achieved by HOG-NN classifier model because HOG feature has an advantage of developing the training sample on a cell/ window basis, which has more information than the whole tile based feature techniques. This has been validated using an independent set of packaged ceramic tiles. It is a quantitative approach, which tells whether the packaged tile is cracked or non-cracked. Further, to visualize the crack location, we have also developed a spatial statistics based model, which is based on image reconstruction approach and provides information about location of the crack also. The statistical parameters (maxima, minima, median, and standard

deviation) of target's image play an important role in determining particular target's characteristics, and also vary largely even for similar type of targets owing to non-uniform illumination, clutter, different multipath reflections, etc. Hence, it is quite essential to develop a statistics based generalized, adaptive crack classification and localization algorithm to make it more robust and adjustable as per frequent changes in image parameters in real scenario. Since, crack could be anywhere on the ceramic tile and of any random type, a window based statistical pattern search model has been proposed to scan the complete tile sequentially and to detect cracked locations, apart from just the crack/ non-crack classification. A mathematical formulation has also been developed for achieving user defined performance goals of accuracy and false alarm and an optimum threshold value is searched through GA optimization for crack/ non-crack location estimation. Here, while algorithm development main emphasis was to achieve near to zero false alarm for non-cracked full packaged ceramic tiles so as to avoid any unwanted loss and to further improve industry quality production. The developed proposed algorithm was also validated through independent packaged ceramic tile targets and was found to perform quite well.

In *chapter 7*, the contributions made in the thesis are summarized and scope of future work is outlined. The proposed MMW robust target's shape identification and adaptive quality monitoring model for ceramic tiles will be certainly helpful to make a complete automated system for industry.

Acknowledgements

Now, at this stage I am totally clueless how to describe my long expedition that I started few years back with lots of dreams, expectations in my mind and that too I have to sum up in this very few paragraphs. I could not have reached at this destination without the support of so many persons that I have come through.

The one person to whom I admire, honor, acclaim, trust, rely and cherish is one and only my GREAT supervisor ‘Prof. Dharmendra Singh’. He has been always there to help me both technically and morally as well as he cares for everyone by all his means and this is his forte that makes him unique in all senses. I am very much thankful for his excellent guidance and inculcating research and personal skills in me. His physical intuition and ability to resolve and simplify complex problems has always helped me excel my research findings. It is his zeal for research that I could have been able to accomplish my research work in an advanced topic of high frequency imaging with limited resources in hand. Without his untiring efforts, stimulating discussions, and motivational examples I would not have been writing this page for completion towards my thesis.

I also want to extend my sincere thanks to the Head, Center of Nanotechnology, Prof. R. Jayaganthan for providing all the necessary facilities to me related to research. This acknowledgement will be incomplete without mentioning the names of my research committee members, chairman sir: Dr. Anil Kumar; my external SRC: Dr. Vipul Rastogi and my internal SRC: Dr. Anand Balusu, for their valuable suggestions and healthy criticism during my research work presentations. I also want to accede other esteemed faculty members Dr. N. P. Pathak, Dr. S. Manhas, Dr. V. Agarwala, for their support and help in different ways, may be it teaching research course works or other technical talks.

I am indebted to Department of Science and Technology (DST), Government of India, New Delhi, for providing me the financial assistance under *Women Scientist Scheme (WOS-A)*

to carry out this research work. My deepest regards goes to Department of Electronics & Communication Engineering, for providing me the working platform and well equipped laboratory to carry out my research tasks. I want to convey my heartfelt obligations to Dr. Dharmendra Singh for providing me a space in his research lab with an ideal research environment.

I will never forget the company I had from my fellow students and friends. In particular, I am thankful to my present and past research colleagues of Microwave Imaging and Space Technology Applications (MISTA) lab Dr. Smitha mam, Dr. Abhishek Sir, Dr. Pooja, Neeraj Sir, Tasneem, Nazim, Ankita, Akanksha, Bambam, and Varsha for the congenial cheering work environment and for the round of discussions altogether sometimes regarding research, sometime social, political and cinematic reviews. My special thanks go to dear Shruti and Ravi for patiently proofreading my thesis and help me in presenting it in a better way. At this point it will be quite unfair not to mention the MISTA lab's young and dynamic brigade comprising Gopal, Deepak and Ankush. I also want to mention my other colleagues and friends Vivek, Sneha mam and Amarjeet in the department for their encouragement and support.

I am thankful to former and present M. Tech. and IDD students with whom I have interacted during different technical, non-technical sessions Ghanshyam, Yogendra, Ankit, Amit, Sandeep, Sonali, Goodwill, Ramesh, Faiz, Santosh, Ajay, Arunima, Jaydeep, Swapnil, Shashi, and Uday. I wish to convey my appreciation and my deepest prayers to all of them to achieve success and happiness in their future endeavors.

I am thankful to lab technicians Mr. Raja Ram, Mr. Gaur and Mr. Giri for helping me out in fabrication, measurement and making arrangement of experiments required for the research work. I would like to thank Shrawan in the Remote Sensing Lab for his helping hand during the experimental work and his serving tea, snacks which comes as a tonic during long, monotonous study hours.

I extend my deepest gratitude to my mother (Mrs. Geeta Agarwal), for her blessings, hardships, prayers and countless fastings, enriching values in my life by showing me that education is not only measured by academic titles but by ethics, integrity, kindness and diversity of interests.

I wish to acknowledge my profound appreciation to my brother (Mr. Sachin Agarwal), my sister (Mrs. Shalini Agarwal), my in-laws (Mrs. Krishna Garg, Mr. Satish Chandra Garg) for their anytime assistance and full support in various ways. It was their patience, encouragement

and faith in me that I could complete this thesis. My this journey would not be possible or even instigated without the firm support of my lovely husband Manoj who had been my all-time best friend, always caring and nurturing when I was stressed or tensed. I admire him for his unconditional love and patience during all these years. His excellent soft skills have made my way of thesis writing much smoother and this thesis documentation is itself a ready example of his expertise in it. Most importantly, my lifeline and my beloved princess 'GAURI', I would like to express my extraordinary thanks and love for her being such a wonderful daughter and always cheering me up with her mind blowing ideas. Kudos to her for bearing exemplary patience through the years and particularly through the course of the long, late night hours spent during completion on this thesis.

It would be impossible to acknowledge all the people who contributed either technically or by offering their friendship towards the completion of this work. I am thankful to all those who were associated with my research journey directly or indirectly and to whom I forgot to mention here unknowingly. My thesis has been a wonderful experience and I cherish the educational and personal growth it has provided to me for my future endeavors.

-Smriti Agarwal

Table of Contents

Abstract	i
Acknowledgements	vii
Table of Contents	xi
List of Tables	xv
List of Figures	xvii
List of Acronyms	xxiii
List of Symbols	xxvii
Chapter 1 Introduction	1
1.1. Motivation	2
1.2. Problem Statement	6
1.3. Framework of the Research	7
1.4. Basics of Antenna Design and SFCW Based Imaging	9
1.4.1. Dual Frequency Planar Antenna Design Prerequisites	9
1.4.2. SFCW Imaging Radar System Design and Imaging Parameters	15
1.5. Organization of the Thesis	22
Chapter 2 Literature Review	23
2.1. Millimetre Wave Frequency Features and its Applications	24
2.2. Review of Work Related to MMW Dual Resonant Planar Antenna Design	25
2.2.1. Dual Band Antenna Techniques at Microwave Frequency	26
2.2.2. Review of Work on MMW Dual Frequency Antennas	27
2.3. Review of Work Related to MMW Imaging	29

2.3.1.	Review of Works Related to Target's Shape/ Size Identification	29
2.3.2.	Review of Work Related to Non-Destructive Testing and Fault Estimation	31
2.3.3.	Review of DIP Techniques for MMW Imaging	33
2.4.	Conclusion	40

Chapter 3 Design of Simple, Cost-Effective and Compact Millimeter Wave Dual Frequency Planar Antenna 43

3.1.	Introduction	43
3.2.	Theoretical Background	45
3.2.1.	Choice of Suitable Substrate	46
3.2.2.	Power Loss Due to Surface Waves	46
3.2.3.	Conductor and Dielectric Losses	47
3.2.4.	Probe Measurement Feasibility	47
3.2.5.	Fabrication Constraint	48
3.3.	Methodology for MMW Dual Frequency Planar Antenna Design	48
3.3.1.	Section 1: Dual frequency Radiating Patch Geometry	48
3.3.2.	Section 2: Feeding Section	52
3.3.3.	Section 3: Matching Network	55
3.4.	Simulation Results	56
3.4.1.	Microstrip Line Characterization at MMW Frequency	56
3.4.2.	FG-CBCPW Transmission Line Simulation	58
3.4.3.	Design of CB-FGCPW to Microstrip Line Transition Structure	59
3.5.	Fabrication and Measurement of Designed MMW Dual Resonant Planar Antenna	60
3.6.	Conclusion	63

Chapter 4 Stand-off Target's Shape Identification and its Material Classification Using Millimeter Wave Imaging System 65

4.1.	Introduction	65
4.2.	Theoretical background	68
4.2.1.	Signal pre-processing	68
4.2.2.	Signal post-processing	69
4.3.	Data used	71

4.4.	Methodology used for development and implementation of target's identification algorithm	72
4.4.1.	Signal pre-processing	72
4.4.2.	Signal post-processing for Target's Shape Identification (Subtask 1)	74
4.4.3.	Signal post-processing for Target's Material classification (Subtask 2)	78
4.5.	Experimental results and discussion	80
4.5.1.	Target's location detection (steps 1-3)	80
4.5.2.	Implementation for Target's Shape Identification (Subtask 1)	81
4.5.3.	Implementation for Target's material classification (Subtask 2)	85
4.6.	Validation	88
4.7.	Overall Results of Fully Developed Target's Shape Identification and Material Classification Technique	90
4.8.	Conclusion	92
Chapter 5 Development of Size and Rotation Invariant Target's Shape Identification Algorithm for Millimeter Wave Imaging System		93
5.1.	Introduction	94
5.2.	Theoretical Background	96
5.3.	Data set used	97
5.4.	Methodology used to develop size and rotation invariant artificial neural network model	100
5.4.1.	Introduction to the ANN model	100
5.4.2.	ANN model development for rotation and size invariant target's image reconstruction	102
5.4.3.	Training of the developed Neural Network Model	105
5.4.4.	Developed ANN Model Testing	106
5.5.	Validation of the developed ANN model	108
5.6.	Conclusion	109
Chapter 6 Development of an Adaptive Quality Monitoring Algorithm to Detect fault (Crack) in Packaged Ceramic Tiles for Industrial Applications with MMW Imaging System		111
6.1.	Introduction	112

6.2.	Theoretical Background	114
6.2.1.	Sub Task 1- Feature Extraction-Based-ANN Classification Model: A Quantitative Approach	114
6.2.2.	Subtask 2- Image Spatial Statistics Based Crack Localization Model: An Approach for Localization of Cracks	115
6.3.	Observations for Non-Invasive Concealed Crack Detection/ Localization of Ceramic Tiles with MMW Imaging Radar	116
6.3.1.	Data Used: Packaged Ceramic Tile	117
6.3.2.	Signal Pre-Processing and C-Scan Image Formation	120
6.3.3.	Critical Investigations on the Need of an Adaptive and Automatic Crack Detection Model	121
6.4.	Methodology for Feature-Based-ANN Crack Classification Model (Subtask 1)	121
6.4.1.	Feature Selection	122
6.4.2.	Implementation of Feature-Based-ANN Model for Crack Classification	132
6.4.3.	Validation	139
6.4.4.	Concluding Remarks (for subtask 1)	142
6.5.	Development of an Adaptive Statistical Model for Crack Localization Based on Image Reconstruction (Subtask 2)	142
6.5.1.	Undercover Target's Image Enhancement: Discrete Convolution	142
6.5.2.	Proposed Statistical Methodology for Crack Localization	144
6.5.3.	Validation of Proposed Adaptive Algorithm	155
6.5.4.	Concluding Remarks (for Subtask 2)	157
6.6.	Conclusion	157
Chapter 7	Conclusions and Future Scope	159
7.1.	Contributions of the Thesis	159
7.2.	Future scope	163
	Author's Publications	167
	References	169

List of Tables

Table 1.1.	Specifications for SFCW based active MMW imaging radar	18
Table 3.1.	Final dimensions of the designed dual frequency MMW planar antenna.	60
Table 3.2.	Measured values of fabricated dual frequency MMW antenna prototype	62
Table 3.3.	Comparison of the performance of reported MMW dual frequency antennas with our designed MMW dual frequency antenna	62
Table 4.1.	Different regular shaped targets used for target's identification algorithm development	71
Table 4.2.	Chi Square best fit test for various distribution functions on different test targets T2 and T3	87
Table 4.3.	Determining range of parameters of Cauchy distribution function for classification	87
Table 4.4.	Validation Results for target's material classification	90
Table 4.5.	Different Signal processing steps and their outcomes for target's shape identification and target's material classification	91
Table 5.1.	Different target's shape, size and orientation variations undertaken for size and rotation invariant target's image recognition ANN model development	98
Table 5.2.	Complete detailed list of different target samples undertaken with varying sizes and orientations	99
Table 5.3.	Tabular presentation of proposed neural network model for four different regular shape targets, viz, rotated rectangle: i26, rotated square: i35, Circle: i16, tilted triangle: i46	107

Table 5.4.	Results of the proposed trained neural network model using a different independent set of test samples, i48 - tilted triangle, i39 - tilted square	108
Table 6.1.	Different crack/ non-crack target tile configurations and their notations used	119
Table 6.2.	DFT-NN classifier model result using test targets	136
Table 6.3.	WT-NN classifier model result using test targets	136
Table 6.4.	PCA-NN classifier model result using test targets	137
Table 6.5.	Texture-NN classifier model result using test targets	138
Table 6.6.	HOG-NN classifier model result using test targets	139
Table 6.7.	Classification accuracy assessment of proposed feature-based-ANN model using independent validation target samples by comparing DFT-NN, DWT-NN, PCA-NN, texture-NN, HOG-NN classifier models	141
Table 6.8.	Mathematical formulations of $OA(x)$ and $FA(x)$ with corresponding R^2 values for different ceramic tile test targets	151
Table 6.9.	Proposed GA Optimized statistical algorithm performance results for few test targets	154
Table 6.10.	Output results of the proposed statistical algorithm for non-destructive undercover crack detection using independent validation target tiles	156

List of Figures

Figure 1.1.	Flowchart for research framework.	9
Figure 1.2.	(a) Rectangular microstrip planar antenna, (b) effective length of antenna and fringing of field.	10
Figure 1.3.	Antenna radiation pattern: (a) 3D graphical representation, (b) 2D Principal plane patterns.	13
Figure 1.4.	Orthogonal-mode dual frequency patch antenna: (a) single feed-using probe, (b) single feed- using aperture coupling, (c) dual feed-using probe, (d) dual feed- using aperture coupling.	14
Figure 1.5.	Multiple-patch dual frequency antennas, (a) co-planar patches, (b) vertically stacked patches.	14
Figure 1.6.	Reactively loaded dual frequency patch antenna using: (a) notch, (b) shorting pin, (c) square slot, (d) stub.	15
Figure 1.7.	Step frequency increment of the transmitted SFCW radar waveform	16
Figure 1.8.	Experimental setup for MMW active imaging radar with the target mounted on a 2D scanning frame.	18
Figure 1.9.	A-scanning at a fixed antenna location.	20
Figure 1.10.	B-scanning at different horizontal scanning positions.	21
Figure 1.11.	Representation for 3D C-scan by stacking multiple B-scans at different vertical scanning positions.	21
Figure 2.1.	Atmospheric and molecular absorption at MMW frequency.	24
Figure 3.1.	CPW fed MMW dual resonant antenna geometry- 60/85 GHz (dimensions not to scale). (a) Antenna 1: single frequency antenna, (b) Antenna 2: dual frequency antenna.	50

Figure 3.2.	Surface current distribution for dual band MMW antenna at: (a) 60 GHz and (b) 85 GHz.	50
Figure 3.3.	Effect of varying stub length (L_s) and stub width (W_s) on: (a) the two dual resonant frequencies f_1 and f_2 and (b) on the frequency ratio (f_2/f_1) characteristic.	51
Figure 3.4.	Geometry of finite ground conductor backed (FG-CBCPW) transmission line: (a) perspective view, (b) cross-sectional and top view.	53
Figure 3.5.	Microstrip line: (a) perspective view, (b) cross-sectional and top view, (c) E-field distribution vector of quasi TEM mode.	54
Figure 3.6.	The quarter-wave matching transformer.	56
Figure 3.7.	Microstrip line characteristic plots: (a) characteristic impedance (Z_0) and effective dielectric constant (ϵ_{eff}) vs conductor normalized width (W_M/H) plot at a fixed frequency ($f = 60$ GHz), dispersion in microstrip line characteristics with frequency for a fixed 50Ω conductor width: (b) variation in Z_0 and (c) variation in reflection/transmission loss.	57
Figure 3.8.	FG-CBCPW transmission line characteristics: (a) E-field vector distribution of fundamental CPW mode, (b) characteristic impedance vs frequency, (c) reflection/transmission characteristic plot vs frequency.	58
Figure 3.9.	A back to back transition of finite ground conductor backed coplanar waveguide (FG-CBCPW) to microstrip transmission line: (a) Geometric structure and (b) Simulated reflection/transmission loss vs frequency plot.	59
Figure 3.10.	Fabricated prototype of designed MMW dual frequency-60/85 GHz antenna & its SEM image (70x-zoom SEM).	61
Figure 3.11.	Comparative (measured vs simulated) reflection coefficient vs frequency plot for the designed dual band (60/85 GHz) MMW antenna.	61

Figure 4.1.	Flowchart showing different signal processing steps for stand-off target's image identification and its material classification	70
Figure 4.2.	Different target shapes mounted on a 2D-scanning wooden frame enabling horizontal and vertical movement for complete C-scan (a) T1: rectangle, (b) T2: triangle, (c) T3: circle, (d) T4: square.	71
Figure 4.3.	(a) Range profile plot, (b) target's downrange distance after sheet calibration, (c) B-scan image of background metal sheet.	81
Figure 4.4.	3D view (slicing) of C-scan images at target's downrange position: (a) T2, (b) T3.	82
Figure 4.5.	Surface distribution plot for pixel intensity of 2D C-scan image: (a) T2, (b) T3.	82
Figure 4.6.	Comparison of two test target's C-scan images; (a) raw image, (b) image after applying image enhancement technique (background subtraction and singular value decomposition).	83
Figure 4.7.	2-D C-scan image of the two test target's after applying mean and standard deviation based global thresholding (a) T2, (b) T3.	84
Figure 4.8.	2-D C-scan image of the two test targets obtained after canny edge detection (a) T2 (b) T3.	85
Figure 4.9.	Comparative probability density function plots for the two target's material classes metal and wood: (a) Cauchy pdf, (b) Normal pdf, (c) Weibull pdf, (d) Rayleigh pdf, for test targets of triangle shape T2.	86
Figure 4.10.	Validation results of the developed methodology for stand-off target's complete information (shape and size estimation): (a) 3D C-scan plot, (b) surface distribution plot, (c) raw C-scan image plot, (d) image after clutter reduction, (e) image after thresholding, (f) image after edge detection.	89
Figure 5.1.	A multilayer perceptron neural network model with one hidden layer, input layer and output layer.	100
Figure 5.2.	Flow chart describing generation of rotation and size invariant neural network model.	103

Figure 5.3.	Configuration of rotation and scale invariant neural network for target's image recognition. It consists of (24 x 32, 25) input units, 30 hidden units and (24 x 32, 25) outputs units.	105
Figure 6.1.	Experimental demonstration of ingeniously configured MMW imaging radar system for non-invasive packaged ceramic tile crack estimation.	117
Figure 6.2.	Target arrangement for concealed crack detection in packaged ceramic tiles: (a) pictorial demonstration, (b) ceramic tile mounted on the scanning frame, (c) ceramic tile covered with the packaging cardboard.	118
Figure 6.3.	Actual photographs of some test targets used for concealed crack detection of ceramic tiles: Final complete covered view of any target is shown in inset (lower left corner), the undercover ceramic tile target's configuration (crack/non-crack) is zoomed in: (a) full non-cracked (<i>fl</i>), (b) horizontally cracked (<i>hc3</i>), (c) vertically cracked (<i>vc3</i>), (d) diagonally cracked (<i>dc5</i>), (e) randomly cracked (<i>rc7</i>).	119
Figure 6.4.	2D C scan image at the target's downrange distance for different tile configurations, (a) <i>fl</i> , (b) <i>f2</i> , (c) <i>f5</i> , (d) <i>dc5</i> , (e) <i>f3</i> , (f) <i>hc6</i> , (g) <i>hc3</i> , (h) <i>rc7</i> , (i) <i>rc2</i> , (j) <i>vc3</i> , (k) <i>vc8</i> .	120
Figure 6.5.	Discrete wavelet transform of image matrix using single level Daubechies decomposition (db2): (a) 2D wavelet transform computation flowchart, (b) Four sub-band image decomposition coefficients: approximation, vertical, horizontal, diagonal.	124
Figure 6.6.	Demonstration of nearest neighbour cells orientation with respect to any central resolution cell entry. Cells 1 & 5 are 0° nearest neighbours and cells 2 & 6 are 135° nearest neighbours to resolution cell (*) and so on.	127
Figure 6.7.	Diagram illustrating division of cell and overlapping of blocks in the extracted image detection window for histogram-of-oriented-gradient (HOG) feature calculation for the tile image of size [12	132

	pixels x 12 pixels], cell size = [3 pixels x 3 pixels], block size = [2 cells x 2 cells].	
Figure 6.8.	Flow Chart for the proposed feature-based-ANN classifier model for non-invasive crack tile classification.	133
Figure 6.9.	Configuration of neural network for target's classification. It consists of input layer (feature vector length x 30 I/p samples), 50 hidden layer, and 2 output layer.	134
Figure 6.10.	HOG feature descriptor representation for different cells of the extracted target's image detection window for (a) Non-cracked full tile, (b) Cracked tile.	138
Figure 6.11.	Test target's images obtained after enhancement for different tile configurations: (a) <i>f1</i> , (b) <i>f2</i> , (c) <i>f5</i> , (d) <i>dc5</i> , (e) <i>f3</i> , (f) <i>hc6</i> , (g) <i>hc3</i> , (h) <i>rc7</i> , (i) <i>vc3</i> , (j), <i>vc8</i> .	144
Figure 6.12.	Graph showing relative behavior of window matrix based statistical measures; ($[Mx-Mn] = [Maxima-Minima]$ and $M - S = [Median - Standard\ deviation]$) for (a) non-cracked window matrices and (b) cracked window matrices of different packaged ceramic tile test targets: <i>hc3</i> , <i>vc3</i> , <i>dc5</i> , <i>rc7</i> .	146
Figure 6.13.	Plots showing the effect of varying scaling parameter ' <i>n</i> ' on the behavior of two statistical metrics ($Mx - Mn$) and $M - (n - 1)S$, for ceramic tile test target <i>hc3</i> for; (a) non-cracked windows, and (b) cracked windows of a test target tile.	148
Figure 6.14.	Performance plot of the proposed window based statistical algorithm showing (a) Overall Accuracy vs <i>n</i> ; and (b) False alarm vs <i>n</i> , for different ceramic tile targets: <i>hc3</i> , <i>vc3</i> , <i>dc5</i> , <i>rc7</i> .	149
Figure 6.15.	Plot of (a) Overall accuracy vs <i>x</i> and, (b) False alarm vs <i>x</i> , for different ceramic tile test targets (<i>hc3</i> , <i>vc3</i> , <i>dc5</i> , <i>rc7</i>).	150
Figure 6.16.	Flow chart showing different implementation steps of the proposed statistical based non-destructive undercover crack detection methodology.	153

Figure 6.17.	Detection of cracked tile windows using proposed adaptive statistical crack localization algorithm for different test tile targets: (a) <i>fl</i> , (b) <i>hc3</i> , (c) <i>vc3</i> , (d) <i>dc7</i> .	154
Figure 7.1.	Complete flow chart for estimating target's shape and target's material information in any practical environment using the ingeniously designed MMW imaging radar system.	162
Figure 7.2.	Pictorial demonstration of proposed non-invasive, non-destructive packaged ceramic tile's fault classification model for industrial quality monitoring applications.	165

List of Acronyms

1D	One dimensional
2D	Two dimensional
3D	Three dimensional
ADS	Agilent's advanced design system
ANN	Artificial neural network
BSS	Blind source separation
BW	Band width
CBCPW	Conductor backed-CPW line
CMOS	Complementary metal-oxide semiconductor
CPM	Coplanar microstrip mode
CPW	Coplanar waveguide
CR	Cross range
DCT	Discrete cosine transform
DFT	Discrete Fourier transform
DUT	Device under test
DWT	Discrete wavelet transform
EM	Electromagnetic
FA	Factor analysis
FG-CBCPW	Finite ground conductor backed CPW line
FMCW	Frequency modulated continuous wave
GLCM	Gray level co-occurrence matrix
GPR	Ground penetrating radar
GSG	Ground-signal-ground
HFSS	High frequency structure simulator
HMMs	Hidden markov models

HNN	Holographic nearest-neighbor algorithm
HOG	Histogram of oriented gradients
HPBW	Half power beam width
ICA	Independent component analysis
IFFT	Inverse fast Fourier transform
LBP	Local binary patterns
LTCC	Low-temperature co-fired ceramic
MIC's	Monolithic integrated circuits
MLP	Multilayer perceptron
MMIC	Millimeter wave monolithic integrated circuit
MMW	Millimeter wave
MOGP	Multi-objective genetic programming
MSA	Microstrip antenna
MSE	Mean square error
MSL	Microstrip line
NDT& E	Non-destructive testing and estimation
NN	Neural network
NRD	Non-radiative dielectric
PC	Principle component
PCA	Principal component analysis
PDF	Probability density function
RADAR	Radar ranging and detection
SAR	Synthetic aperture radar
SFCW	Step frequency continuous wave
SIFT	Scale invariant feature transform
SIW	Substrate integrated waveguide
SNR	Signal to noise ratio
SOM	Self-organizing map
SRD	Segmented range detection
SRRs	Split-ring resonators
STFT	Short time Fourier transform
SURF	Speeded up robust features

SVD	Singular value decomposition
SVM	Support vector machine
TEM	Transverse electromagnetic
TOSM	Through open short and Match
TWI	Through wall imaging
VNA	Vector network analyzer
WPAN	Wireless personal area network

List of Symbols

Chapter 1

Γ	Complex reflection coefficient
μ_0	Free space permeability
ϵ_0	Free space dielectric constant
ϵ_r	Relative permittivity
c	Speed of light
f_r	Resonant frequency
Z_0	Characteristic impedance of microstrip line
ϵ_{eff}	Effective dielectric constant
$D(\theta, \varphi)$	Directivity of antenna
$G(\theta, \varphi)$	Gain of antenna
η_r	Radiation efficiency
θ	Elevation angle
ϕ	Azimuth angle
λ_0	Free space wavelength
τ	SFCW pulse width
ϕ_n	Phase difference of n^{th} SFCW pulse
ΔR	Range resolution of imaging radar
ΔCR	Cross-range resolution of imaging radar

Chapter 3

f_c	Cut-off frequency
ϵ'	Real part of dielectric constant
ϵ	Complex dielectric constant

ε''	Imaginary part of dielectric constant
Q	Quality factor
$\tan\delta$	Dielectric loss tangent
σ	Conductivity
μ	Permeability
Ω	Impedance in ohms
λ_g	Guided wavelength in the dielectric
β	Propagation constant
S_{11}	Reflection coefficient

Chapter 4

N	Number of frequency points in SFCW radar
f_n	n^{th} discrete frequency step
Z_0	Unambiguous range of the radar
Z	Target distance from radar
Δf	Frequency step size of SFCW radar

Chapter 5

δ	Error term in ANN output
ζ	Scaling constant
θ	Weight bias in ANN
w	Connection weight function
α	Learning rate

Chapter 6

σ	Variance
μ	Mean
δ	Standard deviation
ϕ	Wavelet scaling function
Ψ	Wavelet directional sensitive functions

Chapter 1

Introduction

In recent years, millimeter wave (MMW) frequency (30GHz-300GHz) has received tremendous interest among researchers pertaining to its unique and favorable features in contrast to the over flooded microwave frequency band [50, 235]. MMW encounters higher atmospheric attenuation which favors higher frequency re-use over very short distances, thus, allowing high throughput secured network applications. Moreover, due to the large available bandwidth and associated lower wavelength, it supports multi-gigabit data rate (WPAN-IEEE 802.15.3c, IEEE 802.11ad) as well as miniaturized systems. Additionally, MMW's lend themselves as an excellent candidate for high resolution, stand-off imaging applications, like, non-invasive target's shape identification and its quality estimation. The capabilities and applications of the MMW's are vast and diverse, thereby, presently getting tremendous attention among researchers around the globe.

Along with these fascinating applications, MMW experiences certain technological challenges due to correspondingly small sizes of the resonant structures, henceforth, it is quite challenging to realize components, systems without elevating the complexity. Additionally, with the increasing demand for multi-tasking, portable devices, techniques for dual band MMW systems are more stringent. In any MMW system, antenna is an element responsible for routing the EM traffic from transmission line to free space and vice-versa. Presently, different techniques are being practiced for dual band MMW antenna design, but still it is a quiet challenging task to design such an antenna having simple, compact and cost-effective design.

Efforts to capture visions beyond the range of human eye have long fascinated scientists and engineers. Nowadays, imaging devices have been used as a precious tool in many fields of security, meteorological, military, medical and space exploration, etc., and have effect in all aspects of our life [99, 305, 324]. Particularly, radar imaging has become the most ubiquitous

technologies for non-invasive and non-destructive imaging. An EM wave incident on a medium is scattered in all directions when it encounters a change in electric or magnetic properties of the medium. A careful analysis of scattered EM waves leads to a better understanding of the characteristics of the medium in a holistic way. Today, imaging radars are massively used in various fields ranging from mapping the earth and weather patterns, to creating images of objects buried in the ground, or hidden behind obstructions [89, 144]. One of the major concerns of imaging radar that has recently received great significance is the target's shape identification and its material classification apart from just detection in order to capture more realistic, complete information and the proper threat level estimation of the targets. Another, increasingly demanding area is the quality monitoring of packaged goods for industrial applications for an automated, prompt and non-invasive fault inspection system. Any such type of technique will significantly improve the throughput of company as well as the quality of the final output products.

1.1. Motivation

There are several imaging modalities available having different resolution capabilities and unique spectral characteristics. State-of-the-art EM based imaging techniques suffer from several limitations, like, microwave imaging languish from lower resolution, hence, difficult to provide target's shape identification; X-ray imaging generates harmful ionizing radiation, hence, not safe for human exposure, and visible/IR imaging has the incapability to penetrate through concealed objects, hence, inapplicable for non-destructive testing [109]. Hereafter, in the surge of an efficient imaging spectrum, MMW frequency (30 GHz - 300GHz) is presently receiving considerable attention, which offers interesting and favorable features because of its ability to penetrate through clothing in contrast to visible and IR systems limitations; its higher resolution capability in contrast to microwave imaging; and its non-ionizing radiation (MMW radiates power up to $5\text{mW}/\text{cm}^2$ with shallow penetration depth (<0.5 mm), hence, medically safe to the human body) in contrast to ionizing X-rays [110, 351]. Resolution is a property of an image that describes the level of fine details which can be discerned from it. MMW imaging systems provide sufficiently high spatial resolution and can be realized using comparably small antenna sizes needed for a practical and deployable system. MMW finds its use in different practical areas related to personal screening, military applications, concealed objects/weapons, medical

imaging, quality monitoring, moisture content and material characterization, etc. [136, 196, 270]. There exist many challenges for the development of a successful imaging radar system. The system performance should be robust to minimize the ambiguities and inaccuracies in targets and it should be able to function properly under inhomogeneity and non-stationary in the sensing environment.

The science of radar imaging is based on spatial mapping of the distribution of target's image contrast in a scene. In *passive imaging*, this contrast is a function of temperature and emissivity distribution of the background and the reflectance distribution of the target. However, in an indoor environment, this temperature contrast adversely affects the quality of the image formed, hence poses the limitation for passive imaging systems. *Active imaging* uses artificially generated radiation to illuminate the target. Here, the formed image is dominated by the target's reflectance distribution and is independent of surrounding temperature. The RADAR (*Radio Detection and Ranging*) sensor transmits EM waves towards a target (or object), and then receives the scattered EM waves back from it. The two-way travel time (τ) of the EM wave is associated with the range (R) of the target, and is defined as $R = c\tau/2$, where, c is the speed of light in free space [288]. The radar system should also have high range and cross-range resolutions, which could be required for different system applications. To be a high-resolution radar (HRR) sensor, shortened pulse width τ or higher bandwidth (B) of the pulse is needed. The higher bandwidth of the pulse is restricted by available technologies [127]. According to the waveform used for transmission, the radar sensor can be categorized as a pulsed or Continuous - Wave (CW). The *pulsed radar sensor* typically transmits a short pulse train at very low power levels and is cost effective and simple. However, it cannot support both high range resolution and deep penetration simultaneously [288]. The *Frequency Modulated Continuous Wave (FMCW) radar* sensor uses a beat frequency (f_b) to seek the range (R) information of a target, where the beat frequency accounts for the relative time delay (τ) of the transmitted signal to the returned signal [223]. Wide bandwidth of the FMCW radar sensor degrades the receiver's sensitivity and results in reducing penetration depth and degree of accuracy. A *stepped frequency continuous wave radar (SFCW) radar* sensor provides the range resolution of wideband systems with the advantages of narrowband systems [78]. It is a contemporary technology that can be implemented with off-the-shelf components. This makes step-frequency radar cost effective and an attractive technique to achieve high range resolution, particularly in an era of declining defense expenditures towards the development of new radars.

One of the main components of any imaging radar system is an antenna which determines how efficiently a radio device can transfer EM waves from a transmission line to free space and vice versa. At MMW frequencies, the short wavelength enables integration of antenna for monolithic integrated circuits (MIC's), which favors the choice of using a planar antenna [122, 341]. Further, demands of multiprocessing and multitasking applications have accelerated the need for dual frequency antennas and systems [168, 277]. Nevertheless, designing of a dual frequency antenna at MMW frequency is quiet challenging due to associated low dimensions and higher precision requirements. Moreover, parasitic and higher order mode losses need special attention to design a simple, compact and cost-effective MMW dual frequency antenna [172, 238].

In context to imaging, for accurate identification of the targets, its sufficient spatial details have to be extracted for its image formation from the reflectivity data of the targets as recorded by the MMW imaging radar system. These fine target's details would help to estimate the correct target's information in terms of its shape, size which can be useful to the end user for its interpretation [272, 325]. To meet these challenges, research in MMW imaging is mainly directed in areas of signal processing, pattern analysis techniques and adaptive algorithm development, which could facilitate automatic target's shape identification without human intervention. The identification of targets becomes more challenging in the presence of strong clutter. The signal received from radar consists of addition of the desired response of targets with other signals arising mainly from radar system parameters, background reflections, environment and multiple reflections. These undesired components in the received signal are referred to as clutter. Researchers have developed various clutter reduction techniques to enhance target detection/identification accuracy and reduce false alarms, *viz*, factor analysis, principal component analysis, singular value decomposition and factor analysis [2, 46]. In addition, in order to enable the user to discriminate between the object and the background as well as to differentiate between different objects, several image enhancement and segmentation processing steps are applied. For extracting relevant target's information, thresholding and edge detection techniques have been proposed [14, 321, 353]. However, due to varying intensity levels in target/ background and non-uniform illumination, investigations on optimum target's image enhancement technique for MMW imaging requires special devotion. Merely target's identification in terms of its shape and size does not facilitate proper discrimination between simple innocuous items, such as, glasses, belt buckles, keys, toy items, etc., and actual threats, because of possible shape similarities among

them. This may lead to a rather higher number of nuisance alarms. A fundamentally different security measure is required to handle these threat situations, possibly in terms of target's material classification apart from just identification [164, 333]. Thereby, appropriate research is required in order to develop a technique for target's material information extraction.

In many practical, real world imaging scenarios, target's shape identification becomes quite challenging due to distortions in the target's image, which may occur due to randomly varying target's sizes and its orientations. In practical applications, we cannot expect the target's to be imaged will be in the exact position, angle and will be of fixed size. Hence, any fixed methodology may not provide accurate target's shape identification for varying conditions. An invariant and robust methodology is essentially required which could adaptively read the target's changes related to size and orientation and provide the correct target's shape identification. Different invariant feature extraction techniques are available for different applications [178, 215], but in the context of MMW imaging there is a need to develop an adaptive and robust algorithm, which can be applied successfully to reconstruct the target's images defying varying distortion levels, *i.e.*, orientation, scale and translation errors due to noise, non-uniform illumination [6].

Moreover, MMW frequency has the capability to penetrate through an opaque material/clothing and can extract target's characteristic information [117, 182]. MMW, thereby, offers a good imaging tool for inspection of quality and condition of industry goods/ materials towards fatigue, wear and tear without hampering its utility and efficacy. Research works for various non-destructive testing and estimation (NDT& E) applications include wafer inspection for delamination [136], surface crack detection [219, 240], corrosion, void [148, 356], moisture content [194] etc. In addition, it may also provide a good solution towards non-invasive quality inspection of packaged ceramic tiles for industry applications. In view of these possible fascinating MMW features, a critical investigation of different image processing and computer vision techniques towards their fault detection capability is essentially required and a robust methodology is needed to be developed for an automatic crack scanning for the quality check of packaged goods. Henceforth, MMW based imaging systems could provide a good choice towards non-invasive, easy and accurate quality assessment.

1.2. Problem Statement

The present research work aims to utilize MMW frequency for providing a compact, simple and cost-effective dual frequency planar antenna design and a fully adaptive, promising MMW radar imaging solution to the target's shape identification and its material classification. Additionally, objectives of the research work are to explore the applicability of different image processing techniques to develop novel algorithms for devising simple and adaptive solution for concealed target's fault detection/ localization for industrial quality monitoring applications. Some of the key challenges and issues inherent in the development of antenna design and the algorithms include:

- 1) At MMW frequency, radiated power encounters much higher losses due to surface wave and higher order mode propagation and thereby, reduces antenna efficiency. Further, fabrication and measurement constraints are more stringent due to correspondingly much lower dimensions at MMW.
- 2) It is very difficult to extract the desired target's information, *i.e.*, its shape identification and target's material classification due to lack of proper methodology in terms of different post-processing techniques.
- 3) Accurate target's shape identification may be adversely affected due to distortions in the image in real situations in terms of improper target's orientation and size variations.
- 4) Quality monitoring of concealed objects may produce false alarms in practical industrial scenario owing to non-uniform illumination, background noise and unwanted multipath reflections.

Different tasks that were accomplished keeping in mind the above-said challenges and limitations are:

- i. **Task 1:** Design of a simple, cost-effective and compact MMW dual frequency planar antenna.
- ii. **Task 2:** Stand-off target's shape identification and its material classification using MMW imaging system.
- iii. **Task 3:** Development of size and rotation invariant target's shape identification algorithm for MMW imaging system.
- iv. **Task 4:** Development of an adaptive quality monitoring algorithm to detect fault (crack) in packaged ceramic tiles for industrial applications with MMW imaging system.

1.3. Framework of the Research

The complete framework of the proposed research work is presented in Figure 1.1 which is categorized mainly as: (i) A simple, compact and cost-effective concurrent dual frequency MMW antenna design, and (ii) Development of fully adaptive and automatic algorithm for target's shape and fault (crack) detection. Following subtasks have been performed for completing the considered four tasks discussed in section 1.2:

- The Critical review of related literature to the problems corresponding to each task and identify the limitations of the exiting solutions.

Task 1 deal with the design of a simple, cost-effective and compact MMW dual frequency planar antenna that includes following subtasks:

- Development of an appropriate methodology for achieving dual frequency MMW planar antenna design.
- Keeping in view of measurement compatibility, the design of a coplanar transmission line and a CPW-to –microstrip line transition structure.
- Simulation and modelling of different antenna sub-sections and the complete antenna structure using EM wave solver HFSS.
- Fabrication of designed dual frequency antenna on Rogers RT5880 substrate and measurement of antenna parameters, viz., resonant frequency, fractional bandwidth, gain.

Task 2 emphasizes on stand-off target's shape identification and its material classification using MMW imaging system which includes following subtasks:

- To ingeniously design the MMW SFCW imaging radar setup for target's imaging.
- Target's preparation for its shape identification and observations.
- Critical analysis of different signal post processing techniques, viz., clutter reduction, thresholding and edge detection in order to have target's shape information.
- Development of target's material classification algorithm.

Task 3 focuses on the development of size and rotation invariant target's shape identification algorithm for MMW imaging system that includes following subtasks:

- Target's preparation, i.e., targets of four regular shapes, viz., square, rectangle, triangle and circle were taken in different sizes and mounted in different orientation angles between 0° to 90°.

- Development of size and rotation invariant algorithm for target's shape identification for MMW imaging system.
- Validation of the developed algorithm using the independent targets of random sizes and orientations of the four regular shapes.

Task 4 deals with the development of an adaptive quality monitoring algorithm to detect fault (crack) in packaged ceramic tiles for industrial applications, which is accomplished by following subtasks:

- Target's preparation for non-invasive concealed fault (crack) detection by considering packaged ceramic tiles in different crack/ non-crack configurations.
- Investigations on different feature extraction techniques in view of developing an automatic optimum feature-based-fault classification model.
- Development of an adaptive algorithm for fault (crack) localization in packaged ceramic tiles using target's image spatial statistical parameters.

A brief insight to the basics of the two broad objectives of the research work, *i.e.*, (i) MMW dual frequency planar antenna design, and (ii) MMW imaging radar system design is given below:

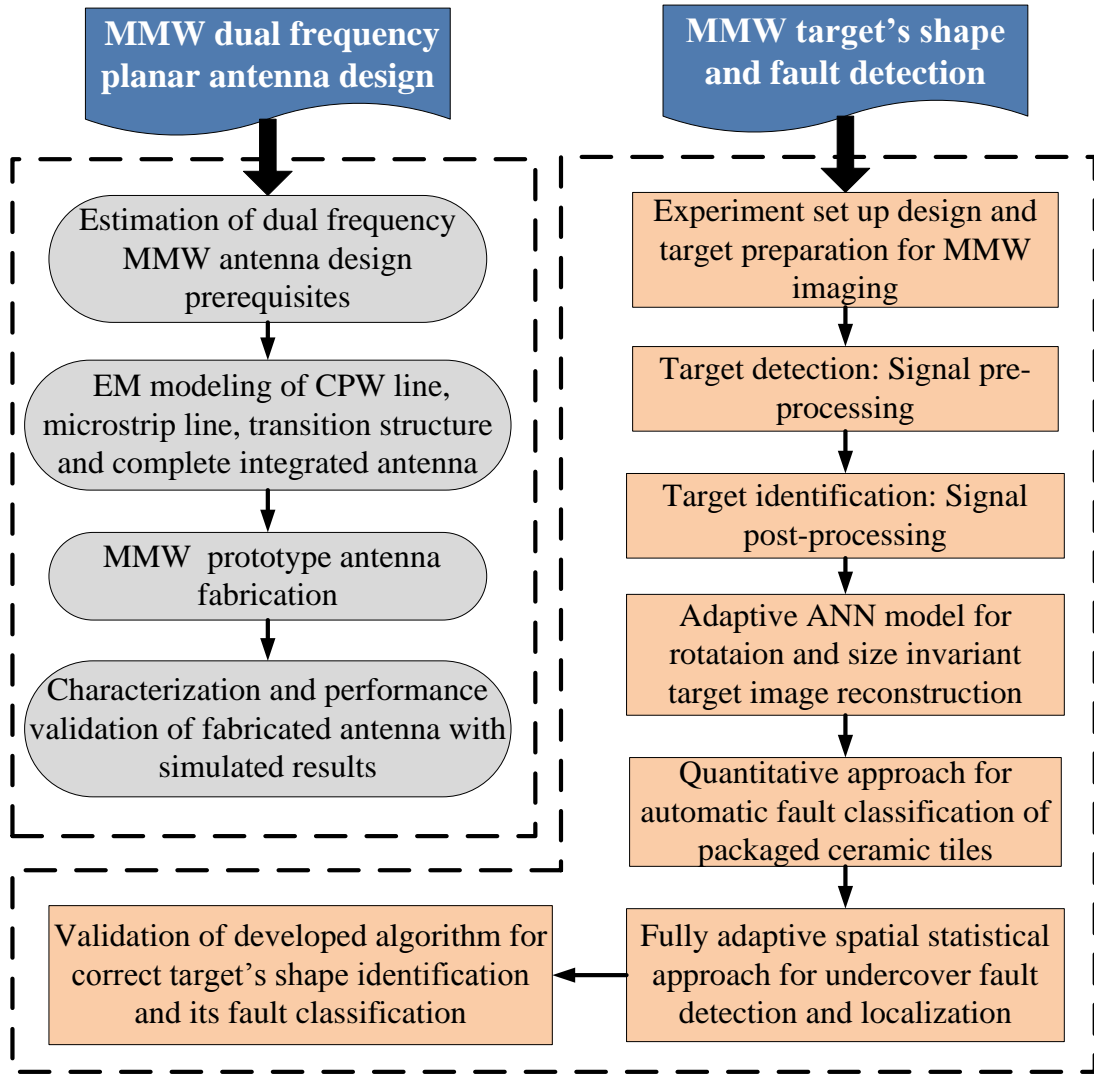


Figure 1.1. Flowchart for research framework.

1.4. Basics of Antenna Design and SFCW Based Imaging

1.4.1. Dual Frequency Planar Antenna Design Prerequisites

One of the important constituents of a successful MMW imaging system, is an efficient antenna design, which should provide simplicity of fabrication, integration for MMIC implementation and should be commercially competent. In this context, planar antennas find natural charm due to their features of low profile, simple, conformable, rigid and robust characteristics [27, 86].

1.4.1.1. Planar Antenna Design Equations

The basic structure of microstrip antenna consists of a rectangular conducting patch of length (L) and width (W) as shown in Figure 1.2(a). The microstrip antenna can be represented by two radiating slots along the length of the patch (each of width W and height h) due to the fringing fields as shown in Figure 1.2(b). For the dominant TM_{010} mode, the resonant frequency (f_r) of microstrip antenna depends on its length (L) and given by [27],

$$(f_r)_{010} = \frac{1}{2L_{eff}\sqrt{\epsilon_{eff}}\sqrt{\mu_0\epsilon_0}} \quad (1.1)$$

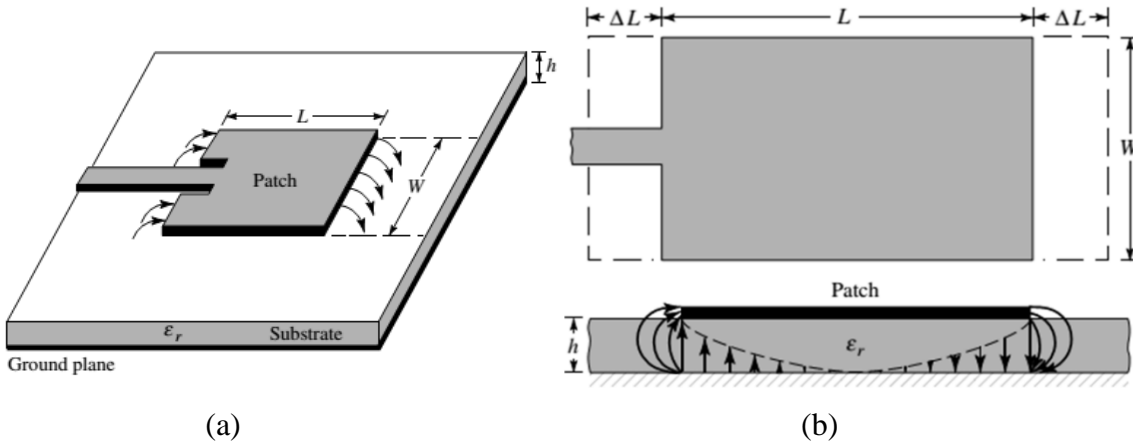


Figure 1.2. (a) Rectangular microstrip planar antenna, (b) effective length of antenna and fringing of field [27].

Here, L_{eff} is the effective length due to fringing electric fields present at the radiating edges, μ_0 is the free space permeability and ϵ_0 is the free space permittivity, ϵ_{eff} is the effective dielectric constant, given by [239]:

$$\epsilon_{eff} = \frac{\epsilon_r + 1}{2} + \frac{\epsilon_r - 1}{2} \left[1 + 12 \frac{h}{W} \right]^{-1/2} \quad (1.2)$$

Here, ϵ_r is the substrate relative permittivity, h is the height of the substrate and W is the patch width. The actual patch length L can be calculated by taking into account fringing field effect, given by [27],

$$L = L_{eff} - 2\Delta L = \frac{1}{2f_r\sqrt{\epsilon_{eff}}\sqrt{\mu_0\epsilon_0}} - 2\Delta L \quad (1.3)$$

$$\frac{\Delta L}{h} = 0.412 \frac{(\varepsilon_{eff} + 0.3) \left(\frac{W}{h} + 0.264\right)}{(\varepsilon_{eff} - 0.258) \left(\frac{W}{h} + 0.8\right)} \quad (1.4)$$

where, ΔL is the extension length due to fringing. The width of radiating patch is given by [27],

$$W = \frac{1}{2f_r \sqrt{\mu_0 \varepsilon_0}} \sqrt{\frac{2}{\varepsilon_r + 1}} \quad (1.5)$$

In this design, microstrip feedline is used to excite the patch. For a given characteristic impedance Z_0 , W/h can be found by the standard formula [27] as follows:

$$\frac{W}{h} = \begin{cases} \frac{8e^A}{e^{2A} - 2} & \text{for } W/h < 2 \\ \frac{2}{\pi} \left[B - 1 - \ln(2B - 1) + \frac{\varepsilon_r - 1}{2\varepsilon_r} \left\{ \ln(B - 1) + 0.39 - \frac{0.61}{\varepsilon_r} \right\} \right] & \text{for } W/h > 2 \end{cases} \quad (1.6)$$

$$\text{Where, } A = \frac{Z_0}{60} \sqrt{\frac{\varepsilon_r + 1}{2}} + \frac{\varepsilon_r - 1}{\varepsilon_r + 1} \left(0.23 + \frac{0.11}{\varepsilon_r} \right) \quad B = \frac{377\pi}{2Z_0\sqrt{\varepsilon_r}}$$

1.4.1.2. Basic Antenna Parameters

The performance of the antenna is evaluated using some basic parameters for all kinds of antennas regardless of its structure or frequency. A brief description of parameters is given below that will be later on used:

➤ Return Loss

It is a measure of the effectiveness of power delivery from a transmission line to a load, *i.e.*, antenna. If the power incident on the antenna is P_{in} and power reflected back to the source is P_{ref} , the degree of mismatch between incident and reflected power is given by ratio P_{in}/P_{ref} . The higher is the power ratio, better the load and line are matched. Return loss is defined as [31]:

$$RL = S_{11} = 10 \log_{10} \left(\frac{P_{in}}{P_{ref}} \right) \text{ dB} \quad (1.7)$$

Which is a *positive* quantity since, $P_{ref} < P_{in}$. Expressing the power in terms of voltage (or, field strength) in a transmission line, then Equation (1.7) becomes

$$RL = 10 \log_{10} \left| \frac{1}{\Gamma^2} \right| dB = -20 \log_{10} |\Gamma| dB \quad (1.8)$$

where, Γ is the complex reflection coefficient at the input of the antenna. That is, return loss is the negative of the reflection coefficient expressed in decibels. As a rule of thumb, return loss > 10 dB is considered to be good for an antenna, which means 90% of incident power is radiated, however, only 10% power is reflected back to the source.

➤ **Bandwidth**

Antennas are based on a resonance phenomenon and hence they have a certain impedance bandwidth (BW). The impedance bandwidth is usually defined as a frequency range, in which the absolute value of the reflection coefficient remains below a certain predefined level. Typically, $|\Gamma|^2 \leq -10$ dB is used as a matching criteria for integrated planar antennas.

➤ **Gain**

One of the parameters defining the radiation properties of an antenna is the gain of the antenna $G(\theta, \phi)$, which is a product of $D(\theta, \phi)$ and radiation efficiency η_r . Radiation efficiency is a ratio of the radiated power P_{rad} and the power accepted by the antenna P_{in} . Directivity $D(\theta, \phi)$, is the power density radiated to a certain direction (θ, ϕ) in the standard spherical coordinate system divided by the average power density. Thereby, realized gain includes the matching losses as well, and is defined as [27]

$$G(\theta, \phi) = \eta_r D(\theta, \phi) \quad (1.9)$$

➤ **Radiation Pattern**

It is the graphical representation of antenna's radiation properties as a function of space coordinates, in the far-field region of the antenna. It describes how the antenna radiates energy out into space (or how it receives energy). Since, the antenna radiates energy in all directions, at least to some extent, so the antenna pattern is actually three-dimensional as shown in Figure 1.3(a). However, antenna radiation can be easily visualized using two *principal planar* patterns, viz., *azimuth plane pattern* and *elevation plane pattern*. The term *azimuth* refers to “the horizon” or “the horizontal” whereas the term *elevation* refers to “the vertical”. In Figure 1.3(b), the x-y plane ($\theta = 90^\circ$) is the azimuth plane. The elevation plane is orthogonal to the x-y plane, say the y-z plane ($\phi = 90^\circ$) [116].

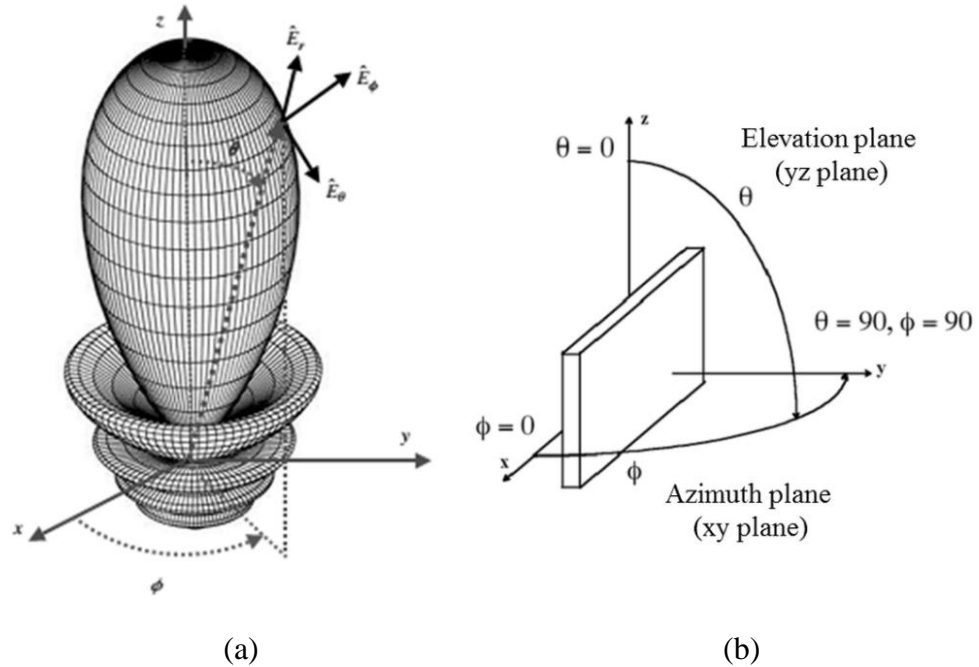


Figure 1.3. Antenna radiation pattern: (a) 3D graphical representation, (b) 2D Principal plane patterns [27].

The radiation pattern of a patch antenna is characterized by a single main lobe of moderate beamwidth. The two radiating slots form a two-element array with a spacing of $\lambda/2$ between them. The components of the field in the two slots add in-phase, in a direction perpendicular to the ground plane, giving a maximum radiation normal to the patch, therefore, microstrip patch is a *broadside radiating antenna* [27].

1.4.1.3. Dual Resonance Techniques

Increasing demand of miniaturized and multi-tasking communication devices, has excel the design of dual band RF systems and hence there is a need for dual resonant MMW antennas that could provide concurrency as well as redundancy. Typically used techniques are:

➤ Orthogonal Mode Dual-Frequency Patch Antennas [181, 304]

It uses the first resonance of two orthogonal dimensions of the patch, *i.e.*, TM_{10} and TM_{01} modes and can be achieved by using single feed or dual feed as shown in Figure 1.4 by the example antenna configurations. The obvious limitation of this approach is that the two different frequencies excite two orthogonal polarizations. However, this is a simple method and very useful in low-cost, short-range applications.

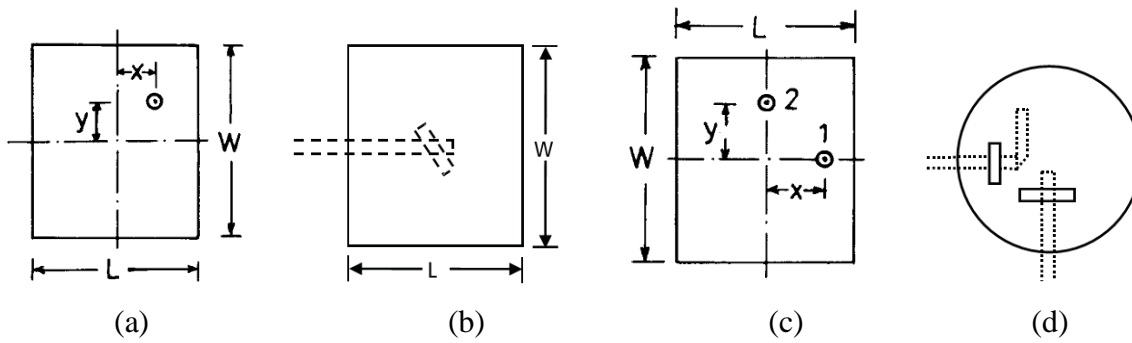


Figure 1.4. Orthogonal-mode dual frequency patch antenna: (a) single feed-using probe, (b) single feed- using aperture coupling, (c) dual feed-using probe, (d) dual feed- using aperture coupling [157].

➤ Multi-Patch Dual Frequency Antennas [3, 7, 177, 275, 314]

It uses multiple radiating elements placed as co-planar patches or vertically stacked patches as shown in Figure 1.5(a) and (b), respectively. It can operate with the same polarization at the two frequencies, as well as with a dual polarization. It allows only a limited value of the frequency ratio also high precision and sophisticated fabrication techniques poses a limitation towards its use as a MMW dual frequency antenna.

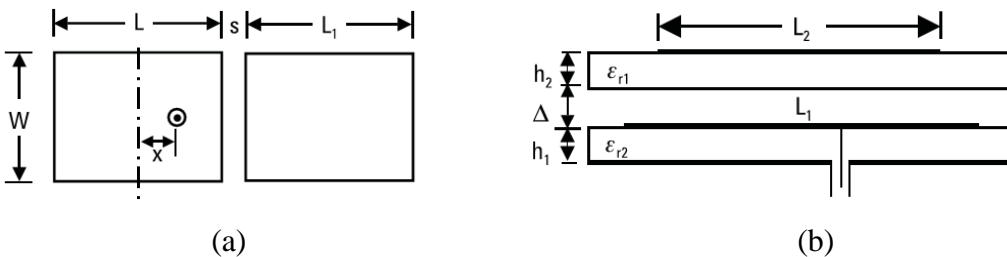


Figure 1.5. Multiple-patch dual frequency antennas, (a) co-planar patches, (b) vertically stacked patches [157].

➤ Reactively Loaded Dual Frequency Patch Antennas [8, 19, 64, 66, 119, 193]

It is one of the popular techniques for obtaining a dual-frequency behavior by introducing reactive loading to a single patch by including notches, pins, capacitors, slots, and shorting vias etc. Few of the example dual band antenna configurations are shown in Figure 1.6. Here, the higher mode resonant frequency is modified by altering the current distribution path. However, at MMW frequency, special attention is required for the choice of proper technique for the dual frequency operation in view cost effectiveness and simplicity of fabrication.

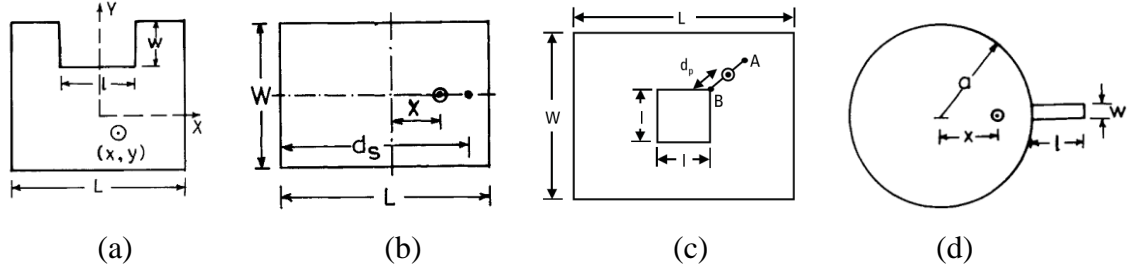


Figure 1.6. Reactively loaded dual frequency patch antenna using: (a) notch, (b) shorting pin, (c) square slot, (d) stub [157].

1.4.2. SFCW Imaging Radar System Design and Imaging Parameters

SFCW radars, transmit and receive consecutive trains of N frequencies changed by the incremental frequency step (Δf) [288]. Instead of using a linear FM signal for a high time-bandwidth product signal, we can obtain similar results by stepping through a number of discrete frequencies as shown in Figure 1.7, such that,

$$f_n = f_0 + (N - 1) \times \Delta f \quad (1.10)$$

Each pulse is τ seconds wide, and the time interval T between the pulses is adjusted for unambiguous range. Note that the frequency stays constant within each pulse. If the reference signal for the N^{th} pulse is

$$A_1 \cos 2\pi(f_0 + N\Delta f)t \quad (1.11)$$

Then, the target signal after a round trip delay of $2R/c$ can be represented as

$$A_2 \cos 2\pi(f_0 + N\Delta f) \left(t - \frac{2R}{c} \right) \quad (1.12)$$

The phase detector output for the n^{th} pulse is $A \cos(\phi_n)$, where

$$\phi_n = \frac{4\pi f_0 R}{c} + 2\pi \left(\frac{\Delta f}{T} \cdot \frac{2R}{c} \right) nT \quad (1.13)$$

The first term represents a constant phase shift, which is not of any practical significance. The second term is the multiplication of the rate of change of frequency $\Delta f / T$ with the round-trip time $2R/c$. Thus, the range (or the round-trip time) is converted into a frequency shift.

Therefore, it is possible to resolve and measure the range by resolving the frequency, by taking the discrete IFFT of the received signal from N frequency-stepped pulses.

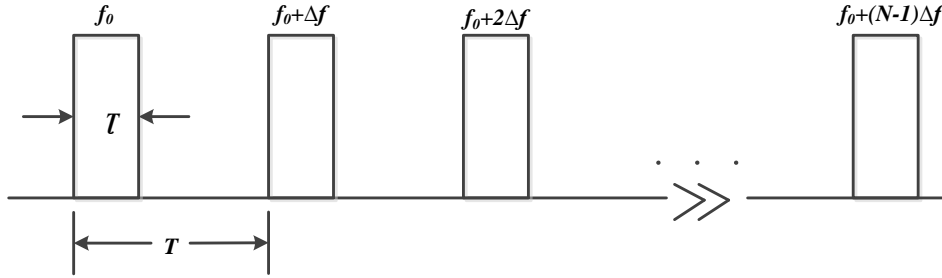


Figure 1.7. Step frequency increment of the transmitted SFCW radar waveform

The advantages of SFCW radar sensors are [13]: (1) a narrow instantaneous bandwidth that significantly improves the receiver's sensitivity while maintaining the average power, (2) a high average transmit power, resulting in a deeper penetration, due to the use of CW signals, (3) since the system transmits only one frequency at a particular instant of time, the received signals propagated through dispersive media can be accurately compensated, (4) enables greater precision and ease in designing the circuits. On the flip side, a few disadvantages of the SFCW radar sensors include their high complexity and cost. Detection of moving targets with SFCW radar is not as straightforward as in conventional radars. Range resolution (or pulse compression) cannot be achieved with a single pulse. It would require transmission, reception, and processing of a group of pulses, hence, SFCW approach has a limitation of acquisition time.

1.4.2.1. SFCW Radar Parameters

➤ Bandwidth

In SFCW radar, pulses of typical time duration have narrow bandwidths, thus making the instantaneous bandwidth of the radar narrow. However, effective large bandwidth can be realized by appropriately processing the N pulses, i.e., $BW = N \cdot \Delta f$ over the complete duration.

➤ Unambiguous Range

The frequency step (Δf) of SFCW waveforms should be kept small enough such that unambiguous range (R_{\max}) is larger than the maximum expected target's range. In the SFCW radar, because of quadrature mixing at the receiver, the baseband spectrum becomes single-sided. Thereby, the Nyquist sampling criterion for SFCW radar reduces to [288]:

$$\left(\frac{1}{\Delta f}\right) \geq \Gamma_{\max} \Rightarrow R_{\max} = \frac{c}{2\Delta f} \quad (1.14)$$

By specifying the start and stop frequencies, f_0 and f_{\max} , and the number of frequencies N_f , we can easily derive the frequency step

$$\Delta f = \frac{f_{\max} - f_0}{N_f - 1} \quad (1.15)$$

➤ Range Resolution

The absolute bandwidth (B) of the transmitted EM waves determines the range (or vertical) resolution ΔR , which shows the radar ability to distinguish closely spaced targets within a specific range R [123].

$$\Delta R = \frac{c}{2B_{\text{eff}}} = \frac{c}{2N\Delta f} \quad (1.16)$$

The SFCW radar resolution does not depend on the instantaneous bandwidth, and the resolution can be increased arbitrarily by increasing $N\Delta f$, which is significantly advantageous.

➤ Number of Points

There is a constraint on selection of Δf (i.e., $\Delta f \leq 1/\Gamma$); however, N can be increased to realize very high range resolution irrespective of waveform and compression method used, but fine range resolution does require large bandwidth. For the step-frequency radar, large bandwidth is obtained sequentially over many pulses by inter-pulse frequency modulation.

1.4.2.2. MMW SFCW Radar Experimental Setup Design

Figure 1.8 shows the experimental setup for MMW active imaging radar system. MMW radar in stepped frequency continuous wave (SFCW) mode has been assembled using vector network analyzer (make: Agilent N5247A (10 MHz-67 GHz) PNA-X), pyramidal horn antenna (make: MESA MW-HF-907V) and VNA cable (make: MMW-N4697F (DC to 67 GHz) – 1.85mm).

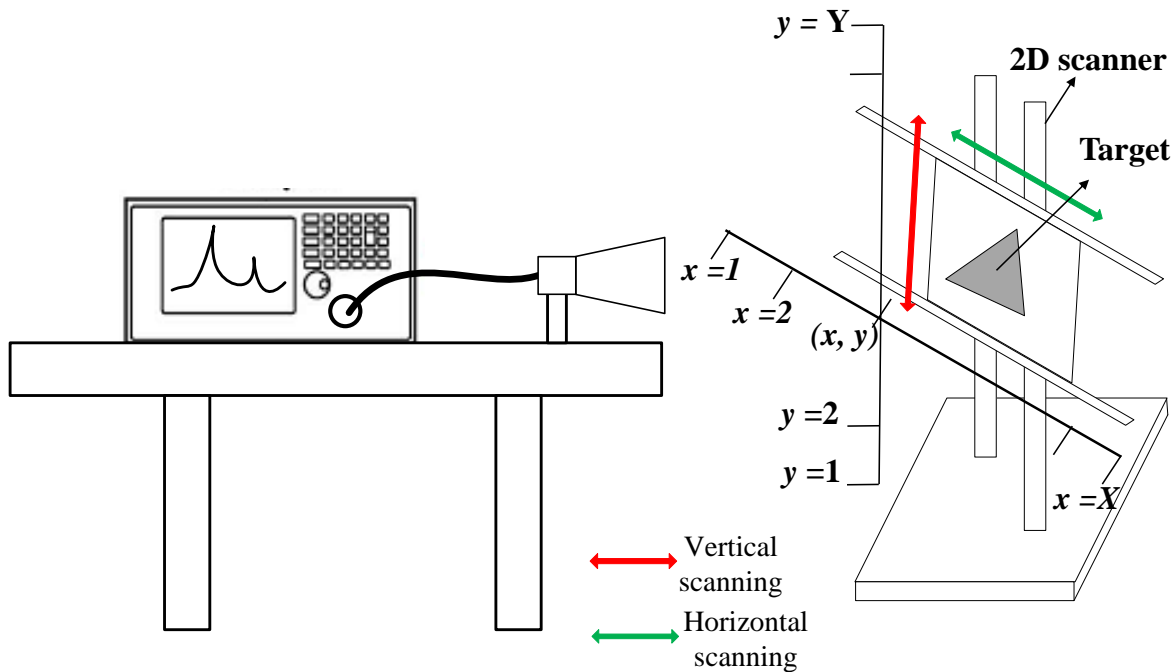


Figure 1.8. Experiment setup for MMW active imaging radar with the target mounted on a 2D scanning frame.

Typical specifications of designed SFCW based MMW active radar are given in Table 1.1. Horn antenna in the mono-static mode was fixed and a movable target was kept at a stand-off distance of 110 cm from the antenna.

Table 1.1. Specifications for SFCW based active MMW imaging radar

S. No.	MMW Active Radar Parameter	Typical Value
1	Operating frequency	60 GHz
2	BW	2GHz (59-61GHz)
3	No. of frequency points	201
4	Transmitted Power	10dBm
5	frequency step size	10 MHz
6	Antenna type	Pyramidal Horn
7	Beamwidth (E, H Plane)	9.1°, 10.4°
8	Gain	25dBi

➤ Scanning for Imaging

Targets were mounted on a two dimensional (2-D) scanning wooden frame such that it can slide smoothly in cross-range as well as in upwards and downwards direction. The MMW

radar system with a single horn antenna has been used to transmit and receive the SFCW signal at one fixed location and then the target is moved to the next horizontal position at a regular interval, until the whole of the target is scanned horizontally. Next, the target is moved upwards and again horizontal scanning process is repeated at this vertical target location, until the whole target is covered laterally. The same procedure is repeated for other vertical target positions, until the complete target is scanned. Using this scanning methodology, the target is scanned fully by the finite narrow beamwidth horn antenna from one edge of the target to the other edge sequentially. The scanning position at any particular target location is denoted by (x, y) as shown in Figure 1.8, where x denotes lateral (or cross range) point (ranging from 1 to X) and y denotes vertical (or height) point, (ranging from 1 to Y). Spacing between two consecutive scan positions is kept 0.02 m in both vertical and horizontal directions.

➤ **Cross-Range Resolution**

Cross-range resolution is the radar system's ability to successfully discriminate two closely spaced objects laterally. According to synthetic aperture theory, it is given by [335]:

$$\Delta CR = \frac{\lambda R}{D} \quad (1.17)$$

where, ΔCR is the lateral resolution of the radar, λ is the wavelength, R is the distance of the target from the synthetic aperture and D is the lateral dimension of synthetic aperture.

➤ **Data Acquisition**

In order to have full imaging information, the target is scanned in two orthogonal directions, *i.e.*, horizontal (along the width) and vertical (along the height), such that, the target is covered completely. Readings of all three types of scans viz. A-scan, B-scan, C-scan were taken [46].

➤ **A-scan (Range Profile)**

A-scan is a plot, in which the reflected signal received from any fixed target position is represented as a function of signal strength vs downrange distance and is also termed as range profile. As shown in Figure 1.8, for any fixed target position (x, y) , the plot of reflection parameter vs down-range distance will be the A-scan. A-scan gives the information related to target

presence or absence as well as target's exact location in downrange. A symbolic demonstration of the A-scan plot for stand-off target detection is given in Figure 1.9. Here, the first peak in the range profile corresponds to the maximum reflection due to antenna-air impedance mismatch. Any second peak in range profile, signifies presence of the target at that particular down-range index. The exact target's location can be found by converting it to the corresponding round trip distance as discussed in the start of section 1.3.2. Since, we have taken $N = 201$ discrete frequency steps, hence, the size of the A-scan matrix will be a vector of dimension $(1, 201)$.

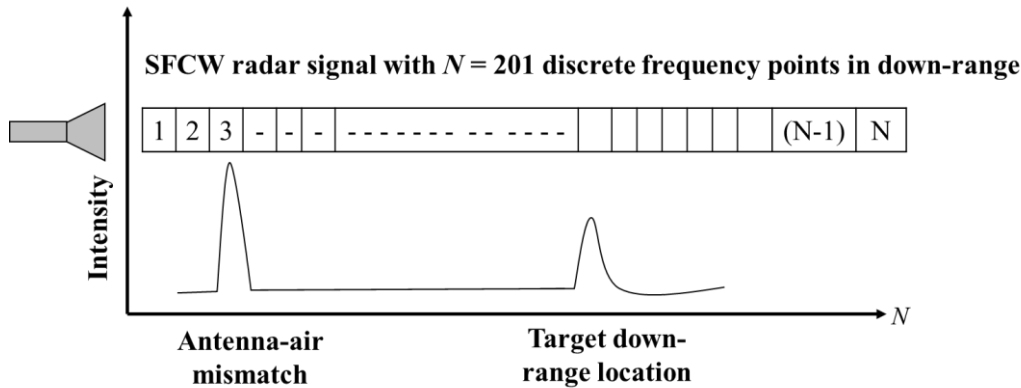


Figure 1.9. A-scanning at a fixed antenna location.

➤ B-Scan

It is an ensemble of multiple A-scans taken along different horizontal scanning positions. B-scan provides information related to the target's horizontal extent, *i.e.*, width of the target. With simple B-scan, the height of the target cannot be found. Figure 1.10 shows the demonstration for accomplishing B-scan. Here, multiple A-scans are taken along horizontal scanning positions, *viz.*, $x = (1, 2, \dots, X)$, hence, the size of B-scan matrix will be a 2D matrix of size $(X, 201)$, where, X represents the total number of horizontal scanning locations.

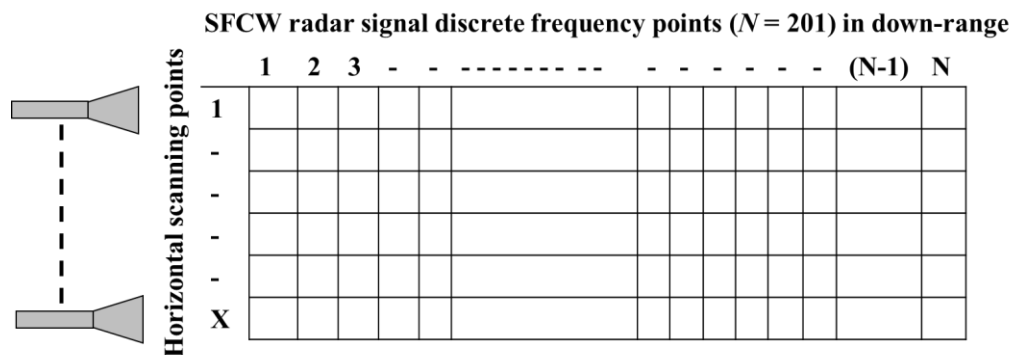


Figure 1.10. B-scanning at different horizontal scanning positions.

➤ C-Scan

C-scan signal is obtained from stacking of multiple B-scans taken along different vertical scanning positions, viz, $y = (1, 2, \dots, Y)$. C-scan provides the target's vertical extent, i.e., height of the target apart from its lateral length. Figure 1.11 gives the pictorial demonstration for performing C-scan by scanning the target in two orthogonal directions, i.e., along x -axis ($x = 1, 2, \dots, X$) and along y -axis ($y = 1, 2, \dots, Y$).

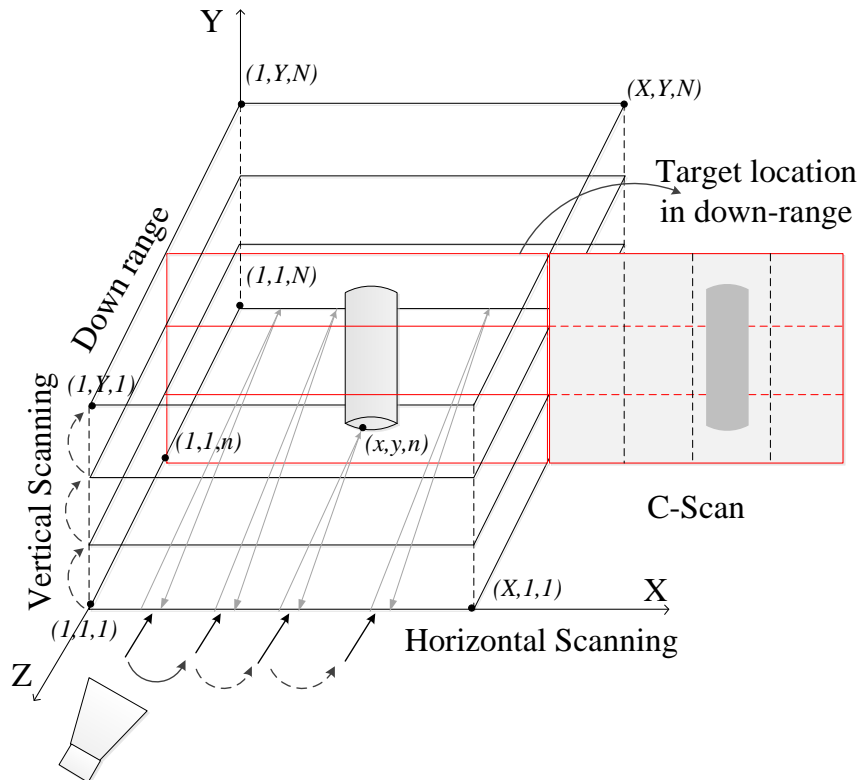


Figure 1.11. Representation for 3D C-scan by stacking multiple B-scans at different vertical scanning positions.

The complete C-scan is a 3D matrix, where, each cell entry represents intensity values as a function of cross range location, vertical location and downrange index, thereby, giving 3D C-scan matrix of size $= (X, Y, N)$. The total C-scan provides essential valuable information for the complete target's shape identification. However, in order to have the target's shape information, 2D C-scan matrix is extracted from the 3D matrix, at particular target downrange index corresponding to peak intensity reflection as discussed in the A-scan plot in Figure 1.9. The extracted 2D vertical slice of the target's image at the downrange index ' n ' is shown in the Figure 1.11 and will be of size (X, Y) .

1.5. Organization of the Thesis

The organization of the thesis is as following. Chapter 2 gives a brief introduction with review on the existing MMW dual frequency antenna design techniques, MMW imaging for target's shape identification and its material classification, and non-invasive quality monitoring applications. Contributions of different digital image processing techniques in radar image analysis have been also briefly discussed. In chapter 3, we propose the design of a MMW simple, compact and cost-efficient concurrent dual frequency planar antenna. Chapter 4 describes the proposed methodology for accurate target's shape identification using different signal processing techniques, *like*, clutter reduction, thresholding, edge detection, and target's material classification using probability density function approach. Chapter 5 deals with the exploration of developing an effective solution for distortions in target's image in terms of orientation and size variations. Thereby, a novel, rotation and size invariant target's shape reconstruction methodology has been proposed employing artificial neural network model. Chapter 6 investigates non-invasive quality monitoring of concealed objects for industrial applications using MMW radar imaging. Our main purpose is the fault detection, here, we have considered cracks in ceramic tiles as a fault and for this purpose, two approaches have been proposed. In the first approach, an image feature extraction technique-based-neural network classification model has been developed, which is a quantitative approach. Whereas, in the second approach, a spatial image statistics based adaptive pattern search algorithm has been proposed which facilitates crack detection as well as its particular location estimation. In chapter 7, a summary of the contribution of research work and future scope of work is presented.

Chapter 2

Literature Review

This chapter starts with the brief review of the characteristics of the millimeter wave (MMW) frequency spectrum, its peculiarities and different applications supported by it. MMWs lend themselves as an excellent modality for the application of non-invasive personnel screening, surveillance, medical and industry applications owing to its high resolution with relatively small, physical or synthetic aperture [23, 48]. Additionally, due to the large available bandwidth and associated lower wavelength, it also delivers miniaturized, high data rate communication systems and devices. The fields and applications of MMW are vast; therefore, during literature survey focus has been given only to the relevant tasks commenced in the thesis.

Firstly, literature review related to dual frequency planar antenna designs at lower microwave frequency has been discussed. Further, advancements in MMW dual resonant antenna design have been discussed and their limitations have been outlined with an emphasis towards simple and cost-effective antenna design. *Secondly*, literature review of the MMW stand-off imaging applications for target's shape identification and non-destructive target's fault estimation have been presented. Digital image analysis techniques are being used widely for extracting meaningful information from camera/radar images for further processing. Thereby, an investigation of different digital image processing (DIP) techniques has also been reviewed for applications, like, clutter reduction, image segmentation, image enhancement, image classification, image feature extraction etc. Further, relevance of these techniques w.r.t. MMW images, their treatment and limitations has been discussed. Thereafter, based on the review of aforementioned MMW applications, this chapter has been concluded for further scope of research.

2.1. Millimetre Wave Frequency Features and its Applications

MMW's principal advantages are its related characteristics of miniaturized system size and high resolution that follows from its short wavelengths. However, these performance improvement comes at the cost of greater atmospheric attenuation, limiting the propagation ability of MMW frequency [21, 32, 233]. The free space propagation loss at 60 GHz is 28 dB more than the loss at 2.4 GHz [53, 214]. Figure 2.1 shows the attenuation curve at MMW frequency. Advantageously, the effective interference levels for MMW are less severe, which favors higher frequency re-use over very short distances, thus allowing the high throughput network. Thereby, MMW communications are mainly used for indoor environments, small cell access and backhaul with cell sizes on the order of 200 m.

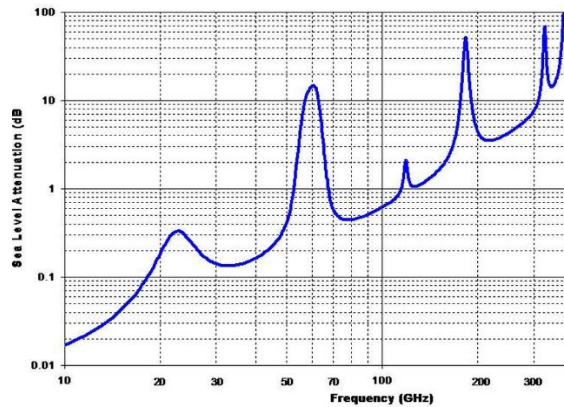


Figure 2.1. Atmospheric and molecular absorption at MMW frequency [214].

The interactions between the MMW and the human body, characterization of dielectric properties of human tissues is essentially desired for wireless body-centric applications and body area networks (BANs) [15, 39, 40, 84]. Additionally, small distributed integrated circuits, components at MMW are difficult to physically realize and fabricate, which are a fraction of the wavelength [53, 191]. A number of MMW applications related to security control and imaging require propagation through different materials e.g., building, packaging and cloth material. The dielectric properties at MMW's have been measured for different materials, but still much information is lacking [5, 76, 259]. Concealed target detection is greatly influenced by the transmission property of clothing on the contraband. Hence, transmissivity values of clothing with different materials and different thickness, like, cotton cloth, plastic, terylene and woolen

sweater, etc. are required to be known at MMW [32, 163, 349]. In addition, the quality of MMW images is not only affected by the antenna beam angle with object, but also on the smoothness and non-uniform thickness of the clothing covering the object. Thereby, techniques to deal with these challenges are being investigated, to make MMW's available for promising new applications.

Various research works have been going on around the world exploiting the vast number of applications that MMW offers, like, stand-off concealed target detection, active or passive imaging sensor [21, 38, 61, 274], precise measurements of air and sea surface temperature using 60 GHz rotating radiometer [296], non-destructive moisture monitoring and disinfestations of artworks at 150 GHz [194], non-contact vital sign detection at 94 GHz [26, 121], collision-predicting sensors for automatic braking systems for automobiles at 35 GHz and 60 GHz [45], detection of cracks, void, surface anomalies [90, 143, 280, 334], an distance measurement of the target with sub-millimeter accuracy [102, 160], soil backscattering using a 60 GHz scatterometer [329], millimeter-wave identification (MMID) for short-range, low-power, high data-rate applications (WPAN-IEEE 802.15.3c, IEEE 802.11ad) [242], etc. With such a diversity of interesting applications, MMW is now gaining tremendous research interest globally among the intellectuals.

2.2. Review of Work Related to MMW Dual Resonant Planar

Antenna Design

The current research trend has now moved towards the design of MMW dual band antennas keeping up with the commercial demand of miniaturized and multi-tasking systems/ applications. In this section, first we elucidate different techniques used for designing a MMW planar antenna. Then, we discuss different prevailing methodologies for achieving dual resonant antennas at microwave frequencies. Later on, contributions made in the field of MMW dual band antennas and the challenges faced will be outlined.

At MMW frequency, microstrip antenna design is quite a challenging task because of concomitant higher losses, unavailability of transmission line models and relatively small dimensional constraints [56]. However, different methodologies have been proposed to reduce these shortcomings and to enhance the antenna efficiency by prohibiting unwanted lossy modes to propagate. Some of these techniques are thin, low dielectric substrate (Teflon / quartz) [197,

211, 260, 339], multilayer or micromachining in high index substrate (Si/GaAs) [19, 231, 257, 282, 341], superstrates [345], substrate integrated waveguide (SIW) [347], low temperature co-fired ceramic (LTCC) [10, 135], and photonic band-gap (PBG) substrates [190, 330, 331].

Artificial periodically loaded substrate electromagnetic bandgap technique has the forbidden frequency range for surface waves around the desired antenna operative frequency, which, therefore, increases the radiated power coupled to space and in-turn, increases its gain and bandwidth, for example: *G.W. Burns et. al.* [34] reported a 3D-woodpile PBG crystal for a co-planar waveguide (CPW) fed slot dipole antenna at W-band (94 GHz), *J. B. Muldavin et. al.* [208] designed 30 GHz and 94 GHz slot antennas on synthesized low dielectric constant substrates ($\epsilon_r = 2.2$). Surface or bulk micromachining [9, 30, 125, 245] of high index silicon is another technique to combat losses, whereby, an air cavity is selectively etched out so as to reduce effective dielectric constant and inhibit any surface wave propagation. For example: an air-dielectric cavity-backed patch antennas at 94 GHz with a 10-dB bandwidth of 3.25 GHz and gain 18 dB [220], 3-D micromachined elevated patch antenna for G-band [70], an aperture-coupled micromachined microstrip antenna at 94 GHz, having 10% bandwidth and 58% efficiency [88], have been reported which also favors easy integration for MMIC's. Likewise, other variants of planar and quasi-planar antenna structures reported are; slot type [47, 208, 338, 339, 346], leaky wave type (dielectric rod, NRD guide) [186, 227, 290, 310], high gain reflector type [212], planar yagi-uda type [16], log-periodic [341], etc.

However, different techniques have been proposed and are being used for design of MMW frequency planar antennas, but, keeping in account the more pronounced effects of surfaces wave and higher order losses, dimensional constraints, and other factors at MMW, still it is quiet challenging to design a simple as well as cost-competent MMW planar antenna.

2.2.1. Dual Band Antenna Techniques at Microwave Frequency

Principally, dual-frequency antennas should operate with nearly similar features at two separate frequencies, both in terms of radiation properties and impedance matching. Obtaining these features by using planar technologies is not a straightforward matter, particularly when the intrinsic structural and technological simplicity, typical of patch antennas is needed to be preserved. Generally, the dual band antenna techniques employed are changing the physical size of the antenna and modifying the radiator shape to allow current paths to travel at longer distances

which, sometime increases the antenna size [67, 72, 119, 152, 255, 277, 313]; adding additional parts such as multilayers [307] or gaps, which makes the antenna structure larger and complex [140, 156]; and appropriately using single or dual feeding to excite the dual band, which adds complicity to the feed design [12, 304]. Other reported dual band antenna designs using combination of techniques are slotted, co-planar dual patch elements for dual band and PIN diodes switches with the feedline for additional re-configurability [3], parasitic patch with reactively loaded driven patch for improved performance [18], notch loaded shorted microstrip patch antenna [199], shorted, quarter-wave U-shaped patch antenna with two unequal arms [342].

Enormous research work has been already carried out for the dual frequency antenna at microwave frequency [4, 18, 66, 119, 315, 342]. However, at MMW frequency different proposed dual resonant techniques demand a high level of precision, may be in terms of modified antenna structure design (slot, notch, spur), proper positioning of feeding section (shorting pin, proximity coupling), alignment accuracy for multiple patches and dual feeds, etc. Thereby, direct extension of these dual resonance techniques for MMW's is not straightforward because of several limitations, like, higher losses due to surface wave, conductor, and dielectric losses, and technological challenges, like, stringent dimensional constraints, specifically when we aim towards a simple, compact and cost-efficient antenna design.

2.2.2. Review of Work on MMW Dual Frequency Antennas

With the incorporation of dual band techniques in MMW systems, it will tremendously raise its capability with added multi-processing and redundancy, making it more commercially attractive, while equivalently maintaining the system size compact. Being a new research field and technological limitations at high frequency, there is need of extensive research in this domain. Very less literature is available for achieving dual resonance at MMW. Some of the works that have been reported, where researchers have used micro-electro-mechanical system (MEMS) [173, 184], low temperature co-fired ceramic (LTCC) [135], metamaterial resonator [128], multilayer [257], C-shape slot on cavity [285] and photonic bandgap (PBG) [320] designed for particular application. However, these investigated techniques pose various limitations in terms of complex and non-planar antenna structure for the dual frequency MMW operation as well as it demands for the higher level of fabrication and alignment accuracies.

L. Marnat et. al. [184] proposed a movable plate concept based vertical antenna utilizing MEMS post-processing, thus, isolating the antenna structure from lossy substrate and hence better antenna efficiency has been achieved as compared to the horizontal position. The designed bowtie antenna has been matched to resonate at 60 / 77 GHz, having gain 3.5/4.8 dBi in vertical position as compared to -3 /-2.1 dBi horizontal position. Further, the antenna supports polarization diversity by providing both horizontal and vertical polarizations. However, the structure proposed is non-planar, thereby, limiting its use for planar and conformable applications. *I. K. Kim et. al.* [128] proposed a dual frequency meta-resonator antenna that uses a pair of split ring resonators (SRR) as the radiating element. The two SRR's support two different frequencies, hence, the antenna operates as the dual band antenna. Here, feeding was through inductive/capacitive coupling, hence, no matching network was used. The simulated antenna has efficiency 76% / 85% and gain 2.5 dB / 1.8 dB at 46 GHz / 51.6 GHz, respectively. The limitation of this proposed antenna is the involvement of the complex fabrication of SRR structure, which is of much lower dimensions. Moreover, the antenna performance has not been validated by the measured results. A micro-electro-mechanical system (MEMs) based 38/ 60 GHz slot antenna was proposed by *G. Liu* [173]. The designed antenna resonant frequency is switched between 38 GHz and 60 GHz, depending upon whether the MEMS switch is 'on' or 'off'. The antenna was designed on the micromachined GaAs substrate to improve efficiency. The limitation of this design is that it does not support concurrent dual frequency operation. *D. S. Hemhdez et. al.* [257] proposed two different dual-band MMW antenna designs with antenna 1 using a stacked patch configuration and antenna 2 using a spur-line technique. Multilayer stacked patch showed the bandwidth of 3.5% ($f_{o1} = 35.65$ GHz) and 1.67% ($f_{o2} = 38.9$ GHz) and with spur-line technique, the measured bandwidth was found to be 0.45% ($f_{o1} = 33.75$ GHz) and 0.55% ($f_{o2} = 36.75$ GHz). The multilayer antenna configuration is sensitive to misalignments of the two resonators and in spur-line structure the small spur dimensions makes the fabrication process complicated. Thereby, both the antenna designs make the dual band structure quite complex and thus raise the fabrication cost.

After reviewing the related literature for MMW dual frequency antenna, it was found that most of these available methods utilize complex dual band techniques rendering the structure complicated. These methodologies also suffer from complicated fabrication procedure and thus, are expensive. Considering the aforementioned limitations, more research and investigations are

required in order to make a simple, compact and cost-effective solution to the MMW dual band antenna.

2.3. Review of Work Related to MMW Imaging

MMW radar sensors have been used as an accurate and effective technique for the variety of stand-off imaging applications in security screening for concealed weapon detection, baggage inspection [11, 73, 96, 108, 112, 250, 287, 328, 335], medical diagnostics [40, 138, 216], nondestructive characterization of surface and subsurface in detecting and localizing buried mines or archeological sites, measuring distances, displacements, thicknesses or moisture contents, profiling the surface or subsurface of pavement, and quality monitoring of packaged goods [192, 195, 250, 352], and polarimetric SAR Imaging for extraction of power line maps at 35 GHz [258], indoor navigation and mapping at 215 GHz [204] etc. Using mm-wave radar, the object of interest is first illuminated by MMW's and then the scattered field is measured and processed in order to reconstruct the object. The image resolution is determined by the radar center frequency, its bandwidth, and its aperture size [11, 198, 219]. For accurate identification of the targets, its sufficient spatial details have to be extracted for image formation and further its shape and size estimation. In view of our commenced research tasks, we have narrowed ourselves specifically to two major MMW radar application areas, *i.e.*, *target's shape/ size identification* and *non-destructive, non-invasive concealed fault detection*.

2.3.1. Review of Works Related to Target's Shape/ Size Identification

Different techniques have been reported for an accurate target identification using MMW imaging, like, compressed sensing [24, 185, 250], matched filter algorithm [334], holographic imaging [73, 272, 352], tomography Imaging [303], cylindrical imaging [270, 287], polarimetric imaging technique [204, 272, 274], envelope phase detection [115], synthetic aperture imaging [117, 258]. Each of these techniques has their advantages, as well as limitations. For example: compressed sensing technique, however, reduces the number of sensors, thus simplifying the system design, but it has the limitation of large computational time [250]. Polarimetric techniques can improve detection and enhance the image by highlighting raised objects, edges, and corners, but suffers from reducing the reflection from smooth surfaces [274].

A. Hirose [115] proposed an active near-field shape extraction method using envelope phase detection, where the envelope phase of the amplitude modulated wave was used to obtain a three dimensional shape of the targets including stacked round cans, plastic bottle filled with water at 76.5 GHz. However, the technique performs better for near field applications.

Harmer *et.al.* [108] demonstrated the decomposition of late time and transient response of metallic objects into damped sinusoidal signals and characterized by aspect-independent poles. This pole information has been utilized for detection and discrimination of threat items (handguns) from the non-threatening items, such as, mobile phone handsets, cameras, keys and pens. The problem with the aforesaid decomposition method is that, it provides only target classification, but not the target's shape information.

Image reconstruction of any target can also be accomplished by putting projections taken at different angles. Algorithms proposed for this are backprojection [61, 118], filtered backprojection [350], bistatic fast-factorized back-projection [206], etc. In [303] MMW inverse SAR imaging has been used for image formation of the concealed metallic gun beneath clothing using near-field backprojection algorithm. Bi-static fast-factorized backprojection image reconstruction of a 75 mm wide metal block, from a stand-off distances of 7 m has been shown using a 300 GHz synthetic aperture array [206]. However, the technique is limited by the high demand of processing time and memory usage.

Artificial neural network has also proved to be an effective signal processing technique for classification/ recognition of target in a noisy environment for various applications, like, speech recognition, character recognition, pattern recognition, face recognition, etc. [43, 54, 59, 251, 311]. S. Watanabe [312] combined an existing acoustical holography with neural networks to reduce the vagueness of reconstruction of the acoustical images from ultrasonic sound waves in air. Moreover, later on he demonstrated image recognition and reconstruction of objects obtained from an active MMW (60 GHz) Yagi Uda array antenna imaging system with 98% recognition rate for ten dissimilar alphabetical letters used as objects and 80% accuracy for distorted images [311].

After reviewing the related literature, it is observed that retrieving target's shape information is still challenging and requires contemplative study. Further, there is a need to develop an adaptive image reconstruction technique, which should be robust towards target's orientation and size variations in view of practical considerations.

2.3.2. Review of Work Related to Non-Destructive Testing and Fault Estimation

Nondestructive testing & evaluation (NDT & E) is the examination of an object with technology that does not affect the object's future usefulness [232]. The role of nondestructive testing (NDT) methods is found in manufacturing, power, construction, and maintenance industries, as well as in basic research and development. However, general concepts and uses of NDT not only exist in industry but also in our everyday lives. For example: at the fruit stall, selection of melon by looking over it for any flaws is –visual NDT, while, tapping its surface or listening for the hollow sound is –acoustic NDT. Finally, depending upon response to these tests and as per our perceived criterion, we decide to take or leave the melon. Almost, all melons at the stall will eventually be sold and there is the problem in NDT; inspector's standards change. Ideally, once the quality standards are set, the inspection should be independent of human perception and should always give the same result. The basic principle of NDT is simple, i.e., to determine the quality or integrity of an item nondestructively, simply to find a physical phenomenon (the interrogating parameter) that will interact with and be influenced by the test specimen (the interrogated parameter) without altering the specimen's function.

There are a wide variety of proven and standard Non-destructive testing (NDT) techniques, like, radiography, ultrasound, dye penetrant, eddy current, visual testing and magnetic particle testing etc. [58, 62, 236, 278, 356]. However, each method has its own application area, advantages and limitations. For example: ultrasonic signals cannot interact with the inner structure of porous materials because of its inability to penetrate. Eddy current methods do not support inspection of lossless dielectric materials in which eddy currents cannot be induced [58, 146]. Also, many times non-contact inspection is required without hampering the material efficacy and usability. In addition, with the advancement of material technology a new range of lighter, durable and electrically insulating composites are now replacing metals in many applications, thereby, standard NDT techniques may not be applicable to inspect them.

Hence, microwave/ MMW techniques provide an accurate and viable NDT solution, where EM signals at these frequencies can easily penetrate the dielectric materials and provide their inner structure information [25, 225, 355]. The depth of penetration is dictated by the loss factor of the dielectric material (ability to absorb microwave energy) and the frequency of operation. Measurements can be conducted in the contact or non-contact fashion while operating

on one side of a material or using its both sides (reflection or transmission techniques). Additionally, measurement/ instrument parameters, like, bandwidth, frequency, polarization, sweep points, phase, and magnitude information can be optimized depending upon particular application. Microwave NDT techniques are sensitive to geometrical and dimensional variations of a medium or a defect. Polarization properties of microwave signals can be used to increase measurement sensitivity of defects of a certain orientation [262, 356]. Areas that may be benefited using EM based NDT are disbond, delamination and void detection, thickness evaluation, porosity in dielectrics, impact damage detection, constituent characterization in dielectric mixtures, detection of surface cracks in metals or cracks covered with various dielectric coatings [91, 94, 101, 136, 144, 153].

Research work related to microwave/MMW NDT imaging broadly employ two measurement techniques: (1) near-field probe imaging which uses open ended rectangular probes and coaxial probes, where the target surface under investigation is in the close proximity of the probe [91, 136, 145, 209, 356, 357] and (2) synthetic aperture imaging employing antenna and scanning array [90, 153]. The probe based crack detection uses surface current perturbation, whereby any crack present inside waveguide aperture disturbs the surface current and causes properties of the reflected wave to change. Few examples are surface-breaking fatigue cracks detection of metal plates using W-band probe and the processed image was formed using gradient filtering [145], crack inspection in cement based civil structure at X band [209], detection of corrosion precursor pitting under paint at V band [92]. Near field probe technique is although non-destructive, easy to perform and provides high resolution (tenth of the wavelength), but it requires extreme sensitivity in terms of constant distance between probe and the target under investigation, and any changes/ non-uniformity during the experiment may severely affect the system detection performance [93, 101]. Moreover, there are different practical applications where near field imaging cannot be used, like, non-planar structure/ surface inspection (aircraft panel joints, industrial applications, etc.). [35, 261].

Hence, radar imaging operated at MMW frequency provides a good alternative towards efficient high resolution imaging. A 30 GHz 1D, linear, 150 mm long imaging array has been demonstrated for NDT applications [90]. It is based on a switched RF multiplexed system and a PIN diode-loaded switchable resonant slot antennas as its array elements. The imaging is done in quasi mono-static reflection mode capable of successfully detecting/ imaging a pair of scissors, square shaped rubber (10 mm x 10 mm x 1 mm) inserted between two (6.5 mm-thick) balsawood

composite panels. A far-field airborne radar operated at X-band was used on the glass fiber reinforced polymer (GFRP) enclosed concrete cylinder targets followed by backprojection imaging algorithm to reconstruct the improved images for its condition assessment [348]. Thereby, MMW imaging radar scanning systems provide fascinating features for non-destructive testing as a non-contact, reliable, high resolution and adaptable (parameter tuning as per required application) technique.

Henceforth, it is required for renewed vigor in applying MMW techniques to new non-invasive inspection problems and a fresh sustained effort in this area should bare many facts.

2.3.3. Review of DIP Techniques for MMW Imaging

In this section, we elucidate the contribution of digital image processing techniques for MMW image analysis. Although, DIP techniques are being used for camera based images as well as microwave radar imaging for uses, like, ground penetrating radar [2, 334] and through wall imaging [68, 123, 161, 318] but, these techniques have not been fully utilized in analyzing MMW images for different applications of image enhancement, feature extraction, image segmentation and material classification etc.

Target's reflected signal intercepted by MMW imaging radar, in its unprocessed raw form may not infer useful target information. This is because, the intercepted reflected EM waves many times not only contains desired target reflections, but additional undesired signals *viz.*, reflection and refractions due to multipath propagation/ background and due to system noise, etc. Hereby, in order to enable the user to discriminate between the object and the background as well as to differentiate between different objects, several image enhancement and segmentation steps are applied. A brief survey of these techniques is given below:

2.3.3.1. Review of Clutter Reduction Techniques

Any unwanted reflection signal in line of sight of the desired target signal is termed as the "clutter". Clutter is a collection of those signals that are not related to the target but occur in the same target sample time window [81]. In radar imaging, reflected target's signal many times consist of the desired response of the target along with additions of other signals arising from radar system parameters, background and multiple reflections, etc. which is known as clutter. These unwanted signal errors must be removed in order to improve the image quality. Researchers have developed various clutter reduction techniques to enhance target's detection

accuracy and for the reduction of false alarm. One of the commonly used methods for clutter reduction is background subtraction [2], where two images taken with and without target are subtracted. But, this technique has the drawback that data should be collected at exactly the same antenna positions in both cases. In addition, it is not possible in real scenarios to collect data without target. Time gating is another method used to reduce clutter. The prevalent unsupervised statistical based clutter reduction techniques are principal component analysis (PCA) [141], independent component analysis (ICA) [175, 302], iterative subspace projections [301], singular value decomposition (SVD) [46, 151], block-based-nonlinear filtering [151], etc. A comparison of different clutter reduction techniques has been given in [2, 46, 302]. In PCA, clutter is reduced by reconstructing from the most significant eigen vectors [141] and SVD uses generalized singular value decomposition for separating clutter and signal spaces [263]. In PCA, performance is limited by the correlation between the components and suffers adversely in case, the uncorrelation between signal and clutter is not enough. In ICA, the subspace formed is not orthogonal as in PCA and the independent components (ICs) are statistically independent providing a stronger measure for clutter removal [302]. In addition, SVD based clutter filtering is better in preserving edge details of any target shape [151].

However, applicability and efficacy of the image enhancement techniques is still to be analysed in view of MMW radar imaging application of stand-off target's shape identification.

2.3.3.2. Review of Image Segmentation Techniques - Thresholding, Edge Detection

Image segmentation is a technique useful in discriminating objects from the background in many classes of scenes, including printed or written documents, concealed objects, blur and non-uniform illumination [139, 321]. Segmentation subdivides an image into its constituent regions or objects. Image segmentation algorithms generally are based on one of two basic properties of intensity values, *i.e.*, discontinuity and similarity. It is important in picture processing to select an adequate threshold of gray level for extracting objects from their background. It is not only important as a standard technique in picture processing, but also essential for unsupervised decision problems in pattern recognition. A variety of thresholding techniques have been proposed in this regard, like, histogram based [221], clustering based [97], entropy based thresholding [353], locally adaptive thresholding [14, 267], hidden markov model (HMM) [111], and the mixture of gaussian densities with iso-counters evolution [328]. The performance of any thresholding operation largely depends on various factors, such as,

nonstationary and correlated clutter, ambient illumination, mixing of gray levels within the object and its background, inadequate contrast and in addition to this object sizes not commensurate with the scene complicate the segmentation procedure [166, 253]. For example: histogram based technique performs better when the object and background is largely separated and have the distinct bimodal valley point, markov and gaussian models although are noise resistant but are computationally inconsistent, entropy method performs fair in uniform images but it is complex because of logarithmic calculations involved [222]. Thereby, the selection of an appropriate segmentation technique largely depends on the type of images and application areas and no single algorithm can be uniformly top-ranked across all test images and performance criteria [354]. Therefore, only one evaluation method would not be enough to judge all properties of an algorithm and different methods should be incorporated.

Debes et. al. [60] demonstrated segmentation of metal dihedral images through a wooden wall using an iterated conditional mode (ICM) method and level set method (LSM). ICM proves to be an effective and computationally attractive method when pdf classes for the different segments are known. LSM is a contour-based approach and is a highly attractive tool in volumetric data reconstruction, e.g., in medical image processing. LSM theory holds for arbitrary dimensions and can directly be applied to 3D TWRI images. The key idea of the LSM is to fit a contour in a higher dimensional space. Further, it was noted that the LSM algorithm performs slightly better than the ICM. However, for ICM implementation prior knowledge of target's pdf is the prerequisite and for LCM contour an initial suitable threshold value is need to be known for better target's shape. *C. H. Fosgate* [75] used multiresolution segmentation and enhancement of anomalies in MMW SAR images for different terrain classifications (*i.e.*, grass and forest) utilizing the characteristic statistical differences in imagery of different terrain types. However, the technique has not been investigated for its capability towards stand-off target applications. *P. E. Keller* [142] proposed a MMW weapons screening system by proposing a privacy algorithm which automatically segment concealed threats and innocuous items from the imagery. To locate plastic items, a pulse-coupled neural network (PCNN) model was proposed for object segmentation and edge detection. The implementation of algorithm was not much successful and additional development and understanding of the technique was therefore required. In [300], a 2.5D volume integral equation (VIE) technique using spatial fourier transform and the galerkin method of moments was used for enhancing/ detecting MMW scattering by large inhomogeneous 2D objects, *i.e.*, dielectric or strongly conducting object hidden underneath clothing. The

proposed technique has been implemented through EM simulations only, and hence, its performance is needed to be validated on real targets.

Thresholding is a technique where target's image is better visualized when implemented in conjunction with edge detection. The edge detection process serves to simplify the analysis of images by drastically reducing the amount of data to be processed, while at the same time preserving useful structural information about object boundaries. Edges characterize boundaries and are therefore considered as prime importance in image processing and target's identification [37]. Many varied edge detection techniques have been proposed in the literature [95, 158, 162, 189, 210]. Different edge detectors present distinct and different responses to the same image, showing different details. Commonly used edge detectors are iteratively refined regularization [95], canny edge detector [37], statistical classifier [159], local threshold and boolean function [14], color edge detection using euclidean distance and vector angle [319], depth edge detection using multi-flash imaging [210], etc. Edge detectors: sobel, prewitt and roberts implement gradient method and are simple to implement, but they are sensitive to noise and suffer from poor localization. Laplacian detector implements zero order crossing and is simpler than gradient method, however, it is more sensitive to noise, poor detection and also does not provide information about edge direction [37]. The boolean function approach is better, but it is somehow complex [14].

M. Moallem [204] demonstrated rectilinear patterns of walls and doors in interior corridor images using Hough transform for line edge detection on the backscatter data from the instrumentation radar operating at 215 GHz. Modified Stripe Hough transform (SHT) for road edge recognition in 77 GHz MMW radar images has been proposed in [158]. The main advantage of the line detection using Hough transform is that it is relatively unaffected by gaps in lines and by noise. All weather automotive vision enhancement for MMW near ground-level positioned radar images for straight and parallel road edge detection problem has been formulated using bayesian approach [137, 162]. However, for more complicated road scenes, such as, slanted roads, curved roads, multiple roads, modifications in the image model and edge detection problem is required.

With the thorough study of existing methodologies, it is proven that the DIP techniques are quite helpful in extracting meaningful information from radar images. Therefore, contemplative studies are needed to resolve any target's ambiguity.

2.3.3.3. *Review of Feature Extraction Techniques*

Features are invariable descriptors of any image that consists of relevant and unique information that could help to detect any relevant target information, viz, shape, irregularity, fault, crack, texture, etc. A number of different feature extraction techniques have been reported in literature and can be broadly classified as; shape based feature, texture based feature, colour based feature [63, 215, 299]. Texture features are important in many applications of computer image analysis for classification, detection, or segmentation of images, which are based on local spatial variations of intensity or colour. Important applications include industrial and biomedical surface inspection for defects and disease [33, 154], ground classification and segmentation of satellite or aerial imagery [114], segmentation of textured regions in document analysis [218], and content-based access to image databases [281]. Any image consists of spatial local gray tone variations, i.e., texture depending upon the image type. Texture analysis techniques can be classified as statistical, structural, filter based and model based approaches [327]. Statistical texture analysis methods measure the spatial distribution of pixel values and have been extensively applied to various computer vision based tasks. A number of statistical texture features have been proposed, ranging from first order statistics to higher order statistics. Few of them are: histogram statistics [33, 240], co-occurrence matrices [234], autocorrelation [343], and local binary patterns (LBP) [207, 218], morphology [48, 188]. The first order statistical features include mean, median, variance, standard deviation, lacunarity, weighted rank fill ratio etc [44, 97]. The second order statistical measures are characterized by gray level co-occurrence matrix (GLCM) [107, 234]. The efficacy of different statistical textural measures may vary depending upon the particular application, hence, choice of suitable texture features is a critical step for the design of any classification model. Despite the fact histogram techniques are simple, low level approach, invariant to translation and rotation, and insensitive to the exact spatial distribution, but it requires fairly separable intensity values between defective and normal regions for optimal performance, which is not always true for practical images [327]. Co-occurrence features also suffer from the shortcomings, like, in order to keep the size of the co-occurrence matrix manageable, reduced number of gray levels is needed, which implies dedicated feature selection procedures. Also, its performance is poor in comparison to other statistical techniques [343]. Autocorrelation function is generally considered as unsuitable for random textures with irregularly arranged textural elements. LBP is relatively invariant w.r.t. changes in illumination

image rotation and computationally simple, however, it has considerably lower performance than co-occurrence matrix and other filtering based approaches [218, 327].

Apart from texture feature, shape based feature extraction techniques are also popular in computer vision based image processing applications [284, 332]. Size and scope of these modern computer vision techniques is enormous, some of which include scale invariant feature transform (SIFT) [178, 179]; speeded up robust features (SURF) which provide a low-dimensional representation of visual images for instance matching with images [28]; (HMMs) to detect and classify landmine responses based on statistical representation of their characteristic hyperbolic shape [205, 243]; histogram of oriented gradients (HOG) which has been successfully used for pedestrian detection, traffic surveillance with occlusion handling [55, 323]; wavelet transform (Harr, Gabor, Hough) having varying scope [22, 189]. Disadvantage of HMM model is that, it is slow in training as well as in the operation, because of more parameters and computation. Additionally, very large database is used to insure the algorithm's robustness [205]. SURF and SIFT features provide automatic matching between images, but require dense grid of uniformly spaced cells and are therefore computationally complex [55]. Performance of Hough transform is limited due to the significant storage and high computational requirements [215]. HOG features are fairly robust to moderate changes in the object's location, but its performance is need to be further investigated for radar imaging. The Harris corner feature is very sensitive to changes in image scale, so it does not provide a good basis for matching images of different sizes [178].

The computer vision based feature extraction techniques have also been tested by various researchers for active imaging radar based applications, *like*; *T. wang* in [297] investigated magnitude and local-contrast features, co-polarization and cross-polarization signals, and polarimetric decomposition features for GPR based land mine detection. Performance of EHD [79] and gabor feature based HMM model [79, 82] were compared for different type of metal land mines [203]. It was shown in [316] that sparse signal decomposition outperforms wavelet decomposition for better GPR signal classification. Additionally, statistical features [74, 248], time–frequency features [263, 317], 3-D Haar-like features [149] and texture features [293] were also examined for GPR based land mine, anti-tank mine subsurface target's detection and classification. However, these said feature extraction techniques have not been investigated for MMW radar imaging applications, like, stand-off target's shape identification or non-destructive quality testing applications, etc.

Similarly, *S. Hang* and *M. Moallem* proposed an advance path measurement for automotive radar applications for collision warning and collision avoidance using Hough transform [204, 276]. Further, an improved stripe Hough transform (HT) model was developed by *K.Y. Guo* [158] for more accurate road feature recognition using 77 GHz MMW imaging radar. *K. B. EOM* [71] used discrete Fourier transform (DFT) feature and maximum likelihood (ML) approach for modeling and classification of high range resolution (HRR) radar signatures with classification accuracy of around 93% at 35 GHz. Accurate power line map information with improved signal ratio and reduced false alarm has been achieved using statistical polarimetric detection algorithm on the MMW polarimetric SAR images at 35 GHz [258]. Other feature extraction techniques are correlogram for pattern matching [161], diffraction tomography (DT) for 3D real-time through-the-wall radar imaging [318], statistical and geometrical features for target's classification in the image-domain in through wall radar imaging [60]. Many of these different feature extraction techniques report the results based on numerical EM simulations only, as well as their applicability still has to be investigated for MMW NDT like applications.

Henceforth, in context to MMW active imaging, computer vision based feature extraction techniques show tremendous scope for correct target's classification/ recognition. Hence, focused research is needed in this context to find application specific optimal features.

2.3.3.4. Target Classification Techniques

Further, for many applications, it is essential to know the specific target material types *such as*, metal, paper, plastic, clothing, etc., in addition to identifying the target's shape because from the security viewpoint it is important to measure how significant is the undercover object towards any possible threat and also to reduce excessive false alarms [153, 187]. Target's classification has been realized using the maximum likelihood estimation of EM based statistical measures for different classes [164]. A number of distribution models were tested and a single/mixture of two models can be assigned to any particular class depending upon target's characteristics [111, 112]. *E. Pasolli* [224] proposed a pattern-recognition system to classify buried objects from GPR using Gaussian kernel function and SVM classifier. Three different type of materials classified were limestone ($\epsilon_r = 8$, $\sigma = 0.1$ S/m), metal (perfect electric conductor) and air (free space) having classification accuracy of 74%, 75%, and 94%, respectively. However, robustness of this Gaussian kernel feature for material classification was not

investigated in the presence of clutter signal, which is very much likely to be present in the natural GPR work environment.

M. S. E. Mahallawy [69] introduced underground utility material identification from noisy GPR images degraded with speckle noise utilizing discrete cosine transform (DCT) coefficient features and support vector machine (SVM) classifier. Six different material types buried under dry sand were taken for algorithm testing including; ductile iron (DI) ($\epsilon_r = 14$, $\mu_r = 481$, $\sigma = 2.23 \times 10^7$ S/m), mild steel (MS) ($\epsilon_r = 3.1$, $\mu_r = 150$, $\sigma = 1.334 \times 10^5$ S/m), clay ($\epsilon_r = 2.5$, $\mu_r = 2$, $\sigma = 2.5 \times 10^{-2}$ S/m), medium density polyethylene (MDPE) ($\epsilon_r = 2.3$, $\mu_r = 2.39$, $\sigma = 10^{-5}$ S/m) in addition to perfect conductor and air voids. The presented approach shows recognition accuracy around 100% in clean environment and 78% in severely degraded environment. *H. Zhang* [103] utilized dielectric spectrum of GPR data in different frequency bands to identify the buried geo-electric structure depth, thickness, and permittivity parameters. The proposed algorithm can be applied for the target's classification of GPR signals. In addition, it offers advantages of low time complexity and strong anti-noise ability. *C. D. Haworth* [112] showed tracking of multiple metallic objects concealed on moving people in MMW images. Probability statistical model and hypothesis density filter has been used to track a variable number of targets. The two-component mixture model Laplacian and Rayleigh showed good fit as compared to Gaussians pdf. These reported material's classification techniques have been investigated on GPR data only, which operates at much lower frequencies (few GHz) as well as the reflected signal quality is fairly high, which supports comparatively easy discrimination among different target's materials.

Although, for the proposed MMW radar imaging applications, it will be interesting to check their applicability towards the correct material classification, where, the received signal will be of very low strength and primarily absorbed by the dielectric material itself and the surrounding. Additionally, due to the lack of correct permittivity models of different dielectric materials at MMW frequency, it will be quiet challenging to differentiate target materials from a stand-off distance, which may be kept in close proximity.

2.4. Conclusion

In this chapter, review of recent advances made in the field of MMW frequency and state-of-the-art MMW dual frequency antenna design and its imaging applications have been discussed. After

doing comprehensive study and critical analysis of the existing methodologies, following conclusions are drawn:

- MMW dual frequency antenna is the new emerging constituent for the dual band MMW systems that facilitates multi-tasking and miniaturized systems. However, at MMW several design challenges arise in terms of higher losses and very low dimensions. Thereby, there is a need to design a simple, compact and cost-efficient antenna.
- MMW imaging has emerged as one of the most favourable imaging modality as compared to the prevalent x-ray, microwave, visible/ IR imaging. It offers the features of high resolution as well as safe imaging.
- DIP techniques have demonstrated their significance in investigating computer vision images as well as are being used for microwave imaging. However, the capabilities of these techniques have to be examined for MMW images for different applications of image enhancement, image segmentation and material classification.
- There has been an increasing demand for an accurate non-destructive fault detection system, for various applications of material's quality estimation and its characterization. Numerous studies have been carried out, but very less amount of work has been done for quality monitoring of packaged goods for industrial applications. Hence, there is a need to develop an automatic fault/ non-fault classification model.
- Further, for the practical industrial scenario, in order to withstand the system noise and varying target contrast/ illumination, there is a need to develop an adaptive model which can take care of varying target's statistics and provide a correct concealed crack/ non-crack classification with minimum false alarm.
- Different machine intelligent techniques (ANN, fuzzy, SVM, etc.) are being extensively used for analysis of computer vision/ satellite image for classification/ recognition but the employment of these techniques for MMW imaging applications is still a major research area which needs to be investigated.

Chapter 3

Design of Simple, Cost-Effective and Compact Millimeter Wave Dual Frequency Planar Antenna

The strength of MMW is in the innovative solutions which, it offers in the fields of sensor technologies and image processing with favorable features of high resolution and safe imaging. In addition, MMW frequency offers portable, light weight systems due to the associated much lower wavelength (order of few mm) [120, 183]. In recent years, with the over-demanding use of the spectrum, number of consumers, and simultaneous applications (like, Bluetooth, GPS, voice/video call, etc.), researchers are moving towards concurrent dual band MMW systems having the capability of multi-tasking and multi-processing. In design of any transceiver system, antenna is an indispensable element, that acts as a transitional structure between the free-space and the guiding device (like, coax line, transmission line or waveguide). A dual frequency system is equipped with a dual frequency antenna, in which a single radiating structure is capable of concurrently resonating at two different frequencies. Different techniques are being used for this at microwave frequency. In spite of this, still the major challenge at MMW frequency is to have a simple and cost-effective dual resonant antenna. Therefore, in this chapter a concurrent 60 GHz/85 GHz microstrip antenna has been proposed taking care of higher losses and dimensional constraints.

3.1. Introduction

The field of antenna is vigorous and dynamic having a variety of antenna structures ranging from simple dipole, loop, slot or planar antennas to complex array structures [266]. However, the

choice of a particular MMW antenna type depends upon the specific application and system requirements [134]. Different high performance application domains, like, aircrafts, satellites, mobiles, radios, etc. have constraints of size, weight, cost, ease of installation, conformity and thus require low-profile antenna types. The low profile antenna design is appealing due to ease of fabrication, and such a design has the potential to be built at low cost. Furthermore, the planar structures can be lighter than reflector antennas of similar performance and are also easier to install. With this concern, planar microstrip antennas lend themselves as a natural choice posing features of compactness, simplicity, mechanically robust, conformity, and compatibility with MMIC designs [27, 283]. Additionally, advantages offered by it overshadow its limitations, such as, narrower bandwidth and low-power capacity.

At MMW frequency, the design of microstrip antenna exhibits several challenges, such as, limited gain, increased noise, higher order mode losses, conductor/dielectric loss and unavailability of transmission line models [56]. However, different substrates (bulk or artificially synthesized) and techniques have been proposed to reduce losses at MMW frequency, such as, low dielectric substrate (Teflon/quartz) [197, 211, 260, 339], high index substrate (Si/GaAs) [19, 231, 257, 282, 341], bulk micromachining [70, 88, 125, 245], synthesized low dielectric substrate [208, 331], superstrates [345], substrate integrated waveguide (SIW) [347], low-temperature co-fired ceramic (LTCC) [10, 135]. Making use of any of these different techniques to combat losses at MMW, a number of planar and quasi-planar MMW antenna structures have been reported in the literature, like, slot type antenna [47, 208, 338, 339, 346], leaky wave type antenna (dielectric rod, NRD guide) [186, 227, 290, 310], high gain reflector type antenna [212], planar yagi-uda type antenna [16], log-periodic antenna [341], and many others for different applications.

At microwave frequency, various techniques are being used for achieving dual frequency antenna design, that includes orthogonal mode dual-frequency patch antennas using single or dual feed that excites dual mode (TM_{10} , TM_{01}) resonance with orthogonal polarization [181]; reactive loading by placing shorting pins [199], slots [41, 65, 165], stubs [152, 255], spur [104, 256] etc., that excites dual resonance with the varying frequency ratio depending on their relative positions [8, 174, 193]; multiple coplanar [3, 156, 244, 254]/vertically stacked patches [18, 307, 314] providing same or dual polarization; artificially structured metamaterials - split-ring resonators (SRRs) [67, 130, 168, 241], which offer high quality factor; capacitive coupling [119, 140, 167], etc. However, design of MMW dual band antenna has been given less attention, despite the fact it offers advantages of size and cost reduction. Few of the reported works are:

58/77 GHz antenna using flip-chip assembly [285], fractal bowtie antenna using movable plate for 60/77 GHz [184], 38/60 GHz switchable MEMS antenna [173], 40/60 GHz split ring resonator (SRR) based antenna [128] and 24/60 GHz antenna using 0.1 μ m standard CMOS process [133], 33.75/36.75 GHz spur based antenna on multilayer GaAs substrate [257]. Most of these reported techniques require high precision fabrication and have the complex structure, making them commercially cost inefficient. Whereas, the need is a simple designed compact antenna, *i.e.*, antenna should be as minimum as possible with a cost-effective substrate. Hence, it will be of great importance to design a simple, cheap and compact, dual resonant MMW antenna. Here, the dual frequencies 60 GHz (V band) and 85 GHz (E band) are selected because of their commercial competency for future communication systems as well as imaging systems. 60 GHz technology is attractive and of significant interest due to the huge unlicensed ISM (Industrial, Scientific and Medical) band of 7 GHz (57 - 64 GHz), which, offers gigabit WPAN (802.15.3c) applications. Similarly, the other resonant frequency 85 GHz lies within the E band (81 - 86 GHz) allocated for 10 Gbps outdoor network future applications. Henceforth, in this chapter, we have proposed a design for 60 GHz/85 GHz concurrent dual frequency microstrip antenna supported by the fabricated prototype measured results.

This chapter is further divided into following sections: section 3.2 discusses theoretical background, section 3.3 gives methodology for MMW dual frequency planar antenna design, section 3.4 details simulation results, section 3.5 details fabricated prototype antenna and measurement results, and finally section 3.6 gives the conclusion.

3.2. Theoretical Background

At MMW frequency, microstrip printed antennas are gaining particular interest due to their planar profile and ease of integration for single chip millimeter monolithic integrated circuit (MMIC) design [3, 7, 135, 344]. Planar antenna performance at high frequencies is severely affected by substrate parameters, conductor/dielectric losses, and higher order mode losses. Several challenges are need to be considered, while designing an optimal antenna at MMW frequency, like:

3.2.1. Choice of Suitable Substrate

For a good planar antenna performance low dielectric and thick substrate is desired since this provides better efficiency, due to the loosely bound fields, higher bandwidth and efficiency [27, 322]. Although, on the low index substrate, antenna require larger physical antenna size for the fundamental mode (TM_{10}) depending upon $L = c/2f(\sqrt{\epsilon_r})$, (ϵ_r) = substrate relative permittivity [134]. Antenna on high index substrates are not desirable because tightly bound fields result in reduced radiated power, higher losses, less efficiency and less bandwidth. In addition, patch antenna stops resonating for thickness (H) $> 0.11\lambda_0$, since antenna impedance becomes purely inductive [238]. *This poses an upper limit on the thickness of the substrate w.r.t. resonant frequency. Thereby, the low index, thin substrate will be an optimal choice for MMW microstrip antenna design. Additionally, for 60/85 GHz operating frequencies the limit of substrate thickness (H) comes to be; $H < 0.388$ mm.*

3.2.2. Power Loss Due to Surface Waves

At MMW, TE and TM surface waves are more likely to be excited on a grounded substrate. Surface waves give rise to end fire radiation, leading to unwanted coupling between elements and can leak through bends or discontinuities, resulting in loss of radiated power, reduced antenna efficiency and degraded polarization. The cut-off frequency of these modes is given by [238]:

$$f_c = \frac{nc}{4H} \sqrt{(\epsilon_r - 1)} \quad (3.1)$$

Where, c = speed of light, H = height of substrate, $n = 0, 1, 2, 3, \dots$ for $TM_0, TE_1, TM_2, TE_3, \dots$ surface mode. TM_0 mode has zero cut-off frequency and can occur in any substrate thickness. For thinner substrates, its effect can be ignored. However, for thicker substrate, it causes more surface waves and thereby, loss of radiated power and antenna efficiency. A suitable substrate needs to be chosen for MMW antenna design, for which, cut off frequency of higher order mode is well above the operating frequency.

For the proposed 60/85 GHz dual band antenna, maximum limit of substrate thickness (H) comes to be; $H < 0.966$ mm corresponding to TM_{10} surface mode.

3.2.3. Conductor and Dielectric Losses

Dielectric behaviour of a substrate can be defined by the complex dielectric constant $(\epsilon) = \epsilon' - j\epsilon''$, with ϵ' = real part of ϵ and ϵ'' = imaginary part of ϵ . This gives relative permittivity $\epsilon_r = \epsilon'/\epsilon_0$, here, ϵ_0 = free space permittivity and dielectric loss tangent $\tan\delta = \epsilon''/\epsilon'$, (or $Q = 1/\tan\delta$) [172]. Loss tangent accounts for losses of power and hence gives reduction in antenna radiation efficiency. Conductor loss is defined as $1/(H\sqrt{\pi f\mu\sigma})$, σ is the conductivity of the patch, μ is the substrate permittivity and H is the height of the substrate [131]. Substrate permittivity and loss tangent varies with frequency, which is termed as frequency dispersion.

Henceforth, dielectric and conductor loss increases at MMW frequency and can be taken care off by choosing substrate of lower loss tangent and higher thickness, respectively.

Thereby, for being in the safe operating limit without exciting surface wave mode and without causing reduction in radiated power (conductor/dielectric loss), we considered the optimal substrate: Rogers RT5880 with specifications: $\epsilon_r = 2.2$, $H = 5$ mil (0.127 mm), $\tan\delta = 0.002$, metallization (t) = 0.017mm for simulation as well as realization of MMW prototype antenna.

3.2.4. Probe Measurement Feasibility

At MMW frequency, fabricated prototype device characterization is done by using coplanar ground-signal-ground waveguide (GSG-CPW) probe measurement, where ground and signal lines are coplanar [170]. However, in the microstrip based circuits ground is in the lower side of the substrate opposite to that of the conductor line, and therefore, on-wafer measurements of microstrip circuits typically require an interface between the device under the test (DUT) and the input CPW probes [308]. Firstly, a 50 Ω CPW line operating in the fundamental CPW mode is needed to be designed according to the dimensions of available measurement probe pitch for proper probe contact. Further, to couple maximum RF power from CPW feed line to the microstrip line, an efficient CPW-to-microstrip transition is needed to be designed for minimizing the overall reflection and maximizing the transmission.

3.2.5. Fabrication Constraint

Most of the reported dual resonance antenna techniques, *such as*, cutting slots, shorting pins, closely placed multiple patches, metamaterials etc., that are commonly used at microwave frequencies require stringent fabrication and alignment accuracies at MMW (due to correspondingly low resonant dimensions $\lambda/2 \approx 1.5$ to 2.5 mm). *But, in order to make the MMW antenna design cost-effective and extendable, a simpler design technique is essentially desired without complicating the fabrication procedures or raising the cost.*

Therefore, in this chapter an attempt has been made to consider all these challenges and hereby, we propose a simple, single layer, compact and cost-effective 60 GHz/85 GHz dual frequency MMW antenna design.

3.3. Methodology for MMW Dual Frequency Planar Antenna

Design

Geometry of the proposed MMW dual frequency planar antenna is shown in the Figure 3.1(b). Here, we have used microstrip line based planar antenna design and further to ensure the proper measurement feasibility, a coplanar feeding line has been integrated into it. The complete antenna design can be subdivided into three major sections depending upon their operating principle, *viz*, (1) radiating patch, (2) feed section, (3) matching network. The behavior and importance of each section will be discussed separately.

3.3.1. Section 1: Dual frequency Radiating Patch Geometry

3.3.1.1. Single Frequency- Basic Patch

The initial antenna structure is a rectangular microstrip patch as shown in Figure 3.1(a). The resonant frequency of the Microstrip antenna (MSA) can be tuned by changing its resonant dimension. For a rectangular MSA, resonant frequency is given by [27]:

$$f_r = \frac{c}{2\sqrt{\epsilon_r}} \sqrt{\left(\frac{m}{L}\right)^2 + \left(\frac{n}{W}\right)^2} \quad (3.2)$$

Where, L is the length and W is the width of the radiating patch, c is the speed of light. Here, m , n represent the number of half-cycle field variations along length and width of the patch.

For the fundamental TM_{10} mode excitation, length of the conducting patch $L = \lambda_g/2$, where, $\lambda_g = \lambda_0/\sqrt{\epsilon_r}$, λ_0 corresponds to the free space wavelength. So, initial dimensions for single frequency (f_1) microstrip antenna can be found by taking the fringing field effect into account as per design equations given in chapter 1, section 1.3.1.1.

3.3.1.2. Dual Frequency- Modified Patch

Further, in order to achieve the dual resonant frequencies using the single radiating patch, a slight modification in the basic geometry has been done by reactively loading one of the radiating edges of the patch. Here, for obtaining dual band from basic MSA, an open circuited stub has been introduced [66, 249]. Input impedance (Z_{oc}) of the open circuit stub is given by,

$$Z_{oc} = Z_0 \frac{Z_L + jZ_0 \tan(\beta l)}{Z_0 + jZ_L \tan(\beta l)} = -jZ_{stub} \cot(\beta l) \quad (3.3)$$

here, ($Z_L = \infty$, $Z_0 =$ stub impedance (Z_{stub}), $l =$ length of stub, $\beta =$ propagation constant).

Input impedance of the open circuited stub is capacitive or inductive around the resonant frequency of the patch depending upon the stub length [239]. When the length of the stub is small, it yields tunability, whereas when it is comparable to $\lambda/4$ ($\beta l = \Pi/2$), it excites the other higher order mode (TM_{11}) resonant frequency (f_2) and yields dual frequency operation [64]. Henceforth, as shown in Figure 3.1(b), to achieve a MMW dual band antenna, an open circuited $\lambda_g/4$ stub at the radiating edge of the patch has been placed. Here, short circuit stub was not used due to the associated complexities in shorting the stub to the ground. Further, our main objective was to propose a simple and cost-effective dual resonant antenna, hence, we tried to keep our design as simple as possible on an inexpensive substrate, which can be fabricated using conventional photolithography technique without raising the fabrication cost.

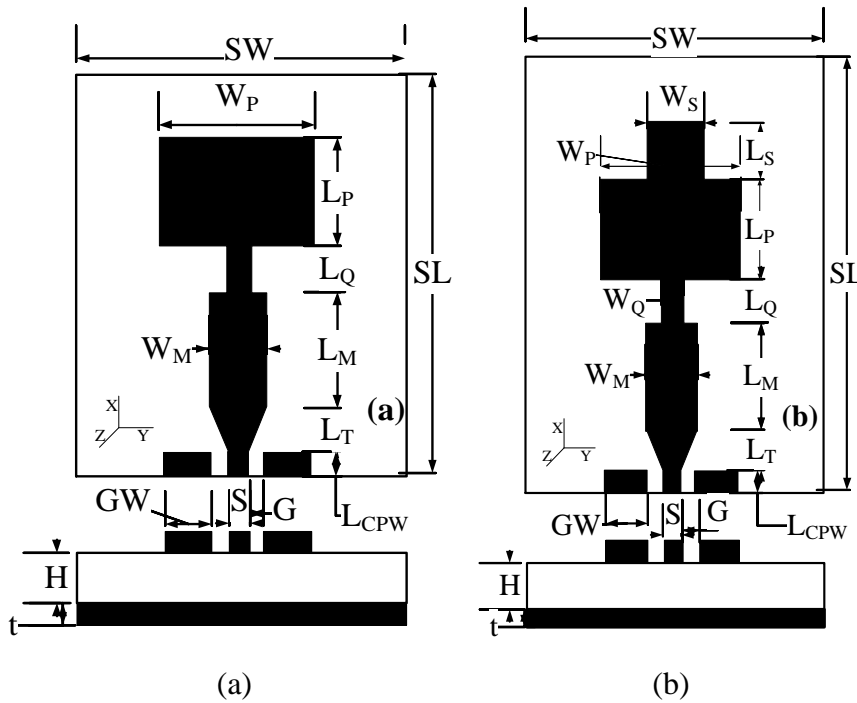


Figure 3.1. CPW fed MMW dual resonant antenna geometry- 60/85 GHz (dimensions not to scale). (a) Antenna 1: single frequency antenna, (b) Antenna 2: dual frequency antenna.

3.3.1.3. Surface Current Distribution

Figure 3.2 shows the surface current distribution of dual band radiating antenna at two resonant frequencies *viz.*, 60 GHz and 85 GHz. As already stated, inclusion of the tuning stub changes the fundamental and higher order mode surface current distribution and thus supports dual resonance.

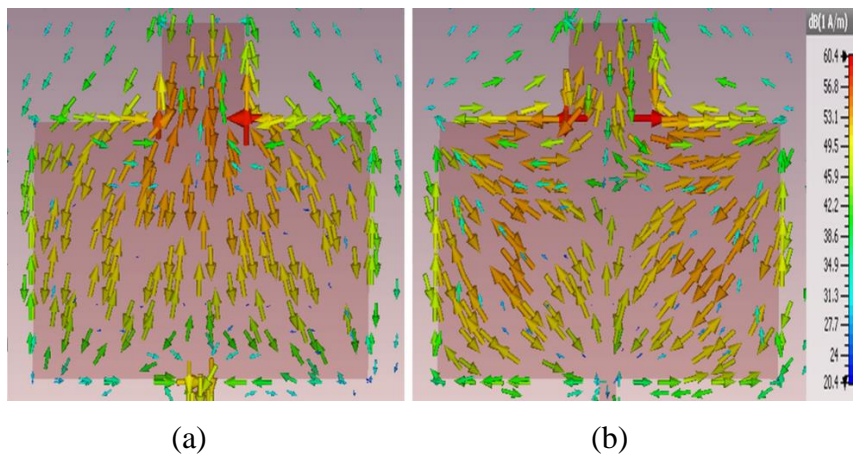


Figure 3.2. Surface current distribution for dual band MMW antenna at: (a) 60 GHz and (b) 85 GHz.

As seen from Figure 3.2(a), the surface current distribution shows one half wavelength variations along the length of the patch, however, along the width there is no change in the direction of current distribution. This signifies fundamental mode TM_{10} propagation at 60 GHz resonant frequency. Further, from Figure 3.2(b), the surface current distribution shows one half wavelength variations along the patch length as well as along the patch width. This signifies, higher order TM_{11} mode propagation at 85 GHz resonant frequency. By adjusting the tuning stub length and width, current distribution direction in the stub and the patch can be varied, and thereby, this structure supports two different resonant frequencies using a single radiating modified patch structure.

3.3.1.4. Effect of Parametric Variations on Antenna Performance

The effect of varying stub length was also investigated on antenna resonance and it was observed that stub modifies the fundamental and higher order mode resonant frequencies of the patch and thereby, realizing dual response. Variation in the two resonant frequencies f_1 and f_2 with varying stub length for different fixed stub widths is shown in Figure 3.3.

On increasing the stub length (L_s), f_1 and f_2 decreases for any fixed stub width (W_s), however, frequency variation is more pronounced for higher stub length values as compared to lower values of stub length as shown in Figure 3.3(a). Frequency ratio (f_2/f_1) increases with increasing stub length (L_s) for any fixed stub width (W_s). Further, frequency ratio increases, with increasing stub width (W_s) for any fixed stub length (L_s), as shown in Figure 3.3(b).

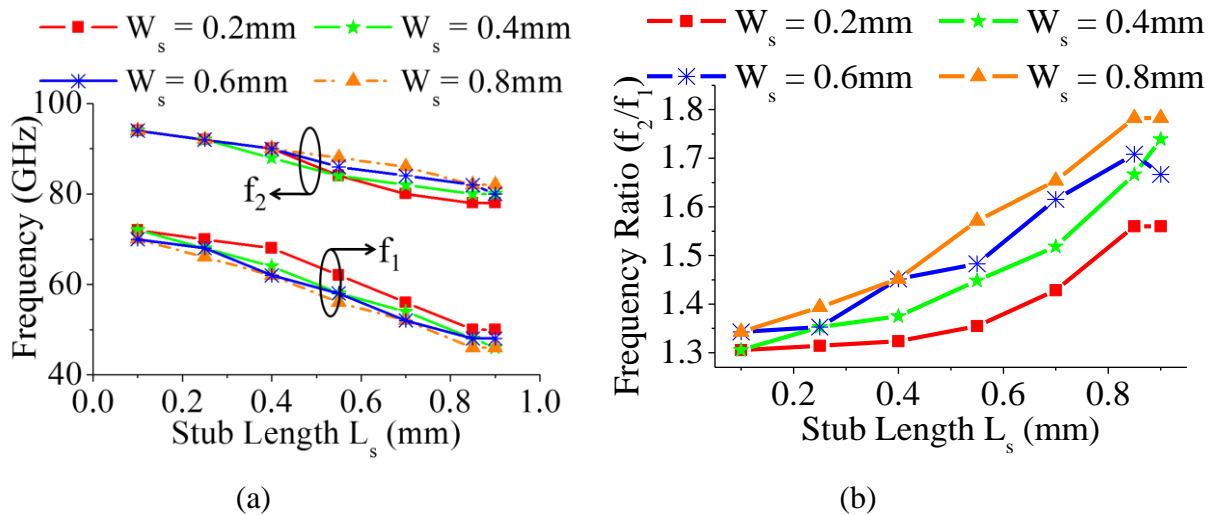


Figure 3.3. Effect of varying stub length (L_s) and stub width (W_s) on: (a) the two dual resonant frequencies f_1 and f_2 and (b) on the frequency ratio (f_2/f_1) characteristic.

3.3.2. Section 2: Feeding Section

The radiating patch feeding has been done through the microstrip line as shown in Figure 3.1. Instead of probe feeding, inline microstrip feeding has been used, since coaxial probe pin at MMW band is approximately of the same cross-section as of MMW planar antenna. So, it is practically infeasible to drill a hole to provide a proper contact between the two, i.e., antenna and the feed. At MMW frequency, device measurement is through on-wafer coplanar probes [170]. The use of probes to measure microstrip circuits is difficult, since the probes could not contact the ground plane of the microstrip transmission line. In this case, it is highly desirable to have a coplanar waveguide (CPW)-to-microstrip transition. The feeding section consists of following three subsections in order to ensure maximum power transfer from the coplanar GSG probe to microstrip patch antenna:

3.3.2.1. Finite Ground-Conductor Backed CPW Line

A coplanar waveguide (CPW) may be viewed as the two symmetrically coupled slot lines as shown in Figure 3.4 [291]. An important feature of the CPW line is that signal line and ground plane lie on one side of the substrate, thus providing a relative ease for passive and active device connection, without requiring a via hole. A CPW line may have a lower ground plane or not, however, the conductor backed CPW line is preferred to provide mechanical strength, since substrates used at MMW frequency are relatively thin and fragile. Additionally, here CPW has to be built on the same microstrip antenna substrate, which consists of a lower ground plane to suppress any backward radiation, so the design preferred to use comes out to be conductor backed-CPW line (CBCPW). Further, upper side ground plane is generally of finite width, for easy analysis, which gives rise to the finite ground conductor backed CPW line (FG-CBCPW) configuration as shown in Figure 3.4. Here, GW is the side ground plane width, S is the conductor width and G is the spacing between conductor and side ground plane line.

FG-CBCPW may also be viewed alternatively as a system of three coupled microstrip lines. Normalized side ground plane width ($GW/(S+2G)$) should be less than $\lambda_g/8$, to keep the radiation losses and dispersion small, and it should be greater than twice the conductor width (S) so as to reduce attenuation due to conductor losses of the signal line [237]. The limiting frequency for FG-CBCPW line for single CPW mode operation corresponds to the maximum frequency,

for which phase constants of the CPW mode and the first lateral higher order mode intersect, beyond which it shows highly dispersive behavior and higher order mode propagation.

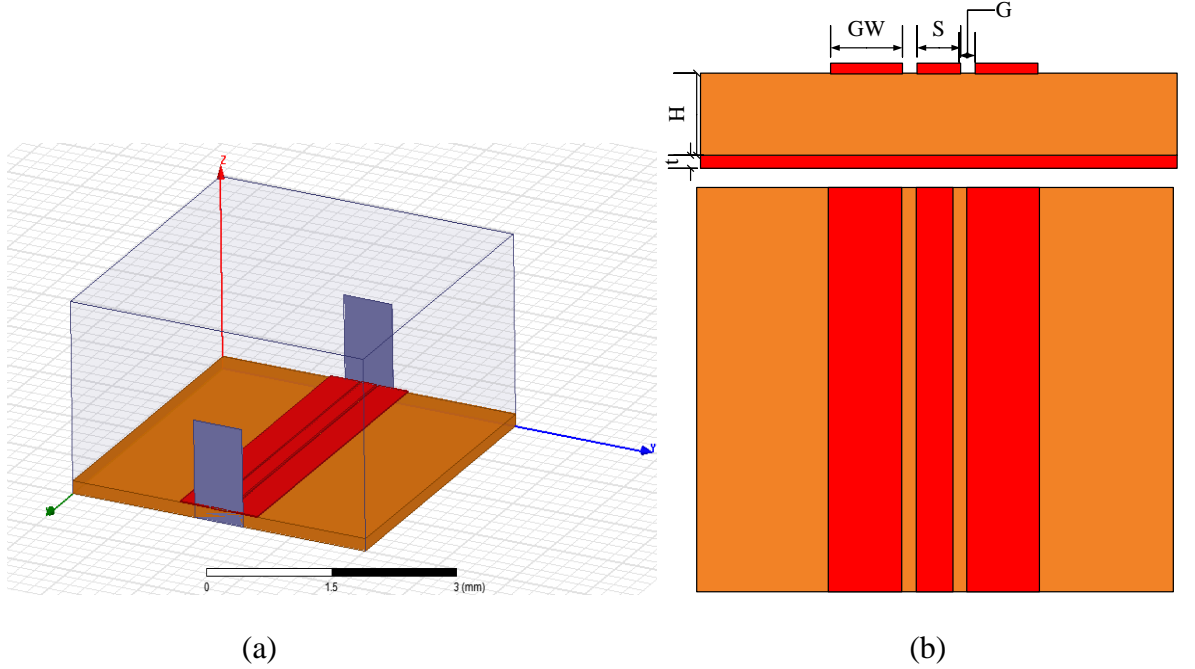


Figure 3.4. Geometry of finite ground conductor backed (FG-CBCPW) transmission line: (a) perspective view, (b) cross-sectional and top view.

This maximum frequency depends upon both lateral line dimensions (W_{tot}) and substrate thickness (H) and is given by [265]:

$$f_g(W_{tot}) = \frac{2}{W_{tot}\sqrt{2\mu_0\epsilon_0(\epsilon_r-1)}} \text{ where, } W_{tot} = S + 2G + 2GW \quad (3.4)$$

$$f_g(H) = \frac{1}{H\sqrt{\mu_0\epsilon_0(\epsilon_r-1)}} \quad (3.5)$$

This means that both substrate thickness (H) and total line width (W_{tot}) have to be kept small enough to maintain the desired single-mode CPW behavior at the desired frequency of operation. Since, FG-CBCPW resembles a system of three coupled microstrip lines, length of FG-CBCPW should be kept much less than half wavelength of microstrip line (MSL) mode, *i.e.*, $L \ll (\lambda_0/\sqrt{\epsilon_r})/2$, to avoid excessive cross-talk or possible resonance [291].

3.3.2.2. Microstrip Line

Microstrip line consists of a conducting strip printed over the grounded dielectric substrate. The conductor strip resides in an inhomogeneous region having an abrupt dielectric

interface, since the region above is air, whereas lower portion is filled with the dielectric. Microstrip line has most of its field lines in the dielectric region, concentrated between the strip conductor and the ground plane, and some fraction in the air region above the substrate. For this reason, the microstrip line cannot support a pure TEM wave [239]. The phase velocity of EM fields in the dielectric region would be $c/\sqrt{\epsilon_r}$, but the phase velocity of EM fields in the air region would be ‘ c ’ only, due to this phase mismatch quasi TEM mode is generated.

The geometry of microstrip line is shown in Figure 3.5, which consists of a conductor strip of finite width (W_M) on a grounded dielectric substrate (ϵ_r), having thickness (H). Figure 3.5(b) shows the cross-sectional and top view of microstrip line and Figure 3.5(c) shows the E-field distribution of fundamental quasi TEM mode propagating in the microstrip line.

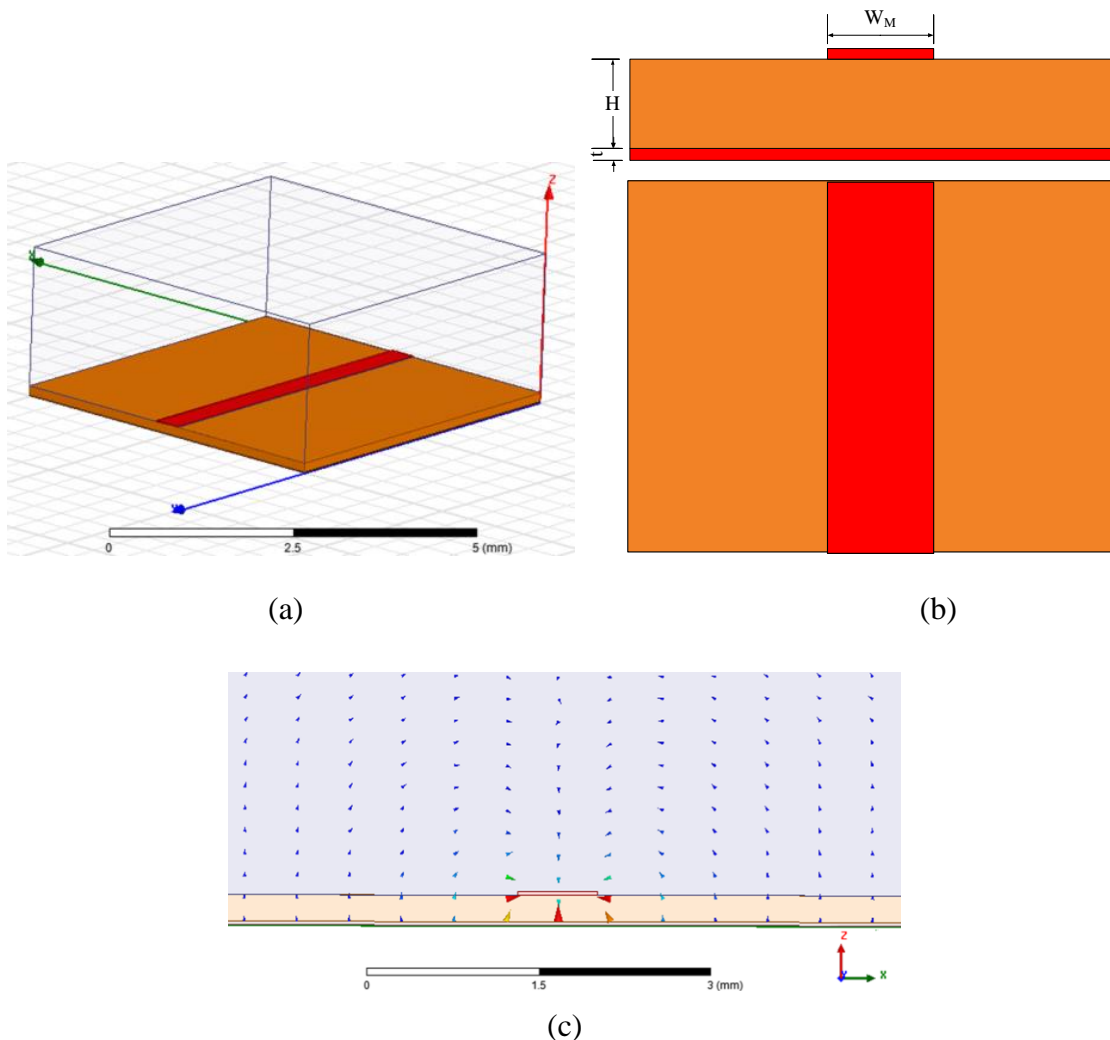


Figure 3.5. Microstrip line: (a) perspective view, (b) cross-sectional and top view, (c) E-field distribution vector of quasi TEM mode.

3.3.2.3. CPW to Microstrip Transition

An effective transition is desired between two different transmission line configurations (CPW & microstrip) in order to transform the EM fields from CPW mode to the microstrip mode [308]. Primarily, there are two types of transitions, one that uses via hole and the second type uses via less transition. Via hole, however, provides broadband transition, but adds complexities in fabrication. Therefore, via less transitions are preferably used [247]. The key idea while designing the transition is to maintain the uniform, gradual change in the characteristic impedances. This approach helps in minimizing the overall reflection and maximizing the transmission.

3.3.3. Section 3: Matching Network

Since, edge impedance of the rectangular patch antenna is different from the feeding 50Ω microstrip line, a proper impedance matching network is needed to interconnect the two structures, in order to ensure maximum power transfer from feedline to the antenna. Thereby, for impedance matching between patch and the microstrip line, a quarter wave transformer has been used as an impedance matching network. The quarter-wave transformer has a length equal to quarter wave in microstrip and its width is determined by the characteristic impedance $Z_{\lambda/4}$, given by [239]:

$$Z_{\lambda/4} = \sqrt{Z_0 Z_{in}} \quad (3.6)$$

where, Z_0 is the characteristic impedance of the feedline and Z_{in} is the input impedance of the radiating patch. Demonstration of matching network is shown in Figure 3.6.

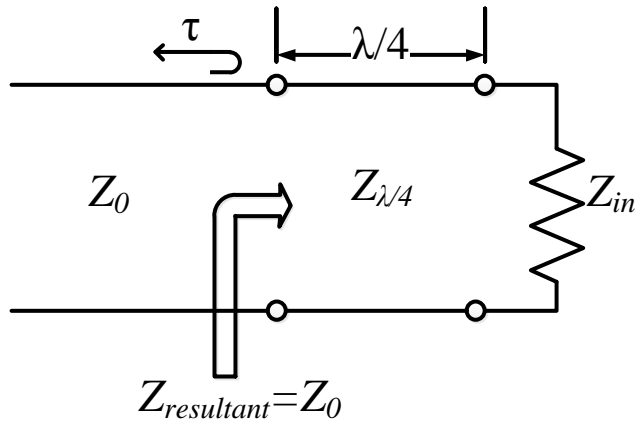


Figure 3.6. The quarter-wave matching transformer.

3.4. Simulation Results

The antenna structure and different transmission line sections were firstly simulated and optimized using 3D full wave EM solver HFSS before going for simulation/fabrication of complete antenna prototype. Since, at MMW frequency no proper closed form expression is available for planar structure design, hence, different sections, *viz.*, microstrip transmission line, co-planar waveguide transmission line (CPW) and transition structure (CPW-to- microstrip line) were separately modeled in terms of characteristic impedance (Z_0) and effective dielectric constant (ϵ_{eff}) *w.r.t.* frequency using HFSS.

3.4.1. Microstrip Line Characterization at MMW Frequency

Microstrip line at MMW was characterized, *i.e.*, dependence of characteristic impedance (Z_0) and effective dielectric constant (ϵ_{eff}) on conductor width and frequency was plotted. Figure 3.7(a) shows Z_0 vs (W_M/H) and ϵ_{eff} vs (W_M/H) plot at 60 GHz, where, (W_M/H) = normalized conductor width. As seen in figure, on increasing conductor width, characteristic impedance (Z_0) of the microstrip line reduces and varies in the range of $Z_0 = 20$ to 120Ω . However, on increasing normalized conductor width, there is only a slight increase in ϵ_{eff} for a fixed frequency (say, $f = 60$ GHz). From these plots, one can easily find microstrip conductor width corresponding to the given microstrip line impedance, and vice versa. For example, for a 50Ω microstrip line impedance, the conductor width is $W_M = 0.38$ mm.

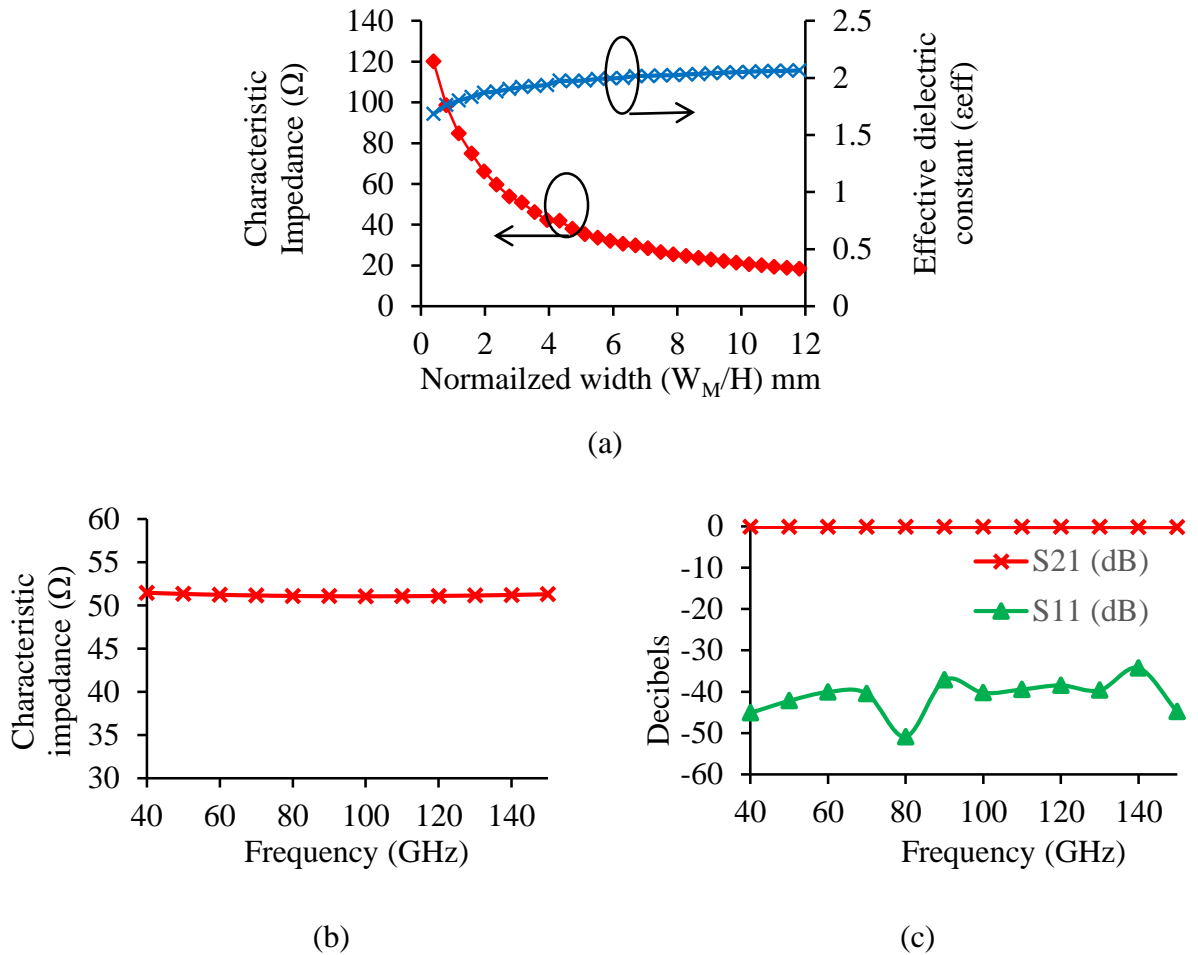


Figure 3.7. Microstrip line characteristic plots: (a) characteristic impedance (Z_0) and effective dielectric constant (ϵ_{eff}) vs conductor normalized width (W_M/H) plot at a fixed frequency ($f = 60$ GHz), dispersion in microstrip line characteristics with frequency for a fixed 50Ω conductor width: (b) variation in Z_0 and (c) variation in reflection/transmission loss.

The frequency dependence of microstrip line is shown in Figure 3.7(b), (c). In Figure 3.7(b) dispersion of characteristic impedance w.r.t. frequency is shown for a fixed conductor width, which shows nearly constant line impedance over the full frequency range of operation. Figure 3.7(c) shows the reflection/insertion loss characteristic w.r.t. frequency, which shows maximum transmission and nearly zero reflection, of the designed MMW microstrip line in full frequency range of interest, i.e., 60 GHz to 100 GHz.

3.4.2. FG-CBCPW Transmission Line Simulation

In order to provide measurement compatibility with coplanar 50 Ω GSG probe (i.e., ground-signal-ground), a 50 Ω CPW feedline is separately designed and later on integrated to the antenna structure on the same substrate.

Keeping in view of the single CPW mode propagation as discussed in section 3.3.2.1, and the dimensional constraints of our available GSG probe pitch 150 μm , i.e., $(S+2G) < 150 \mu\text{m}$, the dimensions of 50 Ω FG-CBCPW line comes out to be, $GW/G/S = 0.4\text{mm}/0.03\text{mm}/0.2\text{mm}$ as shown in Figure 3.8Figure 3.4(b). However, initial dimensions of the CPW line was computed using Agilent's advanced design system (ADS) - Linecalc tool. The E-field distribution of the fundamental CPW mode propagating in the simulated CPW line is shown in Figure 3.8(a).

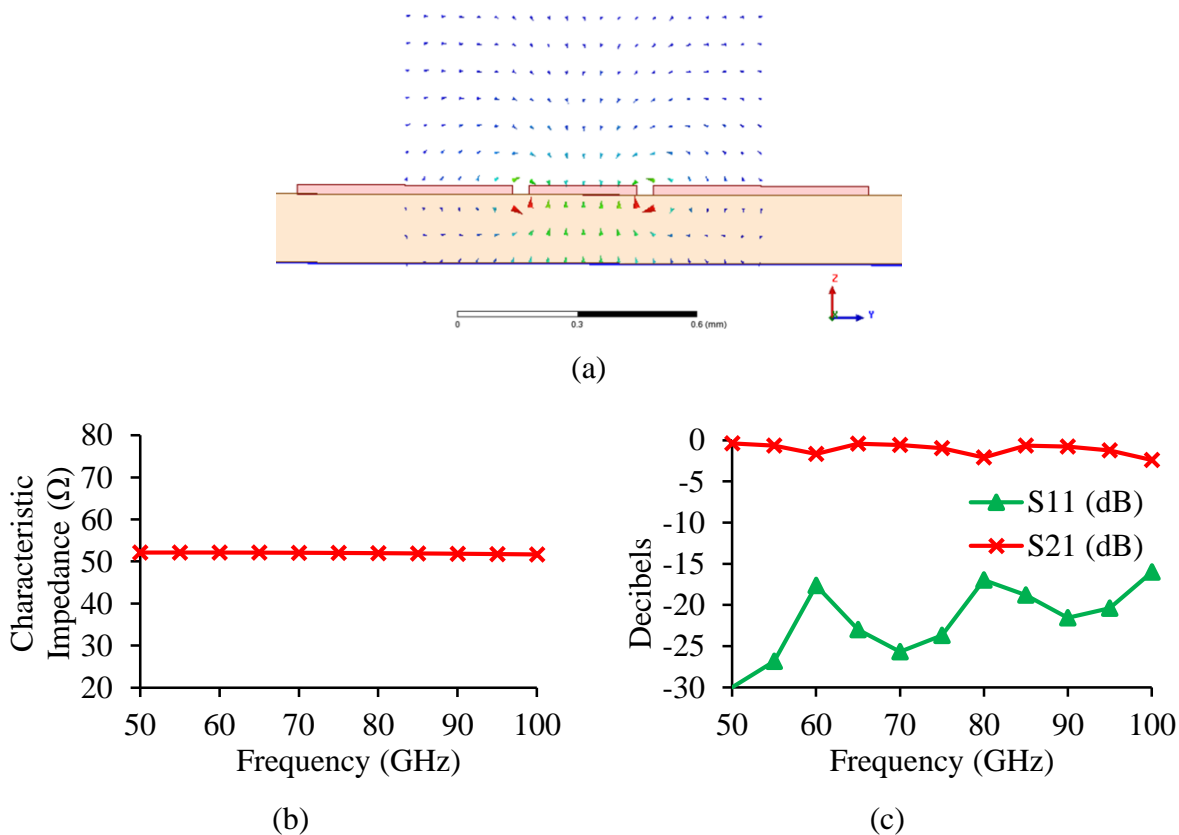


Figure 3.8. FG-CBCPW transmission line characteristics: (a) E-field vector distribution of fundamental CPW mode, (b) characteristic impedance vs frequency, (c) reflection/transmission characteristic plot vs frequency.

Further, Figure 3.8(b) shows FG-CBCPW line characteristic impedance vs frequency plot, which shows nearly constant Z_0 within the frequency range of our interest. Also, transmission/reflection vs frequency plot in Figure 3.8(c) signifies good transmission line behavior of the simulated coplanar transmission line in the considered complete MMW range of operation.

3.4.3. Design of CB-FGCPW to Microstrip Line Transition Structure

A good matching transition is required to effectively propagate the RF signal from the coplanar feed to the antenna. Since, the width of $50\ \Omega$ microstrip line ($W_M = 0.38\ \text{mm}$) and the width of $50\ \Omega$ FG-CBCPW line centre conductor ($S = 0.2\ \text{mm}$) are not the same, hence, a smooth transition structure is required such that to avoid any mismatch between microstrip and CPW line. A back to back CPW to microstrip transition has been simulated as shown in Figure 3.9(a) in order to initially analyse its behaviour, before incorporating it with the antenna. The smooth taper connecting centre conductor of the CPW line to the microstrip line provides gradual change in the impedance and the field lines, minimizing overall reflection and maximizing the transmission. The length of transition is $\approx \lambda_g/4$, where λ is the operating wavelength [170]. Bandwidth of CPW-to-microstrip transition depends upon CPW feed line length, due to the propagation of coplanar microstrip mode (CPM) along the CPW feed-line [247].

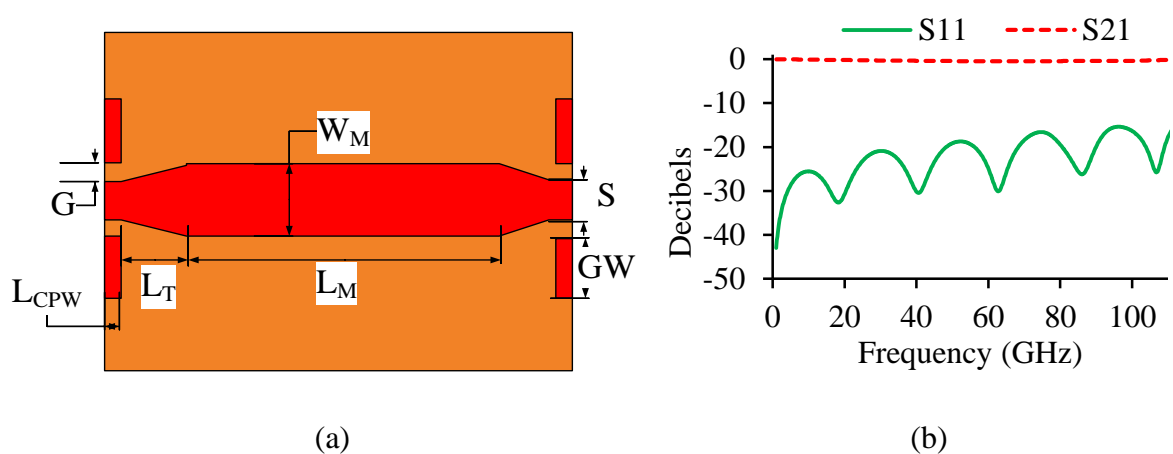


Figure 3.9. A back to back transition of finite ground conductor backed coplanar waveguide (FG-CBCPW) to microstrip transmission line: (a) Geometric structure and (b) Simulated reflection/transmission loss vs frequency plot.

Hereby, by keeping CPW pad length small, a wide bandwidth CPW-to-microstrip transition has been achieved covering the full MMW frequency of interest. Figure 3.9(b) shows the simulated insertion loss and return loss plot of the transition structure. It shows maximum insertion loss of 0.5 dB and return loss lower than -16 dB for the frequency range of 1 GHz to 110 GHz. The designed transition is wide band and via-less, hence, makes the fabrication process relatively less expensive and less complicated.

3.5. Fabrication and Measurement of Designed MMW Dual Resonant Planar Antenna

Once different sections of CPW fed MMW dual frequency planar antenna were separately analyzed, *i.e.*, CPW line, microstrip line, transition structure, matching network, radiating patch; in the next step, the complete integrated antenna structure was simulated. Further, antenna design parameters were optimized using HFSS, to achieve the required dual resonant response at the two respective frequencies 60 GHz (V band) and 85 GHz (E band).

Table 3.1. Final dimensions of the designed dual frequency MMW planar antenna.

S. No.	Design parameter (notation used)	Value (in mm)
1	Microstrip patch length (L_P)	1.25
2	Microstrip patch width (W_P)	2
3	Matching network length (L_Q)	0.6
4	Matching network width (W_Q)	0.1
5	Microstrip line length (L_M)	0.94
6	Microstrip line width (W_M)	0.38
7	Stub length (L_S)	0.48
8	Stub width (W_S)	0.5
9	Transition length (L_T)	0.3
10	CPW feedline length (L_{CPW})	0.1

Actual photograph of the fabricated MMW dual frequency antenna prototype and its scanning electron microscope (SEM) image is shown in Figure 3.10. The substrate dimensions

were taken to be $SL \times SW = 5 \text{ mm} \times 5 \text{ mm}$. The final optimized dimensions of dual frequency MMW antenna are given in Table 3.1. The cross-sectional area of the dual frequency antennas is 3.7 mm^2 .

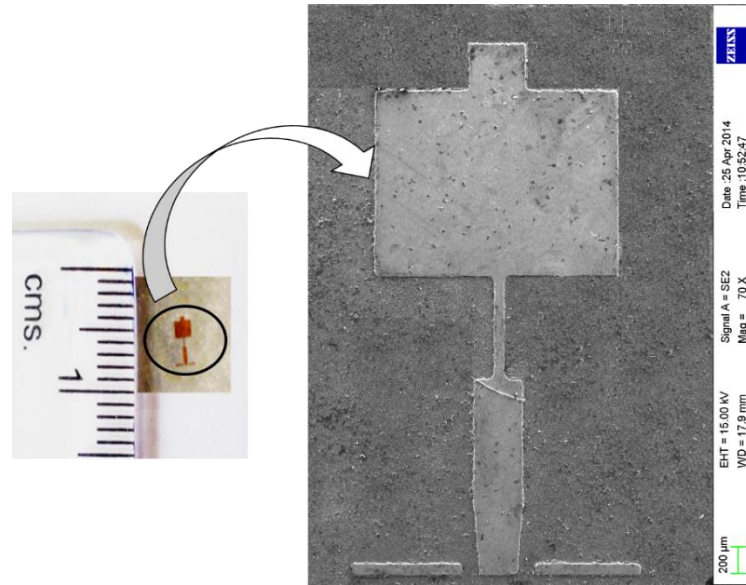


Figure 3.10. Fabricated prototype of designed MMW dual frequency-60/85 GHz antenna & its SEM image (70x-zoom SEM).

Figure 3.11 shows comparative (simulated vs measured) reflection coefficient plot of dual band MMW antenna. The measured S_{11} values are -15.2 dB and -48.15 dB and fractional bandwidths are 1% and 6.4%, at the two respective resonant frequencies.

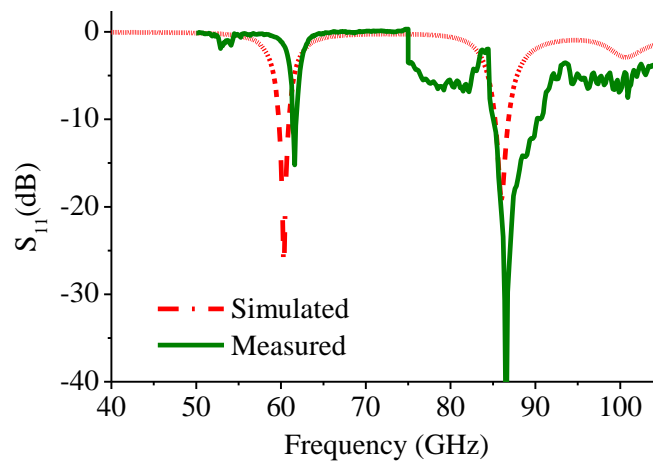


Figure 3.11. Comparative (measured vs simulated) reflection coefficient vs frequency plot for the designed dual band (60/85 GHz) MMW antenna.

Thus, the overall optimized structure provides dual frequency operation with an excellent interband rejection, while simultaneously maintaining low profile characteristic of the antenna. However, there is a slight shift in measured and simulated resonant frequencies viz, 2%, 0.7% corresponding to 60 GHz, 85 GHz that can be accounted for fabrication tolerances, imperfect contact of probe pins to CPW feed-line and parasitic impedance at the feeding point caused due to the three point GSG probe [19, 358]. The fabricated prototype antenna shows good broadside radiation characteristic at the two resonant frequencies concurrently as given in Table 3.2. At $f_1 = 61.2$ GHz measured gain values are 8.49 dBi and 8.95 dBi in E and H planes, respectively. At $f_2 = 85.6$ GHz measured gain values are 5.13 dBi and 5.37 dBi in E and H planes, respectively.

Table 3.2. Measured values of fabricated dual frequency MMW antenna prototype.

S. No.	Resonant frequency (GHz)	Fractional bandwidth	Gain (dBi)
1	61.2	1%	8.49 (E-plane), 8.95 (H-plane)
2	85.6	6.4%	5.13 (E-plane), 5.37 (H-plane)

A comparison of the designed antenna with other reported works is given in Table 3.3. It can be inferred from the table that our proposed MMW dual frequency antenna operates quite well at the two concurrent dual frequencies with appreciably good gain and is of compact size as compared to the other reported MMW dual band antenna techniques.

Table 3.3. Comparison of the performance of reported MMW dual frequency antennas with our designed MMW dual frequency antenna.

S. No.	Parameters	Ref [128]	Ref [184]	Ref [285]	Proposed Dual Band Antenna
1.	Frequency (GHz)	41/52.2	60/77	58/77	60/85
2.	B.W (%)	2/ --	--	6.1/5.8	1/6.4
3.	Gain (dBi)	3.8/ 4.2	3.5/4.8	-2/0.3	8.95/5.37
4.	Fabrication	Complex (SRR)	Complex (MEMS)	Complex (flipchip)	Simple (stub)
5.	Size	----	4.6 mm ²	14 mm ²	3.7 mm²

Further, the antenna design is kept simple to achieve our objective of fabrication simplicity and cost efficiency, which is, very much needed for its commercial usability with concurrent multi-gigabit wireless communication systems at V band (60 GHz) and E band (85 GHz).

3.6. Conclusion

In this chapter, a MMW CPW-fed concurrent dual band antenna design has been proposed and validated through fabricated prototype measurement results. The measured results show fractional bandwidths 1% / 6.4% and E-plane (H-plane) gain 8.49 dBi (8.95 dBi)/5.13 dBi (5.37 dBi) at the two respective frequencies 60 GHz/85 GHz. The designed antenna is having the cross-sectional area of 3.7 mm² and in comparison to available literatures it is lesser in size which reflects its compactness. The proposed MMW dual frequency antenna design does not require any complex fabrication step, like, slot, via hole, notch, etc. and employs only a single, planar radiating structure. This simple design favors easy and user-friendly fabrication using conventional photolithography techniques. Additionally, the substrate used is cheap and commonly available, which, reduces the overall cost of the antenna. Therefore, we have successfully fulfilled our objectives of a simple, compact, and cost effective dual frequency MMW antenna structure design. As a future scope, its extension as an array antenna will provide the high gain and the low cost solution for the concurrent multiple applications as well as additional redundancy in applications related to MMW imaging.

Chapter 4

Stand-off Target's Shape Identification and its Material Classification Using Millimeter Wave Imaging System

Current electromagnetic based screening technologies, such as, metal detectors, microwave imaging, visible/IR and x-ray backscatter are restricted in their stand-off capability, coverage, efficacy, and flexibility they afford. Alternately, MMW has emerged as a remarkable imaging modality pertaining to its unique, favorable features of high resolution capability, non-ionizing radiation and ability to penetrate through clothing/ packaging [50, 110, 235, 351]. A prerequisite of a good imaging system is its ability to form an image with an appreciable contrast between the targets and the background so as to easily discriminate it. Another important requirement is that the image formed should have sufficient spatial details for its correct shape identification and further material classification. Keeping in view of these challenges, a MMW radar system based target's shape identification and its material classification methodology has been proposed in this chapter. Applicability of different pre-processing and post-processing techniques has been investigated in view of the stand-off target's information estimation, *i.e.*, shape identification and material classification. An extensive number of targets with four different regular shapes, *viz.*, rectangle, square, triangle and circle have been used for development and validation of the proposed algorithm.

4.1. Introduction

Very few works have been reported related to MMW based target's detection and identification employing different image processing techniques [85, 121, 271, 311]. A MMW target's detection

system for vehicular collision warning has been discussed using segmented range detection (SRD) at 60 GHz in [337]. A non-destructive crack inspection of civil structures at 94 GHz has been demonstrated in [219, 334]. Concealed weapon detection application at 35 GHz is presented in [51] using physical optics based modeling. Target's identification for standoff personal screening has been reported at 100 GHz/ 350 GHz using cylindrical/ polarimetric imaging technique in [273], at 200 GHz using heterodyne transceiver method in [325], and at 95 GHz using microwave holographic processing technique in [352]. A. Hirose *et.al.* [115] proposed an active near-field shape extraction method using an envelope phase detection for the targets, like, stacked round cans, plastic bottle filled with water at 76.5 GHz. Harmer *et.al.* [108] demonstrated the decomposition of late time and the transient response of metallic objects and characterized them by aspect-independent poles, for detection and discrimination of threat items (handguns) from the non-threatening items, such as, mobile phone handsets, cameras, keys and pens. On reviewing literature related to MMW imaging, it was found that most of the reported work at MMW has emphasized on target's detection and very less attention has been given for target's identification and target material classification. Target's identification and classification plays a crucial role in acquiring correct target's information, which may be of vital importance for different strategic, public safety and commercial applications.

MMW radar imaging uses artificially generated radiation to illuminate the scene of interest. Here, the quality of the formed image is dominated by the scene's reflectance distribution and is sensitive to the target's surrounding reflectance property, multipath reflection, non-uniform illumination and other factors. Thereby, there is a need to apply different suitable pre-processing and post-processing techniques for useful target information extraction from the radar reflectance data. At microwave frequencies for applications, like, ground penetrating radar (GPR) [2, 334] and through wall imaging (TWI) [68, 123] different image processing techniques are being used for enhancing the target's image quality and estimating target material. However, the significance of these techniques has still not been investigated for MMW radar imaging for the stand-off target's identification.

Any unwanted signal reflections (background/ oblique reflection, multipath propagation) in the line of sight of the target's reflection are collectively termed as 'clutter' and may degrade the resultant image quality. Different prevalent *image enhancement* and clutter reduction techniques are available that are commonly known as averaging, background subtraction, statistical clutter reduction using principal component analysis (PCA), independent component

analysis (ICA), singular value decomposition (SVD) etc. [2, 46, 301, 302]. These different techniques have their different working principles and their performance depends upon the particular application type. Hence, there is a need to find a suitable image enhancement technique for the target's identification application at MMW.

Image segmentation is a technique useful in discriminating objects from the background, like, printed or written documents, concealed objects, blur and non-uniform illumination [321]. Segmentation subdivides an image into its constituent regions or objects. Image segmentation algorithms are generally based on the basic properties of intensity values, *i.e.*, discontinuity and similarity. It is important in image processing to select an adequate threshold of gray level for extracting objects from their background. As well as it is an essential step for unsupervised decision problems in pattern recognition. A variety of thresholding techniques are being used like, histogram [221, 328], clustering [97], entropy [353], multi-level expectation maximization [164], and locally adaptive thresholding [14, 267]. However, the choice of any particular thresholding technique will solely depend upon particular image types for better target's identification.

Edges characterize target's boundaries and are of prime importance in image processing for target's identification [37]. *Edge detection* serves to simplify the analysis of images by drastically reducing the amount of data to be processed, while at the same time preserves useful structural information about object boundaries. Commonly used edge detector techniques are iteratively refined regularization [95], canny edge detector [37], statistical classifier [159], local threshold and Boolean function [14], color edge detection using Euclidean distance and vector angle [319], depth edge detection using multi-flash imaging [210], etc. Different edge detectors present distinct and different responses to the same image, showing different details. Hence, there is a need to find an optimum edge detector for accurate shape and size identification for the MMW target's image application.

Apart from mere target's shape identification, many times, it is essential to know the type of the target's material, like, whether the distant target is metal, wood, cardboard, plastic, ceramic, Teflon or any other material. From security viewpoint, it is important to measure how significant is the object towards any possible threat (say, the concealed gun shape object is of metal or it is just a plastic toy gun) and also target's material information is helpful in reducing excessive false alarms [187]. Target's classification can be realized using maximum likelihood estimation of EM based statistical measures for different classes [164]. A number of distribution

models with single or mixture of two models can be assigned to any particular class depending upon the target's characteristics [111, 112]. Other classification techniques include discrete cosine transform (DCT) coefficient features [69], Gaussian kernel function in conjunction with SVM classifier [224], etc. However, at MMW it is still a challenging task for accurate stand-off target's classification in view of low signal to noise ratio (SNR). Henceforth, in this chapter we have proposed and developed an algorithm for MMW stand-off imaging for target's shape identification and its material classification by using different digital image processing techniques, like, image enhancement (background subtraction, windowing, singular value decomposition), image segmentation (thresholding, edge detection), classification (probability density function).

This chapter is organized as follows: section 4.2 discusses theoretical background for target's shape identification and target's material classification, section 4.3 details the targets data used, section 4.4 presents methodology used for development and implementation of MMW SFCW radar. Section 4.5 discusses experimental results and section 4.6 presents the validation of the proposed algorithm using targets of a different regular shape. In section 4.7 an inclusive list of different image processing steps with results is discussed. Finally, section 4.8 presents the conclusion.

4.2. Theoretical background

Data received from MMW radar is the spatial distribution of reflectivity of the stand-off target and its surroundings. Different challenges are needed to be considered for generation of a good quality image *w.r.t.* target's correct shape and its material information estimation. Thereby, the present chapter embodies different signal pre-processing and post-processing techniques for the target's image formation and its analysis for shape identification and material classification. Figure 4.1 shows the flowchart that describes different signal processing steps for complete target's detection, identification and classification.

4.2.1. Signal pre-processing

Data acquired through experiments is in complex, frequency domain form, therefore, before applying different image processing techniques following pre-processing steps are used in order to convert data into the desired form:

- 1) Frequency to time domain conversion (IFFT)
- 2) Time to spatial domain conversion
- 3) Calibration
- 4) Windowing

Details of each of these pre-processing steps will be discussed in section 4.4.1. After pre-processing steps, we will be having two important information related to the stand-off targets, *i.e.*, (1) whether there is any target present in the down-range or not, (2) If target is present, then it's exact downrange location. The target's location detection information can be found by the range profile plot, which will be discussed in detail in the section 4.5.1.

4.2.2. Signal post-processing

In this chapter, our main objective is target's shape identification and classification, therefore, after detection of the targets there is a need to apply different post-processing techniques to extract complete target's information. For this, the raw 2D C-scan image of the target is extracted in accord to the section 1.3.2.2, *i.e.*, vertical slice of 3D C-scan matrix is taken at that downrange location where reflection peak in the range profile plot is obtained. The extracted 2D C-scan image is the function of target's reflectivity *w.r.t.* height and cross-range co-ordinates.

The C-scan data is collected as the reflected signal from the object, however, has the capability to reconstruct target's image, but in its unprocessed raw form it is not possible to do so. This is because, the intercepted reflected EM waves not only contain desired target's information but additional undesired signals, *viz.*, reflection and refractions due to multipath propagation, background reflection and due to non-uniform illumination etc. Hereby, different post-processing techniques are needed to be applied in order to extract relevant and significant target's information. In order to enable the user to discriminate between object and the background as well as to obtain its shape, size and material information, following post processing steps have been applied:

1) Subtask 1: Target's shape identification

- a. Image enhancement – background subtraction and clutter reduction
- b. Image segmentation – thresholding, edge detection

2) Subtask 2: Target's material classification

Details of implementation and significance of each of the post-processing steps is given in the section 4.4.2.

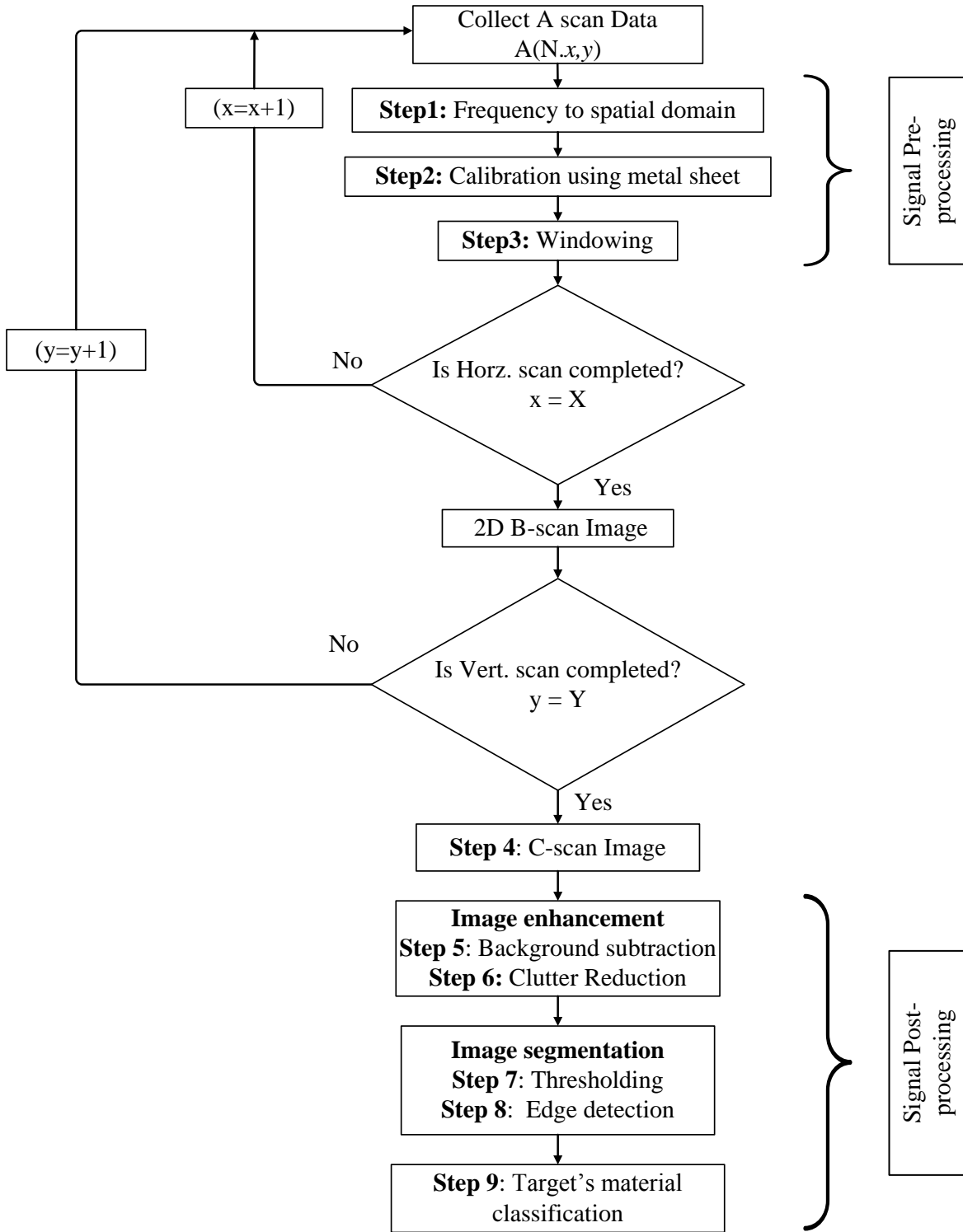


Figure 4.1. Flowchart showing different signal processing steps for stand-off target's image identification and its material classification

4.3. Data used

For the experimental observations of stand-off target's shape identification and its material classification, a large metal (Al) sheet (35cm x 43.6cm) was mounted on the 2D-scanning wooden frame as shown in Figure 4.2. Different wooden regular shaped targets (as given in Table 4.1) were placed at the center of metal sheet at a standoff distance from the antenna. Figure 4.2 shows the pictorial view of few of the physical target's arrangements used.

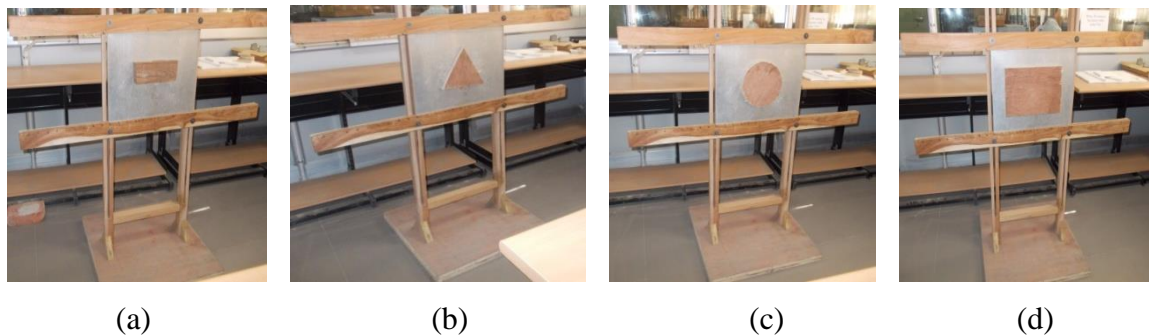


Figure 4.2. Different target shapes mounted on a 2D-scanning wooden frame enabling horizontal and vertical movement for complete C-scan (a) T1: rectangle, (b) T2: triangle, (c) T3: circle, (d) T4: square.

Here, background material is the metallic sheet having high reflectivity and over which wooden targets are mounted, which have the low reflectivity towards the incident EM waves. Wooden targets of four different regular shapes, *viz.*, rectangle, square, triangle and circle have been considered for our target's identification algorithm development. Details of different targets used, *i.e.*, their shape, and size information is summarized in Table 4.1.

Table 4.1. Different regular shaped targets used for target's identification algorithm development

S. No.	Target's shape (symbol used)	Size	Number of target samples taken for each shape
1	Rectangle (T1)	8 cm X 20 cm	5
2	Triangle (T2)	Equilateral (20 cm)	5
3	Circle (T3)	radius 10 cm	5
4	Square (T4)	20 cm x 20 cm	5

This type of target's arrangement acquaint us with the multi-fold target's information, *viz.*, detection based on dielectric contrast (low and high index material), target's location estimation as well as discrimination of target's materials using classification.

4.4. Methodology used for development and implementation of target's identification algorithm

The ingeniously assembled MMW imaging radar setup for identification and classification of targets is the same as shown in Figure 1.8, and the SFCW radar design specifications are the same as given in Table 1.1. The one port S-parameters (S_{11}) were collected at 201 frequency points, after calibrating PNA using 2-port standard calibration process Through Open Short Matched (TOSM). Image parameters of the designed SFCW radar, *i.e.*, range resolution and cross-range resolution are 7.5 cm and 8.59 mm, respectively as obtained from the corresponding equations (1.16) and (1.17). The stand-off target under investigation has been kept at a distance of 110 cm from the antenna and scanned along 32 horizontal and 24 vertical scanning positions with the inter-element spacing of 2 cm, in order to completely image the targets. The full A, B and C-scan has been performed as discussed in section 1.3.2.2. Data thus, acquired undergoes different signal processing steps as discussed in section 4.2, in order to have the required target's information, *i.e.*, detection, shape identification and its material classification.

4.4.1. Signal pre-processing

Different signal pre-processing steps mentioned in the section 4.2.1 are discussed here in detail, outlining their need and the significance. At the end of signal pre-processing, we will be able to know the presence or absence of the target as well as its exact location in downrange by the range profile plot, *i.e.*, an intensity *vs* distance plot. Application of signal pre-processing steps on the experimental data will be discussed in the next section.

4.4.1.1. Frequency to Spatial Domain Conversion (Step 1)

The SFCW radar measures magnitude and phase of received signal corresponding to the transmitted signal at each stepped frequency. Signal transmitted at the discrete frequency step f_n is, $E_t(f_n) = E_0 e^{j2\pi f_n t}$. Received signal reflected from the target at a distance z from radar is in

complex scattering coefficient form $s(z)$, with reference to transmitted signal and is given by [78],

$$S(f_n) = \frac{E_r(f_n)}{E_t(f_n)} = \frac{1}{z_0} \int_0^{Z_0} s(z) e^{-j2\pi f_n \left(\frac{2z}{c}\right)} dz \quad (4.1)$$

$Z_0 = c/2\Delta f$, is the unambiguous range of the radar. Equation (4.1) is in form of Fourier transform. Here, $S(f_n)$ is the received reflected signal in frequency domain at the discrete frequency step (f_n). Hence, SFCW radar measures reflected signal at discrete frequencies, *i.e.*, $f_n = f_0 + n\Delta f$ where, $n = 0, 1, 2, \dots, M - 1$. Here, M is the total number of frequency points in SFCW signal which, in our case is $M = 201$. The received signal is converted into time domain using Inverse Fast Fourier Transform (IFFT) and is represented as:

$$S(t) = \sum_{n=0}^{N-1} S(f_n) e^{j2\pi f_n t} \quad (4.2)$$

Now, in order to have range estimation of the target, time domain signal is converted into spatial domain by converting signal propagation time to the corresponding round trip distance (z).

$$t = \frac{2z}{c} \quad (4.3)$$

Received signal in spatial domain is termed as the range profile as discussed in section 1.3.2.2, which is a plot of reflection intensity vs down range distance z and is given by,

$$S(z) = \sum_{n=0}^{N-1} S(f_n) e^{j2\pi f_n (2z/c)} \quad 0 < z < Z_0 \quad (4.4)$$

4.4.1.2. Calibration Using Metal Sheet (Step 2)

Reflection peak in the range profile plot gives an initial estimate of target's location in down-range as discussed in section 1.3.2.2. Although, VNA cable and antenna system also add some delay to the received signal, which shifts the target's location in downrange from its true position. Hence, in order to get correct downrange distance of the targets, delay calibration is done by placing a large metal sheet (reference) at the flare of horn antenna. Then, range profile of the reflected signal is plotted, in which, dominant intensity peak corresponds to the antenna-air interference point analogous to the delay due to the antenna system [213]. This delay is to be noted and must be subtracted in further calculations, to have the exact target's position. Say, t_{ref}, z_{ref} represents time delay and distance due to metal sheet at antenna flare, respectively. Then, the corrected signal incorporating shift due to antenna system is,

$$S(z) = \sum_{n=0}^{N-1} S(f_n) e^{j2\pi f_n \left(\frac{2z}{c} - \frac{2z_{ref}}{c} \right)} \quad (4.5)$$

4.4.1.3. Windowing (Step 3)

Window function is applied on received scattered signal. It helps in eliminating any oblique surface reflections and background reflections. Windowing function is not applied on transmitted signal so as not to limit the transmitted power, rather it is applied on the received signal. When windowing is applied, the side lobes are reduced which will help to reduce false alarm rate and will improve dynamic range of detection. However, windowing slightly deteriorates range resolution of the radar system. Different available windowing function, like, rectangular, triangular, hanning, hamming, blackman-harris, B-spline, etc. have been tested and it was found that hamming window gives optimal performance *w.r.t.* better side lobe suppression and smoothing operation [169].

Once stand-off target's presence has been detected and its location is known from the range profile plot, the raw C-scan image of the target is obtained by extracting the 2D slice at peak reflection intensity point in the downrange as discussed in section 1.3.2.2. Further, information related to target's shape, size and its material type can be inferred by applying suitable post-processing techniques (image enhancement, segmentation and target's material classification) on the raw C-scan image as discussed in section 4.2.2. The detailed description of each of these post-processing techniques is given below:

4.4.2. Signal post-processing for Target's Shape Identification (Subtask 1)

For target's correct shape identification, there should be an appreciable contrast between the target and the background, which necessitates the use of image enhancement and segmentation techniques as described below:

4.4.2.1. Image Enhancement

➤ Background subtraction (Step 5)

The received reflected signal from target contains unwanted signals due to air-antenna mismatch, background reflection and interference between transmitting and receiving signal. To eliminate these unwanted signals, mean subtraction approach has been applied because of its

simplicity of implementation. Here, mean vector of each B-scan is calculated, followed by mean vector of all these B scans. This mean vector value is subtracted from each individual A-scan [2].

$$X_{ijk} = A_{ijk} - \frac{1}{J} \sum_1^j \left(\frac{1}{I} \sum_1^i A_{ijk} \right) \quad (4.6)$$

Here, $i = 1, 2 \dots I$ (no. of downrange locations), $j = 1, 2 \dots J$ (no. of Bscans),
 $k = 1, 2, \dots \dots K$ (no. of Cscans)

A_{ijk} is the signal received at particular downrange location (i) and X_{ijk} is the resultant signal after background subtraction.

➤ **Clutter reduction (Step 6)**

After mean based background subtraction, clutter reduction technique has been applied so as to further improve signal to noise ratio and enhance target's image. Clutter reduction is a signal processing technique, where, the desired target's signal is separated from mixture of reflected signals without any knowledge of mixing background signals. Reflected signal mainly comprises of desired target's reflection, and clutter signal due to oblique and multiple reflections. As compared to the different available clutter reduction techniques, like, Principle Component Analysis (PCA), Factor analysis (FA), singular value decomposition (SVD) and Independent Component Analysis (ICA), SVD proves to be a robust and reliable orthogonal matrix decomposition technique with added advantages of improved image quality, compressibility and is better in preserving edge details [151]. SVD decomposes received signal into target and clutter signal. Let, we take a single B scan image represented by X_{ij} , with dimension $M \times N$ ($M > N$), Here, i is the index in downrange ($i = 1, 2, \dots \dots M$) and j is the number of antenna positions in horizontal direction ($j = 1, 2, \dots \dots N$). SVD of X is given by [2, 306],

$$X = USV^T \quad (4.7)$$

where, U and V are unitary matrices, $S = \text{diagonal}(\sigma_1, \sigma_2, \dots \sigma_r)$, with $\sigma_1, \sigma_2, \dots \sigma_r > 0$, U is a $M \times M$ matrix and V is a $N \times N$ matrix. The columns of U and V are called the left and right singular vectors, respectively. The matrix S is an $M \times N$ matrix, where non-diagonal elements vanish. The diagonal elements of S are called the singular values. SVD of X is

$$X = \sum_{k=1}^N \sigma_k u_k v_k^T \quad (4.8)$$

$$\text{or,} \quad X = D_1 + D_2 + \dots + D_N$$

where, D_k are matrices of the same dimensions as X and are called X 's modes. This representation of X , as a series of matrices representing the various modes, is one of the most important aspects of SVD. Now let us assume that the data matrices D , can be divided into two parts, $D = [D_{1 \rightarrow p} | D_{p \rightarrow N}]$, where $D_{1 \rightarrow p}$ is associated with the target's signal and $D_{p \rightarrow N}$ is associated with the clutter. The optimum value of p is found where the target is present which corresponds to higher eigen values as compared to noise / clutter signal [1]. On applying SVD on our experimental data and analyzing eigen values, it was found that, eigen mode D_1 ($p = 1$) represents target and $D_{2 \rightarrow N}$ represents noise. Hence, target's signal can be extracted as,

$$S = \sigma_1 u_1 v_1^T = D_1 \quad (4.9)$$

4.4.2.2. Image Segmentation

➤ Thresholding (Step 7)

After, image enhancement, our prime objective in process of target's image identification is to extract target's information from background for successful target's shape recognition. For this, thresholding based image segmentation becomes an intuitive choice because of its simplicity of implementation. Thresholding involves a test against a function T of the form

$$T = T(x, y, p(x, y), f(x, y)) \quad (4.10)$$

Where, $f(x, y)$ corresponds to gray level image at point (x, y) , and $p(x, y)$ denotes some local property of this point, for example, the average gray level of a neighborhood centered on (x, y) .

After thresholding, image $g(x, y)$ is defined as:

$$g(x, y) = \begin{cases} 1 & \text{if } f(x, y) > T \\ 0 & \text{if } f(x, y) \leq T \end{cases} \quad (4.11)$$

When, T depends only on $f(x, y)$, *i.e.*, only on grey level values, it is called global thresholding. If T depends on both $f(x, y)$ and $p(x, y)$, it is called local thresholding. In addition, if T depends on the spatial co-ordinates x and y , the threshold is called dynamic or adaptive threshold [97]. Global thresholding is successful for bimodal image histogram, where, a single threshold value can clearly partition the histogram. Here, we have used statistical analysis based mean and standard deviation global thresholding and the threshold T is defined as,

$$T = \mu + n * \sigma \quad (4.12)$$

where μ and σ are the image mean and standard deviation, respectively and n is a scaling constant dependent upon particular image type and is selected after number of iterations [46]. Since, we have a single wooden target on metal sheet background and not any multiple, irregular shaped targets, so a simple global thresholding will solve the purpose of target's shape identification, instead of using any complex approach, and to have a better interpretation of the threshold value, we used image statistics based threshold criterion.

4.4.2.3. Edge detection (Step 8)

Thresholding segments target and the background distinctly, but, for an improved target's shape/ size visibility, the target's boundaries are need to be known. Thereby, edge detection is an image processing technique for finding the boundaries of objects within images. Edges characterize object boundaries and are useful features for segmentation and object identification in images. It works by detecting discontinuities in brightness. Common edge detection algorithms include Sobel, Canny, Prewitt, Roberts etc. Criterion relevant to edge detector optimum performance are [36]: (1) *Good detection*: low probability of failing to mark real edge points, and low probability of falsely marking non-edge points, hence, this criterion corresponds to maximizing signal-to-noise ratio.(2) *Good localization*: points marked as edge points by the operator should be as close as possible to the center of the true edge (3) *only one response to a single edge*. There are broadly two methods used for edge detection: (1) Gradient method (first order derivative) (2) Zero order crossing (second order derivative). Sobel, prewitt and roberts implement gradient method and are simple to implement, but they are sensitive to noise and suffer from poor localization [37]. Laplacian detector implements zero order crossing and is simpler than gradient method, however, it is more sensitive to noise, poor detection and also does not provide information about edge direction.

In view of these limitations, canny [36] proposed an optimal edge detector that has a simple implementation, where, edges are marked at maxima in gradient magnitude of a Gaussian-smoothed image. It employs special features, like, adaptive thresholding with hysteresis to eliminate streaking (broken edges) of edge contours, ability to cope with varying image signal-to-noise ratios. Canny detector performs well in noisy conditions, provides better localization and improved signal-to-noise ratio [37].

4.4.3. Signal post-processing for Target's Material classification (Subtask 2)

After application of image segmentation techniques, the stand-off target's shape can be identified in the C-scan image. However, apart from having only the target's shape information, many times it becomes vital to accurately classify target's material also, in view of varying threat level of different materials (metal, wood, plastic, ceramic, etc.). Different techniques are being investigated for target's material classification, like, gaussian kernel, discrete cosine features, statistical approaches, probability density function etc. [69, 112, 224]. However, due to the dielectric difference between the wooden shape target and the metal background, we preferred to use probability density function (*pdf*) based approach for our target's material classification because it has the advantage of separating different target's materials based on their varying reflection intensity values.

4.4.3.1. Selection of Suitable Pdf for Target's Material Classification (Step 9)

For target's material classification, image data is grouped into different parts depending upon their pixel intensity variation, *i.e.*, pixels representing different target's materials are separated. These set of pixels are used for analyzing distribution of pixels corresponding to each of the two classes: metal and wood. Commonly used distribution models *i.e.*, Normal, Rayleigh, Cauchy and Weibull were applied on the obtained image data. The respective pdf's of these distributions for x as the pixel intensity are [228]:

- **Normal pdf function**

$$f(x) = \frac{\exp\left(-\frac{(x-\mu)^2}{2\sigma^2}\right)}{\sigma\sqrt{2\pi}} \quad (4.13)$$

Where, σ is continuous scale parameter ($\sigma > 0$) and μ is continuous location parameter.

- **Rayleigh pdf function**

$$f(x) = \frac{x-\gamma}{\sigma^2} \exp\left(-\frac{1}{2}\left(\frac{x-\gamma}{\sigma}\right)^2\right) \quad (4.14)$$

Where, σ is continuous scale parameter ($\sigma > 0$) and γ is continuous location parameter.

- **Cauchy pdf function**

$$f(x) = \frac{1}{\pi\sigma\left(1 + \left(\frac{x-\mu}{\sigma}\right)^2\right)} \quad (4.15)$$

Where, σ is continuous scale parameter ($\sigma > 0$) and μ is continuous location parameter.

- **Weibull pdf function**

$$f(x) = \frac{\alpha}{\beta} \left(\frac{x}{\beta}\right)^{\alpha-1} \exp\left(-\left(\frac{x}{\beta}\right)^\alpha\right) \quad (4.16)$$

where, α is shape parameter and β is scale parameters. Both α and β must be greater than zero.

The best-fit density function for each class may be identified using Chi-Squared goodness of fit (GoF) test. The Chi-squared statistics is defined as:

$$\chi^2 = \sum_{i=1}^k \frac{(O_i - E_i)^2}{E_i} \quad (4.17)$$

Where, O is observed frequency for bin i , E is expected frequency for bin i and k is total number of bins.

Chi-squared statistics (χ^2) is compared with the critical value for all distributions and distribution having lesser chi-square statistics is chosen. If the statistic value is less than the critical value and the p-value is greater than the level of significance (5%), then hypothesis will not be rejected. Thus chi-squared statistics, which is a function of data value, reflects in some way the level of agreement between the data and the hypothesis. For discrimination between different target's material classes (metal and wood), range of scale and location parameters was determined for each class using the best-fit pdf function obtained. Maximum likelihood decision rule is used to discriminate the material classes. For this, mean and standard deviation of both the scale and location parameters were calculated for each class. The upper and lower boundaries of each class (metal and wood) were found by calculating the range of location and scale parameters for the best found pdf function.

4.5. Experimental results and discussion

The proposed MMW SFCW imaging radar based stand-off target's identification and classification algorithm has been implemented and tested on number of test targets of varying shapes. Experimental results of different pre- and post-processing steps are discussed in this section supported by the outcomes of test targets of two different shapes, *viz*, triangle (T2) and circle (T3). Further, validation of the proposed methodology has been done using targets of a different shape 'rectangle (T1)' in section 4.6.

4.5.1. Target's location detection (steps 1-3)

For locating the target's position, A-scan (or range profile) plot in terms of intensity *vs* downrange distance is plotted for any fixed target's position (x, y) in front of antenna as shown in Figure 1.8. The input data is in frequency domain form and is converted to time domain using IFFT and then to corresponding equivalent distance according to equation (4.4). As shown in Figure 4.3(a), the range profile (for target T2) shows the first dominant reflection peak corresponding to antenna air interface impedance mismatch. The second reflection peak shows presence or absence of the target. Here, the second peak is at 1.28 meter distance with normalized intensity 0.24. However, the targets were placed at 1.10 meter distance. So, a metal sheet calibration was done to exactly determine target's downrange distance. Here, delay due antenna and cable system is subtracted as per equation (4.5). This gives nearly exact target's distance *i.e.*, 1.125 meter as depicted in Figure 4.3(b). Further, B-scan plot (down-range *vs* cross-range) is shown in Figure 4.3(c), which presents the lateral extent of the target, as discussed in section 1.3.2.2. Here, peak intensity is observed at distance 1.125 meter (taking into account delay correction) with lateral extent 0.14m to 0.57m *i.e.*, net lateral length = 0.43 meter, which is nearly equal to the width of the background metal sheet, *i.e.*, 43.6 cm, as mentioned in section 4.3.

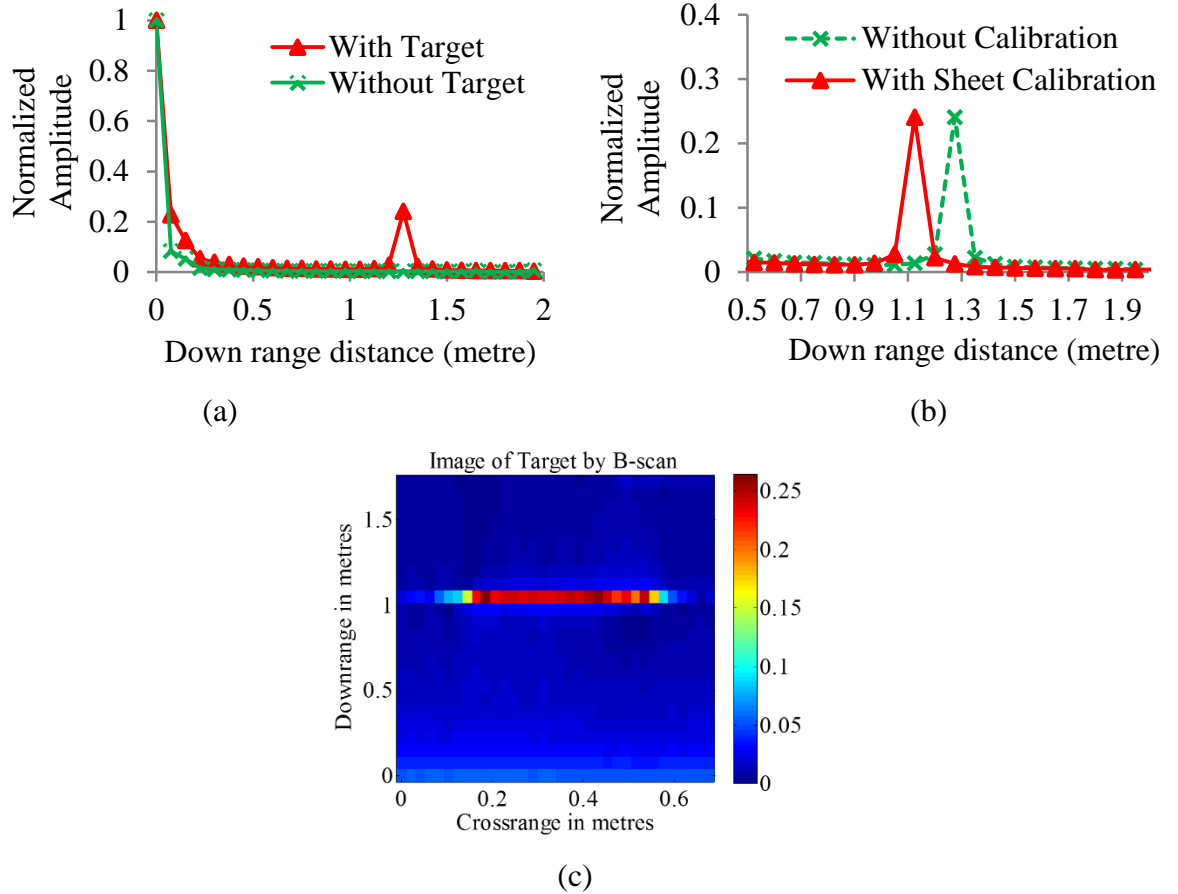


Figure 4.3. (a) Range profile plot, (b) target's downrange distance after sheet calibration, (c) B-scan image of background metal sheet.

4.5.2. Implementation for Target's Shape Identification (Subtask 1)

4.5.2.1. C-Scan Image Formation (Step 4)

Figure 4.4 shows vertical slices at the three different downrange locations for the two test targets, triangle (T2) and circle (T3) (Table 1.3) in the 3-D co-ordinate axis. As seen in the figure 4.4, only the middle vertical slice shows appreciable reflection intensity due to the presence of target at that downrange index which also agrees with the maximum reflection intensity point in the range profile plot in Figure 4.3. Y plane slices at two other downrange positions are also plotted, which shows zero peak intensity at these down-range locations, which, signifies absence of any target there. Figure 4.5 shows the surface intensity distribution plot of the extracted C-scan image. Maximum intensity is received by metal sheet reflection and lower intensity corresponds to the different wood shape targets present in the respective images.

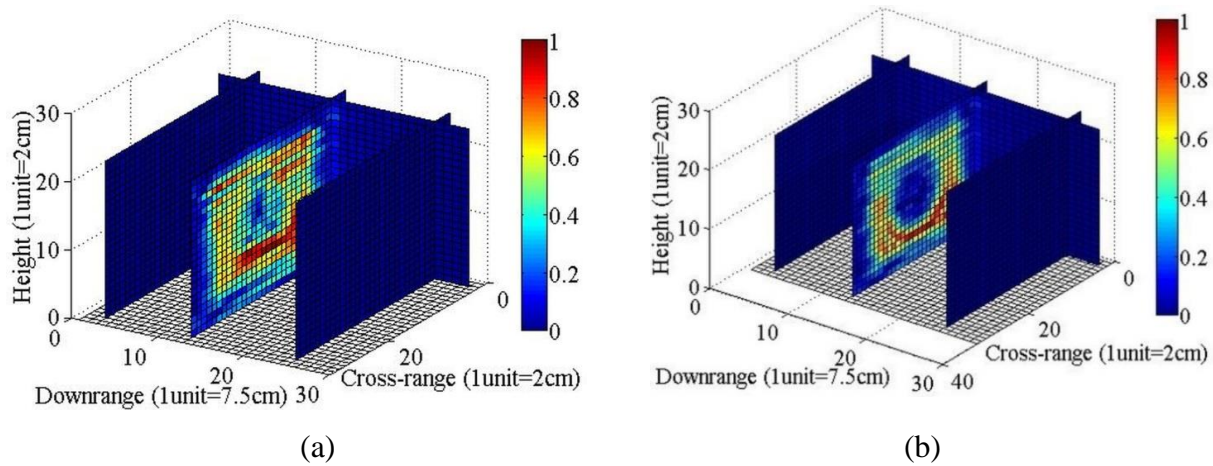


Figure 4.4. 3D view (slicing) of C-scan images at target's downrange position: (a) T2, (b) T3.

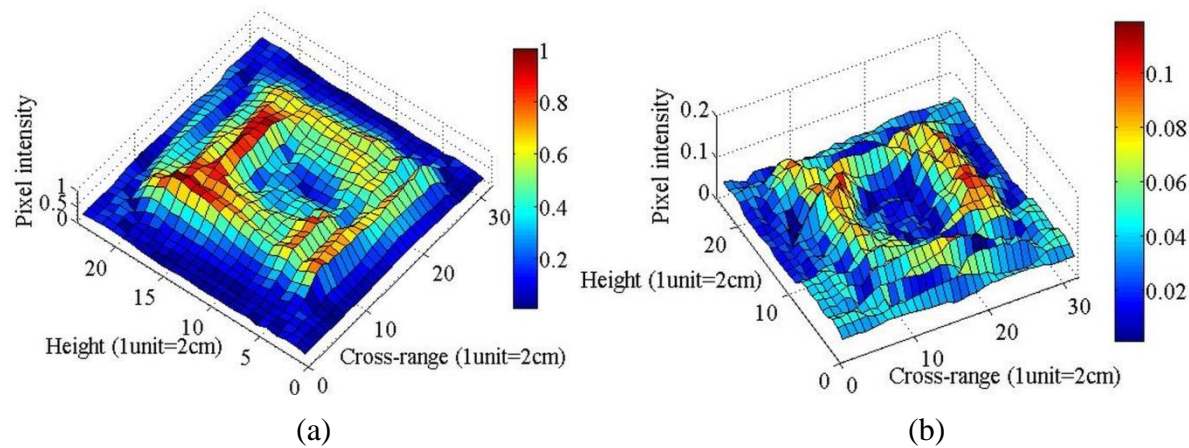


Figure 4.5. Surface distribution plot for pixel intensity of 2D C-scan image: (a) T2, (b) T3.

4.5.2.2. Image Enhancement (Steps 5-6)

The obtained raw C-scan image undergoes image enhancement step, *i.e.*, background subtraction and SVD (clutter reduction), and the resulting image plot shows improvement in target's image intensity as well as its visibility. Figure 4.6 shows the comparison of raw C-scan image and the C-scan image obtained after image enhancement for two sample targets T2 and T3. Major improvement is seen in the image of triangular shape wooden target (T2) on the metal background sheet after image enhancement.

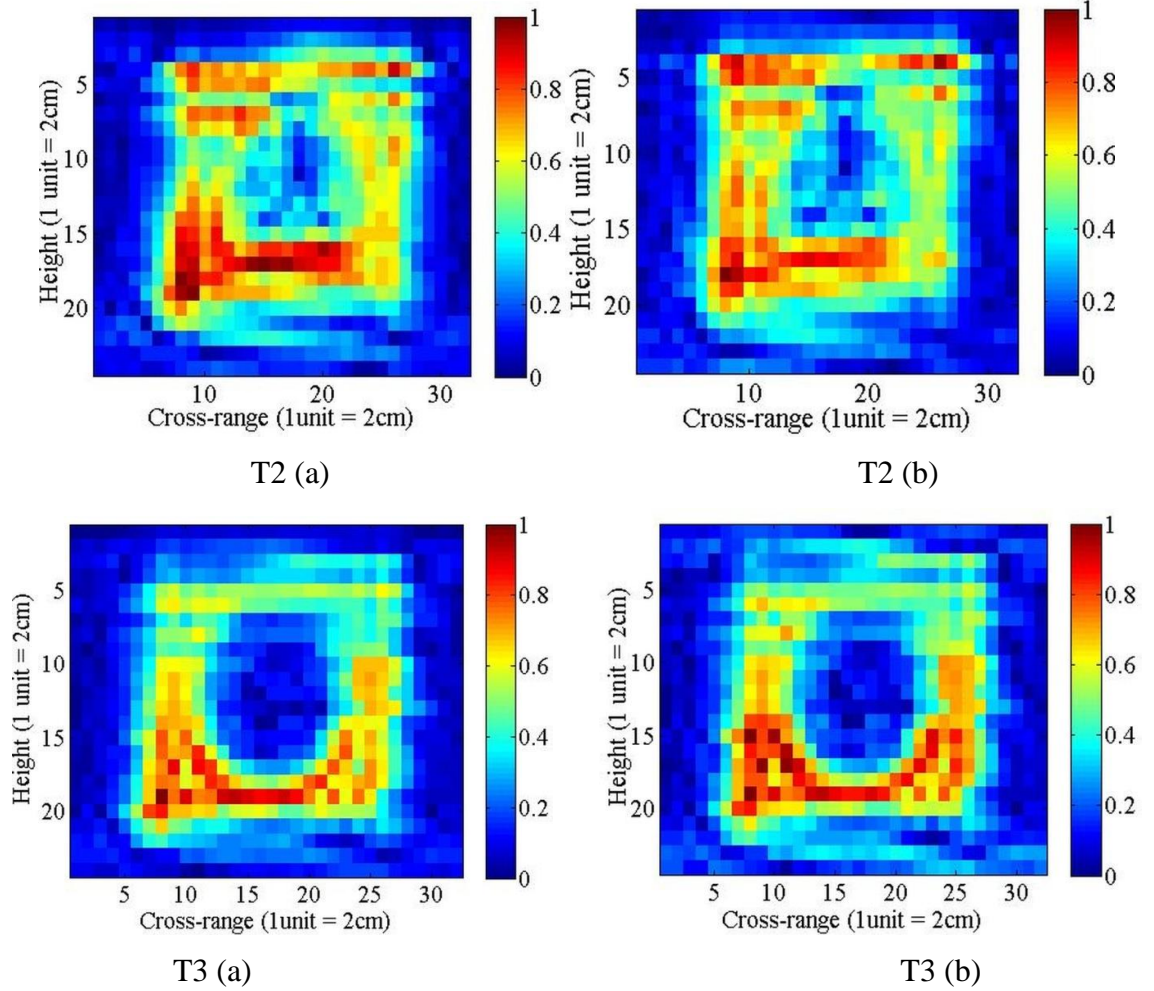


Figure 4.6. Comparison of two test target's C-scan images; (a) raw image,(b) image after applying image enhancement technique (background subtraction and singular value decomposition).

4.5.2.3. Image Segmentation

➤ Thresholding (Step 7)

Thresholding segments image pixels as 0 or 1, relative to their intensity values *w. r. t.* threshold value (T) as discussed in section 4.4.2.2. In order to implement statistical thresholding model, target's image obtained after the image enhancement step is firstly normalized as:

$$p_{normalized} = \frac{p_{max} - p}{p_{max} + p_{min}} \quad (4.18)$$

where, p is the pixel intensity of image at any arbitrary point, $p_{normalized}$ is the normalized pixel intensity and p_{max} , p_{min} are the maximum, minimum intensity values of any image. As per

equation (4.12), the value of threshold depends upon image statistics: mean & standard deviation as well as on the scaling factor (n). On varying the value of $n = 0.05$ to 0.95 with the step increments of 0.05 , the optimal performance was found for the scaling factor $n = 0.25$ for both the test targets T2 and T3. Hence, statistics based thresholding equation (T) comes out to be:

$$T = \text{mean}(\mu) + 0.25 \times \text{standarddeviation}(\sigma) \quad (4.19)$$

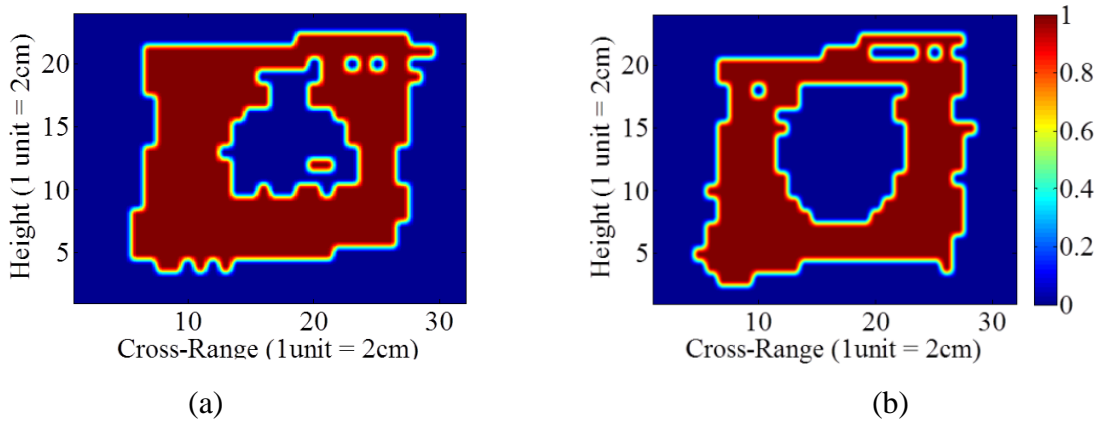


Figure 4.7. 2-D C-scan image of the two test target's after applying mean and standard deviation based global thresholding (a) T2, (b) T3.

As per equation (4.19), threshold values for test targets T2 and T3 are: $T(T2) = 0.368$ and $T(T3) = 0.340$, respectively. C-scan images after thresholding is shown in Figure 4.7. As seen in the figure, two targets T2 & T3 are nearly identified as triangle and circle, respectively, as were our original wooden targets.

➤ Edge detection (Step 8)

After thresholding, stand-off target's shape is identifiable, but the discovered shapes are not accurate enough, *i.e.*, shapes identified are not truly triangular and circular. Therefore, as per our correct target's shape identification objective, edge detection technique has been applied on the C-scan images obtained after thresholding. Thereby, canny based edge detector has been used for finding edges of the respective targets, T2 and T3. Figure 4.8 shows the respective images obtained after canny edge detector [36]. Boundaries of the test target's shapes T2 and T3 are now easily and more correctly identifiable as triangle and circle, respectively.

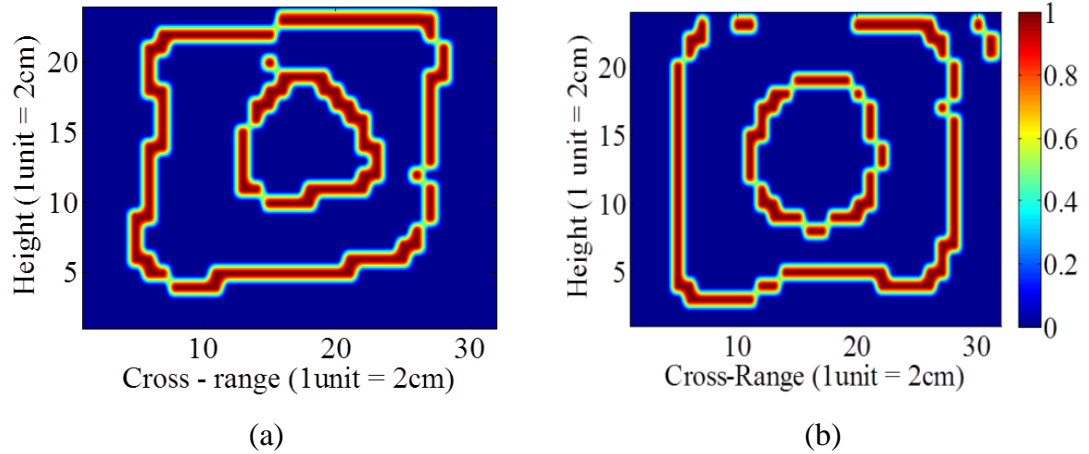


Figure 4.8. 2-D C-scan image of the two test targets obtained after canny edge detection (a) T2 (b) T3.

4.5.3. Implementation for Target's material classification (Subtask 2)

After target's shape identification, next objective is the target's material classification. For target's material classification normalized C-scan images obtained after pre-processing were used for finding probability density function (pdf) of different materials (metal, wood). Firstly, chi square goodness of fit test for all the four pdf functions (Cauchy, Normal, Weibull and Rayleigh) were performed as discussed in section 4.4.3, in order to find the most suitable pdf function to successfully discriminate the two classes under test, *i.e.*, metal and wood. Targets T2 and T3 were used to formulate the classification criterion and the decision boundaries.

4.5.3.1. Selection of Suitable Pdf Function (Step 9)

Figure 4.9 shows comparative plot of the two target material classes for the four considered probability density functions, *i.e.*, Cauchy, Normal, Weibull, Rayleigh for target T2 (triangle shape). Similar plots were achieved by other test target's shape T3 also. As shown in the Figure 4.9, the considered pdf's have the capability to classify the two classes because of their highly separated pdf plots, however, there is an ambiguity in the results upto the 5% significance level. Now, in order to find the best pdf function for a generalized and robust material classification model, chi square test has been performed, *i.e.*, statistic value should be less than critical value and p- value is greater than the level of significance (5%).

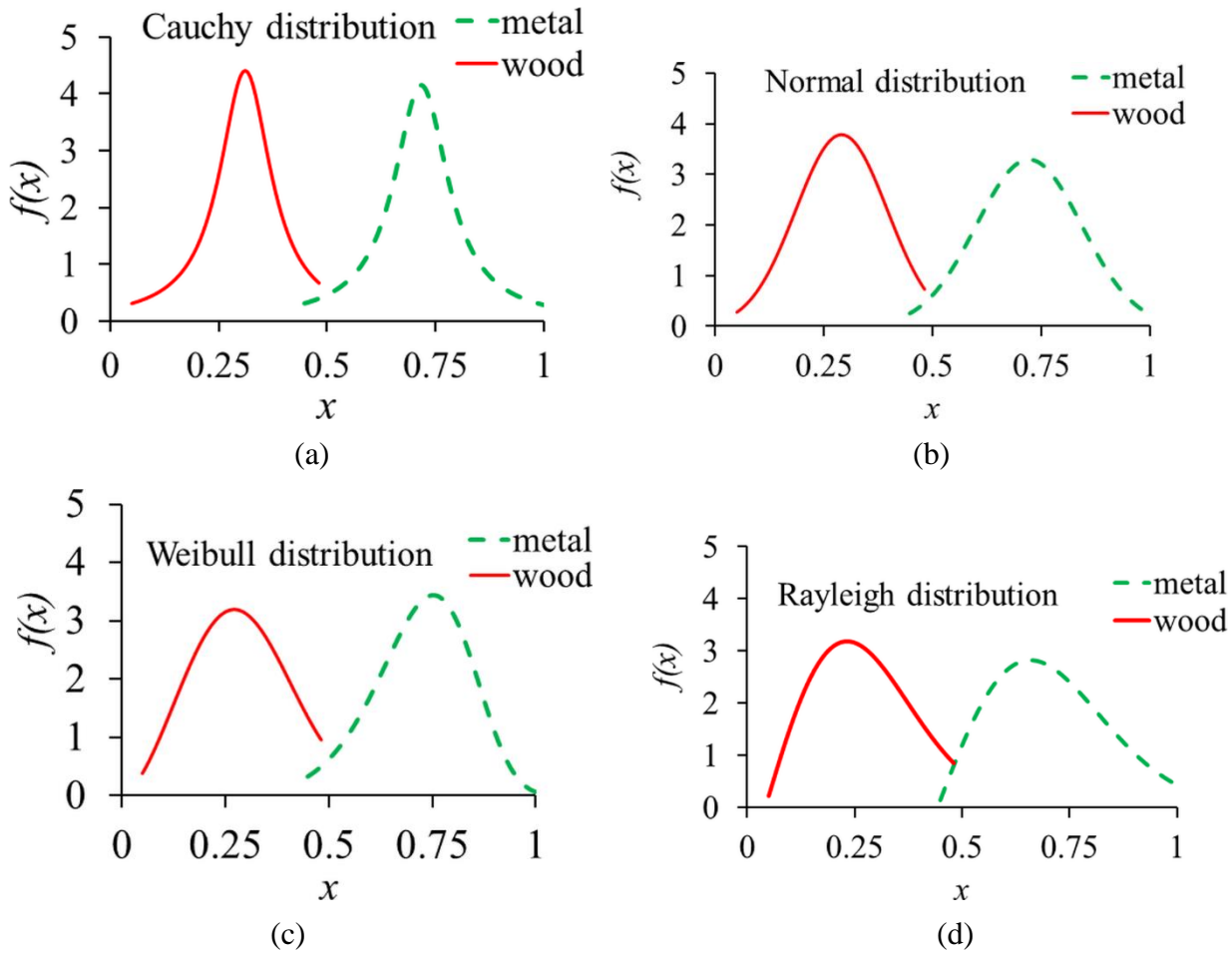


Figure 4.9. Comparative probability density function plots for the two target's material classes metal and wood: (a) Cauchy pdf, (b) Normal pdf, (c) Weibull pdf, (d) Rayleigh pdf, for test targets of triangle shape T2.

Results of chi square test are shown in Table 4.2, which signifies:

for Rayleigh pdf: $\chi^2 < \text{critical value for target T2 (metal class)} \Rightarrow \text{test not satisfied}$.

for normal pdf: $\chi^2 < \text{critical value for target T3 (metal class)} \Rightarrow \text{test not satisfied}$.

for Weibull pdf: $\chi^2 < \text{critical value for target T3 (metal class) and target T2 (wood class)} \Rightarrow \text{test not satisfied}$.

This shows, chi square test does not satisfy for the three pdf functions: Rayleigh, normal and weibull. Moreover, results suggests that only Cauchy pdf passes the chi square test for both

the target shapes T2, T3 and for both the classes metal, wood and hence, demonstrates the best fit characteristics having higher p-values from 5% significance level. *This proves that Cauchy pdf is the most suitable for classification of both metal and wood classes effectively.*

Table 4.2. Chi Square best fit test for various distribution functions on different test targets T2 and T3

CLASS		METAL				WOOD			
Targets	Parameter	Cauchy	Normal	Weibull	Rayleigh	Cauchy	Normal	Weibull	Rayleigh
T2	χ^2	4.5208	9.9229	5.5972	18.472	1.3605	5.6377	11.261	6.4442
	p-value	0.6066	0.1279	0.4698	0.00515	0.7148	0.2279	0.0465	0.09189
	Critical value	12.592	12.592	12.592	12.592	7.8147	9.4877	11.07	7.8147
T3	χ^2	8.6629	16.129	16.774	10.295	1.8573	7.091	5.4618	4.4015
	p-value	0.1934	0.0131	0.0102	0.11278	0.9323	0.3125	0.4861	0.62251
	Critical value	12.592	12.592	12.592	12.592	12.592	12.592	12.592	12.592

Now, for identifying the boundaries between the two classes, range of scale and location parameter were estimated for the best fit Cauchy pdf by calculating its mean and standard deviation, as shown in Table 4.3.

Table 4.3. Determining range of parameters of Cauchy pdf for classification

Data set	Continuous scale parameter (μ)					Continuous location parameter (σ)				
		Mean	Std. Dev.	Max.	Min.		Mean	Std. Dev.	Max.	Min.
Metal 1	0.0872	0.081	0.0089	0.0899	0.0721	0.6678	0.6161	0.0732	0.6893	0.5429
Metal 2	0.0747					0.5643				
Wood 1	0.0426	0.0478	0.0072	0.0549	0.0405	0.2723	0.2182	0.0765	0.2948	0.1417
Wood 2	0.0529					0.1641				

Target's material classification boundary for the two classes: wood and metal for any stand-off target can be found using the range of continuous location parameter (σ) of the Cauchy pdf function, as shown in Table 4.3 (in italics), which comes out to be:

$$\begin{aligned} \textit{For Metal} &\rightarrow 0.54 < \sigma < 0.69; \\ \textit{For Wood} &\rightarrow 0.14 < \sigma < 0.29. \end{aligned} \tag{4.20}$$

Hence, using the above discussed image post-processing techniques (image enhancement, segmentation and classification), we can achieve target's identification (shape estimation) and its material classification for the targets placed at a stand-off distance from MMW imaging system.

4.6. Validation

The developed target's identification and classification methodology has been further validated using a different 'rectangular' shaped target T1 towards optimal performance of different post-processing steps, *viz.*, image enhancement, image segmentation and target's material classification for complete target's information. Figure 4.10 shows validation results after each of the signal processing step. Figure 4.10(a) and (b) shows the C-scan image plot using slicing and surface distribution plots, respectively. Figure 4.10(c) shows the comparison of initial c-scan image with Figure 4.10(d) which is the image obtained after applying image enhancement technique. Further, segmentation has been performed using mean and standard deviation thresholding (threshold value = 0.434) and canny edge detector as shown in Figure 4.10(e) and (f), respectively. Finally, shape of the stand-off targets has been correctly identified as of rectangular shape, which is in accordance to our actual physical wooden target T1 on the metal sheet background.

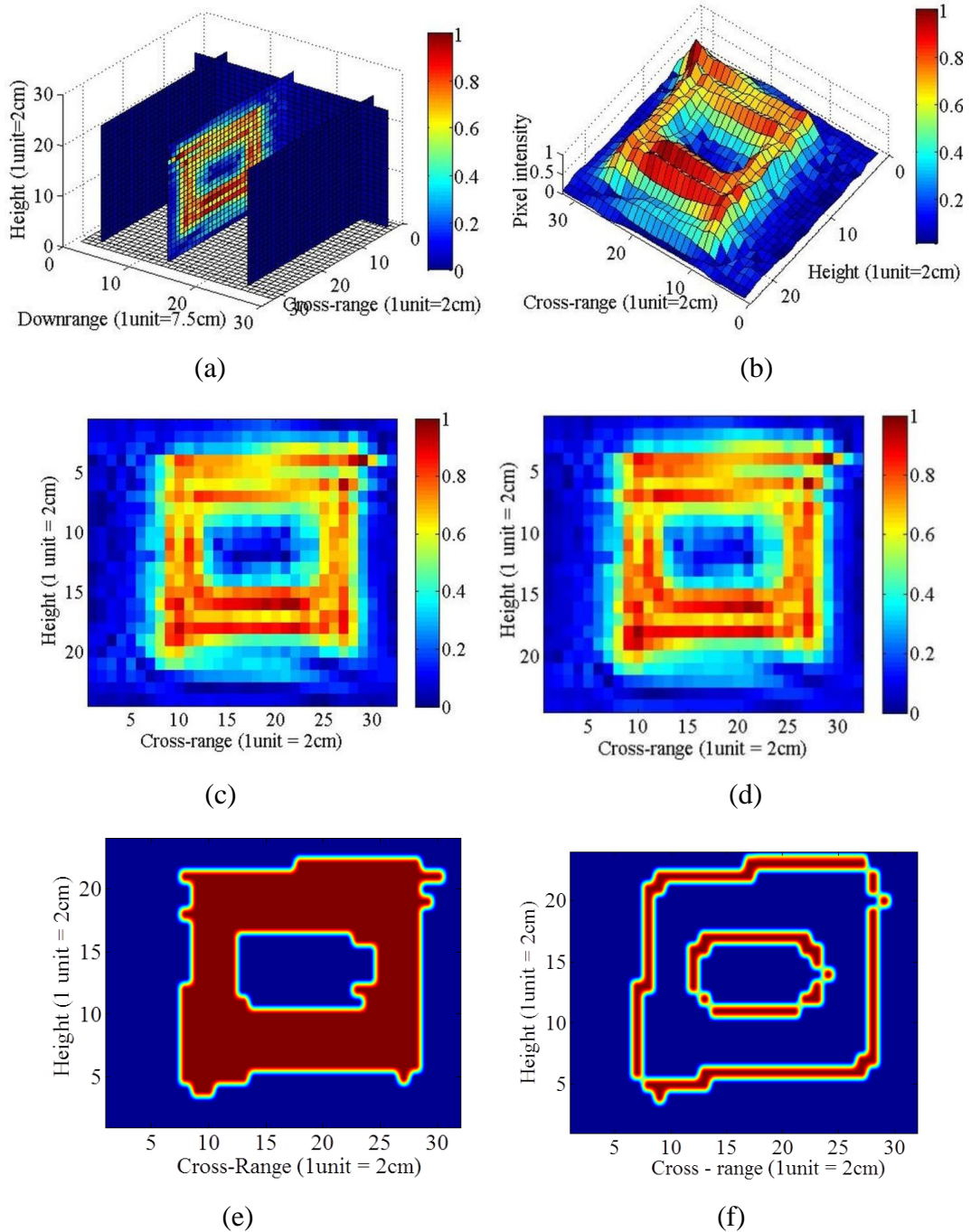


Figure 4.10. Validation results of the developed methodology for stand-off target's complete information (shape and size estimation): (a) 3D C-scan plot, (b) surface distribution plot, (c) raw C-scan image plot, (d) image after clutter reduction, (e) image after thresholding, (f) image after edge detection.

For target's material classification, the developed Cauchy distribution pdf based classification methodology is applied on T1 target's image data and its results are shown in Table 4.4. The Cauchy pdf function's location and scale parameter values were calculated for both the

material classes, *i.e.*, wooden target and metal background. The location parameter values fall well within the stipulated range for both metal and wood as given in equation (4.20). Hence, we can conclude that proposed methodology can successfully differentiate between high index (metal) and low index (wood) material.


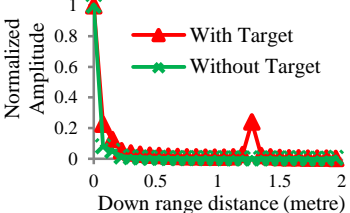
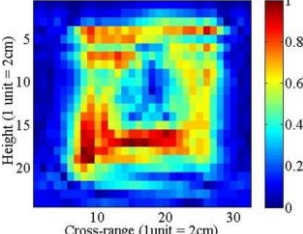
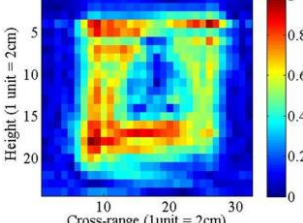
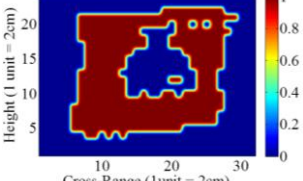
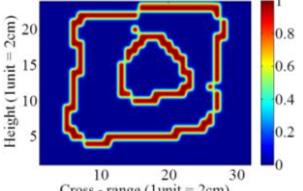
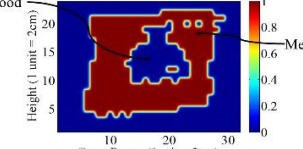
Table 4.4. Validation Results for target's material classification

Cauchy Distribution	Metal		Wood	
	σ	μ	σ	μ
T1	0.6511	0.0719	0.2839	0.0662

4.7. Overall Results of Fully Developed Target's Shape Identification and Material Classification Technique

A target's shape identification and its material classification methodology has been proposed using most commonly used image processing techniques for an ingeniously designed MMW imaging radar. A comprehensive list including the step by step results at each of the signal processing step is shown in Table 4.5, using an example target's shape, *i.e.*, triangular shape wooden target on the metal sheet background.

Table 4.5. Different Signal processing steps and their outcomes for target's shape identification and target's material classification

Input Technique	Result	Interpretation/ Explanation
Target under test		Wooden triangular target on the metal background sheet undergoes C-scanning (horizontal scan and vertical scan) for complete target data acquisition.
Range profile plot		It gives information related to target's presence and its location in downrange, corresponding to the reflection intensity peak.
C-scan target's image		2D raw C-scan image [24, 32] of the detected target is extracted at a downrange index, which is the representation of target's spatial intensity values as a function of cross-range and height coordinates.
Subtask 1: Target's shape Identification		
Image enhancement (Background subtraction, SVD)		It improves the target's raw image quality in order to facilitate correct target's shape identification.
Thresholding (Mean & Standard deviation based global thresholding)		It segments the target from the background, as a result, triangle target's shape is visible.
Edge detection (Canny detector)		This outlines the target's edges, so as to better visualize the targets. Here, triangle shaped target is now correctly and clearly identified.
Subtask 2: Target's Material Classification		
Cauchy Probability distribution function		Cauchy pdf successfully classifies the two target's material classes, i.e., wooden triangle and metal background sheet separately.

4.8. Conclusion

A SFCW radar based millimeter wave (60GHz) imaging system has been indigenously designed for stand-off target's identification and its material classification applications. Here, C-scanning technique has been used for complete target's 2D information. Different post-processing techniques have been proposed for stand-off target's image enhancement (background subtraction, SVD), image segmentation (mean & standard deviation thresholding, canny edge detector) and its material classification (Cauchy probability distribution function). As a proof-of-concept, performance of different signal processing techniques has been tested and validated using an extensive number of targets of four different regular shapes, viz., rectangle, square, circle and triangle. The test and validation results suggest successful target's identification w.r.t. its location, shape and target's material classification. Thereby, MMW imaging may provide a good alternative for stand-off complete target's information retrieval when used in conjunction with appropriate image processing techniques.

Chapter 5

Development of Size and Rotation Invariant Target's Shape Identification Algorithm for Millimeter Wave Imaging System

In the preceding chapter, we have proposed a stand-off target's identification methodology using an ingeniously designed MMW SFCW imaging radar system, where, different signal pre-processing and post-processing techniques have been dealt, in order to identify the target's shape accurately. However, the targets considered there were nearly ideal, in the sense that they won't undertake any sort of orientation or size variations. The performance of target's identification methodology can be made more generalized and adaptive by taking into account target's size and rotation effect. An invariant system of such type will be more robust in practical imaging situations and will be able to withstand real target's deformations, like, orientation or size mismatches. The goal of a typical computer vision/ radar imaging system is to analyze images of a given scene and recognize the content of the scene. Such systems are needed in a variety of fields, like, robotics, military reconnaissance, remote sensing, document processing, and industrial automation. In many instances, the same image in the respective scenes, is not always perfectly aligned and of the identical size. Therefore, there is a need to develop a pattern identification methodology that should be robust towards any such variations in the image. A solution to this is ANN based approach, which provides an adaptive pattern recognition solution as compared to the fixed threshold based classification/ recognition techniques. ANN deals with target's actual image data, and henceforth, it is more flexible and versatile. Therefore in this chapter, target's rotation and size invariant artificial neural network (ANN) based algorithm has

been proposed, which would automatically take care of any such variations and reconstruct the correct target's shape and size irrespective of its orientation discrepancies.

5.1. Introduction

The invariant-object recognition has emerged as a topic of utmost importance, with an aim to identify/ recognize any object independent of its position (translated or rotated) and size (larger or smaller). Artificial intelligence techniques have the capability to develop a system for complex, real world data based on the system's own experiences with data, under a unified model or mathematical framework. The developed model then, can be formally characterized, analyzed and can generalize and adapt across different data and domains [147]. Machine intelligent techniques (viz., ANN, SVM, fuzzy-ANN) have the advantage over simple threshold (fixed or statistically adaptive) based methods that they are capable of learning from experience and performing analytical observation resulting in a system that can continuously self-improve and thereby offer increased efficiency and effectiveness [132, 278, 324, 326]. Researchers are using these soft computing techniques as powerful tools for finding patterns in data and discovering solutions to difficult problems in a wide range of fields, for example: computer vision [171], speech recognition [49], text analysis [147] information extraction [180], and face matching [29, 251] etc.

A. Khotanzad et. al. [147] considered two feature types: geometrical invariant moments, and Zernike moments and compared the performance of neural network classifier with the three other traditional classifiers; Bayes, nearest neighbor, and minimum-mean-distance for the classification of noiseless as well as noisy binary images of English characters (26 classes). It was found that neural network outperforms the other three classifiers. Also, Zernike moment features showed better classification accuracy compared to geometrical moments. However, they have not investigated towards size invariance capability as well as it deals with mere classification but not with pattern reconstruction. *L. A. T. Mendez et. al.* [292] proposed a holographic nearest-neighbor algorithm (HNN) in conjunction with invariant normalized moment of inertia for translation, rotation, and scale-invariant character recognition, using the 26 upper case letters of the alphabet. Only four different orientations and one size for each letter was taken and 98% correct recognition was achieved. However, the algorithm does not explore the size variations and only pattern classification was explored. *S. J. Perantonis et. al.* [230]

demonstrated pattern recognition of typed and handwritten numerals independently of their position, size, and orientation using higher order neural networks and image features extracted by the method of moments. *L. Shao et. al.* [171] developed an evolutionary learning methodology to automatically generate domain-adaptive global feature descriptors for image classification using multi-objective genetic programming (MOGP). Although, it takes quite a long time for evolving or training.

Most of the existing studies make use of these intelligent techniques in image segmentation and classification. The learning algorithm develops a model from the training data provided and which is then used to classify new examples into the correct category. The accuracy of a particular model can be assessed by applying it to unseen examples and comparing the classifications to the “correct” classifications given by a human expert. So far, most of the work is related to pattern classification using neural network model [42, 278], however, capability of ANN for adaptive image reconstruction has not been explored well. Use of neural network for character recognition and reconstruction has been reported in [311] using an active MMW imaging system. A recognition rate of 98% has been obtained for ten dissimilar alphabetical letters used as objects. The success rate of reconstruction of distorted MMW images was 80% when five dissimilar letters were used for the reconstruction. However, orientation and size variation effect of alphabets has not been considered while developing the ANN model.

Thereby, the center of attention of this chapter is the fact that the target's identification methodology developed in the previous chapter, can be enhanced significantly with the exploitation of machine level artificially intelligent neural network technique. The idea here is, if the artificial neural network (ANN) model can be made intelligent by training it towards random target sizes and orientations, the target's image recognition can be immensely enhanced with the use of that learned knowledge while reconstructing the target's image. Therefore, in this chapter, our aim is to reconstruct the respective target shapes (i.e., square, rectangle, triangle and circle), and, for this purpose we have proposed a methodology based on neural network which can take care of rotation and size variations, by which correct target's shape can be recognized.

This chapter is organized as follows: section 5.2 gives the theoretical background, section 5.3 presents the description of target data set used, the methodology used to develop size and orientation invariant ANN image reconstruction model is given in section 5.4, and section 5.5 presents validation of the developed model. The final remarks and conclusions are given in section 5.6.

5.2. Theoretical Background

Pattern recognition is an essential part of any high-level image analysis system. Machine intelligent soft techniques provide pattern recognition/ classification by adaptively calculating the threshold as compared to the fixed threshold classifiers, like, PCA, K-means, Euclidean distance etc. Additionally, Neural Network's (NNs) learn through experiments and thus, continuously evolves their capabilities towards interpreting random variations in the target's shapes and sizes. Recent developments in the field of NN's have provided new potential alternatives to the traditional techniques of pattern recognition. The neural networks are inspired from studies of biological nervous systems and are composed of many simple nonlinear computational elements (neurons or nodes) which are connected by links with variable weights. The inherent parallelism of these networks allows rapid pursuit of many hypotheses in parallel, resulting in high computation rates. Moreover, they provide a greater degree of robustness or fault tolerance than conventional techniques because of the many processing nodes, each of which is responsible for a small portion of the task. Neural networks can perform different tasks, one of which is in the context of a supervised pattern recognition. The stand-off target's recognition process can be made more robust by employing size, rotation, and location invariant capability to the target's identification methodology. This may be accomplished by extracting a suitable set of features with the desired invariance properties from the training patterns given for classification. These unique features help to provide distinct decision boundaries to the neural network classifier model [54, 230].

Pattern recognition using neural network is basically composed of four building blocks:

- *Step 1- data acquisition, i.e.*, converting any scene/image into a matrix of numbers.
- *Step 2- pre-processing*, this involves image enhancement, so that scene can be easily analysed.
- *Step 3- feature extraction*, where the image is represented by a set of numerical 'features' [281, 324]. The selected feature set possesses useful information (in the sense of discrimination ability) present in the original data. Moreover, a robust recognition system must be able to recognize an object irrespective of its orientation and size as well. This requirement necessitates rotation and scale invariance properties for the extracted features [28, 126, 230].

- *Step 4- classification*, where a class/label is assigned to the unknown image/object depending on its extracted features and comparing them with class representations that neural network has learned during its training stage [147].

It is the invariant property of extracted features that enables the neural network to become invariant and classify the objects correctly irrespective of their sizes and orientations. Moreover, in this chapter, instead of using generally used feature extraction process (Step 3) as mentioned above, we have used a different methodology to achieve the invariance property. As well as, instead of doing pattern classification, we aim for a pattern recognition approach.

Therefore, in order to make the stand-off target's identification system more robust towards distortions in target's images, we aim to design a rotation and scale invariant image recognition technique based on artificial neural network (ANN) that will be fully adaptive towards the orientation errors and scaling variations of different targets under test. For developing the proposed ANN model, four regular shape targets, viz., square, rectangle, triangle and circle were considered and each of the target's shapes was taken with varying sizes and was put in random orientations. Thereby, a total of 33 target data sample was generated for training and developing our proposed orientation and size invariant image reconstruction artificial neural network model.

5.3. Data set used

The experimental arrangement of the MMW SFCW imaging radar system as shown in Figure 1.8 has also been used for target's data generation for our ANN model development. The data set for training and developing the proposed ANN model was formed using four considered regular target shapes, viz., rectangle, square, circle, triangle, having randomly varying sizes and orientations.

Any single target's shape has been considered in different sizes and is put into different orientation angles (randomly ranging from 0° to 90°) on a large metal (Al) sheet mounted on the 2D scanning frame, thereby, creating an experimental data set for each of the wooden target shapes as shown in Table 5.1, for example: for a square shape target, a data set of nine samples (i31 – i39) is formed comprising four different sizes (varying between 4 cm^2 to 20 cm^2) and four different orientation angles (varying from 0° to 90°).

Table 5.1. Different target's shape, size and orientation variations undertaken for size and rotation invariant target's image recognition ANN model development

S. No.	Shape	Data Set	Size	Orientation
1.	Square	i31 – i39	4 cm ² -20 cm ² (5 samples)	0° – 90° (4 samples)
2.	Rectangle (2:1)	i21 – i210	8x4 cm ² - 24x12 cm ² (5 samples)	0° – 90° (5 samples)
3.	Triangle (equilateral)	i41 – i48	Each side 10 cm to 24 cm (4 samples)	0° – 90° (4 samples)
4.	Circle	i11 – i16	Radius 4 – 14 cm (6 samples)	--
Total samples		33		

Likewise, for other three regular shaped targets, the data set was formed. A complete list of input targets used is shown in Table 5.2. Here, target's notation used is of three digits, where first digit is an alphabet, such that, 'i' signifies the input target data and 'o' signifies output data; the second digit correspond to particular shape, such that, 1 for circle, 2 for rectangle, 3 for square, 4 for triangle; and the third digit signifies particular size and angle of the considered target's shape. For total 33 target samples, experimental data is captured by the MMW radar system using the complete C-scan, *i.e.*, taking 32 horizontal scans (B-scans) and 24 vertical scans (C-scans) in order to fully cover the target area as discussed in section 4.4. Thereby, the 2D target's image matrix will be of size 24 x 32 (row x column), as extracted at the downrange location corresponding to the reflection peak in the range profile, as discussed earlier in section 1.3.2.2. Moreover, a detailed description of each of the target sample used, its shape, size, orientation and their corresponding training output binary notations are shown in Table 5.2. The description of generation of binary teaching matrix corresponding to the input matrix is given in section 5.4.2.3.

Table 5.2. Complete detailed list of different target samples undertaken with varying sizes and orientations

S. No.	Shape	I/P Target Matrix ID	Size	Angle (degrees)	O/P Binary Teaching Matrix ID
1	Triangle (Isosceles)	i41	10 cm x 10 cm x 10 cm	0	o41
2		i42	10 cm x 10 cm x 10 cm	29	o41
3		i43	16 cm x 16 cm x 16 cm	0	o42
4		i44	16 cm x 16 cm x 16 cm	12	o42
5		i45	20 cm x 20 cm x 20 cm	0	o43
6		i46	20 cm x 20 cm x 20 cm	67	o43
7		i47	24 cm x 24 cm x 24 cm	0	o44
8		i48	24 cm x 24 cm x 24 cm	84	o44
9	Rectangle (2:1)	i21	8 cm x 4 cm	0	o21
10		i22	8 cm x 4 cm	38	o21
11		i23	12 cm x 6 cm	0	o22
12		i24	12 cm x 6 cm	23	o22
13		i25	16 cm x 8 cm	0	o23
14		i26	16 cm x 8 cm	18	o23
15		i27	20 cm x 10 cm	0	o24
16		i28	20 cm x 10 cm	44	o24
17		i29	24 cm x 12 cm	0	o25
18		i210	24 cm x 12 cm	56	o25
19	Square (1:1)	i31	4 cm x 4 cm	0	o31
20		i32	8 cm x 8 cm	0	o32
21		i33	8 cm x 8 cm	58	o32
22		i34	12 cm x 8 cm	0	o33
23		i35	12 cm x 8 cm	34	o33
24		i36	16 cm x 16 cm	0	o34
25		i37	16 cm x 16 cm	42	o34
26		i38	20 cm x 20 cm	0	o35
27		i39	20 cm x 20 cm	23	o35
28	Circle	i11	8 cm Radius	--	o11
29		i12	12 cm Radius		o12
30		i13	16 cm Radius		o13
31		i14	20 cm Radius		o14
32		i15	24 cm Radius		o15
33		i16	28 cm Radius		o16

5.4. Methodology used to develop size and rotation invariant artificial neural network model

In order to develop our proposed automatic, size and rotation invariant target's image reconstruction model, ANN based soft computing technique has been used due to its proven versatility and capability to learn and evolve itself accordingly. Once trained, ANN will have the ability to predict the output for any unknown input target sample with least mean square error when compared to the actual desired output. The inherent parallelism of the ANN allows for rapid pursuit of many hypotheses in parallel, resulting in high computation rates.

5.4.1. Introduction to the ANN model

A neural network topology is also known as multilayer perceptron (MLP) [147]. A MLP is a feed-forward network with one or more layers of nodes between the input and output nodes. These in-between layers are called hidden layers. A NN model with one hidden layer is shown in Figure 5.1. Connections within a layer or from higher to lower layers are not permitted. Each node in a layer is connected to all the nodes in the layer above it.

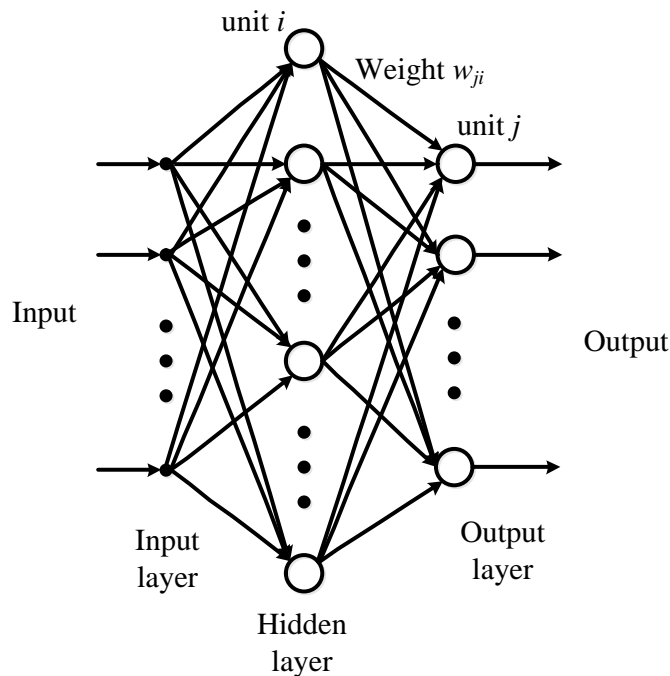


Figure 5.1. A multilayer perceptron neural network model with one hidden layer, input layer and output layer.

Training of NN is equivalent to finding proper weights for all the connections such that a desired output is generated for a corresponding input. Training is done through an iterative gradient procedure known as the back-propagation algorithm, in which for each pattern in the training set, learning of proper weights is conducted by: 1) computing the discrepancy between the desired and actual outputs and 2) feeding back this error signal level by level to the inputs, changing the connection weights in such a way as to modify them in proportion to their minimizing responsibility for the output error. The major steps of any ANN model training are as follows [312]:

Step I: Initialize weight w_{ji} 's to small random values, where w_{ji} is the value of the connection weight between unit i and unit j in any layer.

Step II: The output y_j of each unit j is defined as:

$$y_j = f(\text{net}_j) \quad (5.1)$$

$$\text{net}_j = \sum_i w_{ji} o_i + \theta_j \quad (5.2)$$

where, o_i is the output of unit i , w_{ji} is the weight of the connection from unit i to unit j , θ_j is the bias of unit j , net_j is a summation of every unit i whose output flows into unit j , and $f(\text{net}_j)$ is a monotonously increasing training function. For example, for non-linear sigmoid function output can be written as:

$$y_j = \frac{1}{1 + \exp(-\sum_i y_i w_{ji})} \quad (5.3)$$

Step III: Now, specify the desired output class m for every input pattern. The desired output is zero for all the output nodes except the m^{th} node, which is one.

Step IV: Find an error term, δ_j for all the nodes. If d_j and y_j stand for the desired and actual value of any node, respectively, then for an output node,

$$\delta_j = y_j(d_j - y_j)(1 - y_j) \quad (5.4)$$

and for a hidden layer node,

$$\delta_j = y_j(1 - y_j) \sum_k \delta_k w_{jk} \quad (5.5)$$

where k is over all nodes in the layer above node j .

Step V: Adjust weights by

$$w_{ij}(n + 1) = w_{ij}(n) + \alpha \delta_j y_i + \zeta (w_{ij}(n) - w_{ij}(n - 1)) \quad (5.6)$$

where, $(n + 1)$, (n) , and $(n - 1)$ are index next, present, and previous, respectively. The parameter α is a learning rate similar to step size in gradient search algorithms, and ζ is a constant between 0 and 1 which determines the effect of past weight changes on the current direction of movement in weight space. This provides a kind of momentum that effectively filters out high frequency variations of the error surface.

Step VI: Now, present other input training patterns to the ANN model and repeat the process again from *step II* onwards, so that neural network may learn different possible changes in the input data. All the training inputs are presented cyclically until weights stabilize or converge to user-defined minimum error value. The purpose is to make $E = \sum_p E_p$ small enough for all the patterns by choosing appropriate w_{ji} and θ_j . The squared error pattern E_p for a pattern p is defined as:

$$E_p = \frac{1}{2} \sum_{j \in \text{output layer}} (d_{pj} - y_{pj})^2 \quad (5.7)$$

Summarily, the ANN backpropagation algorithm is an iterative gradient descent procedure in the weight space which minimizes the total error between the desired and actual outputs of all the nodes in the system so as to adapt it towards possible random changes in the given input patterns.

5.4.2. ANN model development for rotation and size invariant target's image reconstruction

In order to formulate our invariant image recognition problem, out of the total 33 experimental target data samples, 25 randomly selected samples (75%) have been used for neural network configuration setup and training. The remaining 8 random samples (25%), were further used to perform independent test on the trained neural network and check its performance. The complete

flow-chart for generation of neural network model for rotation and size invariant target's image recognition is shown in Figure 5.2. The designed neural network configuration consists of:

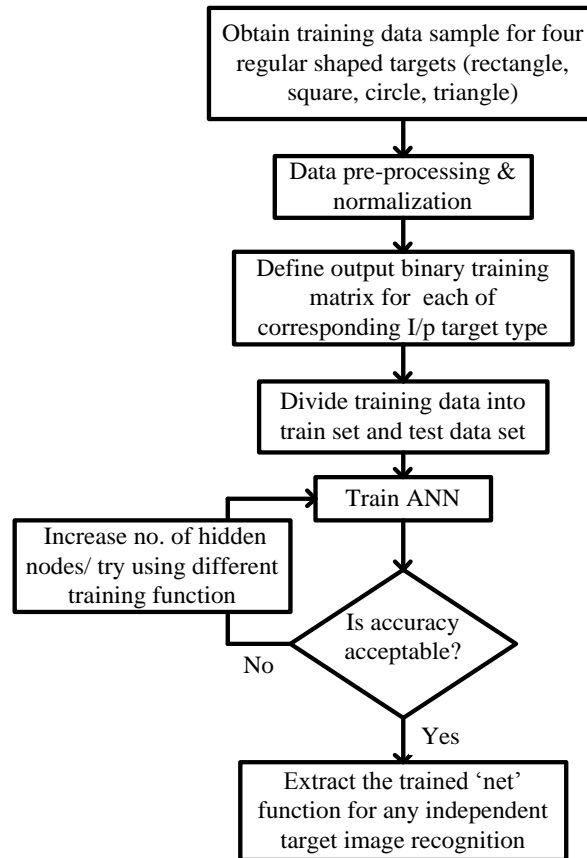


Figure 5.2. Flow chart describing generation of rotation and size invariant neural network model.

5.4.2.1. Input Layer:

For ANN input layer formation, each of the C-scan image matrices (24, 32) is first transformed to the column vector (24x32, 1). Accordingly, for all the considered 25 input target samples, the respective C-scan matrices are stacked as column vectors to form a complete 2-D input matrix (24x32, 25) of the ANN model as shown in Figure 5.3. This input matrix is used as the input layer to the neural network model. Here, we have not used the complex feature extraction process, to achieve size and orientation invariant, distinct features of different target's shapes as discussed in section 5.2. Instead, we have generated a randomly varying target's data set and will train the neural network to learn the random target's image variations as per method, which will be discussed in section 5.4.3. This will enable the trained neural network model to

correctly recognize the image of any size and orientation, for the considered target's shapes, without requiring any feature extraction step.

5.4.2.2. Hidden Layer:

Hidden neurons influence the error at the output nodes and the stability of neural network. In our proposed NN model, the middle hidden layer consists of 30 neurons. Here, numbers of neurons are iteratively chosen keeping the balance between minimizing the output error as well as ANN system complexity. Moreover, excessive hidden neurons will cause over fitting of the NN by overestimating the problem complexity, which may render its ability to correctly reconstruct any unknown target [269].

5.4.2.3. Output Layer:

In the output layer, instead of applying pattern classification labels to different shapes and classifying the targets in terms of class labels, we have used image recognition approach so as to reconstruct the correct target's shape. As we want to recognize the target's shape, the output matrix for training the NN was generated in accordance to the input target's size and is in binary (0,1) matrix form as shown in Table 5.3 column b.

For example: for the rectangle shape, five different sizes starting from 8x4 cm² upto 24x12 cm² have been taken (Table 5.1). Five different binary matrices have been assigned to each of the five sizes of rectangle shape, where, each binary image has been taken of same size as of corresponding rectangular target size. Now, these rectangle targets of five sizes have been oriented at varying angles from 0° to 90° generating other five samples of varying orientations, and for each orientation, the binary image assigned is same as of corresponding size, because our aim is to recognize the correct shape. As shown in Table 5.3, for target id - i26 (rectangle size 16x8 cm²), the binary image assigned is shown in column b, which will be same for any orientation of the same size. Hence, for one size, one binary matrix is assigned whatever be the orientation.

A detailed nomenclature of assigned binary matrices in correlation to respective input image matrices is given in Table 5.2 (last column). Likewise, complete output layer matrix for the proposed ANN model will be of size (24x32, 25) corresponding to the 25 input target's data samples. Figure 5.3 shows the network configuration of the proposed rotation and scale invariant neural network system.

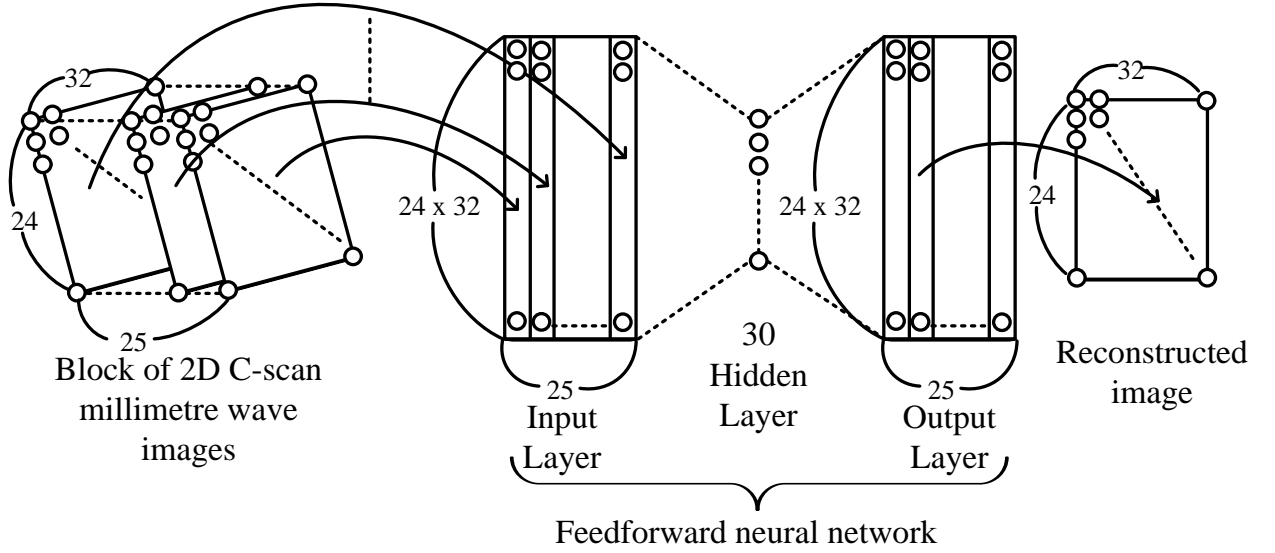


Figure 5.3. Configuration of rotation and scale invariant neural network for target's image recognition. It consists of (24 x 32, 25) input units, 30 hidden units and (24 x 32, 25) outputs units [280].

5.4.3. Training of the developed Neural Network Model

For image recognition problem formulation, a multilayer feed-forward neural network has been used, which consists of a pattern recognition network with *trainscg* training function and *sigmoid* transfer functions in both the hidden layer and the output layer [113]. *Trainscg* is a network training function that updates weight and bias values according to the scaled conjugate gradient method. Sigmoid transfer function constrains the outputs of a network between 0 and 1 as required for pattern recognition/ reconstruction problem. Learning algorithm used for training of the neural network is based on mean squared error (mse) criterion defined as the average squared error between the network outputs 'a' and the target's outputs 't' [252].

$$mse = \frac{1}{N} \sum_{i=1}^N (e_i)^2 = \frac{1}{N} \sum_{i=1}^N (t_i - a_i)^2 \quad (5.8)$$

The system first uses the input vector to produce its own output vector 'a' and then compares this with the desired output or target's vector 't'. If there is no difference, then, no learning takes place. Otherwise the weights are adjusted to reduce the difference. Lower the value of mean squared error better is the performance of the trained network. In order to enable our

designed neural network to be rotation and scale invariant for the considered shapes, it is trained, validated and tested as per following methodology:

- The total 25 input samples of the ANN input matrix are randomly divided into three different parts for training, validation, and testing in a ratio of 80%, 15% and 5%, respectively. Hence, 20 samples have been used for training the neural network, which were randomly selected and represents considered shapes with different random sizes and orientations. Random training data set = (i21, i31, i11, i42, i35, i27, i13, i43, i37, i34, i22, i47, i210, i16, i26, i36, i41, i23, i46, i32, i29), here notations used are given in Table 5.2. Result of few training data samples is shown in table 5.3.
- Rest of 15% (4 samples) data samples have been used as the validation data to measure the mean squared error and retrain the neural network till the mean squared error converged and minimized below 0.01 for optimum performance. Random validation data set = (i25, i15, i45, i38), here notations used are given in Table 5.2.
- Once, the neural network has been trained and validated, a network function has been generated for further use. Any independent test data can be used as the input to this network function and the output generated will help to recognise the correct target's shape and size irrespective of its random orientation and size. Resulting mean square error of the test data output and its reconstructed output image determines the accuracy of trained proposed neural network model.
- Here, we have used independent test data samples to check the performance and practicality of the trained neural network model function. These test samples were earlier never been used in the neural network in any form. Random independent test data set = (i28, i33, i14, i48, i44, i24, i39, i12), here notations used are given in Table 5.2. Results of some independent test samples are shown in section 5.5 (Table 5.4).


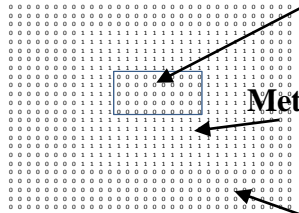
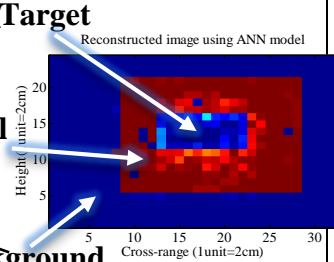

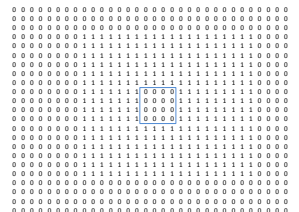
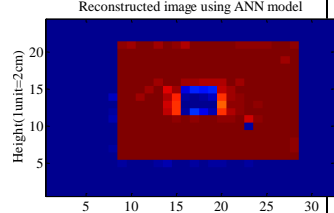

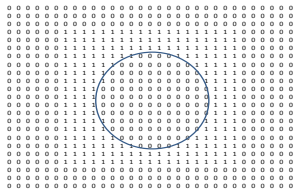
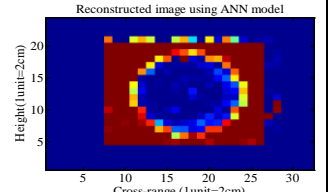

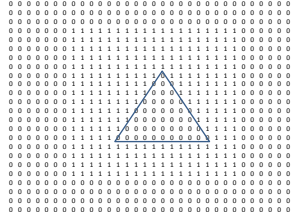
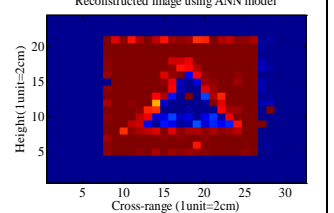
Hereby, this designed neural network approach enables us to recognize and visualize the actual target's shape nullifying any rotation or size variations for the considered regular shapes.

5.4.4. Developed ANN Model Testing

Table 5.3 shows results of the reconstructed images implemented through neural network for few of the training data samples, i.e., i26, i35, i16, i46 (notations as per Table 5.2). Actual photographs of the corresponding targets are also shown for the reference. Neural network has

been trained using corresponding binary matrices; o23, o33, o16, o43, respectively as shown in Table 5.3 (symbol notations as per Table 5.2).

Table 5.3. Tabular presentation of proposed neural network model for four different regular shape targets, viz, rotated rectangle: i26, rotated square: i35, Circle: i16, tilted triangle: i46.

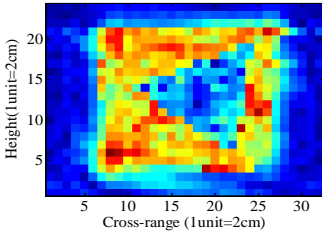
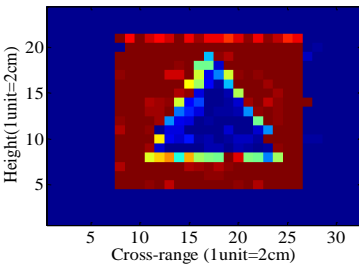
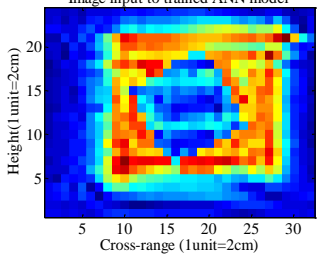
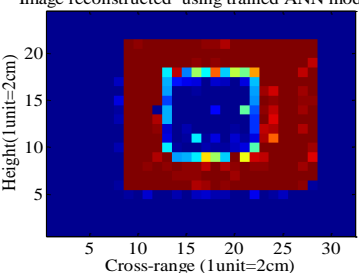
S. No.	Actual target's photograph	Binary training matrix as per I/P shape and size	Output reconstructed image	Mean Square Error (MSE)
	(a)	(b)	(c)	(d)
1	Target's Id - i26 	 o23		0.0028
2	Target's Id - i35 	 o33		0.0134
3	Target's Id - i16 	 o16		0.0082
4	Target's Id - i46 	 o43		0.0152

Once trained, neural network successfully reconstructs the image for respective different target's shapes rectifying any rotation variation, with nearly exact shape and size, and appreciably low mean square error values, viz., 0.0028, 0.0134, 0.0082, 0.0152, respectively.

5.5. Validation of the developed ANN model

After training, performance of the proposed neural network model needs to be verified through independent data for its usefulness and practicality. For this, the trained network performance was validated using completely different test data set, which were earlier never been used as input to the network. With these independent test samples, the trained neural network shows fairly good performance as well. As an example, Table 5.4 shows results from trained neural network for the two independent test targets, i.e., i48 and i39. As shown, tilted triangular and tilted square shape inputs, are recognized with correct shape, size and orientation, as a true triangle and rectangle output images, with mean square error of 0.1029, 0.0776, respectively.

Table 5.4. Results of the proposed trained neural network model using a different independent set of test samples, i48 - tilted triangle, i39 - tilted square.

S. No.	Test Targets	Output reconstructed image	Mean Square Error (MSE)
1	Target's Id - i48 Image input to trained ANN model 	Image reconstructed using trained ANN model 	0.1029
2	Target's Id - i39 Image input to trained ANN model 	Image reconstructed using trained ANN model 	0.0776

Thus, the results verify the capability of proposed rotation and scale invariant neural network for image recognition for the considered four regular target shapes. Further, the proposed neural network methodology can also be trained and applied for other different irregular target shapes.

5.6. Conclusion

In this chapter, a novel neural network based algorithm for rotation and size invariant target's image reconstruction has been developed for the four regular shaped targets, viz., rectangle, square, triangle and circle. As a proof-of-concept, reconstructed rotation corrected images as implemented through the trained neural network model have been shown for the independent validation targets. This neural network based signal processing methodology can be applied for identification and reconstruction for any orientation and size deformed MMW radar image. Further, using the proposed ANN based algorithm, more sophisticated and practical target's shapes may be considered for accurate target's identification once neural network has been trained towards these irregular shapes.

Chapter 6

Development of an Adaptive Quality Monitoring Algorithm to Detect fault (Crack) in Packaged Ceramic Tiles for Industrial Applications with MMW Imaging System

MMW frequency also offers a good imaging tool for inspection of quality and condition of industry goods/ materials towards fatigue, wear and tear without hampering its utility and value. In recent years, there has been a good development of techniques for screening persons, objects etc. from a distance, which could carry variety of weapons beneath their clothing [17, 325]. Likewise, screening of variety of goods beneath the packaging in view of quality control is constantly desired [144, 357]. Currently used different EM based imaging techniques pose several limitations in terms of their target's detection and identification capabilities [110]. For a good non-invasive quality testing system the prerequisites are its capability to provide appreciable contrast between targets and any confined irregularity for discrimination as well as reflected signal should not attenuate much before being received by the imaging system. These preconditions are very well met at MMW spectrum, and hence, it may prove an effective modality for non-invasive quality monitoring [183]. In view of these possible fascinating MMW features, a critical investigation of different computer vision based techniques towards their fault detection capability is essentially desired. A robust methodology is needed to be developed for an automatic fault monitoring for quality check of packaged goods for industrial applications. Our main purpose for non-invasive quality monitoring is the fault detection, and for this, we have

considered crack as a fault. Henceforth, in this chapter a MMW imaging system based non-destructive, non-invasive quality inspection methodology has been proposed to monitor the cracks in packaged ceramic tiles.

6.1. Introduction

Nondestructive testing & evaluation (NDT & E) is the analysis of an object with technology that does not affect the object's future usefulness and its efficacy. MMW techniques provide an accurate and viable NDT solution, where EM signals at these frequencies can easily penetrate dielectric materials and provide their inner structure information. MMW NDT techniques are sensitive to geometrical and dimensional variations of a medium or a defect [62, 356]. Research works for various NDT applications are available which are employing different frequencies and techniques, like, defects in aircraft lap joints using multi-modal structural analysis process that includes intra and inter-modal NDT data fusion based on eddy current, MMW and ultrasonic technique [58], surface crack detection of stress induced fatigue crack in metals using open-ended rectangular probe at 24 GHz and using coaxial probes at 90 GHz [145, 357], wafer inspection for de-lamination in IC packages using coax line sensor at 20 GHz [136, 340], structural health monitoring for hidden wall cracks by near-field inspection of reflected EM wave dispersion at W band [219]. A far-field airborne radar operated at X-band was used on the glass fiber reinforced polymer (GFRP) enclosed concrete cylinder targets followed by backprojection imaging algorithm to reconstruct the improved images for its condition assessment [348]. A 30 GHz linear, 150 mm long imaging array has been demonstrated for NDT applications capable of successfully detecting/ imaging a pair of scissors, square shaped rubber (10 mm x 10 mm x 1 mm) inserted between two (6.5 mm-thick) balsawood composite panels [90]. Apart from these fascinating applications, several important areas are still left to explore in which, one is the quality monitoring of packaged goods for industrial applications. The high demand of quality and reliability of products require a precise detection of defects for a competent and cost efficient manufacturing without causing any damage.

One of the major requirements for non-invasive, robust crack classification is to have a set of unique and relevant numerical features that will conveniently describe a region/ image. Features are invariable descriptors of any image that could help to detect any type of irregularity or crack in the image [28, 178, 286]. A number of different feature extraction techniques have

been reported in literature and are broadly classified as shape based feature, texture based feature, color based feature [63, 215, 299]. A number of texture features have been reported in the literature, having first order and higher order statistics, for example, histogram statistics, co-occurrence matrices [106], local binary patterns (LBP) [217], and morphology [268]. Apart from texture feature, shape based feature extraction techniques are also popular in computer vision based image processing, like, scale invariant feature transform (SIFT) [299], speeded up robust features (SURF) [28] which provide a low-dimensional representation of visual images for instance matching with images, Hidden Markov models (HMMs) to detect and classify landmine responses based on statistical representation of their characteristic hyperbolic shape [49], histogram of oriented gradients (HOG) which has been successfully used for pedestrian detection, traffic surveillance with occlusion handling [124], wavelet transform (Haar, Gabor) [286] having varying scope. Upon extracting the features, it is further applied to a classifier model in order to associate it with a particular class label out of possible class types. Different prevailing classifiers are K-nearest neighbor, Euclidean distance, support vector machine (SVM), self-organizing map (SOM), fuzzy neural network, backpropagation neural network, etc. [278, 311, 336]. However, applicability of these computer vision based feature extraction techniques for MMW imaging radar has not been explored, and hence, there is a need to carefully investigate and find an optimal feature for non-invasive concealed crack monitoring. Moreover, it is a quiet challenging task to non-invasively detect as well as locate the crack point accurately with minimum false alarm, in which image statistics based methodology, may be an alternate approach for accurate localization of cracked windows in the packaged ceramic tiles. Because, image statistics has the maximum spatial information and it can be helpful to develop an adaptive approach for crack monitoring in a more generalized way. Thereby, in this chapter an attempt has been made to investigate the undercover crack detection capability of the ingeniously designed MMW imaging radar system where packaged ceramic tiles are considered as a concealed object for classifying it as a crack or non-crack tile. Two different approaches for this have been proposed, i.e., feature-based-ANN crack classification model and spatial statistics based adaptive crack localization model.

This chapter is further organized as follows: section 6.2 discusses theoretical background for non-invasive concealed crack classification, section 6.3 outlines the design for MMW imaging system and concealed targets for non-invasive quality monitoring application, section 6.4 details subtask 1, i.e., methodology used for feature-based-ANN crack classification model,

section 6.5 discusses subtask 2, i.e., development of an adaptive statistical model for crack localization based on image reconstruction. Finally, section 6.6 presents the conclusion.

6.2. Theoretical Background

Non-destructive quality check of packaged goods is an important step in industrial process monitoring as well as from the consumer satisfaction point of view. Keeping in view of this need and automated, accurate inspection in order to classify the defective items, in this chapter we have attempted to develop a MMW imaging radar based methodology. This proposed objective has been accomplished by executing the following two subtasks, i.e., quantitative basis and image reconstruction basis where localization of crack is identified.

6.2.1. Sub Task 1- Feature Extraction-Based-ANN Classification Model: A Quantitative Approach

Detecting crack in any concealed item is a challenging task because of its varying appearances and positions in the target's image. Different computer vision based image processing techniques are available in literature for different crack detection applications reporting variety of features having different working principles as discussed above and also in chapter 2 (section 2.3.3.3). Therefore, after critical analysis, we have proposed a feature-based-crack-detection and classification methodology for the designed MMW imaging system. Following steps have been executed to develop the proposed methodology:

- For the development of a feature-based-crack-classification model, prerequisite is the target's image features, therefore, feature extraction would be the starting point. There are different types of feature extraction techniques available, as discussed in section 6.1. However, for an accurate crack classification model, features are needed that could correctly detect cracks even in the conditions of non-uniform illumination and target's deformations. Hence, features that are invariant to any slight deformation in the target's image in the sense of rotation, size or non-uniform contrast are to be considered for further analysis.
- Since, there are varieties of invariant features each having a different procedure for extracting unique image characteristics. Thereby, invariant features of different classes have been considered, i.e., Statistical based, Spectral and series expansion based, and

Contextual based features. Out of which the best feature should be selected through feature selection step. The description of different considered features is given in section 6.4.1.

- The next crucial step is the feature selection, i.e., out of the different extracted features, we need to find the best feature for the proposed non-invasive crack classification model. Also, the selected feature would fulfil the basic requirement of robustness towards target's slight deformations and non-uniform target's contrast for the optimal crack classification performance. Selection of an optimal feature would depend upon its maximum classification accuracy.
- For classifier model neural network has been preferably used since, ANN is an adaptive model, which would continuously evolve its decision criterion for crack/non-crack classification through learning. Thereby, it proves to be a better and robust alternative as compared to other fixed threshold based classification techniques, viz., K-nearest neighbor, Euclidean distance, PCA, Bayes classifier, histogram, etc. [44, 49, 278].
- Moreover, cracks in the ceramic tile could be of any random nature, hence, while training any of the feature-based-NN classifier model, random experimental values of possible crack/non-crack tile configurations should be used to improvise the performance.
- Henceforth, the respective feature-based-NN classifier models would be developed and critically analyzed and their performances will be checked on the basis of their crack/non-crack classification accuracy and false alarm.

The detailed implementation and analysis of feature-based-ANN crack classification model is given in section 6.4.

6.2.2. Subtask 2- Image Spatial Statistics Based Crack Localization Model: An Approach for Localization of Cracks

The image spatial statistics based methodology apart from giving packaged ceramic tile crack information also focusses on the particular crack location estimation, which may be many times helpful to provide insight information to estimate the reason of the crack in the packaged tile as well as many times in case of large tiles instead of discarding the whole item, the defected portion may only be cutout. Therefore, following methodology has been adopted for crack localization with MMW imaging system:

- For the development of image reconstruction based spatial statistical model, the respective target's image quality should be enhanced, and therefore, some form of filtering is required before any further signal analysis.
- Since, we know that image characteristics largely depends upon its statistical behaviors, like, mean, median, standard deviation, maximum and minima, etc. Thereby, image's statistical measures will prove to be vital for development our proposed non-invasive crack localization methodology.
- Further, the crack could be anywhere on the ceramic tile and of any random type, hence, a window based pattern search model may be a good way to scan the complete tile sequentially and detect particular cracked locations, apart from just the crack classification.
- Moreover, for the similar targets types also, the image statistics vary largely owing to different aspects of non-uniform illumination, background clutter, different multipath reflections, etc. [87, 201]. Therefore, for a generalized and automatic non-invasive crack localization model, tunability should be included which will take care of any such target's image deformations in practical industrial environment.
- Instead of designing a fixed condition for the test of crack/ non-crack window, an adaptive formulation should be modeled utilizing user defined accuracy and false alarm which will depend upon the image statistics of the particular tile under examination, because, statistical measures can uniquely characterize the different target's images.
- Different types of crack/ non-crack packaged tile configurations should be taken for validation of the proposed algorithm.

Thereby, a novel adaptive, spatial statistics based non-invasive crack localization algorithm has been developed and proposed as the subtask 2, under section 6.5.

6.3. Observations for Non-Invasive Concealed Crack

Detection/ Localization of Ceramic Tiles with MMW

Imaging Radar

Figure 6.1 shows the pictorial demonstration of the MMW SFCW radar setup for non-invasive packaged ceramic tile crack detection, classification and localization application. The similar SFCW radar setup has been used as shown in Figure 1.8 and only the target's arrangement is changed, so as to facilitate non-destructive testing of the concealed objects. Total of 45 ceramic

tiles considered as targets in different crack/non-crack configurations have been used and a detailed description of which is given in section 6.3.1. The typical radar parameters are the same as given in Table 1.1. Further, in order to completely scan the target, 2D C-scanning technique has been used as discussed in section 1.3.2.2, in which $N = 30$ horizontal scanning steps and $M = 18$ vertical scanning steps were taken with the inter-element spacing of 2 cm. Thereby, the image parameters of the designed MMW SFCW imaging radar, *i.e.*, range resolution and cross-range resolution comes out to be 7.5 cm and 8.59 mm, respectively as obtained from the corresponding equations (1.16) and (1.17).

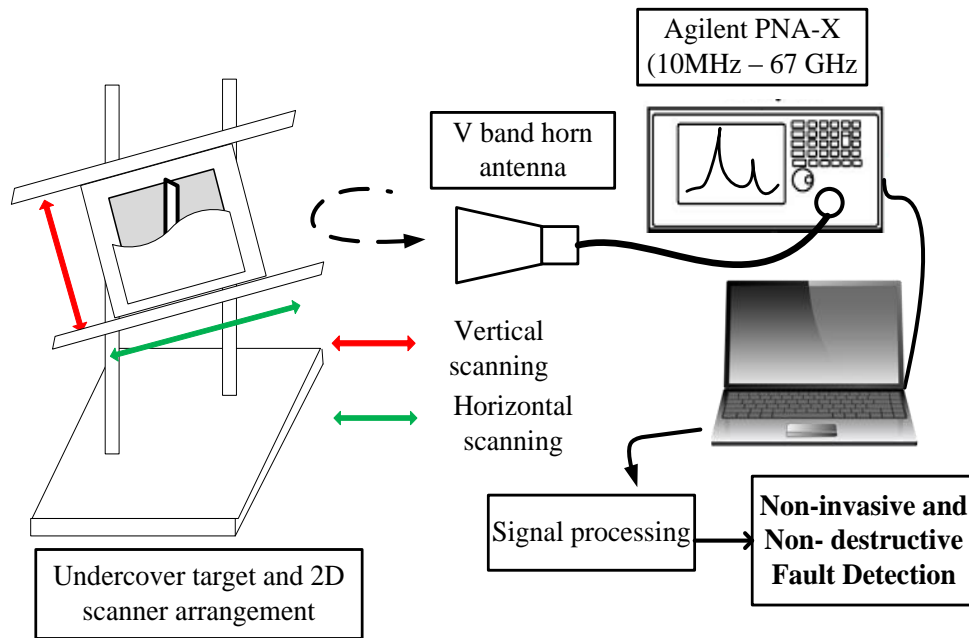


Figure 6.1. Experimental demonstration of ingeniously configured MMW imaging radar system for non-invasive packaged ceramic tile crack estimation.

6.3.1. Data Used: Packaged Ceramic Tile

While designing the targets, care has been taken to make the respective target's optically invisible in view of proposed concealed crack detection application. The pictorial demonstration for concealed tile arrangement is shown in Figure 6.2(a). Firstly, a large wooden sheet of size = 35 cm x 43.6 cm and thickness (t_1) = 5mm has been mounted on the 2D-scanning frame and over to which a thick polystyrene sheet thickness (t_2) = 2.6 cm was placed in order to avoid any reflections from the surrounding background, since polystyrene will absorb maximum of incident

EM waves and suppress any reflection. On this polystyrene sheet, the target under test was placed, i.e., commercially available and commonly used ceramic tiles having thickness (t_3) = 7 mm and size = 30.48 cm x 30.48 cm.

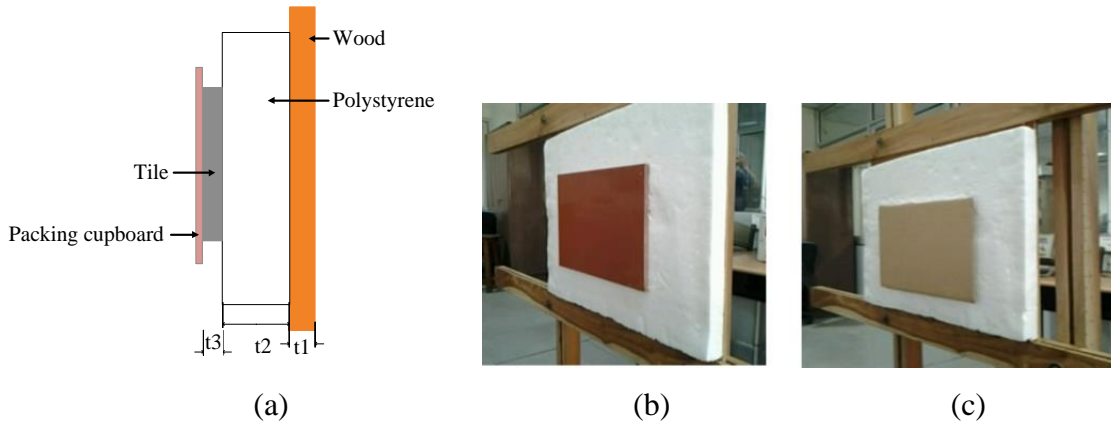


Figure 6.2. Target arrangement for concealed crack detection in packaged ceramic tiles: (a) pictorial demonstration, (b) ceramic tile mounted on the scanning frame, (c) ceramic tile covered with the packaging cardboard.

The respective tiles were covered with commonly used packaging cardboard, so that, by the visual inspection, it will be completely unknown that the undercover target tile is whether cracked or non-cracked. Now, for our concealed crack detection application we have selected tiles such that systematic crack has been introduced, like, horizontally cracked (*hc*), vertically cracked (*vc*), diagonally cracked (*dc*) and randomly cracked (*rc*) tiles. Therefore, it presents various possible cracks in the packaged ceramic tile. Apart from this ceramic tiles without any crack, i.e., full tiles (*f*) were also taken. An extensive 45 number of observations were performed using different concealed target's arrangements of cracked and non-cracked tiles as shown in Table 6.1.

In Table 6.1, first column signifies different considered crack/ non-crack ceramic tile configurations, second and third column represents training and validation targets, respectively and the last column gives the total number of target samples taken for each of the crack/non-crack ceramic tile configurations. Some of the test target tiles with varying crack configurations are shown in Figure 6.3.

Table 6.1. Different crack/ non-crack target tile configurations and their notations used

Target's type (cracked/ non-cracked)	Training / Test target's id's	Independent validation target's Id's	Data set/target's crack type
Non-cracked full Tile	<i>f1, f2, f3, f4, f5, f7</i>	<i>f6, f8, f9, f10, f11</i>	11
Horizontally cracked tile	<i>hc1, hc2, hc3, hc4, hc6, hc8,</i>	<i>hc5, hc7</i>	08
Vertically cracked tile	<i>vc1, vc2, vc3, vc4, vc7, vc8</i>	<i>vc5, vc6, vc9, vc10</i>	10
Diagonally cracked tile	<i>dc1, dc2, dc5, dc6, dc7, dc8,</i>	<i>dc3, dc4</i>	08
Randomly cracked tile	<i>rc1, rc2, rc3, rc4, rc6, rc7</i>	<i>rc8, rc5</i>	08
Total target's data set	30	15	45

In each of the respective targets in Figure 6.3, the inset picture shows fully covered view of target's after covering them with the packaging cardboard, in which, the underneath target's configuration is completely unknown. However, the enlarged uncovered respective targets in the Figure 6.3 show different considered crack/non-crack tile configurations, like, *f1*, *hc3*, *vc3*, *dc5*, *rc7*.

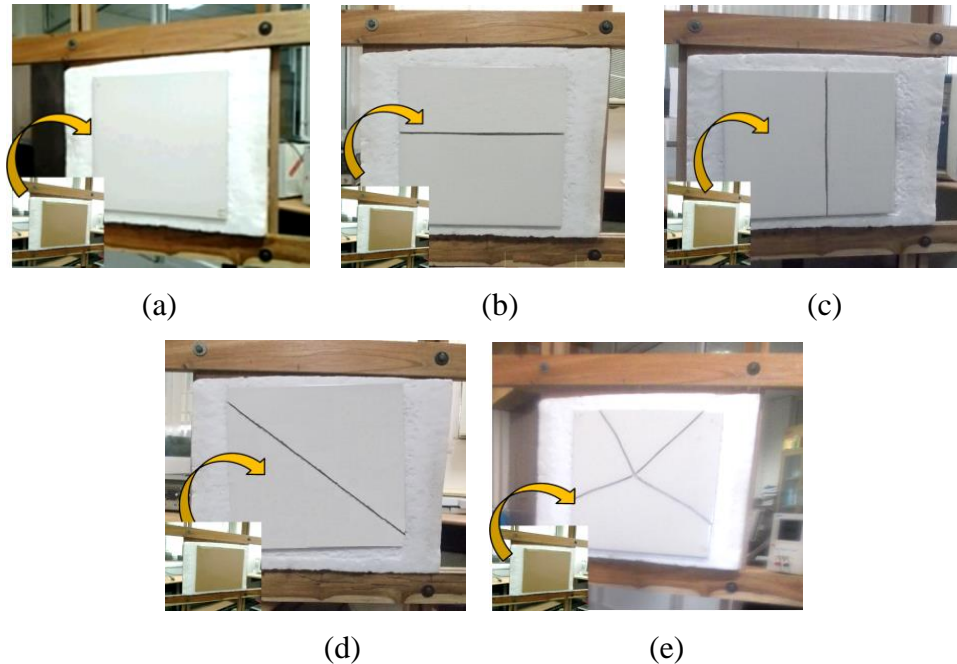


Figure 6.3. Actual photographs of some test targets used for concealed crack detection of ceramic tiles: Final complete covered view of any target is shown in inset (lower left corner), the undercover ceramic tile target's configuration (crack/non-crack) is zoomed in: (a) full non-cracked (*f1*), (b) horizontally cracked (*hc3*), (c) vertically cracked (*vc3*), (d) diagonally cracked (*dc5*), (e) randomly cracked (*rc7*).

6.3.2. Signal Pre-Processing and C-Scan Image Formation

One-port complex scattering coefficients (S_{11}) reflected from the stand-off concealed targets were recorded using PNA-computer interface assembly in real time. The acquired data then undergoes different signal pre-processing steps as discussed earlier in section 4.4.1 in order to retrieve useful target's information [78, 272]. Once pre-processing is carried out, C-scan image of the packaged ceramic tile at the target's downrange location corresponding to reflection peak in the range profile is retrieved as discussed in section 1.3.2.2. As per the total number of vertical and lateral scanning positions mentioned earlier in section 6.3, the C-scan image will be of size [18x30] for different targets. Figure 6.4 shows C-scan images for different packaged test target tiles with different crack /non-crack configurations, *i.e.*, $hc3, f3, f2, f5, hc3, vc3, dc5, rc7, f1, rc2, vc8$, as per the notation given in Table 6.1 (column 2), such that Figure 6.4(a), (b), (c), (e) are for full non-cracked tiles; Figure 6.4(f), (g) correspond to the Horizontal crack tiles; Figure 6.4(j), (k) correspond to Vertical crack tiles; Figure 6.4(d) represent diagonal crack and Figure 6.4(h), (i) represent random crack tiles.

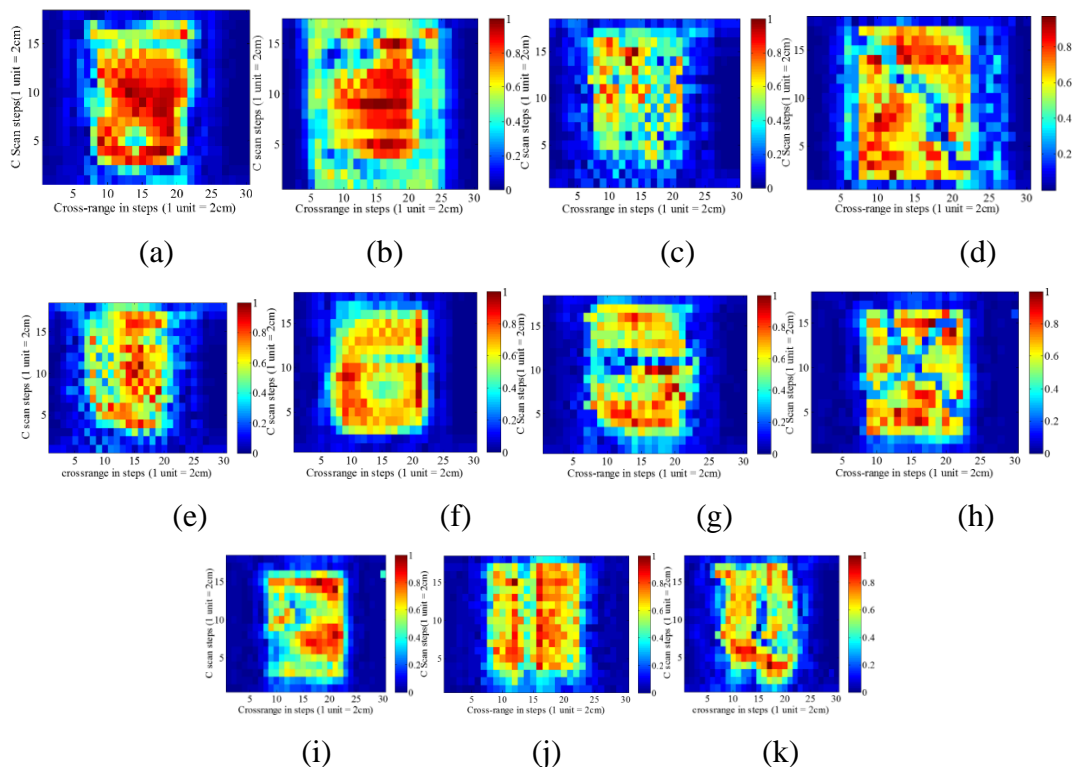


Figure 6.4. 2D C scan image at the target's downrange distance for different tile configurations, (a) $f1$, (b) $f2$, (c) $f5$, (d) $dc5$, (e) $f3$, (f) $hc6$, (g) $hc3$, (h) $rc7$, (i) $rc2$, (j) $vc3$, (k) $vc8$.

6.3.3. Critical Investigations on the Need of an Adaptive and Automatic Crack Detection Model

As seen in Figure 6.4, cracks in few of the packaged cracked tiles are visible, i.e., *dc5*, *hc3*, *rc7*, although for few cracked target tiles it is not clearly visible, i.e., *hc6*, *rc2*, *vc3* (due to low contrast between crack and non-crack pixels). Moreover, for few non-cracked full tiles in Figure 6.4, it shows ambiguity in intensity values, i.e., *f1*, *f2*, *f5* with slight visible crack points. These ambiguities in respective images could lead to any false decision by simply image comparisons. Further, visual inspection of each tile image may be more liable to human error and time consuming. Hence, it is quite challenging to accurately distinguish cracked and non-cracked packaged tile images, because any slight visible crack points even in the non-cracked full tile will cause unnecessary disposal of good tiles and will lead to major fiscal and reputational loss to the company. Therefore, an adaptive, robust and automatic crack detection methodology is essentially needed to be developed for non-invasive, non-destructive crack detection for the packaged ceramic tiles. Furthermore, here our main emphasis is to achieve near minimum (close to zero) false alarm for non-cracked full packaged tiles to avoid any unwanted loss and reduced false alarm for cracked packaged tiles to avoid any quality degradation at dispatch end, which is also of vital importance. Thereby, in this chapter we have proposed two methodologies, i.e., feature-based-ANN model for crack classification and spatial statistics based adaptive model for crack localization.

6.4. Methodology for Feature-Based-ANN Crack Classification

Model (Subtask 1)

As for the reasons mentioned in the preceding section 6.3.3, it is quite obligatory to correctly detect and classify cracked/ non-cracked packaged ceramic tiles non-destructively. Hence, an optimal feature based classification model has been attempted under this subtask 1, which could help to classify cracked and non-cracked tiles separately. Thereby, in order to recognize target's distinct characteristics, suitable descriptors are extracted from target's image, i.e., in present case ceramic tile targets. More importantly, invariance towards scaling, translation and rotation in target's image is desirable for robust and accurate classification under non-uniform practical

environment. Thereby, choice of suitable feature is a determining step for an optimal crack classification model as mentioned in the theoretical background in section 6.2.1.

6.4.1. Feature Selection

Radar line of sight is an important aspect to image any target. Since, our proposed industrial application is aimed towards non-destructive quality scanning of packaged ceramic tiles placed at a stand-off distance. Hence, it may be possible that the packaged tile is not in the correct radar line of sight and is slightly shifted, or having alignment errors. In any of such cases, the radar will treat it in a different way and will have a problem in imaging the targets correctly, henceforth, we have preferred to use features that are least affected by any slight translation, rotation and scaling of the observed object.

Thereby, out of the different available state-of-the-art features conferred in section 6.1, we have used five relatively invariant feature extraction techniques, broadly classified among three different classes, *Statistical based features*, i.e., Principal component analysis (PCA) [279], histogram of oriented gradient (HOG) features [39]; *Spectral and series expansion features*, i.e., Discrete Fourier transform (DFT) descriptors [34], Daubechies wavelet transform (DWT) [35, 40]; and *Contextual features*, i.e., gray level co-occurrence matrix texture features (GLCM) [107]. Statistical based features [155, 295] may be global or regional, and are derived from the statistical distribution of image points globally or window based, for example; PCA is global statistical feature, although HOG is region/ window based feature. Spectral features describe the image intensity variations in various bands of the portion of an electromagnetic spectrum [107, 155], and image signal is decomposed as a linear combination of a series of simpler well defined functions, for example; exponential basis function or wavelet basis function. Coefficients of this series expansion provide a more compact encoding for feature extraction. Additionally, these features are invariant to global deformations, like, translation and rotations. Another third category feature considered is the contextual features [83, 309] based on contextual information in images, i.e., it focuses on the relationship of the nearby pixels of image while feature extraction. The context based features deals with co-occurrence relationship among the images or within the image. For example: Gray level co-occurrence matrix based texture features are the contextual features that depends on positional and angular inter-relationships among the neighboring pixels [107].

These techniques have been commonly used in computer vision based applications, however, applicability of them is less reconnoitered for radar imaging. A brief description of the considered feature extraction techniques is as follows:

6.4.1.1. Discrete Fourier Descriptors (DFT)

Discrete Fourier descriptors (DFT) are based on the well-developed theory of Fourier transformation which has found vast applications, viz, speech recognition, human action classification and image compression [49, 229]. The Fourier transform maps a time domain signal to frequency domain using complex exponential basis functions. Here, for image feature extraction, their 2D discrete Fourier transform (DFT) were evaluated, as given by [246]:

$$F(u, v) = \frac{1}{NM} \sum_{x=0}^{N-1} \sum_{y=0}^{M-1} f(m, n) e^{-i2\pi(\frac{xu}{N} + \frac{yv}{M})} \quad (6.1)$$

where, $f(m, n)$ represents the C-scan image ($M \times N = 18 \times 30$) and is a function of two discrete spatial variables m and n . The variables u and v are frequency variables. The information contained in the Fourier transform can be represented in terms of the magnitude and phase spectra given by,

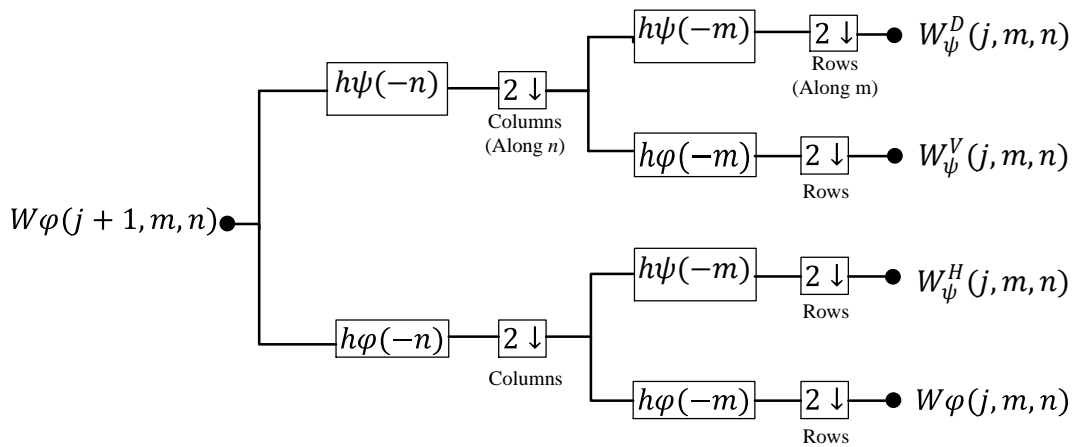
$$|F(u, v)| = [Re^2(F(u, v)) + Im^2(F(u, v))]^{1/2}$$

$$\theta(u, v) = \tan^{-1}[Im(F(u, v))/Re(F(u, v))] \quad (6.2)$$

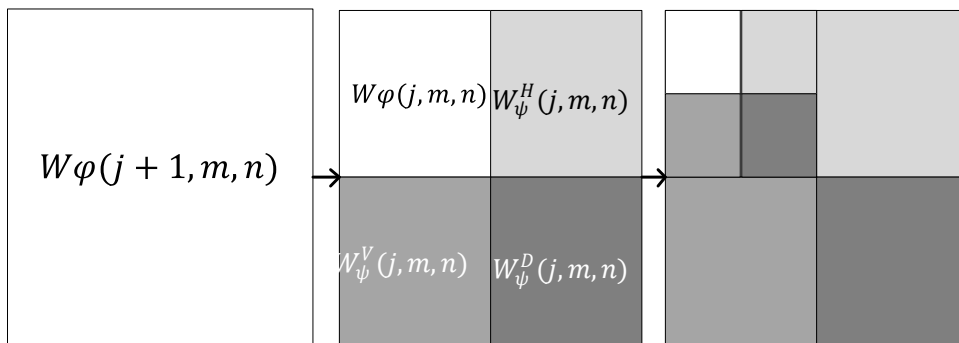
Since, the obtained magnitude and phase spectra are two-dimensional in nature, hence first converted into 1D feature vector prior to use for feature based classification. This is achieved by concatenating the magnitude and phase spectra of the image to extract final Fourier descriptor ($n=2 \times M \times N$). Since, DFT captures the global characteristics depending upon intensity values of dynamic pixels, hence to realize the scaling invariance, normalization is done prior to feature computation. This feature invariance may be required when the target's criterion is not correct. Finally, in order to make the image's Fourier descriptor compact and to avoid redundancy, we iteratively selected first $k < n$ coefficients from magnitude and phase descriptors without losing target's relevant information, for example, in case of our target's image, we chose only 60% of the total fourier descriptors. A detailed description of this is given in section 6.4.2.3 [229].

6.4.1.2. Discrete Wavelet Transform (DWT)

Discrete wavelet transform (DWT) is another important imaging technique having benefits of multi-resolution, compression and de-noising, finding applications in large quantities of information storage and faster transmission [20, 202]. DWT captures both the spatial and frequency information of a signal in contrast to discrete Fourier transform which gives only frequency data of any signal. DWT analyzes the image by decomposing it into sub-bands via low-pass filtering (coarse approximation coefficient) and *via* high-pass filtering (detail information coefficients) as shown in Figure 6.5. Figure 6.5(a) shows the flow diagram for 2D DWT decomposition for any image [202].



(a)



(b)

Figure 6.5. Discrete wavelet transform of image matrix using single level Daubechies decomposition (db2): (a) 2D wavelet transform computation flowchart, (b) Four sub-band image decomposition coefficients: approximation, vertical, horizontal, diagonal [289].

The image decomposition is performed iteratively on low-pass approximation coefficients at each level, until the necessary compression is reached. The discrete wavelet transform of any image function $f(x,y)$ of size $M \times N$ is [57]:

$$W_{\phi}(j_0, m, n) = \frac{1}{\sqrt{MN}} \sum_{x=0}^{M-1} \sum_{y=0}^{N-1} f(x, y) \phi_{j_0, m, n}(x, y)$$

$$W_{\Psi}^i(j_0, m, n) = \frac{1}{\sqrt{MN}} \sum_{x=0}^{M-1} \sum_{y=0}^{N-1} f(x, y) \Psi_{j, m, n}^i(x, y), \quad i = \{H, V, D\} \quad (6.3)$$

$W_{\phi}(j_0, m, n)$ defines an approximation coefficients of $f(x, y)$ at scale j_0 . The $W_{\psi}^i(j, m, n)$ coefficients provide horizontal, vertical, and diagonal details for scale j . Here, scaling function $\phi_{j, m, n}$ and directional sensitive wavelet functions $\psi_{j, m, n}^i$ is given by,

$$\phi_{j, m, n}(x, y) = 2^{j/2} \phi(2^j x - m, 2^j y - n)$$

$$\Psi_{j, m, n}^i(x, y) = 2^{j/2} \Psi^i(2^j x - m, 2^j y - n), \quad i = \{H, V, D\} \quad (6.4)$$

For DWT based image feature extraction, we have considered Daubechies complex wavelet (db2) which are discrete, asymmetric, orthogonal wavelets having the advantages of shift invariance and better directional selectivity as compared to real-valued wavelet transforms, which is beneficial in case of target's misalignment. Using the one level db2 wavelet transform, the respective test target's images [18, 30] were decomposed into four coefficient vectors: W_{app} , W_H , W_D , W_V as shown in Figure 6.5(b). For example: In case of our target's image of size [18, 30], the one level db2 wavelet decomposition will generate four (high and low) coefficients matrices, each of size = [9, 15]. A detailed description of this is given in section 6.4.2.3.

6.4.1.3. Principal Component Analysis (PCA)

Principal component analysis is a method of renovating a number of correlated variables into a smaller number of uncorrelated, independent variables and finds variety of applications in feature selection [286], feature extraction [100, 268], image visualization, classification [77, 298] and noise rejection. PCA can be used for image recognition/ classification by converting the pixels of an image into a number of eigen vector features, which can later on be used to compare

the similarity between two image classes. PCA decomposes any signal/ image into a set of orthogonal basis vectors or eigenvectors, in contrast to Fourier descriptor's orthogonal sinusoids of varying frequencies [176]. First, the image matrix X ($M \times N$) is normalized to zero mean, which centers and scales the data. This makes the extracted PCA feature vector invariant towards translation errors, which may be needed, in case the targets are not correctly aligned. Then, find eigenvectors and eigenvalues of image co-variance matrix; order the eigenvectors in their corresponding decreasing eigenvalues, which gives principal components in order of their significance. The main advantage of PCA is that one can hold only those eigenvectors having largest eigenvalues (*i.e.* principal components) so as to compress feature vector size without loss of any image information.

$$feature\ vector = [eig_1, eig_2, eig_3 \dots \dots eig_k] \quad (6.5)$$

In case of our target's image of size [18, 30], a total 30 principal components (PCs) were generated, out of which only 33%, *i.e.*, 10 PCs were chosen because of their major contribution to the eigen values. A detailed description of this is given in section 6.4.2.3.

6.4.1.4. Texture Features

The textural properties of an image appear to carry useful information for discrimination purposes [327], hence, it is inevitable to use it for non-invasive crack classification of packaged ceramic tiles. Here, textural features used are based on the contextual information of an image [80], which is contained in the overall or "average" spatial relationship which the gray tones in the image hold with one another as described in the starting of section 6.4.1. This property of contextual texture feature makes it invariant, which may be advantageous, in case target is not in correct line of sight of the radar. Context information, based on the interaction among the pixels can help to successfully disambiguate concealed target's characteristics for crack/no-crack classification. Texture features considered here, are the first order and second order gray tone statistical measures and are briefly discussed as:

➤ **Second Order Spatial Statistics (Gray Level Co-Occurrence Matrix GLCM)**

The gray tone spatial dependence approach characterizes texture by the co-occurrence of its gray tones. More specifically, the texture information is adequately specified by a set of gray-tone spatial-dependence matrices which are computed for various angular relationships and distances between neighboring resolution cell pairs on the image, as shown in Figure 6.6 for the

central image pixel '*'. The second order textural features are derived from these nearest neighbor gray tone spatial dependence matrices [107].

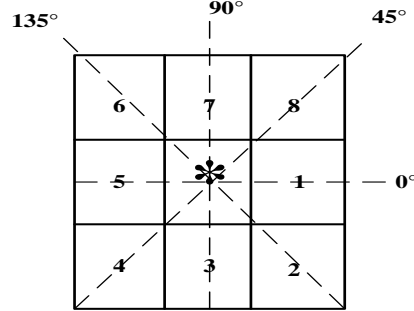


Figure 6.6. Demonstration of nearest neighbour cells orientation with respect to any central resolution cell entry. Cells 1 & 5 are 0° nearest neighbours and cells 2 & 6 are 135° nearest neighbours to resolution cell (*) and so on [107].

The power of the co-occurrence approach is that it characterizes the spatial interrelationships of the gray tones in a textural pattern and can do so in a way that is invariant under monotonic gray tone transformations. Its weakness is that it does not capture the shape aspects. Although these features contain information about the textural characteristics of the image, it is hard to identify which specific textural characteristic is represented by each of these features. The different GLCM features can be defined as [107]:

N_g → Number of distinct gray levels in the quantized image.

$p(i, j) = P(i, j) / R$ → (i, j) th entry in a normalized gray-tone spatial-dependence matrix.

$p_x(i) = \sum_{j=1}^{N_g} P(i, j)$ → i th entry in the marginal-probability matrix obtained by summing rows of $p(i, j)$.

$p_y(j) = \sum_{i=1}^{N_g} p(i, j)$ → j th entry in marginal-probability matrix obtained by summing columns of $p(i, j)$.

$p_{x+y}(k) = \sum_{i=1}^{N_g} \sum_{j=1}^{N_g} p(i, j)$ → $i + j = k, k = 2, 3, \dots, 2N_g$

$p_{x-y}(k) = \sum_{i=1}^{N_g} \sum_{j=1}^{N_g} p(i, j)$ → $|i - j| = k, k = 0, 1, \dots, (N_g - 1)$

$$\text{Angular Second-Moment (ASM) / Homogeneity (f}_1\text{): } f_1 = \sum_i \sum_j \{p(i, j)\}^2 \quad (6.6)$$

$$\text{Contrast (f}_2\text{): } f_2 = \sum_{n=0}^{N_g-1} n^2 \left\{ \sum_{i=1}^{N_g} \sum_{j=1}^{N_g} p(i, j) \right\} \quad (6.7)$$

$$\text{Correlation Feature (f}_3\text{): } f_3 = \frac{\sum_i \sum_j (ij) p(i, j) - \mu_x \mu_y}{\sigma_x \sigma_y} \quad (6.8)$$

$$\text{Entropy (f}_4\text{): } f_4 = - \sum_i \sum_j p(i, j) \log(p(i, j)) \quad (6.9)$$

$$\text{Sum entropy (f}_5\text{): } f_5 = - \sum_{i=2}^{2N_g} p_{x+y}(i) \log\{p_{x+y}(i)\} \quad (6.10)$$

$$\text{Sum average (f}_6\text{): } f_6 = \sum_{i=2}^{2N_g} i p_{x+y}(i) \quad (6.11)$$

$$\text{Sum variance (f}_7\text{): } f_7 = \sum_{i=2}^{2N_g} (i - f_6)^2 p_{x+y}(i) \quad (6.12)$$

$$\text{Inverse Difference Moment (f}_8\text{): } f_8 = \sum_i \sum_j \frac{1}{1 + (i - j)^2} p(i, j) \quad (6.13)$$

$$\text{Difference Entropy (f}_9\text{): } f_9 = \sum_{i=0}^{N_g-1} p_{x-y}(i) \log\{p_{x-y}(i)\} \quad (6.14)$$

$$\text{Information Measure Correlation (f}_{10} \text{ \& } f_{11}\text{): } f_{10} = \frac{HXY - HXY1}{\max\{HX, HY\}} \quad (6.15)$$

$$f_{11} = \left(1 - \exp\left[-2(HXY2 - HXY)\right]\right)^{1/2} \quad (6.16)$$

$$HXY = - \sum_i \sum_j p(i, j) \log(p(i, j))$$

$$\text{where, } HX = - \sum_i p_x(i) \log(p_x(i)) \quad HY = - \sum_j p_y(j) \log(p_y(j))$$

$$HXY1 = -\sum_i \sum_j p(i, j) \log(p_x(i) p_y(j)) \quad HXY2 = -\sum_i \sum_j p_x(i) p_y(j) \log(p_x(i) p_y(j))$$

➤ **First order Statistical Parameters**

Apart from second order statistical GLCM features, the first order image statistical parameters *viz.*, mean, standard deviation, variance and lacunarity etc. are also used as a valuable image features to characterize the textural properties of any target. Thereby, in conjunction to second order statistical measures, first order features were also investigated, in order to develop a better classification model.

Mean (μ): Mean computes average intensity of the image. It helps in discriminating varying textured areas according to their backscattering coefficient, given by [98]

$$\mu = \frac{\sum_{i,j} x_{ij}}{n} \quad \mu = \sum_{i,j} x_{ij} / n \quad (6.17)$$

where, x_{ij} is the intensity of pixel at location (i, j) , n is the number of pixels over which mean is computed.

Variance: The best option to capture boundaries and edges is by computing variance. Value of variance corresponds to the level of heterogeneity. Variance may help in locating boundary regions of smooth textured areas and classifying various textured areas on the basis of their heterogeneity [98] and is given by

$$\sigma^2 = \frac{\sum_{i,j} (x_{ij} - \mu)^2}{(n - 1)} \quad (6.18)$$

where x_{ij} is the intensity of pixel at location (i, j) , n is the number of pixels over which variance σ^2 is computed.

Standard Deviation: It is a measure that is used to quantify the amount of variation or dispersion of a set of data values. A high value of standard deviation indicates that the data points are spread out over a wider range of values. A useful property of the standard deviation is that, unlike the variance, it is expressed in the same units as the data. The standard deviation of experimental data reports the effects that fall much farther away from what would have been expected and is considered statistically significant. Variation in the measurement is in this way distinguished from causal variation [98].

$$\text{Std. dev. } (\delta) = \sqrt{\sigma^2} = \sqrt{\frac{\sum_{i,j} (x_{ij} - \mu)^2}{(n-1)}} \quad (6.19)$$

Lacunarity: It is a multi-scaled method for describing patterns of spatial dispersion. Lacunarity reflects the spatial distribution of gap sizes in texture images. This measure is immensely helpful in the image classification that contain rich textures. Lacunarity is dependent on the mean intensity as well as the variation of pixel values from the mean in the image. Therefore, lacunarity can be used for discriminating both smooth and coarse textures and is defined as [44]

$$\Lambda = \left(\frac{\delta}{\mu}\right)^2 + 1 \quad (6.20)$$

where μ is the mean and σ is the standard deviation.

6.4.1.5. Histogram of Oriented Gradient (HOG)

HOG descriptors provide significant image feature information that may be used for different radar imaging applications, as recently been explored for practical GPR applications and traffic monitoring [294, 323]. In order to recognize the target's distinct characteristics, the suitable descriptors were extracted from the region of interest (ROI) of the image, i.e., in our case test tiles. Features from one type of tile are then compared with other target tiles for classification. Practically, HOG feature extraction is performed by dividing the whole image detection window into small spatial regions, called 'cells' comprising, n pixels x n pixels. The key processing steps for efficient HOG feature vector generation are:

➤ Gradient Computation

HOG features are based on gradient angle and magnitude distributions, and in any visual image data they are robust due to the gradient's natural invariance to slight changes in ambient lighting and color variations, which may be required when the target's criterion is not correct. HOG feature performance is highly dependent on the way by which gradient of the image is computed. For gradient computation, each image pixel is convolved using a 1 D centered, point derivative mask $[-1, 0, 1]$, in contrast to other higher order derivatives (2D, cubic, diagonal, sobel, etc.), which, could lead to large size masks resulting in coarsening of image and loss of significant feature information. Thus, gradient magnitude (G) and gradient angle (θ) are

computed for each pixel in the image detection window [55, 295]. Let g_x and g_y represent the gradient images obtained after convolution of initial image I with h_x and h_y , respectively [295]:

$$g_x = I * h_x; \quad h_x = [-1, 0, 1], \quad (6.21a)$$

$$g_y = I * h_y; \quad h_y = [-1, 0, 1]^T, \quad (6.21b)$$

Hence, Gradient magnitude: $G(i, j) = \sqrt{g_x^2(i, j) + g_y^2(i, j)}$ (6.22a)

Gradient angle: $\theta(i, j) = \tan^{-1} \left(\frac{g_y(i, j)}{g_x(i, j)} \right)$ (6.22b)

Since, individual $G(i, j)$ and $\theta(i, j)$ are highly variable and subject to significant variations across nearby (i, j) locations, even for very similar images, therefore some aggregate statistics of the spatial distribution of the gradient angles and magnitudes over small regions of the images will provide quite robust descriptors of those regions. Thereby, gradient based histogram has been computed for a combination of neighboring pixels called cells.

➤ **Gradient Oriented Histogram**

Each pixel's gradient magnitude and angle contribute to the oriented histogram generation of each cell. Histogram bins are evenly distributed over 0° to 180° for unsigned gradient (or 0° to 360° for signed gradient). Here, each pixel's weighted vote is determined by its gradient magnitude at the corresponding histogram orientation bin. Further, pixel votes are aggregated in the spatial neighborhood, referred to as cells. Cell is a combination of number of pixels and can be of rectangular or radial nature [55].

➤ **Block Normalization**

Further, there are large local variations in the gradient strength through neighborhood cells due to varying illumination and foreground-background contrast. Hence, in order to achieve invariant characteristic feature, a local contrast normalization is essentially sought. This is achieved by grouping cells into larger spatial regions, "blocks" and accumulating local histogram "energy", which is used for normalizing all the cells of that block. Thereby, each of the block is contrast normalized, separately. An overlapping of blocks is also done so that each cell response

contributes to number of different block normalizations. This seems redundant but it adds significant improvement to the performance. The final descriptor of any image detection window is thus formed, as a feature vector comprising normalized cell responses contributed from different overlapping blocks. In contrast to center-surround global normalization, local contrast normalization is an essential component that histogram of oriented gradient (HOG) feature extraction technique owes leading to major performance improvement. Figure 6.7 shows an illustration of HOG feature generation criterion for considered target's image [18, 30]. Here, ROI, *i.e.*, extracted tile image matrix = [12 pixels, 12 pixels], which is subdivided into 4 cells x 4 cells with each cell is a square matrix of [3 pixels, 3 pixels]. The HOG features are then calculated for each of these cells. Additionally, to add robustness to the HOG features block level local normalization has been performed. A detailed description of this is given in section 6.4.2.3.

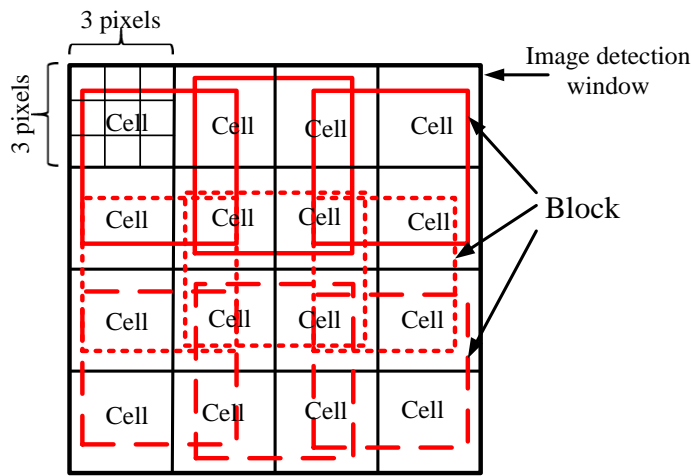


Figure 6.7. Diagram illustrating division of cell and overlapping of blocks in the extracted image detection window for histogram-of-oriented-gradient (HOG) feature calculation for the tile image of size [12 pixels x 12 pixels], cell size = [3 pixels x 3 pixels], block size = [2 cells x 2 cells].

6.4.2. Implementation of Feature-Based-ANN Model for Crack Classification

Flow chart in Figure 6.8 shows the algorithm used to develop optimal feature-based-ANN classifier model. Crack and non-crack packaged ceramic tile classification through neural network requires feature descriptors of the target's image as a precursor. Output of the flowchart will be the optimum feature-based-NN crack/non-crack tile classifier. Steps for implementing feature-based-ANN classification model are:

- First, for all of the 30 test targets (as given in Table 6.1 column 2), feature vectors using the five considered feature extraction techniques, *i.e.*, DFT, WT, PCA, Texture and HOG were calculated as per method discussed in section 6.4.1.
- Taking one feature vector at a time for all the 30 test targets an ANN input matrix and the corresponding output matrix were formed. Thereby, one feature-based-ANN classification model has been generated.
- Similarly, for rest of the feature vectors the respective feature-based-ANN models were developed.
- Thus, for each of the five feature vectors, we have the five respective feature-based-ANN models for crack classification.
- Now, in order to find the optimal feature-based-ANN model, their performances have been compared using similar independent target tiles, by observing their respective crack/non-crack tile classification accuracy.

A detail description of formation and implementation for each of the feature-based-ANN model are given below:

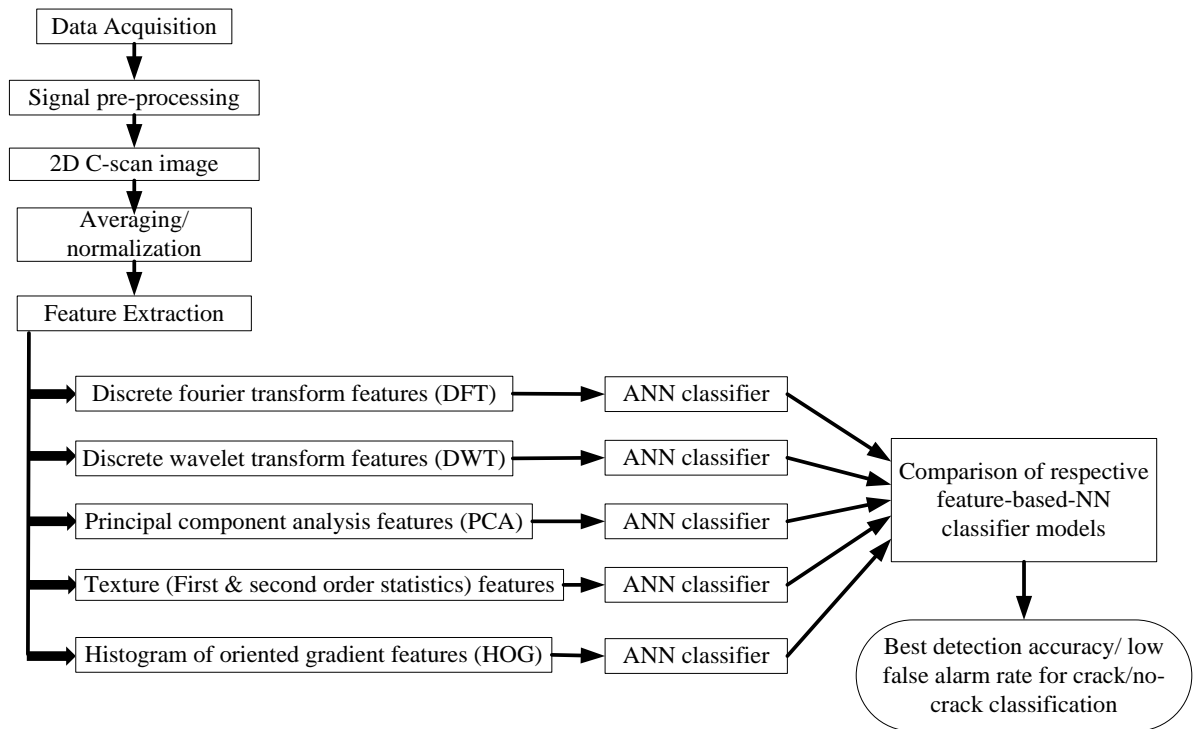


Figure 6.8. Flow Chart for the proposed feature-based-ANN classifier model for non-invasive crack tile classification.

6.4.2.1. Configuration of the Feature-Based-ANN Model

Backpropagation feed-forward neural network (NN) classifier model has been used due to its simpler and speeded implementation. Figure 6.9 shows the configuration of one of the feature-based-neural network model developed for undercover ceramic tile crack classification, which consists of:

- **Input Layer** Input matrix for training the respective neural network models is of size:

Input matrix = [row x column] = [feature vector length x 30 test target samples].

Here, for the respective ANN model's input matrix, the number of rows will depend upon the respective feature vector length and there are 30 number of columns corresponding to the 30 test samples with different cracked/ non-cracked packaged tile configurations as given in Table 6.1 column 2.

- **Hidden Layer** It consists of 50 number of neurons for training the neural network model.
- **Output Layer** The output matrix for training will be of size [2 x 30]. Here, the two rows correspond to the two output classes, *i.e.*, class 1: Full tile without any crack and class 2: Cracked tile. The number of columns are 30 with each column corresponding to the output of the respective input test targets in the input matrix. The output vector corresponding to any input target is thus defined as [1,0] for full tile and [0,1] for cracked tile.

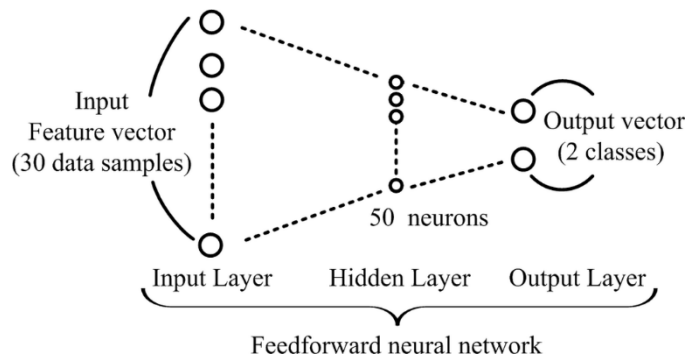


Figure 6.9. Configuration of neural network for target's classification. It consists of input layer (feature vector length x 30 I/p samples), 50 hidden layer neurons, and 2 output layer.

6.4.2.2. Training of the ANN Model

For training the NN towards different possible crack configurations that could occur in any packaged ceramic tile, we have used comprehensively a total of 30 test packaged ceramic

tile targets consisting of full non-cracked tile, horizontally cracked tile, vertically cracked tile, diagonally cracked tile and randomly cracked tile, with each configuration having 6 different data sets as given in Table 6.1 (column 2).

The developed neural network model is trained using '*trainscg*' training function and '*sigmoid*' transfer functions in both the hidden layer and output layer [6]. Output of the ANN is the sigmoid function, which generates output between 0 and 1, required for pattern classification. Learning of neural network is through minimizing the mean squared error criterion between predicted and expected output. For training of the respective feature-based-NN classifier models, the input data of 30 targets is randomly divided into three parts, *viz.*, training, validation and test data samples, so as neural network could learn the random variations of crack and non-crack features in different types of target's configurations. Thereby, we have randomly divided the 30 input data set into training, validation and testing samples in the ratio of 70% (20 samples), 15% (5 samples) and 15% (5 samples), respectively. This ANN configuration has been used for all feature extraction techniques in order to have uniformity while comparing each one's performance. Feature based ANN model once trained, should be capable of any independent accurate classification towards concealed cracked or non-cracked ceramic tiles with minimum false alarm.

6.4.2.3. Critical Investigations of Feature Extraction Techniques towards Accurate Crack Classification Using ANN Model

➤ DFT-NN Classifier Implementation

Fourier descriptors were extracted from the target's image ($M \times N = 18 \times 30$), using 2D discrete Fourier transform in terms of magnitude and phase feature vectors as given in equation (6.2). To make a complete feature vector, both magnitude and phase Fourier features were concatenated giving size $n = [1080, 1]$. However, only $k = 0.6n = 648$, Fourier descriptors were considered, giving feature vector of size $= [648, 1]$ for any particular target's image. The reduced feature vector size was iteratively selected so as to reduce I/P matrix size, complexity of ANN model and redundancy in data without losing any significant target's information. The extracted Fourier descriptors for 30 test targets were then formed as the input matrix $= [648, 30]$ to DFT-NN classifier. While training the DFT-NN model, 15% of total 30 targets (*i.e.*, five targets) were randomly selected as the test targets, which includes: *hc3*, *dc5*, *f3*, *f5*, *vc4* (notation as per Table 6.1). The trained DFT-NN model showed 60% ($=3/5$) classification accuracy, since two test

targets: $f3$, $f5$ were incorrectly classified as cracked tiles. The detailed classification output is shown in Table 6.2 below:

Table 6.2. DFT-NN classifier model result using test targets

S. No.	Test target's types- id's	ANN classifier output	Remark
1	Horizontal crack -hc3	Cracked tile	Correct
2	Diagonal crack-dc5	Cracked tile	Correct
3	Full tile-f3	Cracked tile	<i>Not-correct</i>
4	Full tile -f5	Full tile	<i>Not-correct</i>
5	Vert. crack-vc4	Cracked tile	Correct
Fourier descriptor classification accuracy			60%

➤ Wavelet Transform (WT) Features

2D discrete daubechies orthogonal wavelet (db2) transform with one level decomposition on the target's data matrix [18, 30] is performed. The four sub-band coefficients: approximate, horizontal, vertical, and diagonal each having matrix size = [9, 15] were extracted for 30 different test targets as per equation (6.3) and (6.4). Thus, the WT feature vector were formed by concatenating the high and low frequency components of the image giving feature vector length [540,1]. The extracted db2 wavelet descriptors for 30 test targets were then fed as input matrix of size = [540, 30] to the WT-NN classifier model. While training the WT-NN model, 15% of total 30 targets (i.e., five targets) were randomly selected as the test targets, which include: $rc6$, $vc7$, $f4$, $dc2$, $f5$. The trained WT-NN showed 60% (=3/5) classification accuracy, since two targets: $dc2$, $f5$ were incorrectly classified. The detailed classification output is shown in Table 6.3 below:

Table 6.3. WT-NN classifier model result using test targets

S. No.	Test target's types- id's	ANN classifier output	Remark
1	Random crack - rc6	Cracked tile	Correct
2	Vertical crack -vc7	Cracked tile	Correct
3	Full tile -f4	Full tile	Correct
4	Diagonal crack - dc2	Full tile	<i>Not -Correct</i>
5	Full tile - f5	Cracked tile	<i>Not-Correct</i>
Wavelet descriptor classification accuracy			60%

➤ **Principal Component Analysis (PCA) Feature**

Based on the PCA analysis as discussed in section 6.4.1.3, for the target's 2D data matrix [18, 30], the principal components = [30, 30] were found with columns indicating uncorrelated 30 principal components (PCs) as derived from the eigen matrix [268, 279]. However, we have extracted only first ten principal components = [30, 10], without losing the target's unique characteristic, since, it contributes major portion of eigen values ~ 96%. Thus, the formed PCA feature vector was of length = [300,1], and the input matrix for all 30 target samples was of size = [300, 30]. While training the PCA-NN model, 15% of total 30 targets (*i.e.*, five targets) were randomly selected as the test targets, which includes: *rc6*, *dc6*, *f3*, *dc7*, *hc8*. The trained PCA-NN model classification accuracy was 80% (=4/5), since one target: *hc8* was incorrectly classified. The detailed classification output is shown in Table 6.4 below:

Table 6.4. PCA-NN classifier model result using test targets

S. No.	Test target's types- id's	ANN classifier output	Remark
1	Random crack-rc6	Cracked tile	Correct
2	Diagonal crack - dc6	Cracked tile	Correct
3	Full tile - f3	Full tile	Correct
4	Diagonal crack -dc7	Cracked tile	Correct
5	Horizontal crack - hc8	Full tile	<i>Not-Correct</i>
PCA descriptor classification accuracy			80%

➤ **Texture Features**

Texture features as discussed in section 6.4.1.4, were calculated for the eleven second order spatial statistical features using equation (6.6) to equation (6.16), and for the four first order statistical features using equation (6.17) to equation (6.20). Thereby, total 15 texture features were extracted for each of the 30 different test targets, which gives ANN input matrix of size [15 x 30] for Texture-NN classifier model development. While training the Texture-NN model, 15% of total 30 targets (*i.e.*, five targets) were randomly selected as the test targets, which includes: *vc8*, *f1*, *vc7*, *f4*, *vc3*. The Texture-NN model showed classification accuracy of 60% (=3/5) on the test targets, since two targets: *f1*, *f4* were incorrectly classified. The detailed classification output is shown in Table 6.5 below:

Table 6.5. Texture-NN classifier model result using test targets

S. No.	Test target's types-id's	ANN classifier output	Remark
1	Vertical crack-vc9	Cracked tile	Correct
2	Full tile -f1	Cracked tile	<i>Not-correct</i>
3	Vertical crack - vc7	Cracked tile	Correct
4	Full tile - f4	Cracked tile	<i>Not-correct</i>
5	Verticcal crack - vc3	Cracked tile	Correct
Texture descriptor classification accuracy			60%

➤ Histogram of Oriented Gradient (HOG) Feature

For HOG feature extraction, region of interest (ROI) of the target's C-scan image [30x18] was extracted, *i.e.*, in our case ceramic tile image under test is extracted from the background, which forms the target's detection window of size 12 pixels x 12 pixel. After investigating different cell sizes, *viz.*, 2x2, 3x3 and 4x4, it was found that cell size 3 pixels x 3 pixels gives better feature information with reduced feature vector size for our considered target types. Further, block size of 2 cells x 2 cells (*i.e.*, 36 pixels) was taken, with block overlap of one cell (*i.e.*, 9 pixels). This gives the final HOG feature vector of length [324 x1]. The HOG features of different types of target tiles in different crack and non-crack configurations (as per Table 6.1, column 2) were calculated as discussed in section 6.4.1.5, *i.e.*, image cell based gradient magnitude and angle calculation using equation (6.22) and gradient histogram generation followed by the normalization. Figure 6.10 shows the typical HOG feature vector demonstration for a full tile and for a cracked tile.

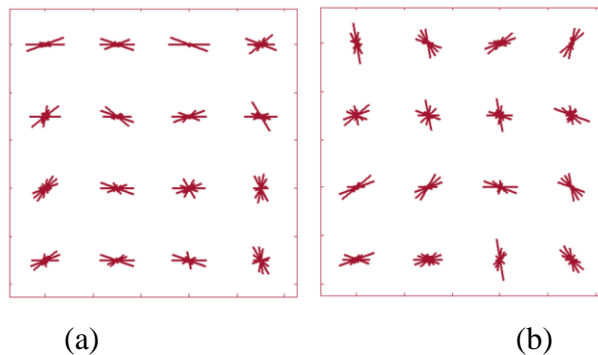


Figure 6.10. HOG feature descriptor representation for different cells of the extracted target's image detection window for: (a) Non-cracked full tile, (b) Cracked tile.

The oriented histogram shows uniform alignment for non-cracked full tiles due to the nearly equal weight contribution from neighborhood cells of blocks, however, for cracked tile it shows varying random orientations due to difference in gradient weight contribution from the cracked cells, while aggregate feature vector calculation.

Thereby, the input matrix was of size = [324, 30] for HOG-NN classifier. While training the HOG-NN model, 15% of total 30 targets (i.e., five targets) were randomly selected as the test targets, which includes: *vc2*, *dc7*, *hc4*, *f4*, *rc3*. The trained HOG-NN classifier model gives 100% (=5/5) classification accuracy, since no tile is incorrectly classified. The detailed classification output is shown in Table 6.6.

Table 6.6. HOG-NN classifier model result using test targets

S. No.	Test target's types- id's	ANN classifier output	Remark
1	Vertical crack- <i>vc2</i>	Faulty tile	Correct
2	Diagonal crack- <i>dc7</i>	Faulty tile	Correct
3	Horizontal crack - <i>hc4</i>	Faulty tile	Correct
4	Full till - <i>f4</i>	Full tile	Correct
5	Random crack- <i>rc3</i>	Faulty tile	Correct
HOG descriptor classification accuracy			100%

6.4.3. Validation

Once the feature-based-neural network classifier model is trained towards different types of possible cracks in the packaged ceramic tiles, it is expected to correctly classify any independent packaged tile targets. Hence, in order to find the optimal feature-based-ANN model for robust and accurate non-invasive crack classification, a comparison of all the respective five features (FT, WT, PCA, texture and HOG) based NN classifiers was carried out as given in Table 6.7, using the fifteen different independent validation targets with different crack/non-crack configurations (as per Table 6.3, column 3).

For all the fifteen considered targets, the five features (FT, WT, PCA, texture and HOG) were extracted, and applied to their respective trained NN models, and their typical classification performances were analyzed and compared. The output of the NN classifier will be in binary vector form as discussed in section 6.4.2.1, i.e., for cracked tile output vector will be [0, 1] and

for non-cracked tile output vector will be [1, 0]. The number of incorrect target classifications for respective feature extraction techniques are; one (*f6*), four (*f6, f8, f11, dc3*), two (*f10, f11*), three (*vc6, vc9, f10*) and four (*f8, f9, f10, f11*), giving corresponding classification accuracies of: 93.33%, 73.33%, 86.67%, 80%, 73.33% for HOG, PCA, WT, DFT, GLCM feature based ANN classifier models, respectively.

On comparing the performance of different feature-based-ANN classifier models, viz, FT-NN, WT-NN, PCA-NN, Texture-NN and HOG-NN, it was found that HOG-NN classifier shows an optimal performance in terms of maximum correct crack classification accuracy, i.e., 93.33%, which may be attributed to its cell based feature extraction in contrast to whole image feature extraction techniques. Further, HOG features employ local normalization and block level redundancy so as to withstand varying and non-uniform illumination.

Table 6.7. Classification accuracy assessment of proposed feature-based-ANN model using independent validation target samples by comparing DFT-NN, DWT-NN, PCA-NN, texture-NN, HOG-NN classifier models

S.No.	Independent validation targets	DFT- NN		DWT- NN		PCA- NN		GLCM- NN		HOG-NN	
		ANN classifier output	Remark	ANN classifier output	Remark	ANN classifier output	Remark	Class 1	Remark	ANN classifier output	Remark
1	<i>Rand crack-rc8</i>	Cracked	Correct	Cracked	Correct	Cracked	Correct	Cracked	Correct	Cracked	Correct
2	<i>Rand crack-rc9</i>	Cracked	Correct	Cracked	Correct	Cracked	Correct	Cracked	Correct	Cracked	Correct
3	<i>Vert. crack-vc5</i>	Cracked	Correct	Cracked	Correct	Cracked	Correct	Cracked	Correct	Cracked	Correct
4	<i>Vert. crack-vc6</i>	Non-cracked	<i>Not-correct</i>	Cracked	Correct	Cracked	Correct	Cracked	Correct	Cracked	Correct
5	<i>Vert. crack-vc9</i>	Non-cracked	<i>Not-correct</i>	Cracked	Correct	Cracked	Correct	Cracked	Correct	Cracked	Correct
6	<i>Vert. crack-vc10</i>	Cracked	Correct	Cracked	Correct	Cracked	Correct	Cracked	Correct	Cracked	Correct
7	<i>Full tile-f6</i>	Non-cracked	Correct	Non-cracked	Correct	Cracked	<i>Not-correct</i>	Cracked	Correct	Non-cracked	<i>Not-correct</i>
8	<i>Full tile-f8</i>	Non-cracked	Correct	Non-cracked	Correct	Cracked	<i>Not-correct</i>	Non-cracked	<i>Not-correct</i>	Cracked	Correct
9	<i>Full tile-f9</i>	Non-cracked	Correct	Non-cracked	Correct	Non-cracked	Correct	Non-cracked	<i>Not-correct</i>	Cracked	Correct
10	<i>Full tile-f10</i>	Cracked	<i>Not-correct</i>	Cracked	<i>Not-correct</i>	Non-cracked	Correct	Non-cracked	<i>Not-correct</i>	Cracked	Correct
11	<i>Full tile-f11</i>	Non-cracked	Correct	Cracked	<i>Not-correct</i>	Cracked	<i>Not-correct</i>	Non-cracked	<i>Not-correct</i>	Cracked	Correct
12	<i>Diag. crack-dc3</i>	Cracked	Correct	Cracked	Correct	Non-cracked	<i>Not-correct</i>	Cracked	Correct	Cracked	Correct
13	<i>Diag. crack-dc4</i>	Cracked	Correct	Cracked	Correct	Cracked	Correct	Cracked	Correct	Cracked	Correct
14	<i>Horz. crack-hc5</i>	Cracked	Correct	Cracked	Correct	Cracked	Correct	Cracked	Correct	Cracked	Correct
15	<i>Horz. crack-hc7</i>	Cracked	Correct	Cracked	Correct	Cracked	Correct	Cracked	Correct	Cracked	Correct
Total accuracy		12/15 = 80%		13/15 = 86.67%		11/15 = 73.33%		11/15 = 73.33%		14/15 = 93.33%	

6.4.4. Concluding Remarks (for subtask 1)

Here, our main focus was to develop such a technique for MMW imaging radar system, which should have the capability to detect cracked/ non-cracked undercover ceramic tiles non-destructively, with minimum false alarms. Now, as per the experimental observations on an extensive number of targets, it was found that HOG-NN classifier outperformance as compared to other techniques where there were more number of false alarms. This indicates that HOG feature has better classification accuracy than others for non-invasive undercover quality testing. However, location of the crack in the concealed target remains completely unknown in this methodology. Thereby, in order to explore the possibility of exact crack location estimation apart from just crack detection, we have designed our next subtask such that, we have attempted to propose a spatial statistics based adaptive crack localization methodology based on image reconstruction.

6.5. Development of an Adaptive Statistical Model for Crack Localization Based on Image Reconstruction (Subtask 2)

So far, in section 6.4, we have investigated feature extraction technique based NN classifier model for classifying packaged ceramic tiles as cracked or non-cracked, which is a quantitative approach. Now, in order to visualize crack locations within the concealed targets, a spatial statistical based adaptive approach has been investigated in this subtask 2. An adaptive pattern search based crack detection/ localization model has been proposed for detection of cracked targets as well as localization of particular crack windows within the targets. Moreover, a generalized optimization model has been formulated to achieve maximum user defined accuracy and minimum false alarm.

6.5.1. Undercover Target's Image Enhancement: Discrete Convolution

Target's C-scan image obtained after signal pre-processing may also include undesirable reflections due to background scattering, multipath propagation and non-uniform illumination etc. (as discussed in section 6.3.3). Hence, for the proposed image reconstruction based spatial statistical model development, firstly, image enhancement has been performed as discussed in

the section 6.2.2, through linear filtering. Here, filtering has been achieved using discrete convolution, because it preserves fine image details while simultaneously enhancing the image quality, and is computed as [129, 215]:

$$h(t) = \sum_{\tau} f(\tau)g(t - \tau) \quad (6.23)$$

where, the function $f(t)$ correspond to the image and $g(t)$ is the filter kernel. Convolution is a neighborhood operation in which each output pixel is the weighted sum of neighboring input pixels. The matrix of weights is called convolution kernel, or filter mask. There is a tradeoff between image sharpness and pixel noise, since, excessive smoothing will reduce the signal-to-noise ratio and could distort the image. Gaussian kernel has been used for optimal image smoothing as compared to direct averaging or box filter kernel [129, 215, 264]. The filter mask at any co-ordinate position (x, y) of the image is determined by gaussian weighing coefficients given by:

$$G_{\sigma}(x, y) = \frac{1}{2\pi\sigma^2} e^{\left(-\frac{x^2+y^2}{2\sigma^2}\right)} \quad (6.24)$$

The value of the filter function at discrete points is controlled by variance σ^2 . Gaussian function essentially removes the influence of points at radial distance greater than 3σ from the center of the template, such that, the template weights drop near to zero at the edges [215]. Figure 6.11 shows test target's filtered images obtained after gaussian kernel. The filtered, enhanced image is further normalized so that the brightness levels are uniformly distributed. When compared with respective raw C-scan images in Figure 6.4, an appreciable improvement in the image quality is observed in Figure 6.11. However, still it is difficult to accurately observe crack and no-crack tiles, because of slight visible crack points even in the non-cracked full tile images, like, Figure 6.11(a), (c) gives an impression of cracked tiles, although it is a non-crack full tile beneath the packaging as shown in Figure 6.3(a). Further, visual inspection of each tile image may be liable to human error and may be time consuming. Therefore, an adaptive, robust and automatic crack detection methodology has been proposed for non-invasive crack detection/localization in the packaged ceramic tiles.

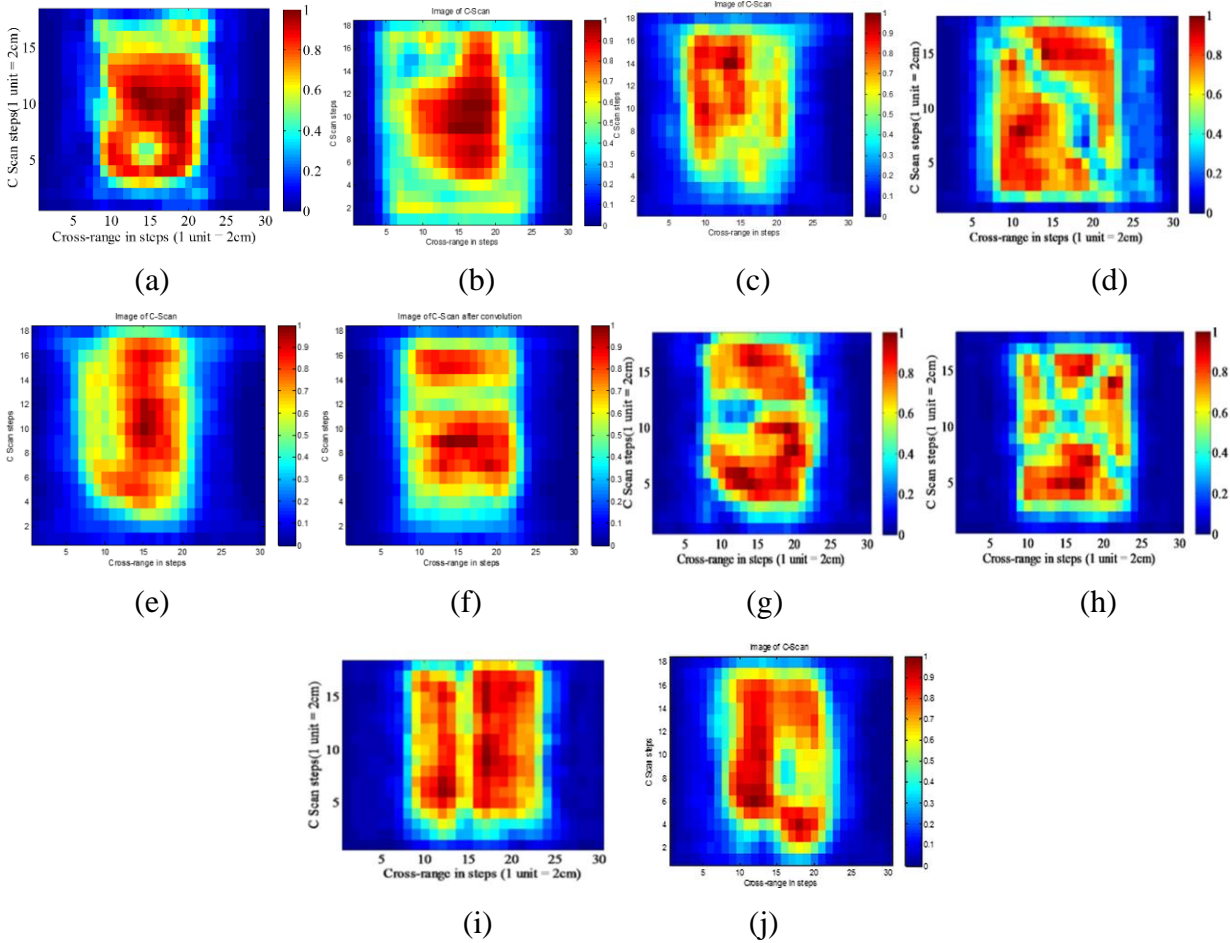


Figure 6.11. Test target's images obtained after enhancement for different tile configurations: (a) f1, (b) f2, (c) f5, (d) dc5, (e) f3, (f) hc6, (g) hc3, (h) rc7, (i) vc3, (j), vc8.

6.5.2. Proposed Statistical Methodology for Crack Localization

Since, our main aim is to avoid any false alarm for non-cracked packaged ceramic tiles because this could lead to unnecessary fiscal loss to the business. Therefore, we have tried to develop an adaptive statistical algorithm so as to detect and identify cracked and non-cracked packaged ceramic tiles non-invasively. Following steps have been performed while developing the pattern based spatial statistical algorithm as discussed in section 6.2.2:

6.5.2.1. Step 1: Image Statistics

For developing a robust model, it is important to have fewer false alarms for packaged cracked tile and no (or very less) false alarm for packaged non-cracked tile. For this purpose, an image spatial statistics based adaptive model has been proposed, since, statistical parameters play a vital role in determining unique image characteristics. Henceforth, four statistical parameters

viz., Maxima, Minima, Median and Standard deviation of the image have been used to design proposed adaptive crack detection model. An adaptive pattern search technique is aimed to be developed, in which location of crack can be detected by scanning the full image matrix of packaged ceramic tile sequentially using a 3x3 window matrix and checking it towards cracked and non-cracked window condition. For this, we have developed a database by comparing original actual test tiles (as given in Table 6.1 column 3) with their corresponding images. In the image of any test ceramic tile, the actual cracked and non-cracked window locations have been marked by comparing each of the matrix windows with the corresponding actual ceramic tile configuration beneath the packaging, which was known to us.

6.5.2.2. Step 2: Window Based Detection

Through exhaustive inspection on number of different packaged ceramic tiles with varying crack configurations, the optimal test condition for detecting crack/ no-crack in any selected window matrix of the given tile image was found as:

$$(Mx - Mn) > [M - S]; \quad \text{cracked window matrix} \quad (6.25a)$$

$$(Mx - Mn) < [M - S]; \quad \text{Non - cracked window matrix} \quad (6.25b)$$

where, $\left. \begin{array}{l} Mx = \text{Maxima}, Mn = \text{minima} \\ M = \text{Median}, S = \text{standard deviation} \end{array} \right\}$ of the selected [3x3] window matrix

In equation (6.25), the right side term $[M - S]$ shows the difference between median and standard deviation and left side term $(Mx - Mn)$ signifies difference between maximum and minimum intensity pixels; for any [3x3] window matrix. The selected window matrix can be cracked or non-cracked depending upon the characteristic of packaged ceramic tile under test and the sequential scanning position.

If there is no crack in the selected [3x3] window, all nine pixels will be of nearly same intensity values. Hence, difference between max. and min. intensity pixels $(Mx - Mn)$ will be very less and therefore, $(Mx - Mn) < [M - S]$ as given in equation (6.25a). This behavior of non-cracked window matrix has been demonstrated by plotting the two statistical terms, $(Mx - Mn)$ and $[M - S]$, for four undercover ceramic tile test targets (*viz.*, *hc3*, *vc3*, *dc5*, *rc7*) with different crack configurations as shown in Figure 6.12(a). From Figure 6.12(a), it is clearly

seen that $(Mx - Mn)$ is less than $[M - S]$ for the non-cracked window matrices of the different considered ceramic tile test targets.

Next, if there lies any crack in the selected $[3 \times 3]$ window, the pixels at the cracked locations will be of low intensity values (near to zero) and pixels at the non-cracked locations will be of high intensity values, therefore, difference between max. and min. intensity values, i.e., $(Mx - Mn)$ will be large and in turn, likely to be greater than $[M - S]$ of that cracked window matrix. In Figure 6.12(b), the behavior of cracked window matrices for packaged ceramic tile test targets (*viz.*, *hc3*, *vc3*, *dc5*, *rc7*) with different crack configurations has been demonstrated. As seen in Figure 6.12(b), the cracked window matrix condition $(Mx - Mn) > [M - S]$ is satisfied for few cracked windows, however, for some cracked windows this condition is not met resulting in $(Mx - Mn) < [M - S]$ even for cracked window matrices, which could lead to misclassification as non-cracked windows.

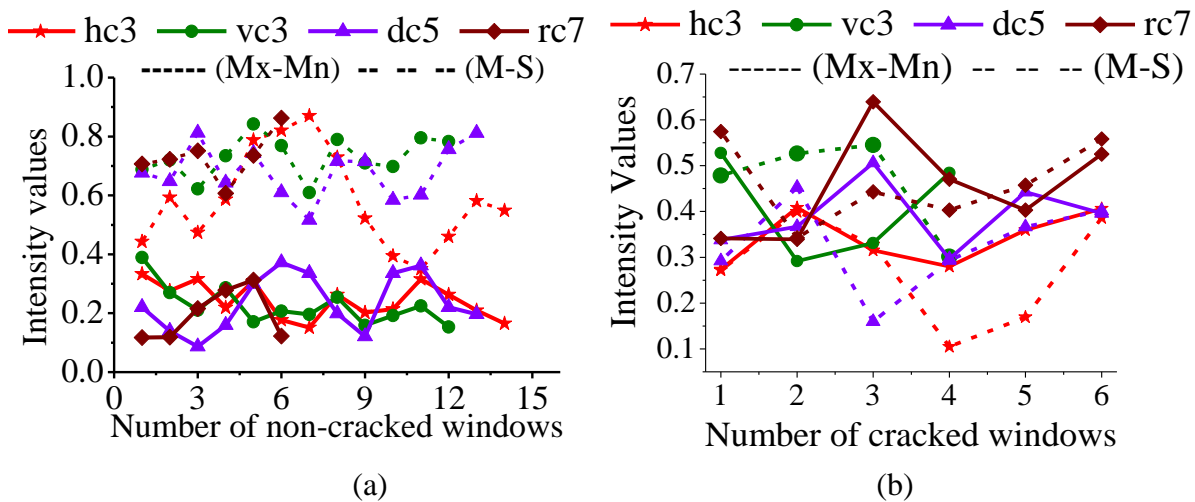


Figure 6.12. Graph showing relative behavior of window matrix based statistical measures; ($[Mx - Mn] = [Maxima - Minima]$ and $[M - S] = [Median - Standard deviation]$) for (a) non-cracked window matrices and (b) cracked window matrices; of different packaged ceramic tile test targets: *hc3*, *vc3*, *dc5*, *rc7*.

The reason for this discrepancy may be attributed to variation in reflection intensity of different target's images, contrast and brightness difference between cracked and non-cracked pixels of the window, etc. Hence, this initial proposed relation can be true for certain cracked matrix windows, but it cannot be a generalized formulation for accurate cracked window

detection in the packaged ceramic tiles. Thereby, there is a need to add some modification / adaptation to make it a valid comprehensive test condition.

6.5.2.3. Step 3: Statistical Analysis and Formulation

In order to resolve the aforementioned problem and to make the test more adaptive and robust towards intensity variations, an unknown term, “ n ” has been included in the spatial statistics based mathematical expression by which the segregation of cracked window from the non-cracked ones can be successfully done. Hence, the cracked / non-cracked window matrix test condition can now be modified as given in equation (6.26). The effect of inclusion of term ' n ' on enhancing detection of cracked windows has been analyzed for different packaged ceramic tile test targets. However, for the sake of representation simplicity it has been illustrated using one of the ceramic tile *i.e.*, test target ' $hc3$ ' in Figure 6.13;

$$(Mx - Mn) > [M - (n - 1)S] \quad \text{cracked window matrix} \quad (6.26a)$$

$$(Mx - Mn) < [M - (n - 1)S] \quad \text{non - cracked window matrix} \quad (6.26b)$$

As shown in Figure 6.13(b), *for the cracked window matrix plot*: on increasing the value of ' n ', the term $[M - (n - 1)S]$ reduces and attains a value less than $(Mx - Mn)$ for all the cracked windows of the packaged ceramic tile ' $hc3$ '. Similar behavior has been obtained for other considered test tiles also. This, now hereby, satisfies the modified proposed test condition given in equation (6.26a) and enables successful crack window identification after a certain value of ' n ' is reached. This value of ' n ' may be different for different ceramic tile targets depending upon their image statistics.

Now, as shown in Figure 6.13(a), *for the non-cracked window matrix plot*: On increasing ' n ', the value of $[M - (n - 1)S]$ for non-cracked windows also reduces and after certain threshold value of ' n_T ' is reached, it would reduce down below the $(Mx - Mn)$ value for some non-cracked window matrices and starts detecting them as a false cracked window locations. So, an optimum value of ' n_T ' is needed to be calculated so as to correctly detect and classify the cracked and non-cracked windows in any ceramic tile image and minimize the possibility of any false alarm.

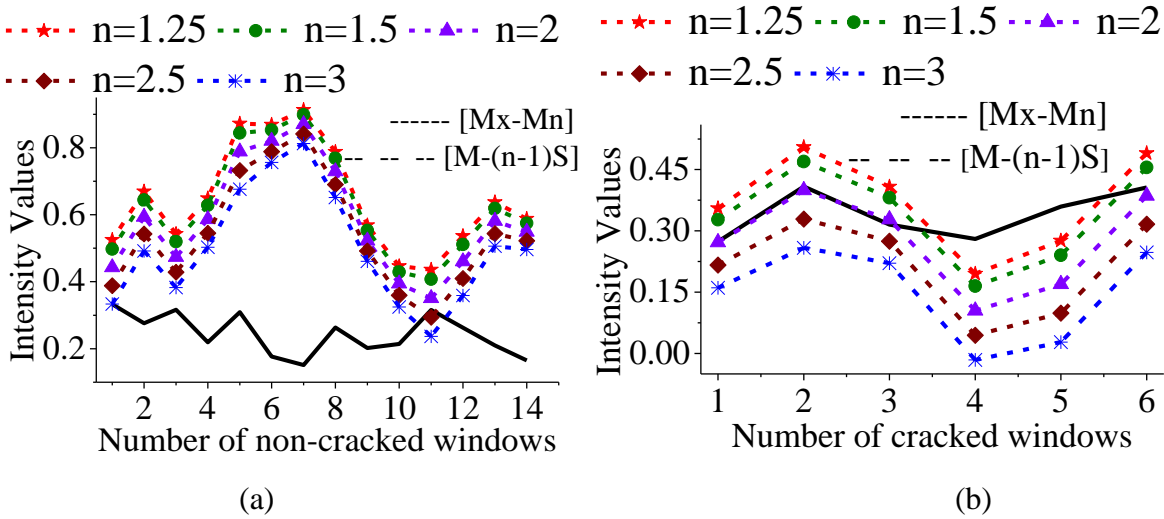


Figure 6.13. Plots showing the effect of varying scaling parameter ' n ' on the behavior of two statistical metrics $[Mx - Mn]$ and $[M - (n - 1)S]$, for ceramic tile test target- *hc3* for; (a) non-cracked windows, and (b) cracked windows of a test target tile.

As the expression $[M - (n - 1)S]$ is used in equation (6.26) for creating the decision boundary for classification of cracked and non-cracked window matrix in any ceramic tile image, likewise, other similar expressions; $[M - nS]$, $[M - (n - 2)S]$, $[M - (n - 3)S]$ can be used equi-probably giving satisfactory results. However, we have selected the expression $[M - (n - 1)S]$. Moreover, $(n - 1)$ or $(n - 2)$ or $(n - 3)$ can also be taken in the formulation, because the decision criterion to segregate the class (cracked / non-cracked) will always be obtained at a certain value of ' n ' for any particular ceramic tile target. For example, if maximum accuracy is obtained at $n = 3.5$, then, maximum accuracy is obtained at $n = 4.5$ by using $(n - 1)$ and at $n = 5.5$ by using $(n - 2)$ in the expressions and so on. Nevertheless, we have considered the term $(n - 1)$ here. Similar, statistical approaches have been used by some other researchers to discriminate the two class types in an image [87, 200].

6.5.2.4. Step 4: Accuracy Assessment and Algorithm:

The proposed statistics based algorithm should behave such that it maximizes the accuracy of crack window detection, while, simultaneously, minimizing any false alarm. Hence, our main goal is that there should not be any false alarm for non-cracked packaged ceramic tiles and for this we need to achieve optimum value of ' n '. In order to achieve the above said performance goal, we firstly computed the overall accuracy (OA) and false alarm (FA), defined as:

$$\text{Overall Accuracy}(OA) = \frac{\text{Correctly detected faulty windows}}{\text{Total no.of faulty windows}} \times 100\% \quad (6.27a)$$

$$\text{False Alarm (FA)} = \frac{\text{Incorrectly detected faulty windows}}{\text{Total no.of windows} - \text{Total no.of faulty windows}} \times 100\% \quad (6.27b)$$

At different values of n for different ceramic tile test targets. Total numbers of cracked windows were determined from the known ceramic tile test target's crack configurations. These performance parameters, *i.e.*, accuracy (OA) and false alarm (FA) were plotted w. r. t. scaling parameter ' n ' as shown in Figure 6.14 for ceramic tile test targets; $hc3$, $vc3$, $dc5$, $rc7$ with varying crack patterns. It is observed that, on increasing n accuracy increases and after a certain critical value of ' n ', accuracy approaches maximum, *i.e.*, 100%. This critical value n_T will be different for different ceramic tile targets ($hc3$, $vc3$, $dc5$, $rc7$), as seen in Figure 6.14(a).

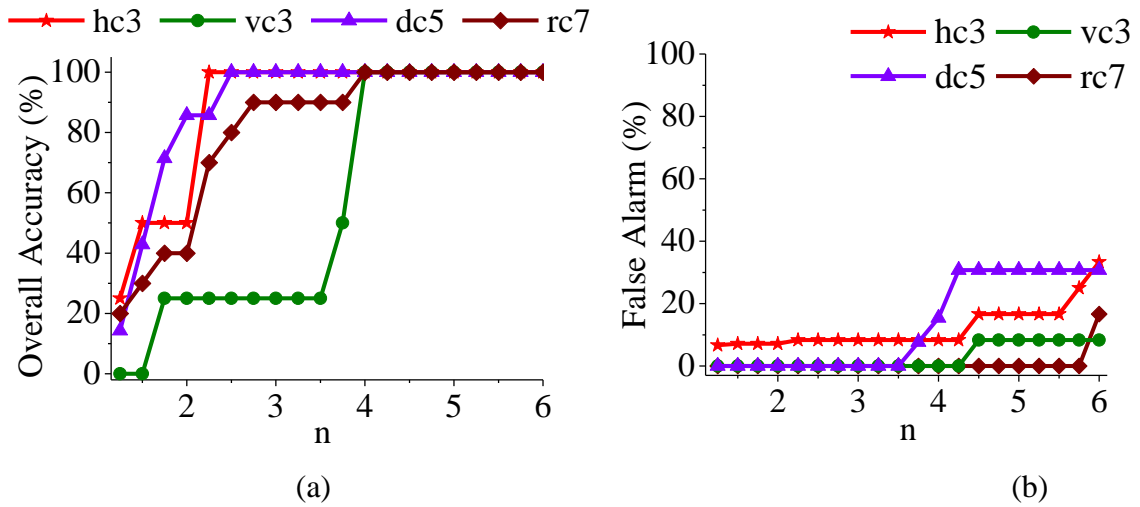


Figure 6.14. Performance plot of the proposed window based statistical algorithm showing (a) Overall Accuracy vs n ; and (b) False alarm vs n , for different ceramic tile targets: $hc3$, $vc3$, $dc5$, $rc7$.

Further, increase in the value of ' n ' also increases the false alarm as shown by the plot in Figure 6.14(b). This trade off in the behavior of overall accuracy and false alarm is needed to be balanced, and hence, there should be an optimum value of ' n ' satisfying maximum accuracy as well as minimum false alarm.

Now, in order to make the proposed algorithm more robust and adaptive in nature, its performance parameters have to be dependent on image spatial statistics. Therefore, the unknown term ' n ' has to be related to the image statistics. Thereby, a variable x is introduced such that:

$$x = M - (n - 1)S \quad (6.28)$$

The direct dependency between overall accuracy and x is hard to relate. However, overall accuracy (OA) and false alarm (FA) in relation to unknown parameter ' n ' may be correlated as shown in Figure 6.16. For each respective values of ' n ', the corresponding values of x can be obtained from equation (6.28). Having known the values of x , accuracy and false alarm can be correlated to the variable x directly. A plot of accuracy (OA) vs x and false alarm (FA) vs x is shown in Figure 6.15 for different ceramic tile test targets; $hc3$, $vc3$, $dc5$, $rc7$.

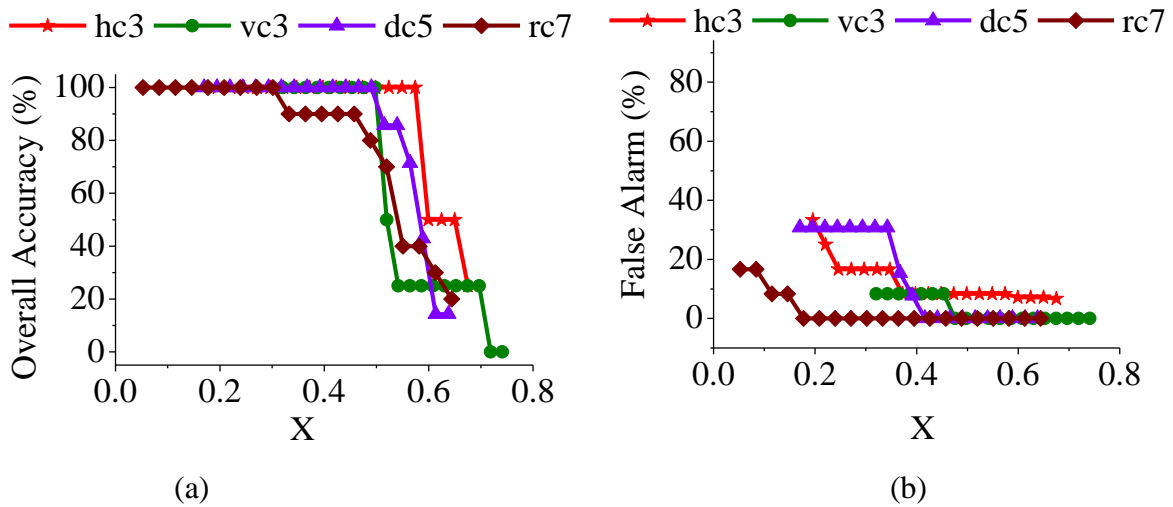


Figure 6.15. Plot of (a) Overall accuracy vs x and, (b) False alarm vs x , for different ceramic tile test targets ($hc3$, $vc3$, $dc5$, $rc7$).

6.5.2.5. Step 6: Formulation for Automatic Crack Detection:

An empirical relationship has been developed for overall accuracy vs x and false alarm vs x using curve fitting approach. Ten randomly selected ceramic tile test targets with different crack configurations *viz.*, $vc1$, $dc5$, $hc2$, $hc3$, $rc4$, $dc1$, $hc4$, $vc3$, $vc8$, $rc7$, were used and following empirical relation was obtained with R^2 (coefficient of determination) values close to 0.9 for both cases:

$$OA(x) = a_1 + b_1 e^{-0.5 \left(\frac{x-c_1}{d_1} \right)^2} \quad (6.29a)$$

$$FA(x) = a_2 + b_2 e^{-0.5 \left(\frac{x-c_2}{d_2} \right)^2} \quad (6.29b)$$

Here, $a_1, b_1, c_1, d_1, a_2, b_2, c_2, d_2$ are the constants. As shown in Table 6.8, R^2 values are close to 0.9 for all the ceramic tile samples for $OA(x)$ and $FA(x)$, hence, the two mathematical expressions are quite acceptable. Further, goodness of fit of the obtained expressions was also tested using Kolmogorov-Smirnov (KS) test with 5% significance level. The obtained p values were greater than the significant level (0.05) and the KS value was lower than the critical value (0.294) for all the ceramic tile test samples. This meant that the obtained relationships of $OA(x)$ and $FA(x)$ are highly significant and statistically justified.

Table 6.8. Mathematical formulations of $OA(x)$ and $FA(x)$ with corresponding R^2 values for different ceramic tile test targets

S. No.	Target id's	$OA = a_1 + b_1 e^{-0.5\left(\frac{x-c_1}{d_1}\right)^2}$					$FA = a_2 + b_2 e^{-0.5\left(\frac{x-c_2}{d_2}\right)^2}$				
		a_1	b_1	c_1	d_1	R^2	a_2	b_2	c_2	d_2	R^2
1	vc1	-2.4e+5	2.4e+5	0.31	15.09	0.92	50.29	-53.17	0.56	0.22	0.89
2	hc3	-3.0e+5	3.0e+5	0.36	14.75	0.85	1.3e+5	-1.3e+5	0.55	19.89	0.87
3	hc4	-49.02	1.5e+2	0.15	0.38	0.96	-0.32	51.31	0.10	0.19	0.97
4	vc3	10.59	98.73	0.39	0.11	0.91	11.77	-12.80	0.64	0.17	0.83
5	hc2	93.72	-97.47	0.64	0.11	0.95	9.6e+4	-9.6e+4	0.66	16.13	0.87
6	dc1	-23.68	1.2e+2	0.21	0.43	0.97	9.3e+4	-9.3e+4	0.50	17.73	0.88
7	rc4	-9.04	1.1e+3	0.18	0.28	0.98	1.7e+5	-1.7e+5	0.47	23.68	0.92
8	dc5	-4.5e+5	4.5e+5	0.33	15.92	0.87	34.89	-38.85	0.54	0.14	0.92
9	vc8	-3.3e+5	3.3e+5	0.32	21.12	0.87	1.4e+5	-1.4e+5	0.59	17.13	0.96
10	rc7	-2.9e+5	2.9e+5	0.21	18.36	0.95	9.4e+4	-9.4e+4	0.44	20.78	0.81

6.5.2.6. Step 6: Genetic Algorithm (GA) Optimization for User Defined Goal Achievement:

After having mathematical formulation of $OA(x)$ and $FA(x)$, the next step is to find the optimum value of 'n' such that OA is maximized and FA is minimized. In order to make our proposed algorithm more adaptive and robust, the performance parameters viz. $OA(x)$ and $FA(x)$ need to be dependent directly on the image spatial statistics. So, we replace x in equation (6.29), with the expression in equation (6.28) to achieve our final expression for optimization. Thus, the final performance equations are dependent on image statistics, i.e., median (M) and standard deviation (S) as well as on the function of 'n', defined as:

$$OA(n) = a_1 + b_1 e^{-0.5\left(\frac{M-(n-1)S-c_1}{d_1}\right)^2} \quad (6.30a)$$

$$FA(n) = a_2 + b_2 e^{-0.5 \left(\frac{M - (n-1)S - c_2}{d_2} \right)^2} \quad (6.30b)$$

Here, values of constants $a_1, b_1, c_1, d_1; a_2, b_2, c_2, d_2$ are -1.63e5, 1.63e5, 0.31, 8.66; 7.34e4, -7.34e4, 0.51, 11.61, respectively as obtained by averaging the values of ceramic tile test targets for OA and FA from Table 6.8. Now, we have two performance metrics accuracy and false alarm as a function of image spatial statistics; median and standard deviation and an unknown term ' n ' that is to be optimized. There is a trade-off between the two (OA and FA), *i.e.*, on maximizing accuracy, false alarm also increases and on minimizing false alarm, accuracy also reduces. This type of optimization problem can be formulated as a multi-objective optimization with bound constraints, *i.e.*, ' n ' will be constraint between $1.25 < n < 6$, the range for which mathematical formulations of OA and FA using curve fitting have been developed. For optimization, we preferred to use Genetic Algorithm (GA) which is a globally iterative numerical optimization technique [105, 150, 226]. In the multi-objective optimization, $F(n)$ is a two valued vector function of $f_1(n)$ and $f_2(n)$ such as:

$$\text{minimize } F(n) = [f_1(n), f_2(n)] ; 1.25 < n < 6$$

$$\text{Such that, } f_1(n) = -OA(n), \quad f_2(n) = FA(n) \quad (6.31)$$

Our objective is to maximize OA and minimize FA . However, since, multi-objective optimization concerns with the minimization of a set of objectives simultaneously, hence, a negative sign is introduced to define $f_1(n)$, which is a function of OA . The optimum value of n must satisfy user defined performance goals *i.e.*, OA should be greater than user defined lower bound (lb_{OA}) and FA should be less than user defined upper bound (ub_{FA}) in order to ensure correct cracked window detection of the extracted ceramic tile image. The goal vector is of same length as the number of objectives and is defined as:

$$Goal = [-lb_{OA}, ub_{FA}] \quad (6.32)$$

$$\text{for fitness function } F(n) = [f_1(n), f_2(n)]$$

This will give the final optimized solution of the multi-objective problem in terms of optimum value of n for which $OA > lb_{OA}$ and $FA < ub_{FA}$. A complete flow chart depicting different signal processing steps for the proposed non-invasive, adaptive concealed crack detection methodology is shown in Figure 6.16.

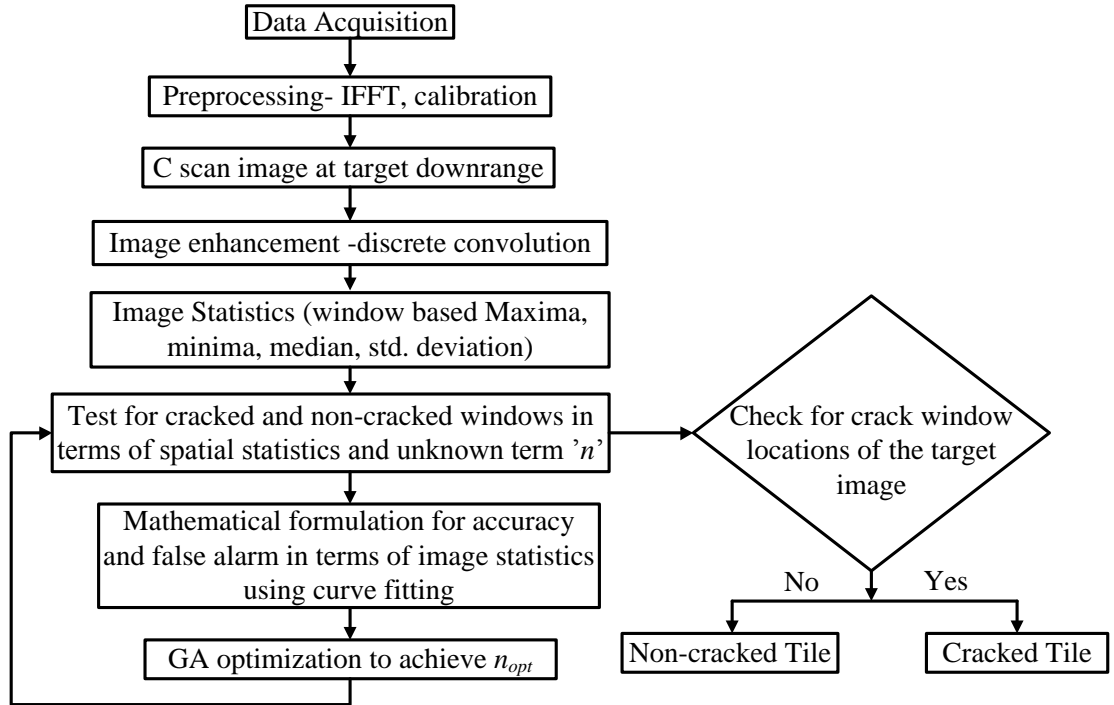


Figure 6.16. Flow chart showing different implementation steps of the proposed statistical based non-destructive undercover crack detection methodology.

6.5.2.7. Step 7: Testing of the Developed Adaptive Cracked Detection Algorithm

The developed concealed crack detection methodology was tested using different ceramic tiles viz., fl , $f3$, $hc3$, $vc3$, $dc5$, $rc7$ for detection of cracked and non-cracked tiles, as well as, detection of particular cracked window locations in the ceramic tile. For this, window based target's image statistics (median and Std. deviation) were calculated and averaged to get complete target's window based spatial statistical values: median and standard deviation. For the different considered test targets, these values are shown in Table 6.9 in column third and fourth.

Next, GA was performed on the fitness function given in equation (6.31) and solved towards user defined goals: $OA \geq 100$ & $FA \leq 2$ (no. of cracked windows) and bound constraints: $1.25 < n < 6$ for finding the optimized value ' n_{opt} '. For the considered test targets, n_{opt}

values are shown in Table 6.9 in column V, which, are different for different ceramic tile targets depending on their particular image statistics.

Table 6.9. Proposed GA Optimized statistical algorithm performance results for few test targets

S.No.	Target's Id	Median (M)	Std. Dev.(S)	n_{opt}	OA (%)	FA (False alarm windows)
1	f1	0.8101	0.06034	5.04	100	0
2	vc3	0.697	0.102	4.57	100	1
3	f3	0.7924	0.0423	5.4	100	0
4	hc3	0.7004	0.101	4.64	100	2
5	dc7	0.681578	0.098454	5.38	100	1
6	rc7	0.675193	0.124534	4.41	100	0

Next, these n_{opt} values for respective test targets are put in equation (6.26) and checked towards cracked/ non-cracked window detection. The test target's results are shown in Table 6.9. The results show successful detection of non-cracked ceramic tiles ($f1$, $f3$) with 100% accuracy (\sim zero false alarm), which was our main aim of the proposed crack detection algorithm to achieve nearly zero false alarm for non-cracked packaged tiles. Further, for cracked tile targets ($hc3$, $vc3$, $dc5$, $rc7$), the algorithm detects them as the cracked ones (\sim 100% accuracy) as well as provide accurate localization of cracked windows w.r.t. actual physical packaged ceramic tile crack configuration. However, for few test tiles; $vc3$, $hc3$, $dc7$, it also detects some (max. upto two) non-cracked windows of the tile as the cracked ones and thereby, gives the false alarm.

Some of few test results are shown in Figure 6.17. Figure 6.17(a), shows detected full non-cracked tile ($f1$) image with no crack. Figure 6.17(b), (c), (d) shows detected cracked tile images: $hc3$, $vc3$, $dc7$, respectively, in which white patches signifies detected cracked windows.

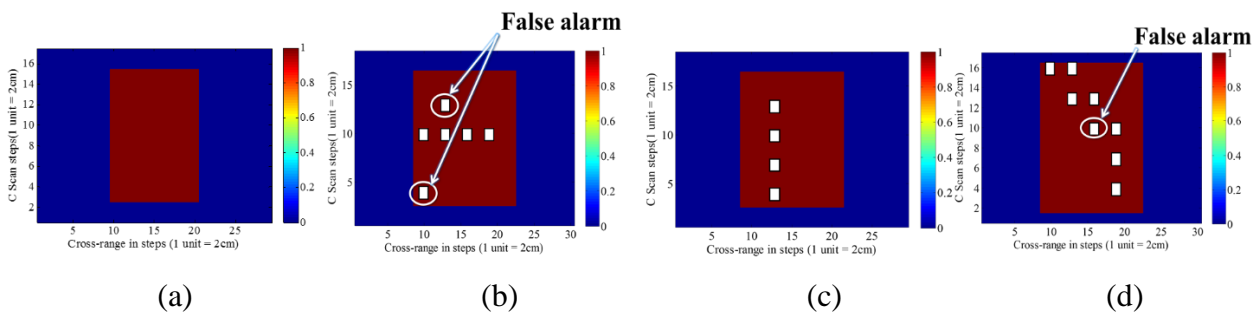


Figure 6.17. Detection of cracked tile windows using proposed adaptive statistical crack localization algorithm for different test tile targets: (a) $f1$, (b) $hc3$, (c) $vc3$, (d) $dc7$.

Figure 6.17(b) and (d) shows detection of few false alarm windows, which were actually not present in the physical targets *hc3* and *dc7*, respectively. Hence, this developed methodology provides a generalized and adaptive optimization technique for non-destructive detection of undercover cracked and non-cracked ceramic tiles as well as estimation of accurate cracked window locations in the cracked ceramic tiles, with appreciably low false alarm.

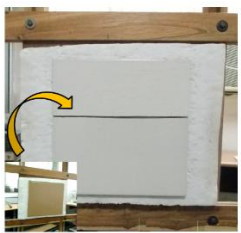
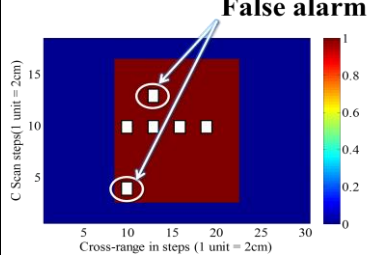

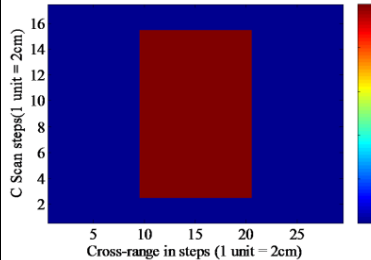
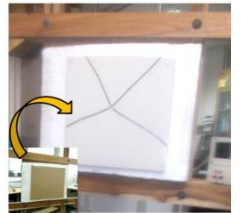
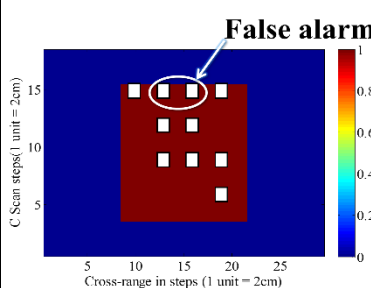
6.5.3. Validation of Proposed Adaptive Algorithm

Further, independent validation of the developed non-destructive crack detection algorithm has been checked on number of packaged ceramic tile targets with different crack (*hc5*, *hc7*, *vc5*, *vc6*, *dc3*, *dc4*, *rc8*, *rc5*) and non-crack (*f6*, *f8*) configurations (as given in Table 6.1, column 3), which were earlier not used while mathematical formulation and algorithm development. Following processing steps were performed for crack/non-crack ceramic tile detection and particular crack window localization in any packaged ceramic tile under test:

- i. The spatial statistical parameter values, *i.e.*, median and std. deviation were calculated from the tile image under test.
- ii. The GA optimization goals were set as per user requirements of accuracy and false alarm. Here, we have considered $OA \geq 100$ & $FA \leq 2$ (no. of cracked windows).
- iii. The optimum value n_{opt} was computed through GA optimization using mathematical formulation as given in equation (6.30), under the bound constraints: $1.25 < n < 6$.
- iv. Now, the obtained values of n_{opt} were put in equation (6.26) and the respective ceramic tile target's quality is checked towards any crack present.
- v. If there is no crack present in the packaged tile, the output tile image is displayed as a plane uniform rectangle, however, if any crack is present, it is displayed by the small white patch at the corresponding crack location in the output tile image.

Table 6.10 shows validation results obtained after applying proposed adaptive statistical crack detection algorithm for ceramic tile targets: *hc7*, *f6*, *rc5* with different crack/non-crack configurations. *For tile target id: f6*; there were no crack windows marked in the output tile image, hence, the undercover packaged tile will be a non-cracked full tile, which is correct as per our actual physical target's knowledge.

Table 6.10. Output results of the proposed statistical algorithm for non-destructive undercover crack detection using independent validation target tiles.

S. No.	Target's id	Actual tile targets	Statistical measures	n_{opt}	Undercover target's crack detection output	OA (%)	False alarm windows
1.	<i>hc7</i>		Median = 0.7033 Std. dev. = 0.0805	5.2		100	02
2.	<i>f6</i>		Median = 0.8499 Std. dev. = 0.0625	5.5		100	00
3.	<i>rc5</i>		Medain = 0.675 Std. dev. =0.124	4.0		90	02

Further, for tile target id's: hc7, rc5; there were white patches present at different locations in the output tile image, which signifies corresponding crack locations, and hence, the undercover tile would be cracked one, which is again true as per our target's knowledge. However, few false cracked windows were also detected in the resulting tile image, but, overall accuracy and false alarm for both the cracked tiles is appreciably good and within acceptable limit. Hence, performance of the developed statistical concealed crack detection algorithm on different types of target tiles confirms its adaptivity, practicality and usefulness. The ingeniously designed 60 GHz active imaging radar system and the proposed methodology provides an image dependent and generalized approach towards non-destructive undercover target's crack detection and localization.

6.5.4. Concluding Remarks (for Subtask 2)

In this subtask 2, our main focus was to develop such a technique using MMW imaging radar, which should have the capability to detect as well as locate particular crack points in the packaged ceramic tiles non-invasively. Moreover, it can adaptively and automatically adjust its threshold criterion for the classification boundary of cracked and non-cracked windows depending upon the image's spatial statistics and user defined goals of accuracy and false alarm. Hence, as per the validation results, it can be inferred that our proposed image statistics based crack localization algorithm performs quiet well and is in accordance with our set design goals of 100% classification accuracy in detecting crack/ non-crack tiles and less than two false alarm windows in case of cracked packaged tiles.

6.6. Conclusion

In this chapter, MMW imaging radar application for non-invasive fault (crack) detection of packaged ceramic tiles has been investigated for automatic quality check of packaged goods at industry dispatch end. However, we have considered crack as a fault. Further, applicability of different image and signal processing techniques has also been critically analyzed for undercover crack classification and its localization. In the first approach, feature based ANN crack classification model is proposed, where, histogram oriented gradient feature-based-NN model showed optimum classification accuracy. HOG features perform optimal, since it extracts target's characteristics on cell/ window basis, involves local normalization and is fairly robust to

moderate changes in illumination and orientation. However, it is a quantitative approach, which provides only cracked / non-cracked tile information.

However, in second approach, a generalized, adaptive image statistics based undercover crack detection as well as localization algorithm was developed using closed form mathematical formulation and multi-objective genetic algorithm optimization. This is an image reconstruction approach, which also provides particular crack window estimation apart from just crack/non-crack classification. For the statistical algorithm, the fitness function adaptively generates the optimized value of unknown term ' n ' maintaining the constraints of accuracy and false alarm as defined by the end user, depending upon target's image statistics. The two proposed algorithms were tested and validated using a number of different packaged ceramic tile targets with varying crack and non-crack configurations. The appreciably good accuracy of results suggest that the proposed algorithms can be used as a generalized technique for an automatic crack scanner (using MMW imaging) for quality monitoring of different packaged goods at the industry dispatch end.

Chapter 7

Conclusions and Future Scope

The main objective of this thesis was to project the advantages of MMW spectrum, its potential applications and challenges. With the current advancements of technologies, MMW can be efficiently modeled with extreme accuracy for different areas. MMW provides high resolution imaging as well as compact systems because of its correspondingly lower wavelength. In view of the associated higher losses and dimensional limitations at MMW frequency, a simple and cost-effective planar antenna design has been investigated in this thesis. Additionally, the motivation behind this research work was to develop a digital image processing based framework which addresses the challenges related to the correct target's shape identification and non-invasive fault (crack) estimation from stand-off distances. An adaptive solution for the automatic target's shape information and its quality monitoring has been developed. This chapter concludes the contributions made in the thesis followed by recommendations for further scope of research.

7.1. Contributions of the Thesis

This thesis has the main emphasis on development of MMW dual frequency planar antenna design with a simple, cost-effective and compact structure and SFCW based MMW radar imaging applications which consists of an algorithm development for target's shape identification and its material classification; an automatic ANN based model for target's rotation and size invariant image reconstruction; and development of a non-invasive concealed target's fault (crack) detection model.

Chapter three, contributes to the field of dual resonant MMW microstrip antenna design. A simple solution towards the design of the dual resonant MMW antenna has been proposed in the form of reactive loading to the antenna. The designed antenna supports two different MMW bands concurrently, viz, V band (60 GHz) and E band (85 GHz). These frequencies are

commercially attractive and have been allocated for unlicensed high data rate communications. The contributions made in this chapter are as follows:

- The prototype antenna showed fractional bandwidths of 1% / 6.4% and broadside E (H) plane gains 8.49 dBi (8.95 dBi)/ 5.13 dBi (5.37 dBi), at the two respective resonant frequencies 60 GHz/85 GHz.
- The designed antenna is of compact size (*i.e.*, cross-sectional area of only 3.7 mm²) in comparison to available antennas and does not require any complex fabrication step which favours easy and simple fabrication using conventional photolithographic procedures.
- Moreover, the substrate used is low-cost and easily available, which makes the proposed antenna design cost competent.

Chapter four, presents MMW imaging application for stand-off targets using an ingeniously designed SFCW radar operating at centre frequency 60 GHz with the bandwidth of 2 GHz. For target's shape identification and its material classification, four regular shaped targets were considered, *viz.*, rectangle, square, triangle and circle. The main contributions of this chapter are as following:

- A critical analysis for various steps for pre-processing has been carried out for imaging the targets and it is found that for clutter reduction, image enhancement techniques, like, background subtraction and singular value decomposition proved to be efficient in improving the target's image quality for an ingeniously developed MMW imaging system.
- On investigating different image segmentation techniques, it was found that mean and standard deviation based global thresholding in conjunction with the canny based edge detection technique performed fairly well for target correct shape identification.
- The results suggest that the different DIP techniques being used for microwave radar/camera imaging can be used equiprobably for MMW radar imaging with an appreciably good performance.
- Moreover, a target's material classification algorithm utilizing the Cauchy probability distribution function has been proposed for discriminating the two target's material classes, *i.e.*, metal and wood, in the MMW radar image.

Chapter five, addresses the problem of target's orientation and its size variation for identification of its shapes. The radar line of sight is one of the very important aspects to image any targets. So, it may be possible that all the time, targets may not be in the same line of sight, *i.e.*, misaligned and of different sizes. Therefore, there is a need to develop such a technique that will take care of these issues and recognizes the correct shape and size of targets. Following inferences have been drawn in this chapter:

- An automatic ANN based image reconstruction model has been proposed which can identify different regular shape targets, viz., rectangle, square, triangle and circle, irrespective of their size and orientation. The obtained results are quite encouraging.

Thereby, as per investigations made in chapter 4 and 5, a complete framework has been outlined for extracting target's comprehensive information, *i.e.*, target's shape, size and target's material type. The flow chart in Figure 7.1 shows the key processing steps of the complete developed algorithm, which utilizes ANN model for target's shape identification and Cauchy pdf model for target's material classification. For example, the triangle shape wooden target on the metal background is kept at a stand-off distance from the antenna. By C-scan imaging its complete reflection data is recorded. After signal pre-processing, the target's image is fed as an input to the developed ANN model and Cauchy pdf model. The resultant output is the reconstructed *triangle shape with the correct orientation* and the Cauchy pdf classifies the *triangular target as wood* and the *background as the metal* correctly.

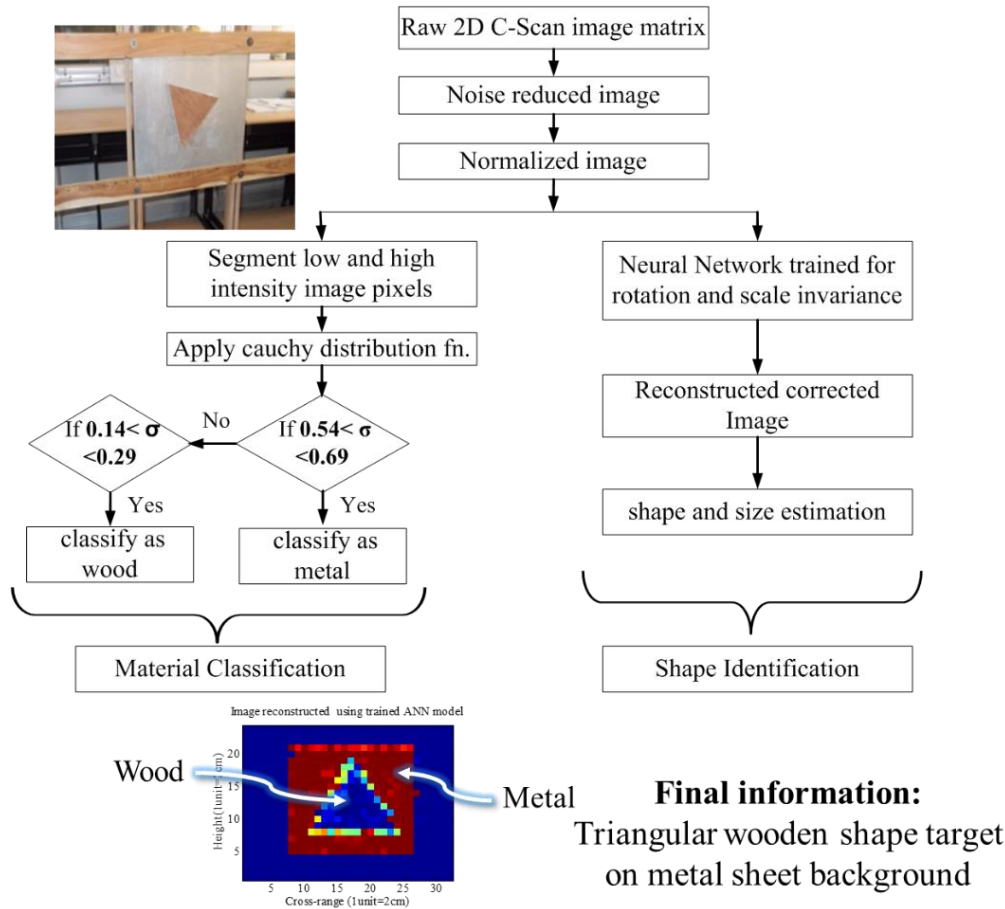


Figure 7.1. Complete flow chart for estimating target’s shape and target’s material information in any practical environment using the ingeniously designed MMW imaging radar system.

Chapter six, contributes to the field of non-destructive, non-invasive quality testing application using MMW imaging radar. A high demand of quality and reliability of products require a precise detection of defects for the competent and cost effective manufacturing. For the concealed target, packaged ceramic tiles have been used and placed at a distance from the antenna. Total 45 numbers of ceramic tiles in different crack/ non-crack configurations have been taken, *i.e.*, horizontally crack tile, vertically crack tile, diagonally crack tile, random crack tile and full tile without any crack. An attempt has been made to develop automatic, non-invasive crack detection/ localization methodology for the quality check of packaged ceramic tiles for industrial applications and two approaches have been proposed for this. The contributions made in this chapter are as follows:

- A target’s feature-based-ANN crack classification model has been proposed for quantitative estimation of crack / non-crack packaged ceramic tiles and to localize the actual

crack position for visual interpretation an adaptive statistical approach with the help of GA optimization approach has been proposed.

- Both the proposed models have the good capability to detect crack / non-crack packaged tiles and localize the crack position with good accuracy and minimum false alarm which may be quite useful for industrial quality monitoring applications.

Overall, it can be concluded that the present research work covers applications of MMW frequency with an emphasis on simple, dual frequency MMW planar antenna design as well as development of novel target's shape and fault (crack) estimation methodology.

7.2. Future scope

Overall, the future is bright for MMW's. The performance capabilities that come with short wavelengths enable many new applications, only a few of which have been covered here. The present thesis work has the scope and possibilities to extend it further in which, some of them are listed as following:

- The present research work provides the simple design for the dual frequency planar antenna at MMW which can be utilized for future compact, multi-tasking dual band MMW systems. The proposed antenna can be fabricated using conventional photolithography procedures, hence, provides a commercially competent cost-effective choice. Using the proposed design strategy, it would be possible to design microstrip antenna arrays with adequate gain, good pattern quality, low VSWR and acceptable efficiency. Hence, very good electrical performance combined with very reasonable size/ weight would make these antennas excellent candidates for future MMW applications of communications, precision radar, radio astronomy and remote sensing systems, including, secure communications systems, meteorological monitoring, aircraft-to-satellite communication and imaging array antennas.
- As per developed algorithm for target's detection and identification for MMW radar imaging, it is further possible to extend the image enhancement/ segmentation techniques by taking into account adaptive nature. Additionally, the proposed pdf approach for material classification can be extended to discriminate more different type of target's materials, *viz.*, teflon, plastic, wood, ceramic etc., since, for many applications knowledge of exact target's material is important from strategic and commercial viewpoint.

- Based on the proposed ANN pattern recognition model in this thesis, a rotation and size invariant target's identification support system can be extended for different irregular target shapes which provide automated image reconstruction irrespective of target's orientation and size. This system will take input as the raw deformed image and will provide the desired correct target's image.
- The present research work provides a solution for an adaptive and automatic classification of different types of packaged goods especially ceramic tiles for their quality monitoring. The implementation of the concept will certainly enhance the productivity of the industry using the fast and accurate surveying approach. Additionally, the applications and capabilities of MMW imaging are vast and new. By properly choosing the image processing techniques a better classification/ identification system can be modelled.
- Fusion of different feature extraction techniques will provide more parameters for discrimination of different target's types and classes. Therefore, proposed classification algorithm can be generalized to make it a target and a sensor independent.
- The design strategies of proposed imaging algorithm can be utilized for applications based on different MMW radar sensors operating at different frequencies.
- MMW NDT is finding a prominent place in a wide realm of applications and its scope can be extended for other fields, like, material permittivity estimation, IC inspection, moisture content in plants, multilayer thickness measurement, composite material characterization, and many more. The advantages of MMW can be used to extract improved and more authentic target's information.
- The Figure 7.2 shows the artistic view of our future proposed industrial application model. Our idea of the practical industrial quality monitoring application is to scan the packaged ceramic tile placed on the conveyor belt moving with the constant speed and the antenna will be mounted on the mechanical frame at a stand-off vertical distance from the packaged tile, such that it is focusing and scanning each of the underneath passing packaged tile on the moving conveyor belt for quality monitoring.

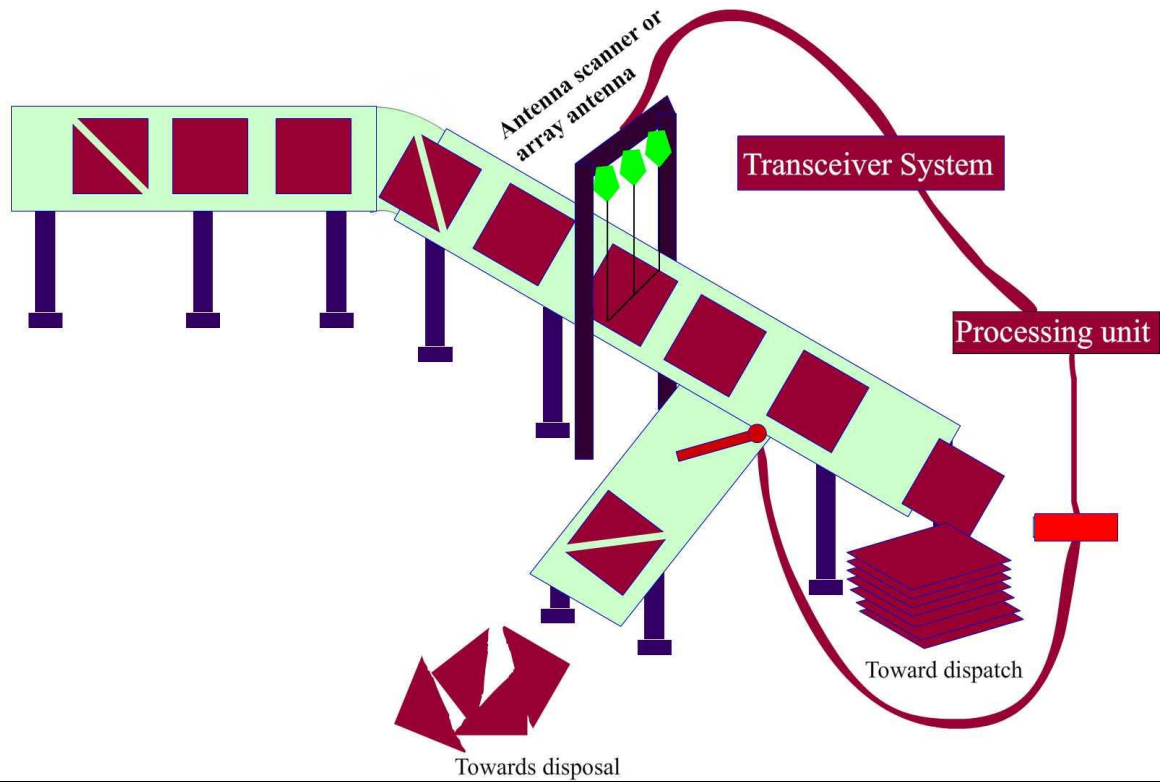


Figure 7.2. Pictorial demonstration of the proposed non-invasive, non-destructive packaged ceramic tile's fault classification model for industrial quality monitoring applications.

Author's Publications

International Journals

1. **Agarwal S.**, Bisht A., Singh D. and Pathak N.P., "A Novel Neural Network based Image Reconstruction Model with Scale and Rotation Invariance for Target Identification and Classification for Active Millimetre Wave Imaging" in *Journal of Infrared, Millimetre, and Terahertz Waves* (Springer) Vol. 35, Issue 12, pp 1045-1067, 2014.
2. **Agarwal S.**, and Singh D., "An adaptive statistical approach for non- destructive underline crack detection of ceramic tiles using millimetre wave imaging radar for industry application", *IEEE Sensors Journal*, 2015. (*accepted*)
3. **Agarwal S.**, and Singh D., "Optimal Non-invasive Fault Classification Model for Packaged Ceramic Tile Quality Monitoring Using MMW Imaging" Springer *Journal of Infrared, Millimetre, and Terahertz Waves*. (**Communicated**)

International Conferences

1. **Agarwal S.**, Pathak N.P. and Singh D., "Active millimetre wave radar system for non-destructive, non-invasive underline fault detection and multilayer material analysis", *IEEE International Microwave and RF Conference (IMaRC2014)*, 2014, 15-17 Dec. 2014.
2. **Agarwal S.**, Pathak N.P. and Singh D., "Concurrent 83GHz/94 GHz Parasitically Coupled defected microstrip feedline Antenna for Millimetre Wave Applications", *4th IEEE Applied Electromagnetics Conference (AEMC)*, 2013, pp. 1-2, 18-19 Dec. 2013.
3. **Agarwal S.**, Pathak N.P. and Singh D., "Concurrent 85GHz/94GHz slotted gap coupled parasitic microstrip antenna for millimetre wave applications," *IEEE National Conference on Communications (NCC)*, 2013, pp.1-5, 15-17 Feb. 2013.

4. **Agarwal S.**, Pathak N.P. and Singh D., "Performance comparison of microstrip patch antenna for 94 GHz imaging applications," *7th IEEE International Conference on Industrial and Information Systems (ICIIS)*, 2012, pp.1-4, 6-9 Aug. 2012.

National Conferences

1. **Agarwal S.** and Singh D., "Non-Invasive and Non-Destructive underline Fault Detection using Active Millimetre Wave Radar", *9th Uttarakhand State Science and Technology Congress 2014-15*, Dehradun 2014-15, 26-28 Feb. 2015. (**earned the young scientist Award**)
2. **Agarwal S.**, Kumar B. and Singh D., "Non-Invasive Conceal Weapon Detection using 60 GHz Millimetre Wave Radar System", National conference on *Recent Advances in Electronics and Computer Engineering (RAECE 2015)*, 2015, 13-15 Feb. 2015.

References

- [1] Abujarad F., Jostingmeier A., and Omar A. S., "Clutter removal for landmine using different signal processing techniques", in *Ground Penetrating Radar, 2004. GPR 2004. Proceedings of the Tenth International Conference on*, 2004, pp. 697-700.
- [2] Abujarad F., Jostingmeier A., and Omar A. S., "Clutter removal for landmine using different signal processing techniques", in *Proceedings of the Tenth International Conference on Ground Penetrating Radar*, 2004, pp. 697-700.
- [3] AbuTarboush H. F., Nilavalan R., Cheung S. W., Nasr K. M., Peter T., Budimir D., *et al.*, "A Reconfigurable Wideband and Multiband Antenna Using Dual-Patch Elements for Compact Wireless Devices", *IEEE Transactions on Antennas and Propagation*, vol. 60, pp. 36-43, 2012.
- [4] Adamiuk G., Beer S., Wiesbeck W., and Zwick T., "Dual-Orthogonal Polarized Antenna for UWB-IR Technology", *IEEE Antennas and Wireless Propagation Letters*, vol. 8, pp. 981-984, 2009.
- [5] Afsar M. N., Tkachov I. I., and Kocharyan K. N., "A novel W-band spectrometer for dielectric measurements", in *IEEE MTT-S International Microwave Symposium Digest*, 2000, pp. 1627-1630 vol.3.
- [6] Agarwal S., Bisht A. S., Singh D., and Pathak N. P., "A novel neural network based image reconstruction model with scale and rotation invariance for target identification and classification for Active millimetre wave imaging", *Journal of Infrared, Millimeter, and Terahertz Waves*, vol. 35, pp. 1045-1067, 2014.
- [7] Agarwal S., Pathak N. P., and Singh D., "Concurrent 83GHz/94 GHz parasitically coupled defected microstrip feedline antenna for millimeter wave applications", in *IEEE Applied Electromagnetics Conference (AEMC)*, 2013, pp. 1-2.

- [8] Agarwal S., Pathak N. P., and Singh D., "Concurrent 85GHz/94GHz slotted gap coupled parasitic microstrip antenna for millimeter wave applications", in *National Conference on Communications (NCC)*, 2013, pp. 1-5.
- [9] Agarwal S., Pathak N. P., and Singh D., "Performance comparison of microstrip patch antenna for 94 GHz imaging applications", in *7th IEEE International Conference on Industrial and Information Systems (ICIIS)*, 2012, pp. 1-4.
- [10] Aguirre J., Hsueh-Yuan P., Hung-Sheng L., Garland P., O'Neill D., and Horton K., "An LTCC 94 GHz antenna array", in *IEEE Antennas and Propagation Society International Symposium*, 2008, pp. 1-4.
- [11] Agurto A., Yong L., Gui Yun T., Bowring N., and Lockwood S., "A Review of Concealed Weapon Detection and Research in Perspective", in *IEEE International Conference on Networking, Sensing and Control*, 2007, pp. 443-448.
- [12] Ahbe D., Beer S., Zwick T., Yang W., and Tentzeris M. M., "Dual-Band Antennas for Frequency-Doubler-Based Wireless Strain Sensing", *IEEE Antennas and Wireless Propagation Letters*, vol. 11, pp. 216-219, 2012.
- [13] Ahmad F. and Amin M. G., "Noncoherent approach to through-the-wall radar localization", *IEEE Transactions on Aerospace and Electronic Systems*, vol. 42, pp. 1405-1419, 2006.
- [14] Ahmad M. B. and Choi T.-S., "Local threshold and boolean function based edge detection", *IEEE Transactions on Consumer Electronics*, vol. 45, pp. 674-679, 1999.
- [15] Alekseev S. and Ziskin M., "Human skin permittivity determined by millimeter wave reflection measurements", *Bioelectromagnetics*, vol. 28, pp. 331-339, 2007.
- [16] Alhalabi R. A. and Rebeiz G. M., "Differentially-Fed Millimeter-Wave Yagi-Uda Antennas With Folded Dipole Feed", *IEEE Transactions on Antennas and Propagation*, vol. 58, pp. 966-969, 2010.
- [17] Andrews D. A., Harmer S. W., Bowring N. J., Rezgui N. D., and Southgate M. J., "Active Millimeter Wave Sensor for Standoff Concealed Threat Detection", *IEEE Sensors Journal*, vol. 13, pp. 4948-4954, 2013.
- [18] Anguera J., Puente C., Borja C., and Soler J., "Dual-Frequency Broadband-Stacked Microstrip Antenna Using a Reactive Loading and a Fractal-Shaped Radiating Edge", *IEEE Antennas and Wireless Propagation Letters*, vol. 6, pp. 309-312, 2007.

-
- [19] Anh T. H., Han M., Baek Y. H., Lee S. J., Van H. N., Kim J. H., *et al.*, "Coplanar waveguide (CPW)-FED circular slot antenna for W-band and imaging system applications", *Microwave and Optical Technology Letters*, vol. 53, pp. 2298-2302, 2011.
- [20] Antonini M., Barlaud M., Mathieu P., and Daubechies I., "Image coding using wavelet transform", *IEEE Transactions on Image Processing*, vol. 1, pp. 205-220, 1992.
- [21] Appleby R. and Wallace H. B., "Standoff Detection of Weapons and Contraband in the 100 GHz to 1 THz Region", *IEEE Transactions on Antennas and Propagation*, vol. 55, pp. 2944-2956, 2007.
- [22] Arivazhagan S., Ganesan L., and Bama S., "Fault segmentation in fabric images using Gabor wavelet transform", *Machine Vision and Applications*, vol. 16, pp. 356-363, 2006.
- [23] Asncombe N., "No place to hide [millimeter wave imaging]", *IEE Review*, vol. 51, pp. 26-30, 2005.
- [24] Babacan S. D., Luessi M., Spinoulas L., Katsaggelos A. K., Gopalsami N., Elmer T., *et al.*, "Compressive passive millimeter-wave imaging", in *18th IEEE International Conference on Image Processing (ICIP)*, 2011, pp. 2705-2708.
- [25] Bahr A. J., "Nondestructive Microwave Evaluation of Ceramics", *IEEE Transactions on Microwave Theory and Techniques*, vol. 26, pp. 676-683, 1978.
- [26] Bakhtiari S., Elmer T. W., Cox N. M., Gopalsami N., Raptis A. C., Liao S., *et al.*, "Compact Millimeter-Wave Sensor for Remote Monitoring of Vital Signs", *IEEE Transactions on Instrumentation and Measurement*, vol. 61, pp. 830-841, 2012.
- [27] Balanis C. A., "Antenna theory: Analysis and Design", ed: Wiley Interscience, 2005.
- [28] Bay H., Ess A., Tuytelaars T., and Van Gool L., "Speeded-up robust features (SURF)", *Computer vision and image understanding*, vol. 110, pp. 346-359, 2008.
- [29] Belongie S., Malik J., and Puzicha J., "Shape matching and object recognition using shape contexts", *IEEE Transactions on Pattern Analysis and Machine Intelligence*, vol. 24, pp. 509-522, 2002.
- [30] Biglarbegian B., Basha M., Taeb A., Gigoyan S., and Safavi-Naeini S., "Silicon-based integrated millimeter-wave CPW-to-dielectric image-guide transition", *International Journal of RF and Microwave Computer-Aided Engineering*, vol. 24, pp. 490-497, 2014.
- [31] Bird T. S., "Definition and Misuse of Return Loss [Report of the Transactions Editor-in-Chief]", *IEEE Antennas and Propagation Magazine*, vol. 51, pp. 166-167, 2009.

- [32] Bjarnason J. E., Chan T. L. J., Lee A. W. M., Celis M. A., and Brown E. R., "Millimeter-wave, terahertz, and mid-infrared transmission through common clothing", *Applied Physics Letters*, vol. 85, pp. 519-521, 2004.
- [33] Broadhurst R., Stough J., Pizer S., and Chaney E., "Histogram statistics of local image regions for object segmentation", in *International Workshop on Deep Structure, Singularities, and Computer Vision*, 2005.
- [34] Burns G. W., Thayne I. G., and Arnold J. M., "Improvement of planar antenna efficiency when integrated with a millimetre-wave photonic crystal", in *7th European Conference on Wireless Technology*, 2004, pp. 229-232.
- [35] Büyüköztürk O. and Yu T.-Y., "Far-field radar NDT technique for detecting GFRP debonding from concrete", *Construction and Building Materials*, vol. 23, pp. 1678-1689, 2009.
- [36] Canny J., "A Computational Approach to Edge Detection", *Pattern Analysis and Machine Intelligence, IEEE Transactions on*, vol. PAMI-8, pp. 679-698, 1986.
- [37] Canny J., "A computational approach to edge detection", *IEEE Transactions on Pattern Analysis and Machine Intelligence*, pp. 679-698, 1986.
- [38] Cetinkaya H., Kizilhan A., Vertii A., Demirci S., Yigit E., and Ozdemir C., "The millimeter-wave imaging of concealed objects", in *IEEE International Symposium on Antennas and Propagation (APSURSI)*, 2011, pp. 228-231.
- [39] Chahat N., Zhadobov M., Alekseev S., and Sauleau R., "Human skin-equivalent phantom for on-body antenna measurements in 60 GHz band", *Electronics Letters*, vol. 48, pp. 67-68, 2012.
- [40] Chahat N., Zhadobov M., Sauleau R., and Alekseev S. I., "New Method for Determining Dielectric Properties of Skin and Phantoms at Millimeter Waves Based on Heating Kinetics", *IEEE Transactions on Microwave Theory and Techniques*, vol. 60, pp. 827-832, 2012.
- [41] Chair R., Chi-Lun M., Lee K. F., Luk K.-M., and Kishk A. A., "Miniature Wide-Band Half U-Slot and Half E-Shaped Patch Antennas", *IEEE Transactions on Antennas and Propagation*, vol. 53, pp. 2645-2652, 2005.
- [42] Chakrabarti S., Bindal N., and Theagarajan K., "Robust radar target classifier using artificial neural networks", *Neural Networks, IEEE Transactions on*, vol. 6, pp. 760-766, 1995.

-
- [43] Chakrabarti S., Bindal N., and Theagarajan K., "Robust radar target classifier using artificial neural networks", *IEEE Transactions on Neural Networks*, vol. 6, pp. 760-766, 1995.
- [44] Chamundeeswari V. V., Singh D., and Singh K., "An analysis of texture measures in PCA-based unsupervised classification of SAR images", *IEEE Geoscience and Remote Sensing Letters*, vol. 6, pp. 214-218, 2009.
- [45] Chandler R. A. and Wood L. E., "System considerations for the design of radar braking sensors", *IEEE Transactions on Vehicular Technology*, vol. 26, pp. 151-160, 1977.
- [46] Chandra R., Gaikwad A. N., Singh D., and Nigam M., "An approach to remove the clutter and detect the target for ultra-wideband through-wall imaging", *Journal of Geophysics and Engineering*, vol. 5, p. 412, 2008.
- [47] Chattopadhyay G. and Zmuidzinis J., "A dual-polarized slot antenna for millimeter waves", *IEEE Transactions on Antennas and Propagation*, vol. 46, pp. 736-737, 1998.
- [48] Chen H.-M., Lee S., Rao R. M., Slamani M.-A., and Varshney P. K., "Imaging for concealed weapon detection: a tutorial overview of development in imaging sensors and processing", *IEEE Signal Processing Magazine*, vol. 22, pp. 52-61, 2005.
- [49] Chengalvarayan R. and Li D., "HMM-based speech recognition using state-dependent, discriminatively derived transforms on mel-warped DFT features", *IEEE Transactions on Speech and Audio Processing*, vol. 5, pp. 243-256, 1997.
- [50] Cheolhee P. and Rappaport T. S., "Short-Range Wireless Communications for Next-Generation Networks: UWB, 60 GHz Millimeter-Wave WPAN, And ZigBee", *IEEE Wireless Communications*, vol. 14, pp. 70-78, 2007.
- [51] Corucci L., Giusti E., Martorella M., and Berizzi F., "Near Field Physical Optics modelling for Concealed Weapon Detection", *Antennas and Propagation, IEEE Transactions on*, vol. 60, pp. 6052-6057, 2012.
- [52] Corucci L., Giusti E., Martorella M., and Berizzi F., "Near field physical optics modelling for concealed weapon detection", *IEEE Transactions on Antennas and Propagation*, vol. 60, pp. 6052-6057, 2012.
- [53] Currie N. C., Parker S. W., and Efurud R. B., "MMW system trade-offs", *IEEE Aerospace and Electronic Systems Magazine*, vol. 3, pp. 21-26, 1988.

- [54] D. Singh N. K. C., K. C. Tiwari, and R. Prasad, "Shape Recognition of Shallow Buried Metallic Objects at X-Band Using Ann and Image Analysis Techniques", *Progress In Electromagnetics Research B*, vol. 13, pp. 257-273, 2009.
- [55] Dalal N. and Triggs B., "Histograms of oriented gradients for human detection", in *IEEE Computer Society Conference on Computer Vision and Pattern Recognition*, 2005, pp. 886-893.
- [56] Daniels R. C. and Heath R. W., "60 GHz wireless communications: emerging requirements and design recommendations", *IEEE Vehicular Technology Magazine*, vol. 2, pp. 41-50, 2007.
- [57] Daubechies I., "The wavelet transform, time-frequency localization and signal analysis", *IEEE Transactions on Information Theory*, vol. 36, pp. 961-1005, 1990.
- [58] De S., Gupta K., Stanley R. J., Ghasr M. T., Zoughi R., Doering K., *et al.*, "A comprehensive multi-modal NDE data fusion approach for failure assessment in aircraft lap-joint mimics", *IEEE Transactions on Instrumentation and Measurement*, vol. 62, pp. 814-827, 2013.
- [59] de Vries J., "Object Recognition: A Shape-Based Approach using Artificial Neural Networks", *Department of Computer Science, University of Utrecht*, 2006.
- [60] Debes C., Hahn J., Zoubir A. M., and Amin M. G., "Target Discrimination and Classification in Through-the-Wall Radar Imaging", *IEEE Transactions on Signal Processing*, vol. 59, pp. 4664-4676, 2011.
- [61] Demirci S., Cetinkaya H., Yigit E., Ozdemir C., and Vertiy A. A., "A study on millimeter-wave imaging of concealed objects: Application using back-projection algorithm", *Progress In Electromagnetics Research*, vol. 128, pp. 457-477, 2012.
- [62] Deng Y. and Liu X., "Electromagnetic imaging methods for nondestructive evaluation applications", *Sensors*, vol. 11, pp. 11774-11808, 2011.
- [63] Deselaers T., Keysers D., and Ney H., "Features for image retrieval: an experimental comparison", *Information Retrieval*, vol. 11, pp. 77-107, 2008/04/01 2008.
- [64] Deshmukh A. A., Baxi P., Kamdar C., Vora B., and Ray K. P., "Analysis of stub loaded rectangular microstrip antenna", in *National Conference on Communications (NCC)*, 2012, pp. 1-5.

-
- [65] Deshmukh A. A. and Ray K. P., "Formulation of Resonance Frequencies for Dual-Band Slotted Rectangular Microstrip Antennas", *IEEE Antennas and Propagation Magazine*, vol. 54, pp. 78-97, 2012.
- [66] Deshmukh A. A. and Ray K. P., "Stub loaded multi-band slotted rectangular microstrip antennas", *IET Microwaves, Antennas & Propagation*, vol. 3, pp. 529-535, 2009.
- [67] Di J., Yuehang X., Ruimin X., and Weigan L., "Compact dual-band-notched UWB planar monopole antenna with modified CSRR", *Electronics Letters*, vol. 48, pp. 1250-1252, 2012.
- [68] Dionisio C. R. P., Tavares S., Perotoni M., and Kofuji S., "Experiments on through-wall imaging using ultra wideband radar", *Microwave and Optical Technology Letters*, vol. 54, p. 339, 2012.
- [69] El-Mahallawy M. S. and Hashim M., "Material Classification of Underground Utilities From GPR Images Using DCT-Based SVM Approach", *IEEE Geoscience and Remote Sensing Letters*, vol. 10, pp. 1542-1546, 2013.
- [70] Emhemmed A. S., Elgaid K., and Lok L. B., "Integrated micromachined millimeter wave patch antenna", in *IEEE International Workshop on Antenna Technology*, 2009, pp. 1-4.
- [71] Eom K. B., "Time-varying autoregressive modeling of HRR radar signatures", *IEEE Transactions on Aerospace and Electronic Systems*, vol. 35, pp. 974-988, 1999.
- [72] Fan Y., Xue-Xia Z., Xiaoning Y., and Rahmat-Samii Y., "Wide-band E-shaped patch antennas for wireless communications", *IEEE Transactions on Antennas and Propagation*, vol. 49, pp. 1094-1100, 2001.
- [73] Farhat N. H., "Millimeter wave holographic imaging of concealed weapons", *Proceedings of the IEEE*, vol. 59, pp. 1383-1384, 1971.
- [74] Ferro A. and Bruzzone L., "Analysis of Radar Sounder Signals for the Automatic Detection and Characterization of Subsurface Features", *IEEE Transactions on Geoscience and Remote Sensing*, vol. 50, pp. 4333-4348, 2012.
- [75] Fosgate C. H., Krim H., Irving W. W., Karl W. C., and Willisky A. S., "Multiscale segmentation and anomaly enhancement of SAR imagery", *IEEE Transactions on Image Processing*, vol. 6, pp. 7-20, 1997.
- [76] Frazier L. M., "Radar surveillance through solid materials", in *Enabling Technologies for Law Enforcement and Security*, 1997, pp. 139-146.

- [77] Fredembach C., Schroder M., and Susstrunk S., "Eigenregions for image classification", *IEEE Transactions on Pattern Analysis and Machine Intelligence*, vol. 26, pp. 1645-1649, 2004.
- [78] Freundorfer A. P. and Iizuka K., "A study on the scattering of radio waves from buried spherical targets using the step frequency radar", *IEEE Transactions on Geoscience and Remote Sensing*, vol. 31, pp. 1253-1255, 1993.
- [79] Frigui H. and Gader P., "Detection and Discrimination of Land Mines in Ground-Penetrating Radar Based on Edge Histogram Descriptors and a Possibilistic K -Nearest Neighbor Classifier", *IEEE Transactions on Fuzzy Systems*, vol. 17, pp. 185-199, 2009.
- [80] Fuan T. and Jhe-Syuan L., "Feature Extraction of Hyperspectral Image Cubes Using Three-Dimensional Gray-Level Cooccurrence", *IEEE Transactions on Geoscience and Remote Sensing*, vol. 51, pp. 3504-3513, 2013.
- [81] Gaballah M. and Sato M., "A new approach to enhancement of ground penetrating radar target signals by pulse compression", *Exploration Geophysics*, vol. 40, pp. 77-84, 2009.
- [82] Gader P. D., Mystkowski M., and Yunxin Z., "Landmine detection with ground penetrating radar using hidden Markov models", *IEEE Transactions on Geoscience and Remote Sensing*, vol. 39, pp. 1231-1244, 2001.
- [83] Galleguillos C. and Belongie S., "Context based object categorization: A critical survey", *Computer Vision and Image Understanding*, vol. 114, pp. 712-722, 2010.
- [84] Gandhi O. P. and Riazi A., "Absorption of Millimeter Waves by Human Beings and its Biological Implications", *IEEE Transactions on Microwave Theory and Techniques*, vol. 34, pp. 228-235, 1986.
- [85] Gao X., Li C., Gu S., and Fang G., "Design, analysis and measurement of a millimeter wave antenna suitable for stand off imaging at checkpoints", *Journal of Infrared, Millimeter, and Terahertz Waves*, vol. 32, pp. 1314-1327, 2011.
- [86] Garg R., *Microstrip antenna design handbook*: Artech House, 2001.
- [87] Gautam R. S., Singh D., and Mittal A., "An efficient contextual algorithm to detect subsurface fires with NOAA/AVHRR data", *IEEE Transactions on Geoscience and Remote Sensing*, vol. 46, pp. 2005-2015, 2008.

-
- [88] Gauthier G. P., Raskin J. P., Katehi L. P. B., and Rebeiz G. M., "A 94-GHz aperture-coupled micromachined microstrip antenna", *IEEE Transactions on Antennas and Propagation*, vol. 47, pp. 1761-1766, 1999.
- [89] Ghasr M. T., Case J. T., and Zoughi R., "Novel Reflectometer for Millimeter-Wave 3-D Holographic Imaging", *IEEE Transactions on Instrumentation and Measurement*, vol. 63, pp. 1328-1336, 2014.
- [90] Ghasr M. T., Kharkovsky S., Bohnert R., Hirst B., and Zoughi R., "30 GHz Linear High-Resolution and Rapid Millimeter Wave Imaging System for NDE", *IEEE Transactions on Antennas and Propagation*, vol. 61, pp. 4733-4740, 2013.
- [91] Ghasr M. T., Kharkovsky S., Zoughi R., and Austin R., "Comparison of near-field millimeter-wave probes for detecting corrosion precursor pitting under paint", *IEEE Transactions on Instrumentation and Measurement*, vol. 54, pp. 1497-1504, 2005.
- [92] Ghasr M. T., Kharkovsky S., Zoughi R., and Austin R., "Comparison of near-field millimeter-wave probes for detecting corrosion precursor pitting under paint", *Instrumentation and Measurement, IEEE Transactions on*, vol. 54, pp. 1497-1504, 2005.
- [93] Ghasr M. T., Ying K. P., and Zoughi R., "SAR imaging for inspection of metallic surfaces at millimeter wave frequencies", in *Instrumentation and Measurement Technology Conference (I2MTC) Proceedings, 2014 IEEE International*, 2014, pp. 1202-1206.
- [94] Ghasr M. T., Ying K. P., and Zoughi R., "SAR imaging for inspection of metallic surfaces at millimeter wave frequencies", in *IEEE International Instrumentation and Measurement Technology Conference (I2MTC) Proceedings*, 2014, pp. 1202-1206.
- [95] Gokmen M. and Li C. C., "Edge detection and surface reconstruction using refined regularization", *IEEE Transactions on Pattern Analysis and Machine Intelligence*, vol. 15, pp. 492-499, 1993.
- [96] Goldsmith P. F., Hsieh C. T., Huguenin G. R., Kapitzky J., and Moore E. L., "Focal plane imaging systems for millimeter wavelengths", *IEEE Transactions on Microwave Theory and Techniques*, vol. 41, pp. 1664-1675, 1993.
- [97] Gonzalez R. C., *Digital image processing*: Pearson Education India, 2009.
- [98] Gonzalez R. C. and Woods R. E., *Digital Image Processing (3rd Edition)*: Prentice-Hall, Inc., 2006.

- [99] Guangyi Z., Yi C., Yilun C., Jian Y., Rashvand H., and Yamaguchi Y., "Linear Feature Detection in Polarimetric SAR Images", *IEEE Transactions on Geoscience and Remote Sensing*, vol. 49, pp. 1453-1463, 2011.
- [100] Gui Yun T., Sophian A., Taylor D., and Rudlin J., "Multiple sensors on pulsed eddy-current detection for 3-D subsurface crack assessment", *IEEE Sensors Journal*, vol. 5, pp. 90-96, 2005.
- [101] Haddadi K. and Lasri T., "60-GHz Near-Field Six-Port Microscope Using a Scanning Slit Probe for Subsurface Sensing", *IEEE Sensors Journal*, vol. 12, pp. 2575-2576, 2012.
- [102] Haddadi K., Wang M. M., Glay D., and Lasri T., "A 60 GHz Six-Port Distance Measurement System With Sub-Millimeter Accuracy", *IEEE Microwave and Wireless Components Letters*, vol. 19, pp. 644-646, 2009.
- [103] Hairu Z., Shan O., Guofu W., Suolu W., and Faquan Z., "Dielectric Spectrum Feature Vector Extraction Algorithm of Ground Penetrating Radar Signal in Frequency Bands", *IEEE Geoscience and Remote Sensing Letters*, vol. 12, pp. 958-962, 2015.
- [104] Hammad H. F., Antar Y. M. M., and Freundorfer A. P., "Dual band aperture coupled antenna using spur line", *Electronics Letters*, vol. 33, pp. 2088-2090, 1997.
- [105] Hantscher S. and Diskus C. G., "Pulse-based radar imaging using a genetic optimization approach for echo separation", *IEEE Sensors Journal*, vol. 9, pp. 271-276, 2009.
- [106] Haralick R. M., Shanmugam K., and Dinstein I. H., "Textural Features for Image Classification", *Systems, Man and Cybernetics, IEEE Transactions on*, vol. SMC-3, pp. 610-621, 1973.
- [107] Haralick R. M., Shanmugam K., and Dinstein I. H., "Textural features for image classification", *IEEE Transactions on Systems, Man and Cybernetics*, pp. 610-621, 1973.
- [108] Harmer S. W., Andrews D. A., Rezgui N. D., and Bowring N. J., "Detection of handguns by their complex natural resonant frequencies", *IET Microwaves, Antennas & Propagation*, vol. 4, pp. 1182-1190, 2010.
- [109] Harmer S. W., Bowring N., Andrews D., Rezgui N. D., Southgate M., and Smith S., "A Review of Nonimaging Stand-Off Concealed Threat Detection with Millimeter-Wave Radar [Application Notes]", *IEEE Microwave Magazine*, vol. 13, pp. 160-167, 2012.
- [110] Harmer S. W., Bowring N., Andrews D., Rezgui N. D., Southgate M., and Smith S., "A Review of Nonimaging Stand-Off Concealed Threat Detection with Millimeter-Wave Radar [Application Notes]", *Microwave Magazine, IEEE*, vol. 13, pp. 160-167, 2012.

- [111] Haworth C. D., González B. G., Tomsin M., Appleby R., Coward P. R., Harvey A. R., *et al.*, "Image analysis for object detection in millimetre-wave images", in *European Symposium on Optics and Photonics for Defence and Security*, 2004, pp. 117-128.
- [112] Haworth C. D., Saint-Pern Y., Clark D., Trucco E., and Petillot Y. R., "Detection and Tracking of Multiple Metallic Objects in Millimetre-Wave Images", *International Journal of Computer Vision*, vol. 71, pp. 183-196, 2007/02/01 2007.
- [113] Haykin S., *Neural Networks: A Comprehensive Foundation*. New York Macmillan, 2005.
- [114] He C., Li S., Liao Z., and Liao M., "Texture classification of PolSAR data based on sparse coding of wavelet polarization textons", *IEEE Transactions on Geoscience and Remote Sensing*, vol. 51, pp. 4576-4590, 2013.
- [115] Hirose A., Hamada S., and Yamaki R., "Envelope phase detection for millimetre-wave active imaging", *Electronics Letters*, vol. 45, pp. 331-332, 2009.
- [116] http://www.cisco.com/c/en/us/products/collateral/wireless/aironet-antennas-accessories/prod_white_paper0900aecd806a1a3e.html. Antenna Patterns and Their Meaning [Online].
- [117] Hu H., Karim M., Ong L., Leyman A., Luo B., Chiam T., *et al.*, "Millimeter wave imaging using SAR modeling", in *IEEE MTT-S International Microwave Workshop Series on RF and Wireless Technologies for Biomedical and Healthcare Applications (IMWS-BIO)*, 2013, pp. 1-3.
- [118] Hu Z., Karim M., Ong L., Luo B., and Chiam T., "A simple and efficient method of millimeter-wave image formation using back-projection algorithm", in *Asia-Pacific Microwave Conference Proceedings (APMC)*, 2013, pp. 984-986.
- [119] Huang C. Y., Ling C. W., and Kuo J. S., "Dual-band microstrip antenna using capacitive loading", *IEE Proceedings Microwaves, Antennas and Propagation*, vol. 150, pp. 401-404, 2003.
- [120] Huang K.-C. and Edwards D. J., *Millimetre Wave Antennas for Gigabit Wireless Communications: A Practical Guide to Design and Analysis in a System Context*: John Wiley & Sons, 2008.
- [121] Huey-Ru C., Hsin-Chih K., Fu-Ling L., Tzuen-Hsi H., Chi-Shin K., and Ya-Wen O., "60-GHz Millimeter-Wave Life Detection System (MLDS) for Noncontact Human Vital-Signal Monitoring", *IEEE Sensors Journal*, vol. 12, pp. 602-609, 2012.

- [122] Hui C., Yong-Xin G., Teck-Guan L., Yee Mong K., and Xiangquan S., "135-GHz Micromachined On-Chip Antenna and Antenna Array", *IEEE Transactions on Antennas and Propagation*, vol. 60, pp. 4582-4588, 2012.
- [123] Hunt A. R., "Use of a frequency-hopping radar for imaging and motion detection through walls", *IEEE transactions on geoscience and remote sensing*, vol. 47, pp. 1402-1408, 2009.
- [124] Hurney P., Waldron P., Morgan F., Jones E., and Glavin M. (2015, Night-time pedestrian classification with histograms of oriented gradients-local binary patterns vectors. *IET Intelligent Transport Systems* 9(1), 75-85. Available: <http://digital-library.theiet.org/content/journals/10.1049/iet-its.2013.0163>
- [125] Hyung Suk L., Jeong-Geun K., Songcheol H., and Jun-Bo Y., "Micromachined CPW-fed suspended patch antenna for 77 GHz automotive radar applications", in *The European Conference on Wireless Technology*, 2005, pp. 249-252.
- [126] Iamsa-at S. and Horata P., "Handwritten Character Recognition Using Histograms of Oriented Gradient Features in Deep Learning of Artificial Neural Network", in *International Conference on IT Convergence and Security (ICITCS)*, 2013, pp. 1-5.
- [127] Iizuka K., Freundorfer A. P., Wu K. H., Mori H., Ogura H., and Van-Khai N., "Step frequency radar", *Journal of Applied Physics*, vol. 56, pp. 2572-2583, 1984.
- [128] In Kwang K. and Varadan V. V., "Electrically Small, Millimeter Wave Dual Band Meta-Resonator Antennas", *IEEE Transactions on Antennas and Propagation*, vol. 58, pp. 3458-3463, 2010.
- [129] Jacobson L., "A matched filter data smoothing algorithm", *IEEE Transactions on Nuclear Science*, vol. 36, pp. 1227-1231, 1989.
- [130] Jaegeun H., Youngki L., and Jaehoon C., "Triple band patch antenna for Wibro/WLAN applications using a CRLH unit cell", in *Asia-Pacific Microwave Conference Proceedings (APMC)*, 2011, pp. 437-440.
- [131] James J. R., Hall P. S., and Wood C., *Microstrip antenna theory and design*: Iet, 1981.
- [132] Jianxin W., "Efficient HIK SVM Learning for Image Classification", *IEEE Transactions on Image Processing*, vol. 21, pp. 4442-4453, 2012.
- [133] Jie-Huang H., Jin-Wei W., Yi-Lin C., and Jou C. F., "A 24/60GHz dual-band millimeter-wave on-chip monopole antenna fabricated with a 0.13- μm CMOS technology", in *IEEE International Workshop on Antenna Technology*, 2009, pp. 1-4.

- [134] Johnson R. C. and Jasik H., "Antenna engineering handbook". vol. 1, ed: McGraw-Hill Book Company, New York, 1984, p. 1356.
- [135] Jong-Hoon L., Dejean G., Sarkar S., Pinel S., Kyutae L., Papapolymerou J., *et al.*, "Highly integrated millimeter-wave passive components using 3-D LTCC system-on-package (SOP) technology", *IEEE Transactions on Microwave Theory and Techniques*, vol. 53, pp. 2220-2229, 2005.
- [136] Ju Y., Saka M., and Abe H., "NDI of delamination in IC packages using millimeter-waves", *IEEE Transactions on Instrumentation and Measurement*, vol. 50, pp. 1019-1023, 2001.
- [137] Kaliyaperumal K., Lakshmanan S., and Kluge K., "An algorithm for detecting roads and obstacles in radar images", *IEEE Transactions on Vehicular Technology*, vol. 50, pp. 170-182, 2001.
- [138] Kao T. Y. J., Yan Y., Shen T. M., Chen A. Y. K., and Lin J., "Design and Analysis of a 60-GHz CMOS Doppler Micro-Radar System-in-Package for Vital-Sign and Vibration Detection", *IEEE Transactions on Microwave Theory and Techniques*, vol. 61, pp. 1649-1659, 2013.
- [139] Kapilevich B. and Einat M., "Detecting Hidden Objects on Human Body Using Active Millimeter Wave Sensor", *Sensors Journal, IEEE*, vol. 10, pp. 1746-1752, 2010.
- [140] Kapur R. and Kumar G., "Hybrid-coupled shorted rectangular microstrip antennas", *Electronics Letters*, vol. 35, pp. 1501-1502, 1999.
- [141] Karlsen B., Larsen J., Sorensen H. B. D., and Jakobsen K. B., "Comparison of PCA and ICA based clutter reduction in GPR systems for anti-personal landmine detection", in *Proceedings of the 11th IEEE Signal Processing Workshop on Statistical Signal Processing*, 2001, pp. 146-149.
- [142] Keller P. E., McMakin D. L., Sheen D. M., McKinnon A. D., and Summet J. W., "Privacy algorithm for cylindrical holographic weapons surveillance system", in *IEEE 33rd Annual 1999 International Carnahan Conference on Security Technology, 1999. Proceedings*, 1999, pp. 177-181.
- [143] Kharkovsky S., Case J. T., Abou-Khousa M. A., Zoughi R., and Hepburn F. L., "Millimeter-wave detection of localized anomalies in the space shuttle external fuel tank insulating foam", *IEEE Transactions on Instrumentation and Measurement*, vol. 55, pp. 1250-1257, 2006.

- [144] Kharkovsky S., Ghasr M. T., and Zoughi R., "Near-Field Millimeter-Wave Imaging of Exposed and Covered Fatigue Cracks", *IEEE Transactions on Instrumentation and Measurement*, vol. 58, pp. 2367-2370, 2009.
- [145] Kharkovsky S., Ghasr M. T., and Zoughi R., "Near-field millimeter-wave imaging of exposed and covered fatigue cracks", *Instrumentation and Measurement, IEEE Transactions on*, vol. 58, pp. 2367-2370, 2009.
- [146] Kharkovsky S. and Zoughi R., "Microwave and millimeter wave nondestructive testing and evaluation - Overview and recent advances", *IEEE Instrumentation & Measurement Magazine*, vol. 10, pp. 26-38, 2007.
- [147] Khotanzad A. and Lu J. H., "Classification of invariant image representations using a neural network", *IEEE Transactions on Acoustics, Speech and Signal Processing*, vol. 38, pp. 1028-1038, 1990.
- [148] Klenner M., Zech C., Hulsmann A., Tessmann A., Leuther A., Schlechtweg M., *et al.*, "Multilayer material analysis using an active millimeter wave imaging system", in *14th International Radar Symposium (IRS)*, 2013, pp. 207-213.
- [149] Klesk P., Godziuk A., Kapruziak M., and Olech B., "Fast Analysis of C-Scans From Ground Penetrating Radar via 3-D Haar-Like Features With Application to Landmine Detection", *IEEE Transactions on Geoscience and Remote Sensing*, vol. 53, pp. 3996-4009, 2015.
- [150] Kobashigawa J. S., Youn H.-s., Iskander M. F., and Yun Z., "Classification of buried targets using ground penetrating radar: Comparison between genetic programming and neural networks", *IEEE Antennas and Wireless Propagation Letters*, vol. 10, pp. 971-974, 2011.
- [151] Konstantinides K., Natarajan B., and Yovanof G. S., "Noise estimation and filtering using block-based singular value decomposition", *IEEE Transactions on Image Processing*, vol. 6, pp. 479-483, 1997.
- [152] Koohestani M., Pires N., Skrivervik A. K., and Moreira A. A., "Band-reject ultra-wideband monopole antenna using patch loading", *Electronics Letters*, vol. 48, pp. 974-975, 2012.
- [153] Krebs C., Warok P., Heinen S., Brauns R., Hommes A., Kose S., *et al.*, "The development of a compact millimeter wave scanning system", in *36th International Conference on Infrared, Millimeter and Terahertz Waves (IRMMW-THz)*, 2011, pp. 1-2.

- [154] Kumar A., "Computer-vision-based fabric defect detection: a survey", *IEEE Transactions on Industrial Electronics*, vol. 55, pp. 348-363, 2008.
- [155] Kumar G. and Bhatia P. K., "A Detailed Review of Feature Extraction in Image Processing Systems", in *Fourth International Conference on Advanced Computing & Communication Technologies (ACCT)*, 2014, pp. 5-12.
- [156] Kumar G. and Gupta K. C., "Nonradiating edges and four edges gap-coupled multiple resonator broad-band microstrip antennas", *IEEE Transactions on Antennas and Propagation*, vol. 33, pp. 173-178, 1985.
- [157] Kumar G. and Ray K., *Broadband microstrip antennas*: Artech House, 2002.
- [158] Kun-Yi G., Hoare E. G., Jasteh D., Xin-Qing S., and Gashinova M., "Road Edge Recognition Using the Stripe Hough Transform From Millimeter-Wave Radar Images", *IEEE Transactions on Intelligent Transportation Systems*, vol. 16, pp. 825-833, 2015.
- [159] Kundu A. and Mitra S. K., "A new algorithm for image edge extraction using a statistical classifier approach", *IEEE Transactions on Pattern Analysis and Machine Intelligence*, pp. 569-577, 1987.
- [160] Kuroki F., Wagatsuma Y., and Yoneyama T., "60 GHz FM-CWR Using NRD guide for distance estimation", *IEEE Aerospace and Electronic Systems Magazine*, vol. 24, pp. 42-45, 2009.
- [161] Lagunas E., Amin M. G., Ahmad F., and Najar M., "Pattern Matching for Building Feature Extraction", *IEEE Geoscience and Remote Sensing Letters*, vol. 11, pp. 2193-2197, 2014.
- [162] Lakshmanan S. and Grimmer D., "A deformable template approach to detecting straight edges in radar images", *IEEE Transactions on Pattern Analysis and Machine Intelligence*, vol. 18, pp. 438-443, 1996.
- [163] Lamb J. W., "Miscellaneous data on materials for millimetre and submillimetre optics", *International Journal of Infrared and Millimeter Waves*, vol. 17, pp. 1997-2034, 1996.
- [164] Lee D.-S., Yeom S., Son J.-Y., and Kim S.-H., "Automatic image segmentation for concealed object detection using the expectation-maximization algorithm", *Optics Express*, vol. 18, pp. 10659-10667, 2010/05/10 2010.
- [165] Lee K. F., Luk K. M., Tong K. F., Shum S. M., Huynh T., and Lee R. Q., "Experimental and simulation studies of the coaxially fed U-slot rectangular patch antenna", *IEE Proceedings on Microwaves, Antennas and Propagation*, vol. 144, pp. 354-358, 1997.

- [166] Lee S. U., Yoon Chung S., and Park R. H., "A comparative performance study of several global thresholding techniques for segmentation", *Computer Vision, Graphics, and Image Processing*, vol. 52, pp. 171-190, 11// 1990.
- [167] Lee W.-S., Jin-Hyun K., Won-Gyu L., Kwang-Seop S., Hyung-sun L., and Jong-Won Y., "Capacitively Coupled Band-Stop Filter with an Integrated Antenna", in *IEEE MTT-S International Microwave Symposium Digest*, 2006, pp. 2019-2022.
- [168] Li Y. and Feng Q., "A compact tri-band monopole antenna with metamaterial loaded for WLAN/WiMAX applications", *Journal of Electromagnetic Waves and Applications*, vol. 27, pp. 772-782, 2013.
- [169] Lim J. S., "Image restoration by short space spectral subtraction", *IEEE Transactions on Acoustics, Speech and Signal Processing*, vol. 28, pp. 191-197, 1980.
- [170] Lin Z. and Melde K. L., "On-wafer measurement of microstrip-based circuits with a broadband vialess transition", *IEEE Transactions on Advanced Packaging*, vol. 29, pp. 654-659, 2006.
- [171] Ling S., Li L., and Xuelong L., "Feature Learning for Image Classification Via Multiobjective Genetic Programming", *IEEE Transactions on Neural Networks and Learning Systems*, vol. 25, pp. 1359-1371, 2014.
- [172] Liu D., Pfeiffer U., Grzyb J., and Gaucher B., *Advanced millimeter-wave technologies: antennas, packaging and circuits*: John Wiley & Sons, 2009.
- [173] Liu G., Law C. L., Rajanik M. J., and Yang H., "A switchable MEMS antenna for 38/60 GHz millimeter wave communications", in *ICMMT 4th International Conference on, Proceedings Microwave and Millimeter Wave Technology*, 2004, pp. 86-89.
- [174] Liu H., Sun L., and Shi Z., "Dual-bandgap characteristics of spurline filters and its circuit modeling", *Microwave and Optical Technology Letters*, vol. 49, pp. 2805-2807, 2007.
- [175] Liu J., Zhang B., and Wu R., "GPR ground bounce removal methods based on blind source separation", *PIERS Online*, vol. 2, pp. 256-259, 2006.
- [176] Liwei W., Xiao W., and Jufu F., "On image matrix based feature extraction algorithms", *IEEE Transactions on Systems, Man, and Cybernetics, Part B: Cybernetics*, vol. 36, pp. 194-197, 2006.
- [177] Long S. A. and Walton M., "A dual-frequency stacked circular-disc antenna", *IEEE Transactions on Antennas and Propagation*, vol. 27, pp. 270-273, 1979.

- [178] Lowe D. G., "Distinctive image features from scale-invariant keypoints", *International journal of computer vision*, vol. 60, pp. 91-110, 2004.
- [179] Lowe D. G., "Object recognition from local scale-invariant features", in *The proceedings of the seventh IEEE international conference on Computer vision*, 1999, pp. 1150-1157.
- [180] Maazi M., Benzaim O., Glay D., and Lasri T., "Detection and Characterization of Buried Macroscopic Cracks Inside Dielectric Materials by Microwave Techniques and Artificial Neural Networks", *IEEE Transactions on Instrumentation and Measurement*, vol. 57, pp. 2819-2826, 2008.
- [181] Maci S. and Gentili G. B., "Dual-frequency patch antennas", *IEEE Antennas and Propagation Magazine*, vol. 39, pp. 13-20, 1997.
- [182] *Millimeter Wave Propagation: Spectrum Management Implications*, F. C. C.-O. O. E. A. TECHNOLOGY, 1997.
- [183] Marcus M. and Pattan B., "Millimeter wave propagation; spectrum management implications", *IEEE Microwave Magazine*, vol. 6, pp. 54-62, 2005.
- [184] Marnat L., Carreno A. A. A., Conchouso D., Martinez M. G., Foulds I. G., and Shamim A., "New Movable Plate for Efficient Millimeter Wave Vertical on-Chip Antenna", *IEEE Transactions on Antennas and Propagation*, vol. 61, pp. 1608-1615, 2013.
- [185] Martinez-Lorenzo J. A., Rodriguez-Vaqueiro Y., Rappaport C. M., Lopez O. R., and Pino A. G., "A compressed sensing approach for detection of explosive threats at standoff distances using a Passive Array of Scatters", in *IEEE Conference on Technologies for Homeland Security (HST)*, 2012, pp. 134-139.
- [186] Martinez-Ros A. J., Gomez-Tornero J. L., and Goussetis G., "Microstrip half-mode leaky-wave antenna operating at 94 GHz", in *IEEE MTT-S International Microwave Workshop Series on Millimeter Wave Integration Technologies (IMWS)*, 2011, pp. 45-48.
- [187] Martinez O., Ferraz L., Binefa X., Gómez I., and Dorronsoro C., "Concealed object detection and segmentation over millimetric waves images", in *IEEE Computer Society Conference on Computer Vision and Pattern Recognition Workshops (CVPRW)*, 2010, pp. 31-37.
- [188] Mashford J., Rahilly M., and Davis P., "An approach using mathematical morphology and support vector machines to detect features in pipe images", in *Digital Image Computing: Techniques and Applications (DICTA)*, 2008, pp. 84-89.

- [189] Mashford J., Rahilly M., Lane B., Marney D., and Burn S., "Edge Detection in Pipe Images Using Classification of Haar Wavelet Transforms", *Applied Artificial Intelligence*, vol. 28, pp. 675-689, 2014.
- [190] Mbairi F. D. and Hesselbom H., "Microwave Bandstop Filters Using Novel Artificial Periodic Substrate Electromagnetic Band Gap Structures", *IEEE Transactions on Components and Packaging Technologies*, vol. 32, pp. 273-282, 2009.
- [191] McMillan R., "Terahertz imaging, millimeter-wave radar", in *Advances in sensing with security applications*, ed: Springer, 2006, pp. 243-268.
- [192] Mead J. B., Pazmany A. L., Sekelsky S. M., and McIntosh R. E., "Millimeter-wave radars for remotely sensing clouds and precipitation", *Proceedings of the IEEE*, vol. 82, pp. 1891-1906, 1994.
- [193] Mehranpour M., Nourinia J., Ghobadi C., and Ojaroudi M., "Dual Band-Notched Square Monopole Antenna for Ultrawideband Applications", *IEEE Antennas and Wireless Propagation Letters*, vol. 11, pp. 172-175, 2012.
- [194] Meriakri V. V. and Von Gratowski S. V., "Millimeter waves for moisture testing and treatment culture objects", in *37th International Conference on Infrared, Millimeter, and Terahertz Waves (IRMMW-THz)*, 2012, pp. 1-1.
- [195] Mikhelson I. V., Lee P., Bakhtiari S., Elmer T. W., Katsaggelos A. K., and Sahakian A. V., "Noncontact Millimeter-Wave Real-Time Detection and Tracking of Heart Rate on an Ambulatory Subject", *IEEE Transactions on Information Technology in Biomedicine*, vol. 16, pp. 927-934, 2012.
- [196] Min-Chun Y., Woo Kyung M., Wang Y. C. F., Min Sun B., Chiun-Sheng H., Jeon-Hor C., *et al.*, "Robust Texture Analysis Using Multi-Resolution Gray-Scale Invariant Features for Breast Sonographic Tumor Diagnosis", *IEEE Transactions on Medical Imaging*, vol. 32, pp. 2262-2273, 2013.
- [197] Ming-yi L., Rodenbeck C. T., and Kai C., "Millimeter-wave dual-beam scanning microstrip patch antenna arrays fed by dielectric image lines", in *IEEE Antennas and Propagation Society International Symposium*, 2002, pp. 196-199 vol.2.
- [198] Minin I. V. and Minin O. V., "Recent Developments in Active Millimeter/Thz Waves High-Quality 3D Imaging for Scientific, Medical and Homeland Security Applications", in *5th International Conference on Microwave Electronics: Measurements, Identification, Applications*, 2005, pp. 161-176.

-
- [199] Mishra A., Singh P., Yadav N. P., Ansari J. A., and Vishvakarma B. R., "Compact shorted microstrip patch antenna for dual band operation", *Progress In Electromagnetics Research C*, vol. 9, pp. 171-182, 2009.
- [200] Mishra P. and Singh D., "A Statistical-Measure-Based Adaptive Land Cover Classification Algorithm by Efficient Utilization of Polarimetric SAR Observables", 2013.
- [201] Mishra P. and Singh D., "A statistical-measure-based adaptive land cover classification algorithm by efficient utilization of polarimetric sar observables", *IEEE Transactions on Geoscience and Remote Sensing*, vol. 52, pp. 2889-2900, 2014.
- [202] Misiti M., Misiti Y., Oppenheim G., and Poggi J.-M., *Wavelets and their Applications*: John Wiley & Sons, 2013.
- [203] Missaoui O., Frigui H., and Gader P., "Land-Mine Detection With Ground-Penetrating Radar Using Multistream Discrete Hidden Markov Models", *IEEE Transactions on Geoscience and Remote Sensing*, vol. 49, pp. 2080-2099, 2011.
- [204] Moallem M. and Sarabandi K., "Polarimetric Study of MMW Imaging Radars for Indoor Navigation and Mapping", *IEEE Transactions on Antennas and Propagation*, vol. 62, pp. 500-504, 2014.
- [205] Mohamed M. A. and Gader P., "Generalized hidden Markov models. II. Application to handwritten word recognition", *IEEE Transactions on Fuzzy Systems*, vol. 8, pp. 82-94, 2000.
- [206] Moll J., Schops P., and Krozer V., "Towards Three-Dimensional Millimeter-Wave Radar With the Bistatic Fast-Factorized Back-Projection Algorithm"; Potential and Limitations", *IEEE Transactions on Terahertz Science and Technology*, vol. 2, pp. 432-440, 2012.
- [207] Monadjemi A., "Towards efficient texture classification and abnormality detection", University of Bristol, 2004.
- [208] Muldavin J. B. and Rebeiz G. M., "Millimeter-wave tapered-slot antennas on synthesized low permittivity substrates", *IEEE Transactions on Antennas and Propagation*, vol. 47, pp. 1276-1280, 1999.
- [209] Nadakuduti J., Chen G., and Zoughi R., "Semiempirical electromagnetic modeling of crack detection and sizing in cement-based materials using near-field microwave

- methods", *IEEE Transactions on Instrumentation and Measurement*, vol. 55, pp. 588-597, 2006.
- [210] Nadernejad E., Sharifzadeh S., and Hassanpour H., "Edge detection techniques: Evaluations and comparison", *Applied Mathematical Sciences*, vol. 2, pp. 1507-1520, 2008.
- [211] Nguyen B. D., Lanteri J., Yonemoto N., Pichot C., and Migliaccio C., "94 GHz printed reflectors using C-shape patches", in *IEEE Antennas and Propagation Society International Symposium*, 2007, pp. 5311-5314.
- [212] Nguyen B. D., Migliaccio C., Pichot C., Yonemoto N., and Yamamoto K., "Compact primary source for W-band reflector antenna", *Electronics Letters*, vol. 41, pp. 1262-1263, 2005.
- [213] Nicolaescu I. and van Genderen P., "Archimedean spiral antenna calibration procedures to increase the downrange resolution of a SFCW radar", *International Journal of Antennas and Propagation*, vol. 2008, 2008.
- [214] Niu Y., Li Y., Jin D., Su L., and Vasilakos A. V., "A Survey of Millimeter Wave (mmWave) Communications for 5G: Opportunities and Challenges", *arXiv preprint arXiv:1502.07228*, 2015.
- [215] Nixon M., *Feature extraction & image processing*: Academic Press, 2008.
- [216] Obeid D., Sadek S., Zaharia G., and Zein G. E., "Noncontact heartbeat detection at 2.4, 5.8, and 60 GHz: A comparative study", *Microwave and Optical Technology Letters*, vol. 51, pp. 666-669, 2009.
- [217] Ojala T., Pietikainen M., and Maenpaa T., "Multiresolution gray-scale and rotation invariant texture classification with local binary patterns", *Pattern Analysis and Machine Intelligence, IEEE Transactions on*, vol. 24, pp. 971-987, 2002.
- [218] Ojala T., Pietikainen M., and Maenpaa T., "Multiresolution gray-scale and rotation invariant texture classification with local binary patterns", *IEEE Transactions on Pattern Analysis and Machine Intelligence*, vol. 24, pp. 971-987, 2002.
- [219] Oka S., Togo H., Kukutsu N., and Nagatsuma T., "Latest trends in millimeter-wave imaging technology", *Progress In Electromagnetics Research Letters*, vol. 1, pp. 197-204, 2008.

- [220] Oliver J. M., Rollin J. M., Vanhille K., and Raman S., "A W-Band Micromachined 3-D Cavity-Backed Patch Antenna Array With Integrated Diode Detector", *IEEE Transactions on Microwave Theory and Techniques*, vol. 60, pp. 284-292, 2012.
- [221] Otsu N., "A threshold selection method from gray-level histograms", *Automatica*, vol. 11, pp. 23-27, 1975.
- [222] Pal N. R. and Pal S. K., "A review on image segmentation techniques", *Pattern Recognition*, vol. 26, pp. 1277-1294, 9// 1993.
- [223] Park J., "Development of microwave and millimeter-wave integrated-circuit stepped-frequency radar sensors for surface and subsurface profiling", Doctoral dissertation, Texas A&M University, 2003.
- [224] Pasolli E., Melgani F., and Donelli M., "Automatic Analysis of GPR Images: A Pattern-Recognition Approach", *IEEE Transactions on Geoscience and Remote Sensing*, vol. 47, pp. 2206-2217, 2009.
- [225] Pastorino M., Caorsi S., and Massa A., "A global optimization technique for microwave nondestructive evaluation", *IEEE Transactions on Instrumentation and Measurement*, vol. 51, pp. 666-673, 2002.
- [226] Pastorino M., Caorsi S., and Massa A., "A global optimization technique for microwave nondestructive evaluation", *Instrumentation and Measurement, IEEE Transactions on*, vol. 51, pp. 666-673, 2002.
- [227] Patrovsky A. and Ke W., "94-GHz Planar Dielectric Rod Antenna With Substrate Integrated Image Guide (SIIG) Feeding", *IEEE Antennas and Wireless Propagation Letters*, vol. 5, pp. 435-437, 2006.
- [228] Peck R., Olsen, C. and Devore, J., *Introduction to Statistics and data analysis*, 4 ed. Singapore: Duxbery Thomson Learning, 2001.
- [229] Peng C., Fei W., Li-Feng S., Jian-Wei Z., and Shi-Qiang Y., "A Matrix-Based Approach to Unsupervised Human Action Categorization", *IEEE Transactions on Multimedia*, vol. 14, pp. 102-110, 2012.
- [230] Perantonis S. J. and Lisboa P. J. G., "Translation, rotation, and scale invariant pattern recognition by high-order neural networks and moment classifiers", *IEEE Transactions on Neural Networks*, vol. 3, pp. 241-251, 1992.
- [231] Person C., "Antennas on Silicon for millimeterwave applications - Status and trends", in *IEEE Bipolar/BiCMOS Circuits and Technology Meeting (BCTM)*, 2010, pp. 180-183.

- [232] Peter J. S., *Nondestructive Evaluation: Theory, Techniques, and Applications*: CRC Press, 2002.
- [233] Petkie D. T., De Lucia F. C., Castro C., Helminger P., Jacobs E. L., Moyer S. K., *et al.*, "Active and passive millimeter-and sub-millimeter-wave imaging", in *European Symposium on Optics and Photonics for Defence and Security*, 2005, pp. 598918-598918-8.
- [234] Pham T. A., "Optimization of Texture Feature Extraction Algorithm", TU Delft, Delft University of Technology, 2010.
- [235] Pi Z. and Khan F., "An introduction to millimeter-wave mobile broadband systems", *IEEE Communications Magazine*, vol. 49, pp. 101-107, 2011.
- [236] Pla-Rucki G. F. and Eberhard M. O., "Imaging of reinforced concrete: State-of-the-art review", *Journal of infrastructure systems*, vol. 1, pp. 134-141, 1995.
- [237] Ponchak G. E., Tentzeris E. M., and Katehi L. P., "Characterization of finite ground coplanar waveguide with narrow ground planes", *International Journal of Microcircuits and Electronic Packaging*, vol. 20, pp. 167-173, 1997.
- [238] Pozar D. M., "Considerations for millimeter wave printed antennas", *IEEE Transactions on Antennas and Propagation*, vol. 31, pp. 740-747, 1983.
- [239] Pozar D. M., *Microwave Engineering*. New York: John Wiley & Sons, 2004.
- [240] Prasanna P., Dana K., Gucunski N., and Basily B., "Computer-vision based crack detection and analysis", in *SPIE Smart Structures and Materials+ Nondestructive Evaluation and Health Monitoring*, 2012, pp. 834542-834542-6.
- [241] Pucci E., Rajo-Iglesias E., Kehn M. N. M., and Quevedo-Teruel O., "Enhancing the Efficiency of Compact Patch Antennas Composed of Split-Ring Resonators by Using Lumped Capacitors", *Antennas and Wireless Propagation Letters, IEEE*, vol. 11, pp. 1362-1365, 2012.
- [242] Pursula P., Vaha-Heikkila T., Muller A., Neculoiu D., Konstantinidis G., Oja A., *et al.*, "Millimeter-Wave Identification—A New Short-Range Radio System for Low-Power High Data-Rate Applications", *IEEE Transactions on Microwave Theory and Techniques*, vol. 56, pp. 2221-2228, 2008.
- [243] Pyun K. P., Johan L., Chee Sun W., and Gray R. M., "Image Segmentation Using Hidden Markov Gauss Mixture Models", *IEEE Transactions on Image Processing*, vol. 16, pp. 1902-1911, 2007.

-
- [244] Qing S. and Xue-Xia Z., "A study on wideband gap-coupled microstrip antenna arrays", *IEEE Transactions Antennas and Propagation*, vol. 43, pp. 313-317, 1995.
- [245] Raman S., Weller T. M., Katchi L. P. B., and Rebeiz G. M., "A double folded-slot antenna at 94 GHz", in *AP-S. Digest Antennas and Propagation Society International Symposium*, 1995, pp. 710-713 vol.1.
- [246] Ramuhalli P., Kim J., Udpa L., and Udpa S. S., "Multichannel signal processing methods for ultrasonic nondestructive evaluation", in *Sensor Array and Multichannel Signal Processing Workshop Proceedings*, 2002, pp. 229-233.
- [247] Raskin J. P., Gauthier G., Katehi L. P., and Rebeiz G. M., "Mode conversion at GCPW-to-microstrip-line transitions", *IEEE Transactions on Microwave Theory and Techniques*, vol. 48, pp. 158-161, 2000.
- [248] Ratto C. R., Torrione P. A., and Collins L. M., "Exploiting Ground-Penetrating Radar Phenomenology in a Context-Dependent Framework for Landmine Detection and Discrimination", *IEEE Transactions on Geoscience and Remote Sensing*, vol. 49, pp. 1689-1700, 2011.
- [249] Richards W. F., Davidson S., and Long S. A., "Dual-band reactively loaded microstrip antenna", *IEEE Transactions on Antennas and Propagation*, vol. 33, pp. 556-561, 1985.
- [250] Rodriguez-Vaqueiro Y., Alvarez Lopez Y., Gonzalez-Valdes B., Martinez J. A., Las-Heras F., and Rappaport C. M., "On the Use of Compressed Sensing Techniques for Improving Multistatic Millimeter-Wave Portal-Based Personnel Screening", *IEEE Transactions on Antennas and Propagation*, vol. 62, pp. 494-499, 2014.
- [251] Rowley H. A., Baluja S., and Kanade T., "Neural network-based face detection", *IEEE Transactions on Pattern Analysis and Machine Intelligence*, vol. 20, pp. 23-38, 1998.
- [252] Rumelhart D. E., Hinton G. E., and Williams R. J., "Learning internal representations by error propagation", in *Parallel distributed processing: explorations in the microstructure of cognition, vol. 1*, E. R. David, L. M. James, and C. P. R. Group, Eds., ed: MIT Press, 1986, pp. 318-362.
- [253] Sahoo P. K., Soltani S., and Wong A. K. C., "A survey of thresholding techniques", *Computer Vision, Graphics, and Image Processing*, vol. 41, pp. 233-260, 2// 1988.
- [254] Salvador C., Borselli L., Falciani A., and Maci S., "Dual frequency planar antenna at S and X bands", *Electronics Letters*, vol. 31, pp. 1706-1707, 1995.

- [255] Sanchez-Hernandez D. and Robertson I., "Triple band microstrip patch antenna using a spur-line filter and a perturbation segment technique", *Electronics Letters*, vol. 29, pp. 1565-1566, 1993.
- [256] Sanchez-Hernandez D. and Robertson I. D., "Analysis and design of a dual-band circularly polarized microstrip patch antenna", *IEEE Transactions on Antennas and Propagation*, vol. 43, pp. 201-205, 1995.
- [257] Sanchez-Hernandez D., Wang Q. H., Rezazadeh A. A., and Robertson I. D., "Millimeter-wave dual-band microstrip patch antennas using multilayer GaAs technology", *IEEE Transactions on Microwave Theory and Techniques*, vol. 44, pp. 1590-1593, 1996.
- [258] Sarabandi K. and Moonsoo P., "Extraction of power line maps from millimeter-wave polarimetric SAR images", *IEEE Transactions on Antennas and Propagation*, vol. 48, pp. 1802-1809, 2000.
- [259] Sato K., Manabe T., Polivka J., Ihara T., Kasashima Y., and Yamaki K., "Measurement of the complex refractive index of concrete at 57.5 GHz", *IEEE Transactions on Antennas and Propagation*, vol. 44, pp. 35-40, 1996.
- [260] Sato M., Hirose T., Kobayashi H., Sato H., Sawaya K., and Mizuno K., "Tapered slot antennas with MMIC for 94 GHz band passive millimeter-wave imager", in *Proc. Int. Symp. Antennas and Propagation, Japan, 2007*, pp. 1023-1026.
- [261] Sato M., Liu H., Koyama C., and Takahashi K., "Fundamental Study on NDT of Building Wall Structure by Radar", in *EWSHM-7th European Workshop on Structural Health Monitoring, 2014*.
- [262] Sato M., Liu H., Koyama C., and Takahashi K., "Fundamental Study on NDT of Building Wall Structure by Radar", in *EWSHM - 7th European Workshop on Structural Health Monitoring, Nantes, France, 2014*.
- [263] Savelyev T. G., van Kempen L., Sahli H., Sachs J., and Sato M., "Investigation of Time–Frequency Features for GPR Landmine Discrimination", *IEEE Transactions on Geoscience and Remote Sensing*, vol. 45, pp. 118-129, 2007.
- [264] Schaller S., Wildberger J. E., Raupach R., Niethammer M., Klingenbeck-Regn K., and Flohr T., "Spatial domain filtering for fast modification of the tradeoff between image sharpness and pixel noise in computed tomography", *IEEE Transactions on Medical Imaging*, vol. 22, pp. 846-853, 2003.

-
- [265] Schnieder F., Tischler T., and Heinrich W., "Modeling dispersion and radiation characteristics of conductor-backed CPW with finite ground width", *IEEE Transactions on Microwave Theory and Techniques*, vol. 51, pp. 137-143, 2003.
- [266] Schoebel J. and Herrero P., *Planar antenna technology for mm-wave automotive radar, sensing, and communications*: INTECH Open Access Publisher, 2010.
- [267] Sezgin M. and Sankur B. I., "Survey over image thresholding techniques and quantitative performance evaluation", *Journal of Electronic Imaging*, vol. 13, pp. 146-168, 2004.
- [268] Shahbeig S., "Automatic and quick blood vessels extraction algorithm in retinal images", *IET Image Processing*, vol. 7, pp. 392-400, 2013.
- [269] Sheela K. G. and Deepa S. N., "Review on Methods to Fix Number of Hidden Neurons in Neural Networks", *Mathematical Problems in Engineering*, vol. 2013, p. 11, 2013.
- [270] Sheen D. M., McMakin D. L., and Hall T. E., "Active millimeter-wave and sub-millimeter-wave imaging for security applications", in *36th International Conference on Infrared, Millimeter and Terahertz Waves (IRMMW-THz)*, 2011, pp. 1-3.
- [271] Sheen D. M., McMakin D. L., and Hall T. E., "Three-dimensional millimeter-wave imaging for concealed weapon detection", *Microwave Theory and Techniques, IEEE Transactions on*, vol. 49, pp. 1581-1592, 2001.
- [272] Sheen D. M., McMakin D. L., and Hall T. E., "Three-dimensional millimeter-wave imaging for concealed weapon detection", *IEEE Transactions on Microwave Theory and Techniques*, vol. 49, pp. 1581-1592, 2001.
- [273] Sheen D. M., McMakin D. L., Hall T. E., and Severtsen R. H., "Active millimeter-wave standoff and portal imaging techniques for personnel screening", in *Technologies for Homeland Security, 2009. HST '09. IEEE Conference on*, 2009, pp. 440-447.
- [274] Sheen D. M., McMakin D. L., Hall T. E., and Severtsen R. H., "Active millimeter-wave standoff and portal imaging techniques for personnel screening", in *IEEE Conference on Technologies for Homeland Security*, 2009, pp. 440-447.
- [275] Shireen R., Hwang T., Shi S., and Prather D. W., "Stacked patch excited horn antenna at 94 GHz", *microwave and optical technology letters*, vol. 50, pp. 2071-2074, 2008.
- [276] Shiu Hang T., Hall P. S., Hoare E. G., and Clarke N. J., "Advance Path Measurement for Automotive Radar Applications", *IEEE Transactions on Intelligent Transportation Systems*, vol. 7, pp. 273-281, 2006.

- [277] Si L. M., Zhu W., and Sun H. J., "A Compact, Planar, and CPW-Fed Metamaterial-Inspired Dual-Band Antenna", *IEEE Antennas and Wireless Propagation Letters*, vol. 12, pp. 305-308, 2013.
- [278] Sinha S. K. and Karray F., "Classification of underground pipe scanned images using feature extraction and neuro-fuzzy algorithm", *IEEE Transactions on Neural Networks*, vol. 13, pp. 393-401, 2002.
- [279] Smith L. I., "A tutorial on principal components analysis", *Cornell University, USA*, vol. 51, p. 52, 2002.
- [280] Smriti Agarwal D. S., Nagendra P. Pathak "Active millimeter wave radar system for non-destructive, non-invasive underline fault detection and multilayer material analysis", presented at the International Microwave and RF Conference (IMaRC) Bangalore, India, 2014.
- [281] Sosa E. G., "Feature extraction for biometric recognition using millimetre-wave images", Madrid, 2013.
- [282] Stotz M., Gottwald G., Haspeklo H., and Wenger J., "Planar millimeter-wave antennas using SiN_x-membranes on GaAs", *IEEE Transactions on Microwave Theory and Techniques*, vol. 44, pp. 1593-1595, 1996.
- [283] Strohm K. M., Buechler J., Kasper E., Luy J. F., and Russer P., "Millimeter wave transmitter and receiver circuits on high resistivity silicon", in *IEE Colloquium on Microwave and Millimetre Wave Monolithic Integrated Circuits*, 1988, pp. 11/1-11/4.
- [284] Szeliski R., *Computer vision: algorithms and applications*: Springer Science & Business Media, 2010.
- [285] Ta-Yeh L., Tsenchieh C., and Da-Chiang C., "Design of Dual-Band Millimeter-Wave Antenna-in-Package Using Flip-Chip Assembly", *IEEE Transactions on Components, Packaging and Manufacturing Technology*, vol. 4, pp. 385-391, 2014.
- [286] Taehyung L. and Chang Ouk K., "Statistical Comparison of Fault Detection Models for Semiconductor Manufacturing Processes", *IEEE Transactions on Semiconductor Manufacturing*, vol. 28, pp. 80-91, 2015.
- [287] Tan W., Hong W., Wang Y., and Wu Y., "A novel spherical-wave three-dimensional imaging algorithm for microwave cylindrical scanning geometries", *Progress In Electromagnetics Research*, vol. 111, pp. 43-70, 2011.
- [288] Taylor J. D., *Ultra-wideband radar technology*: CRC press, 2000.

- [289] Tello Alonso M., Lopez-Martinez C., Mallorqui J. J., and Salembier P., "Edge Enhancement Algorithm Based on the Wavelet Transform for Automatic Edge Detection in SAR Images", *IEEE Transactions on Geoscience and Remote Sensing*, vol. 49, pp. 222-235, 2011.
- [290] Thakur J. P., Kim W.-G., and Kim Y.-H., "Large aperture low aberration aspheric dielectric lens antenna for W-band quasi-optics", *Progress In Electromagnetics Research*, vol. 103, pp. 57-65, 2010.
- [291] Tien C. C., Tzuang C. K. C., Peng S. T., and Chung-Chi C., "Transmission characteristics of finite-width conductor-backed coplanar waveguide", *IEEE Transactions on Microwave Theory and Techniques*, vol. 41, pp. 1616-1624, 1993.
- [292] Torres-Mendez L. A., Ruiz-Suarez J. C., Sucar L. E., and Gomez G., "Translation, rotation, and scale-invariant object recognition", *IEEE Transactions on Systems, Man, and Cybernetics, Part C: Applications and Reviews*, vol. 30, pp. 125-130, 2000.
- [293] Torrione P. and Collins L. M., "Texture Features for Antitank Landmine Detection Using Ground Penetrating Radar", *IEEE Transactions on Geoscience and Remote Sensing*, vol. 45, pp. 2374-2382, 2007.
- [294] Torrione P. A., Morton K. D., Sakaguchi R., and Collins L. M., "Histograms of oriented gradients for landmine detection in ground-penetrating radar data", *Geoscience and Remote Sensing, IEEE Transactions on*, vol. 52, pp. 1539-1550, 2014.
- [295] Torrione P. A., Morton K. D., Sakaguchi R., and Collins L. M., "Histograms of Oriented Gradients for Landmine Detection in Ground-Penetrating Radar Data", *IEEE Transactions on Geoscience and Remote Sensing*, vol. 52, pp. 1539-1550, 2014.
- [296] Trokhimovski Y. G., Westwater E. R., Yong H., and Leuski V. Y., "Air and sea surface temperature measurements using a 60-GHz microwave rotating radiometer", *IEEE Transactions on Geoscience and Remote Sensing*, vol. 36, pp. 3-15, 1998.
- [297] Tsaipai W., Keller J. M., Gader P. D., and Sjahputera O., "Frequency Subband Processing and Feature Analysis of Forward-Looking Ground-Penetrating Radar Signals for Land-Mine Detection", *IEEE Transactions on Geoscience and Remote Sensing*, vol. 45, pp. 718-729, 2007.
- [298] Turhan-Sayan G., "Real time electromagnetic target classification using a novel feature extraction technique with PCA-based fusion", *IEEE Transactions on Antennas and Propagation*, vol. 53, pp. 766-776, 2005.

- [299] Tuytelaars T. and Mikolajczyk K., "Local invariant feature detectors: a survey", *Foundations and Trends® in Computer Graphics and Vision*, vol. 3, pp. 177-280, 2008.
- [300] Van den Bulcke S. and Franchois A., "A Full-Wave 2.5D Volume Integral Equation Solver for 3D Millimeter-Wave Scattering by Large Inhomogeneous 2D Objects", *IEEE Transactions on Antennas and Propagation*, vol. 57, pp. 535-545, 2009.
- [301] Van der Merwe A., Gupta I. J., and Peters Jr L., "Clutter reduction technique for GPR data from minelike targets", in *AeroSense'99*, 1999, pp. 1094-1105.
- [302] Verma P. K., Gaikwad A. N., Singh D., and Nigam M. J., "Analysis of clutter reduction techniques for through wall imaging in UWB range", *Progress In Electromagnetics Research B*, vol. 17, pp. 29-48, 2009.
- [303] Vertiy A., Cetinkaya H., Panin S., Pavlyuchenko A., Tekbas M., Unal A., *et al.*, "Image reconstruction in SAR, ISAR and tomography applications at millimeter-wave band", in *Microwaves, Radar and Remote Sensing Symposium (MRRS)*, 2011, pp. 184-189.
- [304] Veysi M., Kamyab M., and Jafarholi A., "Single-Feed Dual-Band Dual-Linearly-Polarized Proximity-Coupled Patch Antenna", *IEEE Antennas and Propagation Magazine*, vol. 53, pp. 90-96, 2011.
- [305] Vizard D. R. and Doyle R., "Invited Paper : Advances in Millimeter Wave Imaging and Radar Systems for Civil Applications", in *IEEE MTT-S International Microwave Symposium Digest*, 2006, pp. 94-97.
- [306] Wall M., Rechtsteiner A., and Rocha L., "Singular Value Decomposition and Principal Component Analysis", in *A Practical Approach to Microarray Data Analysis*, ed: Springer US, 2003, pp. 91-109.
- [307] Wang J., Fralich R., Wu C., and Litva J., "Multifunctional aperture coupled stack patch antenna", *Electronics Letters*, vol. 26, pp. 2067-2068, 1990.
- [308] Wang Y. and Lancaster M. J., "Coplanar to microstrip transitions for on-wafer measurements", *Microwave and Optical Technology Letters*, vol. 49, pp. 100-103, 2007.
- [309] Wang Y., Mei T., Gong S., and Hua X.-S., "Combining global, regional and contextual features for automatic image annotation", *Pattern Recognition*, vol. 42, pp. 259-266, 2// 2009.
- [310] Wang Y. and Qi L., "NRD leaky-wave antenna for narrow beams in 94GHz", *International Journal of Infrared and Millimeter Waves*, vol. 16, pp. 2019-2024, 1995/11/01 1995.

-
- [311] Watabe K., Shimizu K., Yoneyama M., and Koji M., "Millimeter-wave active imaging using neural networks for signal processing", *IEEE Transactions on Microwave Theory and Techniques*, vol. 51, pp. 1512-1516, 2003.
- [312] Watanabe S. and Yoneyama M., "Ultrasonic robot eyes using neural networks", *IEEE Transactions on Ultrasonics, Ferroelectrics, and Frequency Control*, vol. 37, pp. 141-147, 1990.
- [313] Weigand S., Huff G. H., Pan K. H., and Bernhard J. T., "Analysis and design of broadband single-layer rectangular U-slot microstrip patch antennas", *IEEE Transactions on Antennas and Propagation*, vol. 51, pp. 457-468, 2003.
- [314] Wen-Chung L., Chao-Ming W., and Yen-Jui T., "Parasitically Loaded CPW-Fed Monopole Antenna for Broadband Operation", *IEEE Transactions on Antennas and Propagation*, vol. 59, pp. 2415-2419, 2011.
- [315] Wen-Shyang C., "Single-feed dual-frequency rectangular microstrip antenna with square slot", *Electronics Letters*, vol. 34, pp. 231-232, 1998.
- [316] Wenbin S., Bouzerdoum A., and Son Lam P., "Sparse Representation of GPR Traces With Application to Signal Classification", *IEEE Transactions on Geoscience and Remote Sensing*, vol. 51, pp. 3922-3930, 2013.
- [317] Wenbin S., Bouzerdoum A., Son Lam P., Lijun S., Indraratna B., and Rujikiatkamjorn C., "Automatic Classification of Ground-Penetrating-Radar Signals for Railway-Ballast Assessment", *IEEE Transactions on Geoscience and Remote Sensing*, vol. 49, pp. 3961-3972, 2011.
- [318] Wenji Z. and Hoorfar A., "Three-Dimensional Real-Time Through-the-Wall Radar Imaging With Diffraction Tomographic Algorithm", *IEEE Transactions on Geoscience and Remote Sensing*, vol. 51, pp. 4155-4163, 2013.
- [319] Wesolkowski S., Dony R. D., and Jernigan M., "Global color image segmentation strategies: Euclidean distance vs. vector angle", in *Proceedings of the IEEE Signal Processing Society Workshop*, 1999, pp. 419-428.
- [320] West J. B., Herting B. J., and Mather J. C., "Measured Results of a Dual-Band Dual-Mode Millimeter Wave Analog EMXT Waveguide Phase Shifter Electronically Scanned Antenna (ESA)", *IEEE Antennas and Wireless Propagation Letters*, vol. 5, pp. 7-10, 2006.

- [321] Weszka J. S. and Rosenfeld A., "Threshold evaluation techniques", *IEEE Transactions on Systems, Man and Cybernetics*, vol. 8, pp. 622-629, 1978.
- [322] Wong K.-L., *Compact and broadband microstrip antennas* vol. 168: John Wiley & Sons, 2004.
- [323] Wu B.-F., Kao C.-C., Jen C.-L., Li Y.-F., Chen Y.-H., and Juang J.-H., "A Relative-Discriminative-Histogram-of-Oriented-Gradients-Based Particle Filter Approach to Vehicle Occlusion Handling and Tracking", *IEEE Transactions on Industrial Electronics*, vol. 61, pp. 4228-4237, 2014.
- [324] Xiabi L., Ling M., Li S., Yanfeng Z., Xinming Z., and Chunwu Z., "Recognizing Common CT Imaging Signs of Lung Diseases Through a New Feature Selection Method Based on Fisher Criterion and Genetic Optimization", *IEEE Journal of Biomedical and Health Informatics*, vol. 19, pp. 635-647, 2015.
- [325] Xiang G., Chao L., Shengming G., and Guangyou F., "Study of a New Millimeter-Wave Imaging Scheme Suitable for Fast Personal Screening", *IEEE Antennas and Wireless Propagation Letters*, vol. 11, pp. 787-790, 2012.
- [326] Xiaoming L. and Jinshan T., "Mass Classification in Mammograms Using Selected Geometry and Texture Features, and a New SVM-Based Feature Selection Method", *IEEE Systems Journal*, vol. 8, pp. 910-920, 2014.
- [327] Xie X., "A review of recent advances in surface defect detection using texture analysis techniques", *Electronic Letters on Computer Vision and Image Analysis*, vol. 7, 2008.
- [328] Xilin S., Dietlein C. R., Grossman E., Popovic Z., and Meyer F. G., "Detection and Segmentation of Concealed Objects in Terahertz Images", *IEEE Transactions on Image Processing*, vol. 17, pp. 2465-2475, 2008.
- [329] Yamasaki H., Awaka J., Takahashi A., Okamoto K., and Ihara T., "Measurement of soil backscattering with a 60-GHz scatterometer", *IEEE Transactions on Geoscience and Remote Sensing*, vol. 30, pp. 761-766, 1992.
- [330] Yang F., Qian Y., and Itoh T., "Low-profile cavity-backed slot antenna using UC-PBG substrate", in *IEEE Antennas and Propagation Society International Symposium*, 2000, pp. 1796-1799 vol.3.
- [331] Yang F. R., Coccioli R., Qian Y., and Itoh T., "PBG-assisted gain enhancement of patch antennas on high-dielectric constant substrate", in *IEEE Antennas and Propagation Society International Symposium*, 1999, pp. 1920-1923 vol.3.

- [332] Yang M., Kpalma K., and Ronsin J., "A survey of shape feature extraction techniques", *Pattern recognition*, pp. 43-90, 2008.
- [333] Yeom S., Lee D.-S., Son J.-Y., Jung M.-K., Jang Y., Jung S.-W., *et al.*, "Real-time outdoor concealed-object detection with passive millimeter wave imaging", *Optics Express*, vol. 19, pp. 2530-2536, 2011/01/31 2011.
- [334] Yigit E., Demirci S., Unal A., Ozdemir C., and Vertiy A., "Millimeter-wave ground-based synthetic aperture radar imaging for foreign object debris detection: experimental studies at short ranges", *Journal of Infrared, Millimeter, and Terahertz Waves*, vol. 33, pp. 1227-1238, 2012.
- [335] Yigit E., Unal A., Kaya A., Demirci S., Cetinkaya H., Ozdemir C., *et al.*, "Millimeter-wave ground based synthetic aperture radar measurements", in *XXXth URSI General Assembly and Scientific Symposium*, 2011, pp. 1-4.
- [336] Yin H., "The self-organizing maps: Background, theories, extensions and applications", in *Computational intelligence: A compendium*, ed: Springer, 2008, pp. 715-762.
- [337] Yizhong W., Ying B., Zhiguo S., Jiming C., and Youxian S., "A Novel Range Detection Method for 60GHz LFMCW Radar", in *IEEE 72nd Vehicular Technology Conference Fall (VTC 2010-Fall)*, 2010, pp. 1-5.
- [338] Yngvesson K. S., "Review of integrated millimeter wave tapered slot antennas and arrays", in *Antennas and Propagation Society International Symposium*, 1990, pp. 1406-1408 vol.4.
- [339] Yngvesson K. S., Korzeniowski T. L., Young-Sik K., Kollberg E. L., and Johansson J. F., "The tapered slot antenna-a new integrated element for millimeter-wave applications", *IEEE Transactions on Microwave Theory and Techniques*, vol. 37, pp. 365-374, 1989.
- [340] Yoda H., Ohuchi Y., Taniguchi Y., and Ejiri M., "An automatic wafer inspection system using pipelined image processing techniques", *IEEE Transactions on Pattern Analysis and Machine Intelligence*, vol. 10, pp. 4-16, 1988.
- [341] Yong-Hyun B., Le Huu T., Sun-Woo P., Sang-Jin L., Yeon-sik C., Eung-Ho R., *et al.*, "94-GHz Log-Periodic Antenna on GaAs Substrate Using Air-Bridge Structure", *IEEE Antennas and Wireless Propagation Letters*, vol. 8, pp. 909-911, 2009.
- [342] Yong-Xin G., Luk K.-M., Lee K. F., and Chair R., "A quarter-wave U-shaped patch antenna with two unequal arms for wideband and dual-frequency operation", *IEEE Transactions on Antennas and Propagation*, vol. 50, pp. 1082-1087, 2002.

- [343] Yong H. and Kap Luk C., "Texture decomposition by harmonics extraction from higher order statistics", *IEEE Transactions on Image Processing*, vol. 13, pp. 1-14, 2004.
- [344] Young-Jin P., Herschlein A., and Wiesbeck W., "A photonic bandgap (PBG) structure for guiding and suppressing surface waves in millimeter-wave antennas", *IEEE Transactions on Microwave Theory and Techniques*, vol. 49, pp. 1854-1859, 2001.
- [345] Yu-Chin O. and Rebeiz G. M., "Differential Microstrip and Slot-Ring Antennas for Millimeter-Wave Silicon Systems", *IEEE Transactions on Antennas and Propagation*, vol. 60, pp. 2611-2619, 2012.
- [346] Yu-Chin O. and Rebeiz G. M., "On-Chip Slot-Ring and High-Gain Horn Antennas for Millimeter-Wave Wafer-Scale Silicon Systems", *IEEE Transactions on Microwave Theory and Techniques*, vol. 59, pp. 1963-1972, 2011.
- [347] Yu Jian C., Wei H., and Ke W., "94 GHz Substrate Integrated Monopulse Antenna Array", *IEEE Transactions on Antennas and Propagation*, vol. 60, pp. 121-129, 2012.
- [348] Yu T.-Y. and Büyükoztürk O., "A far-field airborne radar NDT technique for detecting debonding in GFRP-retrofitted concrete structures", *NDT & E International*, vol. 41, pp. 10-24, 1// 2008.
- [349] Zelong X., Jianzhong X., and Taiyang H., "Research on the transmissivity of some clothing materials at millimeter-wave band", in *International Conference on Microwave and Millimeter Wave Technology*, 2008, pp. 1750-1753.
- [350] Zeng G., "Image reconstruction—a tutorial", *Computerized Medical Imaging and Graphics*, vol. 25, pp. 97-103, 2001.
- [351] Zhadobov M., Chahat N., Sauleau R., Le Quement C., and Le Drean Y., "Millimeter-wave interactions with the human body: state of knowledge and recent advances", *International Journal of Microwave and Wireless Technologies*, vol. 3, pp. 237-247, 2011.
- [352] Zhang L., Hao Y., and Parini C. G., "Millimetre wave imaging system parameters at 95 GHz", *IET Microwaves, Antennas & Propagation*, vol. 5, pp. 528-534, 2011.
- [353] Zhang Y. and Wu L., "Optimal multi-level thresholding based on maximum Tsallis entropy via an artificial bee colony approach", *Entropy*, vol. 13, pp. 841-859, 2011.
- [354] Zhang Y. J., "A survey on evaluation methods for image segmentation", *Pattern Recognition*, vol. 29, pp. 1335-1346, 8// 1996.

- [355] Zoughi R., "Review of NDT Techniques at Radio and Microwave Frequencies", in *Review of Progress in Quantitative Nondestructive Evaluation*, D. Thompson and D. Chimenti, Eds., ed: Springer US, 1989, pp. 337-344.
- [356] Zoughi R. and Ganchev S., "Microwave Nondestructive Evaluation: State-of-the-Art Review", DTIC Document1995.
- [357] Zoughi R. and Kharkovsky S., "Microwave and millimetre wave sensors for crack detection", *Fatigue & Fracture of Engineering Materials & Structures*, vol. 31, pp. 695-713, 2008.
- [358] Zwick T., Baks C., Pfeiffer U. R., Duixian L., and Gaucher B. P., "Probe based MMW antenna measurement setup", in *IEEE Antennas and Propagation Society International Symposium*, 2004, pp. 747-750 Vol.1.